



Studienabschlussarbeiten

Fakultät für Physik

Gröters, David:

Diffraction-limited Imaging and Trapping of Ultracold Ytterbium Atoms in Optical Tweezer Arrays

Masterarbeit, Wintersemester 2023

Gutachter*in: Hebbe Madhusudhana, Bharath und Darkwah Oppong, Nelson

Fakultät für Physik

Lehrstuhl für Quantenphysik

Master Physik

Ludwig-Maximilians-Universität München

<https://doi.org/10.5282/ubm/epub.108487>

Diffraction-limited Imaging and Trapping of Ultracold Ytterbium Atoms in Optical Tweezer Arrays

Master Thesis
David Gröters



Supervisors:

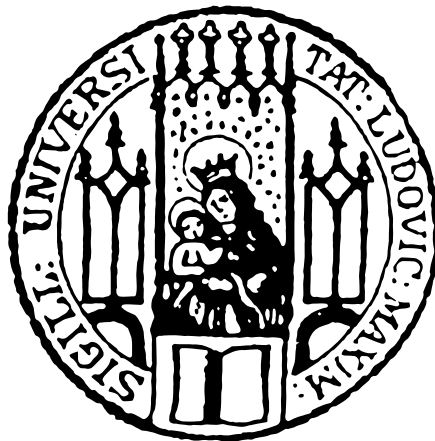
Dr. Bharath Hebbe Madhusudhana, Dr. Nelson Darkwah Oppong

January 5, 2023

Chair for Quantum Optics
Prof. Dr. Monika Aidelsburger
Ludwig-Maximilians-Universität München

Beugungslimitiertes Abbilden und Fangen von ultrakalten Ytterbium Atomen in optischen Pinzetten

Masterarbeit
David Gröters



Betreuer:
Dr. Bharath Hebbe Madhusudhana, Dr. Nelson Darkwah Oppong

January 5, 2023

Lehrstuhl für Quantenoptik
Prof. Dr. Monika Aidelsburger
Ludwig-Maximilians-Universität München

Abstract

A new path for quantum gas experiments with high resolution is a combination of the advantages of highly uniform optical lattices with the flexibility offered by optical tweezer arrays. Those hybrid tweezer lattices require performant microscope objectives that can simultaneously image individual atoms in the optical lattice and generate diffraction-limited optical tweezers for single-site addressing. In this thesis the imaging performance is characterized for two custom made high-resolution objectives at 399 and 532 nm as well as the tweezer-generation capabilities with 532 nm light. To this end, we build and optimize an optical test setup that can perform automated focus scans with sub-wavelength axial step size to test the objective point spread function and optical tweezer generation. We confirm diffraction-limited operation in both cases for each objective and in a field of view of $100 \times 100 \mu\text{m}$. Furthermore we generate 2D tweezer arrays using two acousto-optical deflectors in a crossed configuration and characterize their shape in 3D. An in-depth discussion on the error estimates and various compensation techniques used for analysis is presented as well. Finally, we successfully integrate the objective into the main setup including the trapping and imaging of ultracold ytterbium atoms in a 5×5 optical tweezer array.

Zusammenfassung

Ein neuer Weg für hochauflösende Quantengas-Experimente ist die Verbindung der Vorteile von ultra-gleichmäßigen optischen Gittern mit der Flexibilität von optischen Pinzetten. Solche hybriden Pinzettengitter verlangen nach hochwertigen Mikroskopobjektiven, die gleichzeitig einzelne Atome in einem optischen Gitter abbilden und beugungslimitierte optische Pinzetten für räumlich aufgelöstes Adressieren erzeugen können müssen. In dieser Masterarbeit charakterisieren wir die Abbildungsqualität für unsere beiden maßangefertigten hochauflösenden Objektivs bei 399 und 532 nm, sowie die Fähigkeit, Pinzetten mit 532-nm-Licht zu erzeugen. Dazu haben wir optische Testaufbauten vorbereitet und optimiert, um automatische Fokus-Abtastungen mit Schrittweite unterhalb der Wellenlänge des Lichts zu ermöglichen, mit denen die Punktspreizfunktion bzw. die optischen Pinzetten der Objektivs getestet werden können. Wir bestätigen den beugungslimitierten Betrieb für beide Fälle und Objektivs innerhalb eines Sichtfeldes von $100 \times 100 \mu\text{m}$. Des Weiteren erzeugten wir zweidimensionale Gitter aus optischen Pinzetten mithilfe von zwei gekreuzten akusto-optischen Deflektoren und charakterisierten ihre Form in drei Dimensionen. Eine tiefgreifende Diskussion zu den Fehlerquellen und den verschiedenen Kompensationstechniken, die in der Analyse eingesetzt wurden, ist ebenfalls dargestellt. Zuletzt wird die erfolgreiche Integration der Objektivs in den Hauptaufbau beschrieben, inklusive dem Fangen und Abbilden von ultrakalten Ytterbium Atomen in einem 5×5 optischen Pinzetten-Gitter.

Contents

List of Figures	ix
List of Tables	xii
List of Symbols	xv
List of Acronyms	xvii
1 Introduction	1
2 Background and theory	5
2.1 Ytterbium hybrid tweezer lattice	5
2.2 High-resolution imaging	6
2.2.1 Foci and imaging in geometrical optics	6
2.2.2 Spatially confining light - the diffraction limit	10
2.2.3 Optical aberrations and Zernike coefficients	17
2.2.4 Strehl ratio and wavefront error	21
2.3 2D Tweezer array	24
2.3.1 Dipole potential, trap depth and trap frequency	25
2.3.2 AOD-generated tweezer arrays	26
2.3.3 Imaging of optical tweezers	28
2.3.4 Effect of a Gaussian input beam envelope	29
3 Experimental results	33
3.1 Device calibration	33
3.1.1 Sub-wavelength pinholes	33
3.1.2 Sub-wavelength motion control	34
3.2 Showing diffraction-limited imaging performance	40
3.2.1 Imaging test setup	40
3.2.2 Imaging magnification measurement	43
3.2.3 Focus scan analysis	45
3.2.4 Measured point spread functions	50
3.2.5 Field of view analysis	62
3.2.6 Impact of additional optics on the PSF	67
3.3 Showing diffraction-limited tweezers	72
3.3.1 Tweezer test setup	72
3.3.2 High-resolution tweezer imaging	75
3.3.3 Single tweezers	82

3.3.4	Single tweezers with two AODs in the beam path	96
3.3.5	2D tweezer arrays and field of view	98
3.3.6	Tweezer statistics and correlations	110
3.3.7	Angle alignment sensitivity	113
3.3.8	Impact of different optics in transmission	117
3.3.9	Impact of the imaging FOV limit	120
3.4	Integration into the main experiment	122
3.4.1	Tweezer array and high resolution imaging setup	122
3.4.2	Tweezer test setup results	125
3.4.3	Imaging single Yb atoms in optical tweezer arrays	131
3.5	Technical details for data analysis	137
3.5.1	Pixel centering	137
3.5.2	Pixel averaging	139
3.5.3	Background noise	142
3.5.4	Region of interest size	144
3.5.5	Discretization	150
3.5.6	Tweezer overlap	153
3.5.7	Convolution	153
3.5.8	Tweezer imaging imperfections	157
3.5.9	Fluctuation effects	159
3.5.10	Summary	160
4	Conclusion and Outlook	163
A	Construction and alignment of a high-resolution imaging system	165
B	Construction and alignment of an AOD-based 2D tweezer array setup	179
C	Setup shaking and stabilization	191
D	Custom mounts	195
E	Cs objective tests	199
F	Ideal and aberrated example scans	205
	References	215
	Acknowledgements	221

List of Figures

1	Schematic symbol overview	xv
1.1	Goal of this work.	3
2.1	Quantum simulator setup	6
2.2	Focus of a curved surface	7
2.3	Infinity-corrected imaging	8
2.4	The diffraction limit.	16
2.5	Zernike polynomials.	20
2.6	AOD working principle	27
2.7	Gaussian input beam tweezer simulation	31
3.1	Resolution test chart, picture and SEM images.	35
3.2	Interferometric motor step size calibration	39
3.3	SQM objective imaging test setup	42
3.4	SQM Objective imaging magnification calibration	44
3.5	SQM objective 001 imaging 399 nm: PSF shape	51
3.6	SQM objective 001 imaging 399 nm: PSF analysis	53
3.7	SQM objective 002 imaging 399 nm: PSF analysis	54
3.8	SQM objective 001 imaging 532 nm: PSF shape	56
3.9	SQM objective 001 imaging 532 nm: PSF analysis	57
3.10	SQM objective 002 imaging 532 nm: PSF analysis	58
3.11	SQM objective imaging measurement overview	61
3.12	SQM objective 001 imaging FOV 399 nm	64
3.13	SQM objective 002 imaging FOV 399 nm	65
3.14	SQM objective 001 imaging FOV 532 nm	66
3.15	SQM objective 002 imaging FOV 532 nm	67
3.16	Additional optics imaging tests	71
3.17	Tweezer array optical test setup	73
3.18	Nikon objective imaging test setup	76
3.19	Nikon objective imaging magnification calibration	77
3.20	Nikon objective imaging: PSF shape	78
3.21	Nikon objective imaging: PSF analysis	79
3.22	Nikon objective imaging measurement overview	80
3.23	Nikon objective imaging alignment and FOV tests	82
3.24	Single tweezer, no AODs, flat top beam, 001: Tweezer shape	85
3.25	Single tweezer, no AODs, flat top beam, 001: Tweezer analysis	86

3.26	Single tweezer, no AODs, flat top beam, 002: Tweezer shape	87
3.27	Single tweezer, no AODs, flat top beam, 002: Tweezer analysis	88
3.28	Single tweezer, no AODs, Gauss beam, 001: Tweezer shape	92
3.29	Single tweezer, no AODs, Gauss beam, 001: Tweezer analysis	93
3.30	Single tweezer, no AODs, Gauss beam, 002: Tweezer shape	94
3.31	Single tweezer, no AODs, 33 mm incoming beam, 002: Tweezer analysis	95
3.32	Single tweezer vs RF voltage, 2 AODs, Gauss beam, 002	98
3.33	2D optical tweezer array example	99
3.34	Tweezer FOV measurement: complete image	101
3.35	Tweezer FOV measurement: heatmaps forward scan	104
3.36	Tweezer FOV measurement: heatmaps backward scan	105
3.37	Tweezer FOV measurement: histograms	108
3.38	Tweezer FOV measurement: azimuth averages	109
3.39	Strehl ratio brightness correlation	111
3.40	Strehl ratio resolution correlation	112
3.41	Alignment test 100 mm lens #3	114
3.42	Alignment test 1 m lens	115
3.43	Alignment test glass window	116
3.44	Tested optics in 2D tweezer array setup.	117
3.45	Tweezer arrays with test optics	119
3.46	Imaging FOV limit	121
3.47	Main lab tweezer setup schematic	124
3.48	Main lab test setup alignment signals.	127
3.49	Typical tweezer from the main lab test setup: shape	128
3.50	Typical tweezer from the main lab test setup: analysis	129
3.51	Tweezer alignment statistics in main lab test setup	130
3.52	Main lab objective integration.	133
3.53	Fluorescence images of Yb atoms in optical tweezers	136
3.54	Pixel centering simulation	138
3.55	Pixel averaging simulation	140
3.56	ROI size effect on NA-limited analyses	148
3.57	ROI size effect on Gaussian beam tweezers	149
3.58	Discretization effect	152
3.59	Discretization effect on Gaussian beam tweezers	153
3.60	Effect of convolution	156
3.61	Summarized effect of error compensation	161
A.1	Internal back reflections	173
A.2	Spherical aberration compensation	174
A.3	Focusing lens on stripe pattern	175
A.4	Spherical aberration compensation position markings	176
A.5	Angle alignment examples	177
A.6	Translation alignment examples	178

B.1	Tweezer setup axial distance calibrations	185
B.2	Back reflections through AODs	188
B.3	Beam shape after AODs	190
C.1	Cardboard cover used for stabilization	192
C.2	Shaking analysis	193
D.1	Mounts part 1	196
D.2	Mounts part 2	197
E.1	Cs objective old: shape	200
E.2	Cs objective old: analysis	201
E.3	Cs objective repaired: shape	202
E.4	Cs objective repaired: analysis	203
F.1	Simulated ideal Airy pattern: shape	206
F.2	Simulated ideal Airy pattern: analysis	207
F.3	Spherical aberration example: shape	208
F.4	Spherical aberration example: analysis	209
F.5	Coma example: shape	210
F.6	Coma example: analysis	211
F.7	Astigmatism example: shape	212
F.8	Astigmatism example: analysis	213

List of Tables

1	List of acronyms	xvii
3.1	Resolution chart structure sizes	34
3.2	Interferometric picomotor step size calibration	38
3.3	Alignment accuracies for SQM objective imaging tests	42
3.4	Analysis error sources	49
3.5	Expected point spread function characteristics	59
3.6	SQM objective imaging test results	59
3.7	Computed five-axis translation stage picomotor step sizes from tweezer analysis	89
3.8	Single tweezer results: "Flat top" input beam	90
3.9	Single tweezer results: Gaussian input beam	96
3.10	FOV measurement labeling	100
3.11	Main experiment alignment accuracies	134
3.12	Overview on the technical sources of error	160
3.13	Typical Strehl ratio error contributions after compensation	160
E.1	Cs objective expected point spread function characteristics	199
E.2	Cs objective imaging test results	199

List of Symbols

















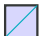




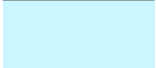
Beam dump		Fiber coupler	
Mirror		Objective (custom/commercial)	
Dichroic mirror		Camera	
Test target		Lens tube	
Glass plate		Iris	
Lens		Laser	
$\lambda/2$ waveplate		Translation stage	
Polarizing beam cube		Translation stage /w picomotor	
Non-polarizing beam cube		Tip/tilt knob	
AOD		Removable element	
Laser beams		Rail	

Figure 1 - Schematic symbol overview

List of Acronyms

xD	x-dimensional	MOT	Magneto-optical trap
AOD	Acousto-optic deflector	NA	Numerical aperture
AR	Anti reflection	Norm	Normalized
Avg	Average	NPBS	Non-polarizing beam splitter
AWG	Arbitrary waveform generator	PTF	Optical transfer function
BG	Background	Ph	Pinhole
BS	Beam sampler	PA	Pixel averagnig
CAD	Computer assisted design	PBS	Polarizing beam splitter
Conf	Confinement	PC	Pixel centering
C/Conv	Convolution	PCF	Photonic crystal fiber
Corr	Corrected/Correction	Pix	Pixel
DC	Dichroic mirror	PSF	Point spread function
Diff lim	Diffraction limit	PV	Peak to valley
Dis/Discr	Discretization	Res	(Rayleigh) resolution
DMD	Digital mirror device	RF	Radio frequency
Foc	Focus	RMS	Root mean square
FOV	Field of view	ROI	Region of interest
Hor	Horizontal	SEM	Scanning electron microscope
Im	Image/Imaging	SLM	Spatial light modulator
Int	Intensity	SQM	Synthetic quantum matter
Lin	Linear	SR	Strehl ratio
Log	Logarithmic	TOF	Time-of-flight (imaging)
Lppmm	Line pairs per millimeter	Vert	Vertical
Max	Maximum	Yb	Ytterbium
Min	Minimum		

Table 1 - List of acronyms

Introduction

Ever since the first creation of laser-cooled atomic clouds, the field of ultracold quantum gases has developed and played a significant part in the development of fields like quantum simulation, quantum computing and metrology [1–3]. Trapping and cooling alkali atoms in a *magneto-optical trap* (MOT) paved the way for the first high precision spectroscopic measurements [4], before the use of far off-resonant *dipole traps* and *optical lattices* enabled researchers to pioneer the simulation of solid state systems [5].

Due to the rising interest in exploring novel phases of matter, spin systems and high-precision optical clocks[6–8], neutral atom quantum gases were prepared in hyperfine states that served as spin qubits with coherence times on the order of milliseconds [9]. Since then, different atomic species have been investigated that provide a useful alternative to alkali metals. Mostly alkali-earth-like elements that have two valence electrons were investigated, as they offer singlet and triplet electronic states whose intercombination transitions are usually exceptionally narrow with lifetimes on the order of seconds. This so-called *clock transition* thus offers a new type of optical qubit that is now widely used in quantum metrology and information [10, 11]. Moreover, state-(in)dependent addressing of the ground and excited states is made possible by the recent measurement of the (magic) tune-out wavelengths for these elements which made them even more attractive for quantum simulation proposals [12].

To investigate many-body physics, interactions were tuned via Feshbach resonances or Rydberg interactions [13, 14]. However, time-of-flight (TOF) imaging only allows one to gather information on the momentum distribution of the *ensemble*, quantum simulators were still limited to probing collective many-body effects and global observables of the system. Also, the preparation of non-trivial initial states remained challenging.

This hurdle was overcome by the introduction of high-resolution instruments to quantum gas setups that were previously most common in biological research [15]. The inclusion of high-resolution objectives that allow for *in-situ* single-site imaging of individual atoms trapped in optical lattices opened the door for the quantum gas microscope experiments [16–18]. In these experiments, previously inaccessible local observables and correlations could be measured directly by investigating the atom distribution in lattices. This led to a plethora of new discoveries [19–21].

Apart from local observation, single-site control was achieved as well thanks to the advances in biophysics where the optical tweezers enabled single-particle based research and were awarded the nobel prize in 2018 [22]. After successfully trapping and cooling individual atoms in optical tweezers [23–26] they gained increasing popularity in the field of quantum metrology as frequently implemented with optical clocks [27]. Subsequently, in plenty quantum simulation experiments researchers integrated individual tweezers [28] as well as 2D arrays [29] which enabled great flexibility of the array geometry, tweezer-specific control and helped with preparation of exotic initial states [30, 31].

The generation of tweezer arrays has been demonstrated using *digital mirror devices* (DMDs) [32], *spatial light modulators* (SLMs) [33] and *acousto-optic deflectors* (AODs) [34]. While DMD- and SLM-based arrays offer the largest degree of flexibility including aberration control, AODs are superior in terms of array stability.

Recently, the success of resorting algorithms for tweezer arrays has enabled low-entropy initial state preparation [35, 36] which provides an advantage over the previously stochastic loading process. It also closes the gap to optical lattices which previously had the advantage that the creation of Mott insulators was a reliable path to homogeneous filling [37].

However, in optical tweezer arrays it remains challenging to achieve the same degree of homogeneity and stability of an optical lattice. This motivates the newest development in ultracold atom experiments, to combine the best of both approaches to form an *optical tweezer lattice hybrid setup* [28]. While the tweezers are used for deterministic loading and single-site manipulations, the lattice allows the experiment to exhibit the characteristic large-scale order and coherence properties that optical lattices are known for.

Our experiment in the *synthetic quantum matter* (SQM) lab at LMU Munich aims to build such a hybrid setup for fermionic *ytterbium* (Yb) atoms. We plan to use the clock qubit trapped in a 3D optical lattice with additional state-dependent optical tweezer arrays while observing the dynamics of the studied quantum system with a high-resolution quantum gas microscope. This versatile setup is capable of enabling fascinating insights ranging from fundamental physics like the simulation of lattice gauge theories, up to quantum information and computing applications.

The goal of this work is to test and characterize our custom high-resolution objectives with respect to their imaging and tweezer-generating performance, to assess their capability to create 2D tweezer arrays using AODs in the whole field of view and to finally integrate one of them in the main setup to demonstrate trapping and imaging of individual Yb atoms. The final achievement of this thesis is shown in Figure 1.1, an averaged high-resolution image of a 5x5 array of ultracold ytterbium atoms trapped in optical tweezers.

Outline:

In Chapter 2 we give an overview of our main experiment and its setup before discussing the theory behind high-resolution imaging and the generation of optical tweezer arrays using AODs. Chapter 3 then contains the main results of this work distributed

among the Chapters 3.1, where relevant devices are calibrated, 3.2 that illustrates the imaging performance of the objectives, 3.3 where the tweezer array is characterized, and Chapter 3.4 in which the first results with ultracold ytterbium atoms are shown. Finally, Chapter 3.5 concludes the results of this thesis by discussing the data analysis particularities and error sources. Chapter 4 summarizes this work and gives an outlook on the next steps in our lab.

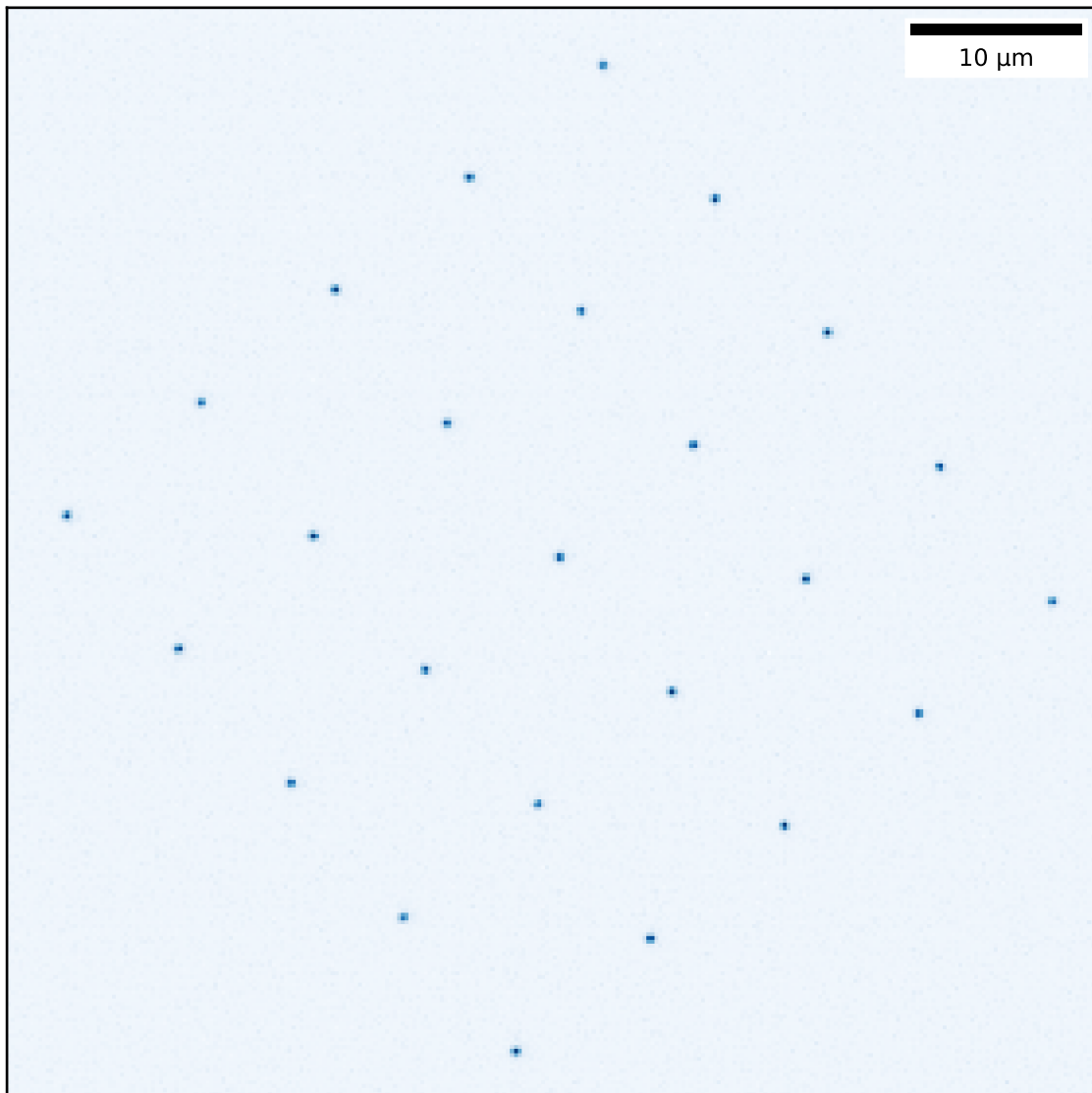


Figure 1.1 – An averaged fluorescence image of atoms trapped in a 2D optical tweezer array. This Figure shows the main result of this work, trapping and imaging individual ytterbium atoms in a 2D optical tweezer array.

Background and theory

In this Chapter, we will give an overview of our experimental apparatus, as well as provide the relevant theoretical background for high-resolution imaging and optical tweezer array generation using AODs.

2.1 Ytterbium hybrid tweezer lattice

In our quantum simulation experiment we use the alkaline earth-like *ytterbium* (Yb) atoms that offer stable bosonic (^{168}Yb , ^{170}Yb , ^{172}Yb , ^{174}Yb , ^{176}Yb) and fermionic isotopes (^{171}Yb , ^{173}Yb)[38] with the property of offering a doubly dipole forbidden transition with lifetime of tens of seconds lifetime (and thus small linewidth) which is referred to as the *optical clock transition*. The coupled states thus serve as highly stable qubits as mentioned in the introduction. Furthermore we address the ground and excited states using magic and tune-out frequencies which enable us to equally affect both states or to selectively only manipulate one respectively.

The potentials are generated in our experiment by 2D magic optical lattices with a vertical magic lattice serving to isolate a single plane. State-selective access is then enabled by AOD-generated tune-out optical tweezer arrays which alter the overall potential experienced by the atoms in the lattice. To observe the dynamics we use a high-resolution quantum gas microscope for site-resolved imaging.

To realize such a systems, we built an experimental setup consisting of a commercial Yb source with integrated Zeeman slower and 2D MOT¹ that is followed by differential pumping tubes that maintain a ultra-high vacuum in our experimental chamber. After passing a shutter, the atom beam enters the custom octagonal glass cell with the 3D MOT optics surrounding it (see Figure 2.1). Apart from the MOT beams, horizontal and vertical lattice, imaging, clock and repumper beams access the experimental chamber through its various windows, yet are not shown for clarity reasons. The bottom MOT beam is overlapped with the optical tweezer beams through a dichroic mirror (referred to as NPBS in Chapter 3.4) and are projected into the cell by a custom microscope objective. The latter is also used to collect atom fluorescence which is separated from the tweezer beam by another dichroic mirror and imaged onto a scientific camera as shown later in Figure 3.47.

¹AOSense, Beam-RevC- Yb

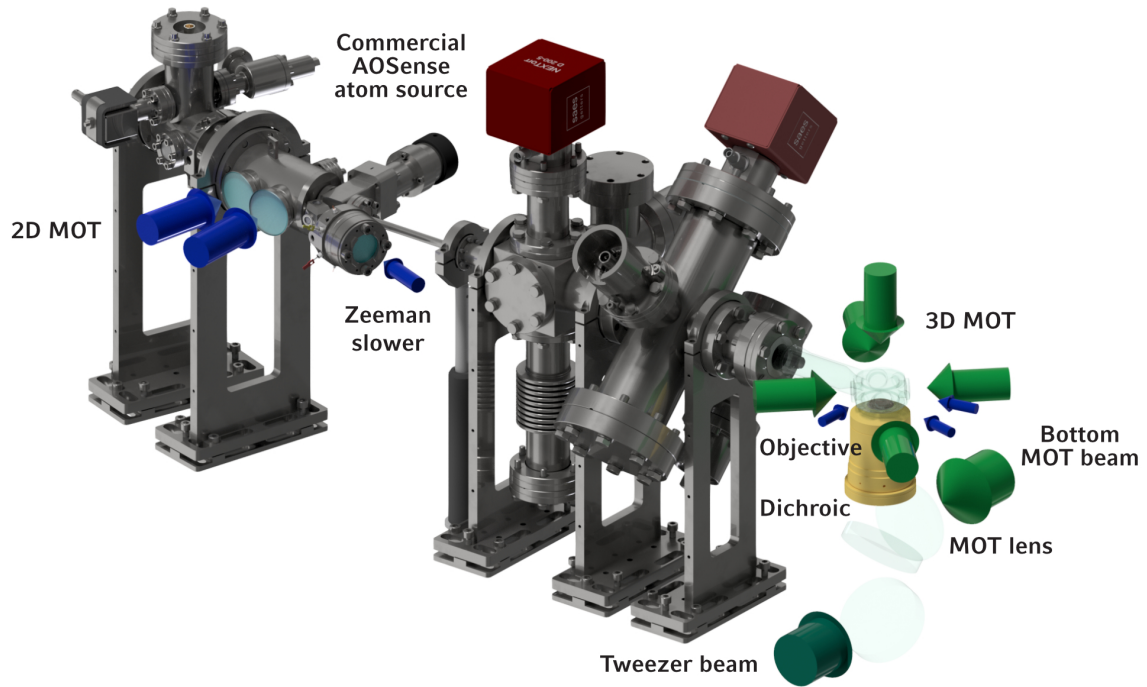


Figure 2.1 – The vacuum and schematic optical setup for the quantum simulation experiment. The vacuum setup is taken from CAD renders with illustrations added to display the most relevant laser beams and how they are shone onto the atoms.

2.2 High-resolution imaging

In this section we will discuss the details of high-resolution imaging including the difference between ray and wave optics, the notion of a point spread function, and where the diffraction limit comes from. To also consider imperfect systems, a summary of optical aberration theory is given as well as the Strehl ratio figure of merit and how it relates to the wavefront error of a laser beam. Polarization effects are neglected.

2.2.1 Foci and imaging in geometrical optics

In geometrical optics, one thinks of light as being composed of light *rays* that are defined by its distance to the optical axis and angle. In that picture, focusing a well-collimated beam that consists of only parallel rays with an ideal lens, leads to an infinitely sharp point the *focus* where all parallel rays intersect. For an ideal thin lens and rays that are close to the optical axis compared to the curvature radius of the lens, the *paraxial* approximation allows for linearization of Snells refraction law [39]:

$$1 = \frac{n_1 \sin \theta_1}{n_2 \sin \theta_2} \approx \frac{n_1 \theta_1}{n_2 \theta_2} \quad (2.1)$$

where n_i refers to the refractive index and θ_i to the angle of incidence of the beam on the side i of the interface. In our case we now assume collimated beam propagating

through vacuum, at height y_0 and impinging on a spherical surface with a linearized local slope of $\theta_1(y) = dz/dy = y/R$ and refractive index n_2 . A sketch of this scenario is depicted in Figure 2.2. Using the small angle approximation, the rays will focus in a distance f on the optical axis independent on y_0 :

$$\begin{aligned}
 0 &\stackrel{!}{=} y(f) = y_0 + f \cdot \tan(\theta_2(y_0) - \theta_1(y_0)) \\
 &\approx y_0 + f \cdot \tan((1/n_2 - 1)\theta_1(y_0)) \\
 &\approx y_0 + f \cdot \tan((1/n_2 - 1)y_0/R) \\
 &\approx y_0 + f \cdot (1/n_2 - 1)y_0/R \\
 &= y_0(1 + (1/n_2 - 1)f/R)
 \end{aligned} \tag{2.2}$$

which is always fulfilled for

$$f = R \left(\frac{n_2}{n_2 - 1} \right). \tag{2.3}$$

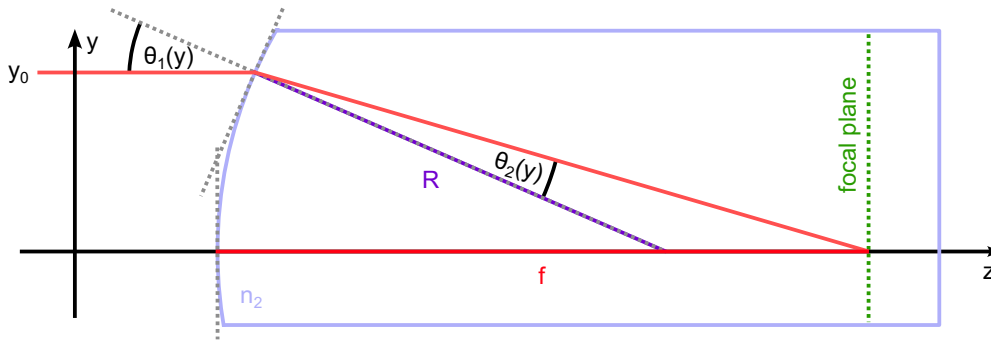


Figure 2.2 – Focus of a curved surface.

Without proof, ray bundles that enclose a non-zero angle with the optical axis will also focus at the same distance, laterally offset from the optical axis in the *focal plane*. For rays that are sufficiently far from the optical axis, the paraxial approximation fails such that nonlinear terms enter the relationship between refraction angle and ray position. This leads to a different focus position as a function of y_0 that ultimately causes focus broadening that is known as *spherical aberration* (see Appendix F).

The same concept applies to imaging point sources when we invert the beam path collecting the light instead of projecting a focus. A simple so-called *infinity-corrected* imaging setup is shown in Figure 2.3 A. The term "infinity-corrected" refers to a setup consisting of two lenses with parallel rays in between them. One element collects and collimates the emitted light from a point source and the other focuses the light down to create the image.

In general, ideal optical imaging can be thought of as a particular collinear transformation which uniformly maps points from object into image space. Corresponding element pairs in the object and imaging plane are referred to also being *conjugate*. During the mapping process only the relative distances between points are altered globally

by a factor that is called *transverse magnification* M_T [40]. However, in the presence of imperfections this magnification or, more generally, the metric of the points in image space becomes dependent on the conjugate position in the object plane which creates different sorts of aberrations. Note that because the Maxwell equations are *linear*, the same also applies to optical imaging. This means that we can think of the imaging process as simultaneously mapping the whole object, only transforming bundles of parallel rays or imaging every point after another to compose the final image. This also implies that if we know how an optical system transforms any single point in the object space, we have complete information on how this system will image any composite object. As a direct consequence, the impact of the system on any pattern can be calculated convoluting its point-source response with the object to obtain the image. Depending on the coherence of the light, the convolution is either performed with the electric field or intensity distributions.

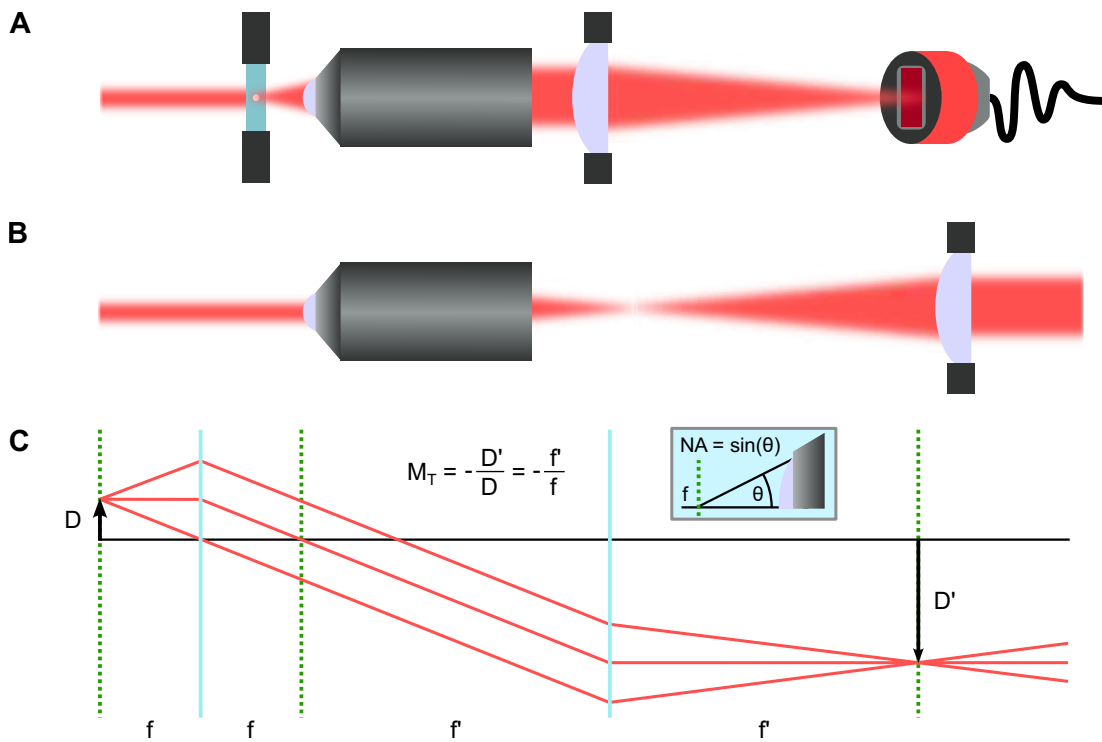


Figure 2.3 – Infinity-corrected imaging. In **A** a typical infinity-corrected imaging system is shown. **B** depicts the telescope orientation of an objective and a tube lens, leading to a collimated and magnified output beam. In **C** a ray tracing diagram is shown where a point is imaged by an infinity-corrected system. The vertical light blue lines mark the lens positions and the green dotted lines indicate the focal planes. Next to the graph the inset illustrates the definition of the numerical aperture.

The element that collects the light from the point source is referred to as *high-resolution objective lens* and usually consists of several specifically designed lenses. In microscopy applications, the object is placed in its focus while the image is generated in the focal plane of the second element that is known as the *tube lens*. When only

considering the in-focus imaging of planar objects with an infinity-corrected system, the distance between objective and tube lens is irrelevant. In case an object in a distance that is much larger than the focal length of the objective is to be imaged, two lenses can also be placed in a *telescope* orientation where object and image both appear at infinity and the optics spacing is equal to the sum of their focal lengths. Such a system that is particularly useful for (de-)magnification of collimated beams is depicted in Figure 2.3 B. Both system exhibits a transverse magnification that is given by:

$$M_T = -\frac{f_{tube}}{f_{obj}} \quad (2.4)$$

A ray tracing illustration in Figure 2.3 C displays the imaging of point with distance D to the optical axis by showing the propagation of three individual beams. Lenses are indicated as vertical light blue lines while green dotted lines represent the corresponding focal planes. One finds parallel rays between both optics characteristic for the infinity-corrected imaging system.

Since microscope objectives are usually characterized by a small effective focal length compared to its exit pupil size, it requires a high degree of complexity to compensate for all kinds of aberrations that are dominant for optics with particularly large ray acceptance angles. This is owing to the larger angles, as the step-wise angle changes leading to collimation need to be kept small for every individual interface, as otherwise nonlinearities cause the small angle approximation to break down and generate aberrations. That makes the composition of a microscopy objective more complex and its manufacturing and alignment susceptible to errors. A quantity describing the maximum light acceptance angle is the f -number, denoted as $f\#$. It is given by the quotient of the objective effective focal length to its entrance pupil diameter, $f\# = f_{obj}/D_O$. It is therefore a measure of the cone angle of the focused light and indicates the sensitivity of the lens ensemble to aberrations. A different parametrization of the light collecting capability of a lens is the *numerical aperture* (NA) defined as:

$$NA = n \sin(\theta) \quad (2.5)$$

with n denoting the refractive index outside the objective and θ being the opening half-angle of a focused or imaged ray ensemble [40], as illustrated in the inset of Figure 2.3 C. For simplicity, in the following n is set to 1. As argued in [41, p. 97], according to the *Abbe sine condition* we can find a relationship between the numerical aperture and the f -number that holds in particular for well-corrected objectives, where the focal plane is actually rather a segment of a circle with radius f centered around the focus:

$$f\# = \frac{1}{2 \sin \theta} = \frac{1}{2NA} \quad (2.6)$$

Using an infinity-corrected setup has the advantage that the object-resolving and image-generating elements are separated, making changes to the tube lens and therefore the magnification simple.

In the geometrical optics picture, any ideal objective has infinite resolution as it can map any point in object space to the conjugate point in image space with unlimited precision. However, in the next chapter we will find that the existence of points of light is unphysical to begin with.

2.2.2 Spatially confining light - the diffraction limit

While geometrical optics is a useful theory to describe extended optics and large beam propagation, it fails to explain phenomena that arise on length scales close to the wavelength of light. More generally, any effect from geometrical optics as well as behaviors based on the wave nature of light can be described by the theory of Fourier optics [42].

There opens up a rich field of physics containing aforementioned novel effects, yet this Section will only focus on the consequences for high-resolution imaging and tight focus generation. We start by directly addressing the question that arose in the previous discussion; what limits light to be focused to a single point. Due to the superposition principle localizing monochromatic waves to a point that is narrower than its wavelength would require constituents that itself have a smaller wavelength which is a contradiction to the assumption. This is particularly obvious in Fourier space, where the smallest structure in real space is represented by the highest spatial frequency available that is the \vec{k} -vector of the light, which is again fixed by the wavelength. So to further localize light one would have to squeeze the wavelength to enable smaller foci. Therefore, optics cannot localize light below the wavelength of light.

Moreover, it is important to discuss what is the smallest structure that one can generate focusing down monochromatic light. We first notice that when interfering two waves their relative angle corresponds to the spatial frequency of the interference pattern perpendicular to the optical axis. As Figure 2.4 A illustrates, the ultimate bound is given by the interference of the highest spatial frequency waves creating a vertical standing wave. Here, two Gaussian running waves are interfered with an enclosed angle of 2θ and the intensity of the superposition is plotted (for an instant in time). Using this train of thought, the minimal confinement perpendicular to the optical axis can be calculated to be

$$d = \frac{\lambda}{2 \sin(\theta)} \quad (2.7)$$

which is already very close to the final result from the next paragraphs. In Figure 2.4 B the same scenario is depicted for twice the angle of Figure 2.4 A resulting in narrower peaks. It is essential to understand that this process is not limited to focus generation, but also to light collection and imaging scenarios. In case a point-like emitter is imaged by an optical system, the highest spatial frequencies that the system can collect and propagate are governed by the above equation.

In the case of focusing light that is homogeneously illuminating a lens, the \vec{k} -vector projections perpendicular to the optical axis will add up to localize the partial waves at the focus. This is the spatial analogue to confining ultra-short laser pulses in time which cannot become shorter than one optical half-cycle. A schematic of this process is depicted in Figure 2.4 C and D. These plots help to obtain an intuitive understanding of this process as they show the sum of individual partial waves with different relative phases indicated by the point displacement in the right column. While for C all phases align, yielding a sharp, well-defined peak, in D randomly distributed phases cause the peak to be weaker, since more power is located in the side-lobes. Gray dashed lines indicate the ideal center position of the peak and the zero-phase position respectively.

To calculate the smallest structure that can be generated by focusing monochromatic light, we will use the property that the pattern lenses create in focus is precisely described by a Fourier transform of the aperture *field* distribution (pupil function) as shown in [42, p. 104]. If we assume a coherent and monochromatic plane wave $E(x, y, z) = E_0 \exp(-i2\pi(z/\lambda))$ incident on a lens with focal length f , the field in the focal plane $E(u, v)$ can be written as:

$$E(u, v) = \frac{E_0}{\lambda f} \int_{-\infty}^{\infty} \int_{-\infty}^{\infty} T(x, y) \exp\left(-i\frac{2\pi}{\lambda f}(xu + yv)\right) dx dy. \quad (2.8)$$

Here $T(x, y)$ refers to the transmittance function of the lens that can encode an intensity envelope of the incoming wave, account for inhomogeneous transmission properties of the lens, or incorporate a finite lens aperture size. In particular we consider a radially symmetric transmittance function of the form

$$T(r) = S_R(r) \cdot \mathcal{G}_w(r) \quad (2.9)$$

with the 2D circular aperture function with radius R

$$S_R(r) := \begin{cases} 1 & r \leq R \\ 0 & r > R \end{cases} \quad (2.10)$$

And the Gaussian field envelope $\mathcal{G}_w(r)$

$$(2.11)$$

In general Equation (2.8) has no analytical solution with a transmittance function of the form above, which will be of particular interest for the optical tweezer generation and is thus discussed in Chapter 2.3.4. In the case of imaging a point source or creating a tiny focus by illuminating the entire objective entrance pupil homogeneously, we can drop the Gaussian field envelope and obtain the following [43, pp. 350–363]:

$$\begin{aligned}
E(u, v) &= \frac{E_0}{\lambda f} \int_{-\infty}^{\infty} \int_{-\infty}^{\infty} S_R(r) \exp\left(-i \frac{2\pi}{\lambda f} (xu + yv)\right) dx dy \\
&= \frac{E_0}{\lambda f} \int_0^R \int_0^{2\pi} \exp\left(-i \frac{2\pi}{\lambda f} r\tilde{r}(\cos(\phi)\cos(\tilde{\phi}) + \sin(\phi)\sin(\tilde{\phi}))\right) r dr d\phi
\end{aligned}$$

where we switched to polar coordinates ($x, y \rightarrow r, \phi$ and $u, v \rightarrow \tilde{r}, \tilde{\phi}$) and truncated the radial integral at $r = R$. Next we apply a trigonometric identity to obtain

$$= \frac{E_0}{\lambda f} \int_0^R \int_0^{2\pi} \exp\left(-i \frac{2\pi}{\lambda f} r\tilde{r} \cos(\phi - \tilde{\phi})\right) r dr d\phi.$$

Now we can identify the azimuthal integral with the formula for the zeroth-order *Bessel function* of the first kind:

$$\begin{aligned}
J_0(w) &= \frac{1}{2\pi} \int_0^{2\pi} \exp(-iw \cos(\phi - \tilde{\phi})) d\phi \\
E(\rho) &= \frac{2\pi E_0}{\lambda f} \rho^2 \int_0^{R/\rho} w J_0(w) dw
\end{aligned}$$

In the last step we defined $w = r/\rho$ with $\rho := \frac{\lambda f}{2\pi\tilde{r}}$. We can easily perform the integral using the convenient formula for Bessel functions $\frac{d(wJ_1)}{dw} = wJ_0$ in which J_1 is the first order Bessel function of the first kind. We find

$$\begin{aligned}
&= \frac{2\pi E_0 \rho^2}{\lambda f} [wJ_1(w)]_0^{R/\rho} \\
&= \frac{2\pi E_0 \rho^2}{\lambda f} R/\rho J_1(R/\rho).
\end{aligned}$$

Note that we used $J_1(0) = 0$. Reinserting the definition of ρ we obtain the final result for the electric field distribution in the focus of a lens for an incident monochromatic plane wave:

$$\begin{aligned}
 E(\tilde{r}) &= \frac{E_0 R}{\tilde{r}} J_1\left(\frac{2\pi \tilde{r} R}{\lambda f}\right) \\
 &= E_0 \frac{\pi R^2}{\lambda f} \cdot \frac{2J_1\left(2\pi \frac{\tilde{r} NA}{\lambda f}\right)}{2\pi \frac{\tilde{r} NA}{\lambda f}} \\
 &= E_0 \frac{\pi R^2}{\lambda f} \cdot \frac{2J_1\left(1.22\pi \frac{\tilde{r}}{\xi_0}\right)}{1.22\pi \frac{\tilde{r}}{\xi_0}} \tag{2.12}
 \end{aligned}$$

With the corresponding intensity distribution

$$I(\tilde{r}) = I_0 \left[\frac{2J_1\left(1.22\pi \frac{\tilde{r}}{\xi_0}\right)}{1.22\pi \frac{\tilde{r}}{\xi_0}} \right]^2. \tag{2.13}$$

Here we used the first zero of $J_1(x)$ is located at $x = 1.22\pi$ and remembered the definition of the numerical aperture $NA = \sin \theta = R/f$ (comp. Eq. (2.6)) to define:

$$\xi_0 = \frac{1.22\lambda}{2 \sin \theta} = \frac{1.22\lambda}{2NA} \tag{2.14}$$

The distribution $I(r)$ is known as an *Airy pattern*, named after *G.B. Airy* who first described it theoretically in 1835 [44, 283–291]. In the following we will distinguish the field and intensity Airy patterns referring to equations (2.12) and (2.13) respectively. The center peak with diameter $2\xi_0$ is called *Airy disk*, while the radius ξ_0 will be referred to as the **diffraction limit** for a given wavelength λ and numerical aperture NA . It will be used alongside ξ which is the size of any Airy pattern which does not necessarily need to be diffraction-limited. As aforementioned, the result for $2\xi_0$ is surprisingly close to the back-of-the-envelope calculation in (2.7) that has the same parameter dependence and, as it poses a lower bound, underestimates the width by a factor of 2.

We find that the diffraction limit is only dependent on the used wavelength and the NA of the lens. Due to the Abbe sine condition mentioned in the previous chapter, even for apertures whose diameter is arbitrarily large, the Airy disk will not shrink below 0.61λ in radius.

Following the properties of Bessel functions [43, p. 362], the we calculate the limit:

$$\lim_{\epsilon \rightarrow 0} \left(I_0 \left[\frac{2J_1(\epsilon)}{\epsilon} \right]^2 \right) = I_0 = I_A \left(\frac{\pi R^2}{\lambda f} \right)^2. \quad (2.15)$$

Here $I_A = \frac{1}{2}\epsilon_0 c E_0^2$ stands for the plane wave intensity incident on the lens, with the dielectric constant ϵ_0 and the speed of light c . As a consequence of the *Plancherel theorem* for the Fourier transform, the integral of the Airy pattern (P_F) must be

$$P_F = \iint_{\mathbb{R}^2} \left(I_0 \left[\frac{2J_1(r)}{r} \right]^2 \right) dx dy = I_A \pi R^2 = P_A, \quad (2.16)$$

the power transmitted through the lens, due to conservation of power.

Note that this pattern created by a focusing lens is identical to the one that arises from diffraction off a circular aperture, observed in the far-field or *Fraunhofer* approximation [39, p. 307]. The Airy pattern inherits its rotational symmetry from the aperture geometry which motivates visualization as a function of the radial coordinate r . Such a radial plot is shown in Figure 2.4 E. It shows the peak-normalized field (green) and intensity (blue) pattern in linear scale as a function of the radial coordinate r in units of ξ_0 . In the inset a logarithmic plot of the intensity curve is depicted.

To close the loop to the discussion on image formation, the image of an object is in every point also restricted in resolution to the (possibly magnified) Airy pattern. Therefore, the Airy pattern can be identified as the point-source response of the imaging system. Mathematically, this means that because of the linearity of optical systems, the wave nature of light causes the ray optics image to be convolved with the (field) intensity Airy pattern in the case of (coherent) incoherent light being emitted from the object [42, p. 114]. Its Fourier transform is given by the auto-correlation of the pupil function and is usually referred to as the *optical transfer function* (OTF). The OTF exhibits an NA-limited spatial cutoff frequency that can be calculated to be $2NA/\lambda$ [45, p. 235], similar to Equation (2.7). Since that convolution blurs every point of the ideal image, the Airy pattern is also known as the *point spread function* (PSF) for imaging systems with circular aperture. The PSF of real optics are usually affected by aberrations and therefore look slightly different to the ideal Airy pattern (see next Chapter). In addition, the point spread function can also become *local* and depend on the lateral position relative to the optical axis. The area in object space in which the PSF is still diffraction-limited is known in microscopy as the *field of view* (FOV) of the imaging system. To characterize the PSF for the objectives of our experiment was one of the main tasks of this work.

The concept of *resolution* of an imaging system can now be formalized by defining a minimum-resolvable distance d under which the PSFs of two incoherent point sources are difficult to separate. It is also possible to define corresponding quantities for coherent sources, see e.g. [46]. Among the incoherent criteria, there is the well-known lateral Abbe resolution limit

$$d_{\text{Lateral,Abbe}} = \frac{\lambda}{2NA}, \quad (2.17)$$

the lateral Rayleigh limit that requires the peak of one Airy pattern to coincide with the first radial zero of the other [47], [48] (see Figure 2.4F)

$$d_{\text{Lateral, Rayleigh}} = \frac{1.22\lambda}{2NA} = \xi_0, \quad (2.18)$$

and the axial Rayleigh limit that similarly to the lateral limit uses the first axial zero crossing of the PSF

$$d_{\text{Axial, Rayleigh}} = \frac{2\lambda}{NA^2} := \zeta_0. \quad (2.19)$$

The latter will in the following be referred to as ζ_0 and can be computed analogously to the lateral Rayleigh limit from the sinc^2 -like axial intensity distribution

$$I(z) = I_0 \left[\frac{\sin\left(\pi \frac{z NA^2}{2\lambda}\right)}{\pi \frac{z NA^2}{2\lambda}} \right]^2 \quad (2.20)$$

following the derivation in [46]. In the imaging context the axial resolution is essential for the *depth of field* in the object plane and correspondingly after magnification for the *depth of focus* in the image plane. They describe how far the object and image plane might be shifted while preserving a sharp image. In Figure 2.4 F the lateral Rayleigh criterion is displayed by two PSFs that are positioned accordingly (gray dotted lines). Their sum (solid blue line) shows the small yet sufficient contrast to barely resolve both peaks.

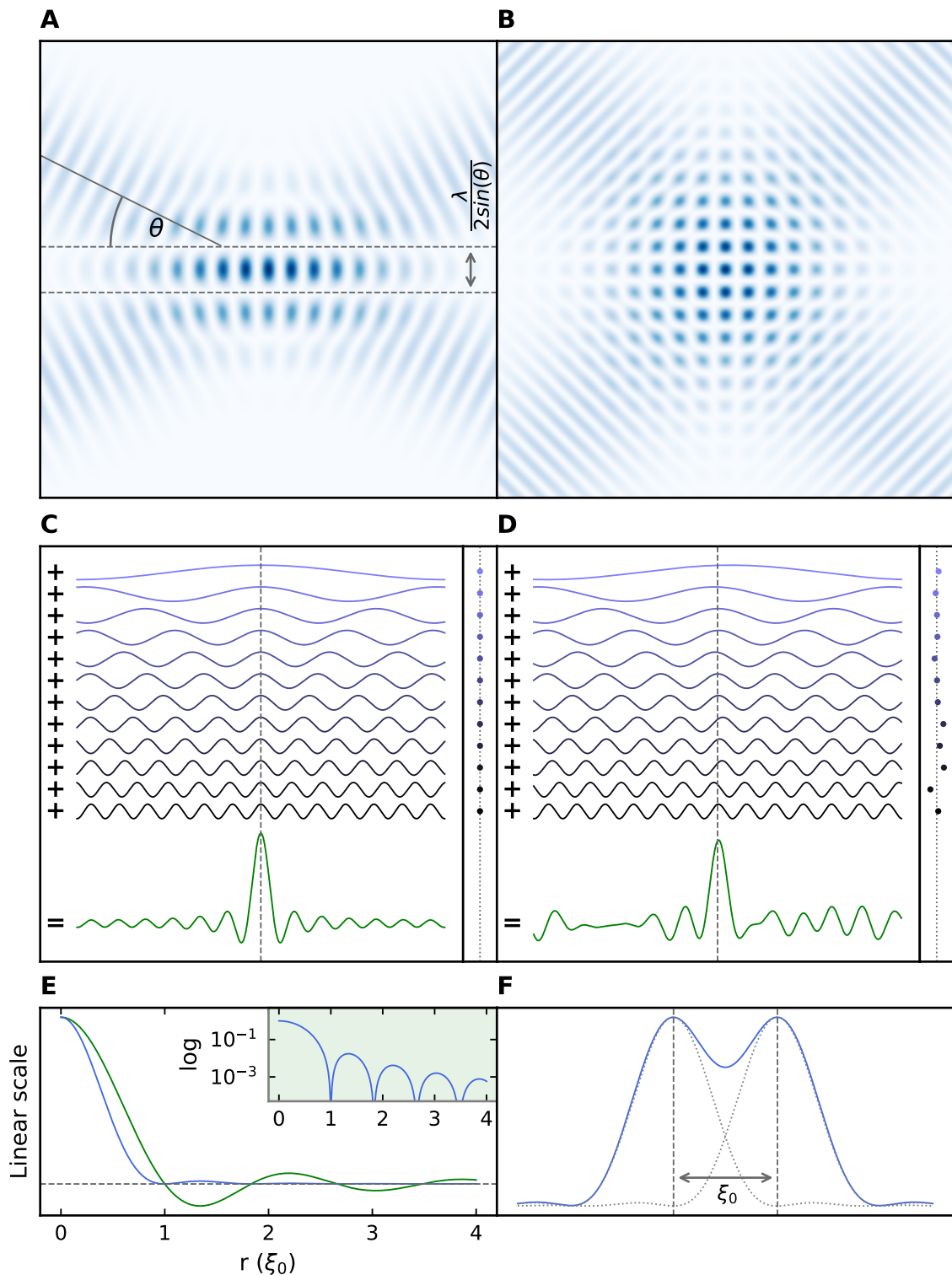


Figure 2.4 - Different illustrations to the diffraction limit of wave optics. In **A** and **B**, two collimated Gaussian beams cross in different half angles θ that create an interference pattern of vertical spacing $\lambda/(2 \sin(\theta))$. **C** and **D** show how superposition of partial waves with different wave vectors lead to a spatially confined wave packet in the case of aligned phase (**C**) and to broader pattern for a random phase distribution (**D**). The phases are indicated by the displacement of the points on the right. In **E** the peak-normalized field (green) and intensity (blue) Airy patterns are visualized with an inset showing the intensity in log-scale. **F** illustrates the Rayleigh resolution limit.

A more detailed visualization of the PSF of a circular aperture in 3D can be found in Appendix F.

There exists a useful relation for fitting an Airy pattern with a Gaussian function defined as

$$\mathcal{G}(r, w_G) = I_0 \left[\exp\left(-\frac{r^2}{w_G^2}\right) \right]^2. \quad (2.21)$$

The relation of the widths w_G/ξ_0 can be determined in the case of demanding the equal peak height or volume which leads to 0.84/1.22 and 0.90/1.22 respectively [49].

2.2.3 Optical aberrations and Zernike coefficients

There are various potential reasons for non-ideal imaging such as a failing paraxial approximation for large angles or off-center rays, insufficiently corrected optics or manufacturing errors in the lenses. All deviations from a linear object-image relationship are referred to as *optical aberrations* that are again separated into chromatic aberrations (dependent on the light frequency) and geometrical aberrations (for monochromatic radiation). In this Section only the monochromatic aberrations will be discussed [39, 48].

The pupil function of a lens imaging a point source will have an inhomogeneous *phase* distribution in the presence of aberrations that creates a PSF which deviates from the ideal Airy pattern. More specifically, they lead to broadening, similar to the considerations in Figure 2.4 C, D. For circularly symmetric imaging systems, these wavefront errors can be described by a distribution on the unit circle that is being mapped onto the beam for every step of propagation and for every point in the object plane. Any further phase delays in the optical system will add up to the circular wavefront until the image is measured on a camera. Therefore, a useful description of geometrical aberrations is analyzing the phase error in terms of the *Zernike polynomials* [50]. They represent an orthogonal basis defined on the unit circle and thus decompose any real phase front which is useful for characterization. The polynomials have the following form in polar coordinates (ρ, ϕ) :

$$\tilde{Z}_n^{\pm m}(\rho, \phi) = R_n^m(\rho) e^{\pm i m \phi}, \quad (2.22)$$

where

$$R_n^m(\rho) = \begin{cases} \sum_{s=0}^{\frac{n-m}{2}} (-1)^s \frac{(n-s)!}{s! \left(\frac{n+m}{2} - s\right)! \left(\frac{n-m}{2} - s\right)!} \rho^{n-2s} & \text{if } n \bmod 2 = |m| \bmod 2 \\ 0 & \text{else.} \end{cases} \quad (2.23)$$

This thesis uses a different convention with real Zernike polynomials defined as

$$Z_n^m(\rho, \phi) = R_n^m(\rho) \cos(m\phi), \quad (2.24)$$

$$Z_n^{-m}(\rho, \phi) = R_n^m(\rho) \sin(m\phi). \quad (2.25)$$

Here n is an integer and refers to the order of the radial polynomial while $l = |m| \leq n$ determines the number of azimuthal zeros. Note that l always has the same parity as n . The Zernike polynomials are not normalized, as can be seen from $R_n^m(1) = 1$. Instead, it holds the relation:

$$N_n^m = \frac{1}{\pi} \iint_{S_1} |Z_n^m(\rho, \phi)|^2 \rho \, d\rho \, d\phi = \frac{1 + \delta_{m0}}{2(n+1)} \quad (2.26)$$

In aberration theory every polynomial can be assigned a specific impact on the PSF. As they form a basis this allows one to uniquely determine the composition of any wavefront in terms of independent phase contributions. An arbitrary wavefront $W(\rho, \phi)$ can thus be written as

$$W(\rho, \phi) = \sum_{n=0}^{\infty} \sum_{m=-n}^n c_n^m Z_n^m(\rho, \phi) \quad (2.27)$$

with

$$c_n^m := \frac{1}{N_n^m} \frac{1}{\pi} \iint_{S_1} W(\rho, \phi) Z_n^m(\rho, \phi) \rho \, d\rho \, d\phi. \quad (2.28)$$

The magnitude of a particular component is calculated by the normalized overlap of the Zernike polynomial with the wavefront and is referred to as the corresponding *Zernike coefficient* c_n^m . The total wavefront error can then be computed by summing the squared Zernike coefficients. In particular the root mean square (RMS) error is given by [50, 51]:

$$\sigma := RMS = \sqrt{\frac{1}{\pi r^2} \int_{S_r} (W(\rho, \phi))^2 \rho \, d\rho \, d\phi} = \sqrt{\sum_{n,m} (N_n^m c_n^m)^2} \quad (2.29)$$

where c_n^m is the Zernike amplitude of radial order n and angular order m . As the spatial frequencies of the Zernike polynomials are increasing with n and l , real wavefronts are usually well described by including only the first 10-20 contributions. The following list gives an overview of the most relevant components of a wavefront in the Zernike basis:

1. **Piston** - Z_0^0

Any global phase offset is absorbed in the piston contribution. It does not have any physical effect on a single PSF

2. **Tip/tilt** - $Z_1^{\pm 1}$
A linear phase gradient corresponding to a tilted wavefront which shifts the PSF in the image plane.
3. **Defocus** - Z_2^0
This quadratic phase pattern leads to ideal focusing of a plane wave. A wavefront with vanishing defocus is collimated. Note that up to this contribution, all components can be made zero by linear transformations of the position of the object and image planes. Therefore, these four Zernike coefficients are usually omitted as they are *removable*.
4. **Astigmatism** - $Z_2^{\pm 2}$
If there are two lateral principal axes with different degree of defocus, the phase error cannot be removed by linear transformations. This lowest-order aberration is called astigmatism and causes partial waves in the respective planes to focus at distinct distances. It is frequently found in setups operating with large beams that are more sensitive to finite mirror curvature.
5. **Coma** - $Z_3^{\pm 1}$
A common aberration which creates a comet-like tail towards one side of the PSF. It can be observed for beams which are focused with high-*NA* and that are passing a tilted planar window.
6. **Trefoil** - $Z_3^{\pm 3}$
A less common aberration that exhibits a threefold rotationally symmetric PSF distortion.
7. **Spherical aberrations** - Z_4^0
This aberration is a typical consequence of failing paraxial approximation for rays impinging on a lens far off center. It causes different focus position for partial waves with the same distance to the optical axis which is observable as axial asymmetry of the PSF.

Figure 2.5 illustrates the connection between certain phase imprints on the wavefront following specific Zernike polynomials and their consequence for the observed PSF. Shown are tilt (A), defocus (B), astigmatism (C), coma (D) and spherical aberrations (E). On the left a ray diagram visualizes how a certain component arises in the geometrical optics framework. Here, the vertical dotted line marks the plane of observation and the horizontal indicates the optical axis. The fringe map column shows the interference pattern one obtains by superimposing a plane wave with the wavefront whose phase profile is shown to the right. Below the plot of each Zernike polynomial its functional form is given. Finally, the rightmost column depicts the effect on the in-focus PSF for three different coefficient magnitudes. More specifically as the focus is not necessarily well-defined for an aberrated PSF, the images are taken from the center of the *region of least confusion*, where the PSF peakedness (i.e. Strehl ratio, see next Section) is highest. This Figure was recreated with permission from [52].

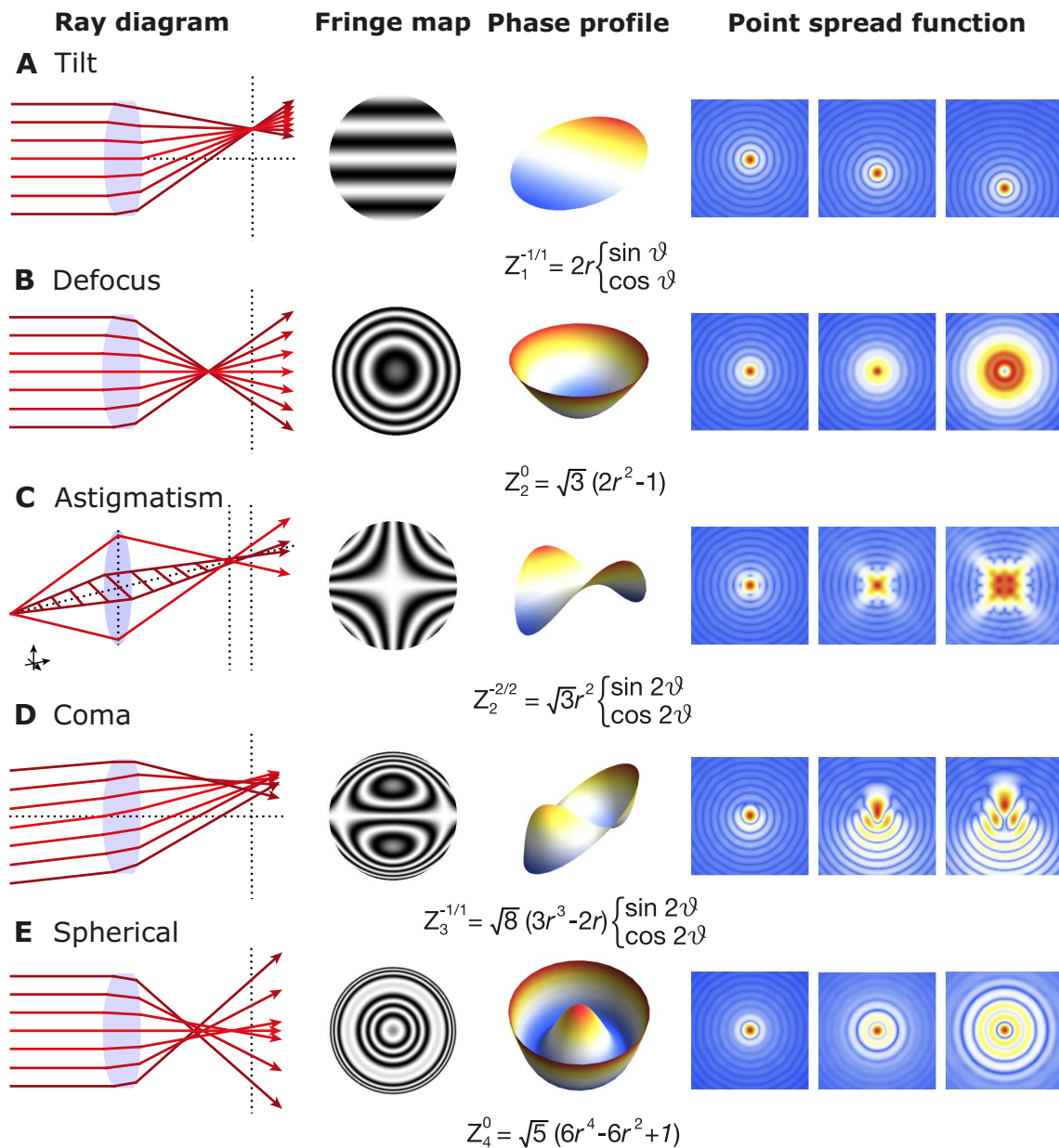


Figure 2.5 – Zernike polynomials and their impact on the PSF. The influence of non-vanishing lowest order Zernike coefficients is discussed. For every component a Ray diagram, a typical fringe map, the phase profile and the PSF is shown with three different coefficient magnitudes. Below each phase profile the Zernike polynomial function is given as well. The components tilt (A), defocus (B), astigmatism (C), coma (D), and spherical aberrations (E) are illustrated. This Figure was recreated with permission from [52].

It is important to mention that aberrations and phase errors are usually not homogeneous in the FOV but instead affects the PSF differently depending on its position. This can also turn the quasi-aberrations tilt and defocus into real aberrations as soon as they become *local* quantities as it usually is the case for real optics. So leads inhomogeneous tilt into *distortion* that is radially dependent magnification and defocus

into *field curvature* which describes the focus location to typically follow a parabola as a function of the lateral displacement from the optical axis.

2.2.4 Strehl ratio and wavefront error

Apart from the RMS wavefront error σ there is another useful quantity to describe a PSF or focus quality with a single number. The *Strehl ratio* named after Karl Strehl describes the ratio of the measured to the ideal peak intensity of a PSF [40, 51, 53]:

$$SR = \frac{I_0}{J_0} \quad (2.30)$$

Using the Strehl ratio has several advantages:

1. It is **easy to calculate**.
2. It offers **greater sensitivity** to imaging errors than the resolution. This is because the direct consequence of wavefront error is the leakage of intensity into the side lobes while interference suppresses broadening of the Airy disk for a certain error range.
3. It **relates to different quantities** which is shown in the next paragraphs.

However, it is also very susceptible to noise and all sorts of technical errors which are discussed in more detail in Chapter 3.5.

To find an alternative definition we recall the integral for the electric field in the focus of a lens from Equation (2.8) and set $u = v = 0$:

$$E(u, v) = \frac{E_0}{\lambda f} \int_{-\infty}^{\infty} \int_{-\infty}^{\infty} T(x, y) dx dy$$

we assume

$$T(x, y) = S_R(x, y) \exp\left(i \frac{2\pi}{\lambda} W(x, y)\right)$$

such that the integral collapses to the aperture of size R and only the phase profile $W(x, y)$ remains

$$E(0, 0) = \frac{E_0}{\lambda f} \iint_{S_R} e^{i \frac{2\pi}{\lambda} W(x, y)} dx dy.$$

We can now compute the Strehl ratio by dividing by the same expression with the ideal $W = 0$ and squaring:

$$SR = \frac{1}{(\pi R^2)^2} \left| \iint_{S_R} e^{i\frac{2\pi}{\lambda} W(x,y)} dx dy \right|^2 \quad (2.31)$$

$$= \left| \left\langle e^{i\frac{2\pi}{\lambda} W(x,y)} \right\rangle_{S_R} \right|^2 \quad (2.32)$$

According to this, the Strehl ratio can be described in terms of the phasors corresponding to the phase error W/λ averaged over the pupil. The formula can be understood intuitively as the coherent superposition of all partial waves emerging from the aperture. Interference will only lead to the ideal maximum if the contributions have optimal phase coherence and thus a wavefront error of zero.

At the same time this means that the actual peak intensity is connected to the ideal one via the Strehl ratio:

$$I_0 = J_0 \cdot SR \quad (2.33)$$

We continue to manipulate Equation (2.32) assuming a Gaussian distribution of the wavefront error across the aperture with $RMS = \sigma$:

$$P(W) = \frac{1}{\sqrt{2\pi\sigma^2}} \exp\left(-\frac{(W - \bar{W})^2}{2\sigma^2}\right) \quad (2.34)$$

With that we average over the wavefront:

$$\begin{aligned} SR &= \left| \left\langle \int_{-\infty}^{\infty} \frac{1}{\sqrt{2\pi\sigma^2}} \exp\left(i\frac{2\pi}{\lambda} W(x,y) - \frac{(W - \bar{W})^2}{2\sigma^2}\right) dW \right\rangle_{S_R} \right|^2 \\ &= \left| \left\langle \int_{-\infty}^{\infty} \frac{1}{\sqrt{2\pi\sigma^2}} \exp\left(-\frac{\left(W - \left(i\frac{2\pi\sigma^2}{\lambda} + \bar{W}\right)\right)^2}{2\sigma^2} - i\frac{2\pi}{\lambda}\bar{W} - \frac{4\pi^2\sigma^2}{2\lambda^2}\right) dW \right\rangle_{S_R} \right|^2 \\ &= \left| \left\langle \exp\left(-i\frac{2\pi}{\lambda}\bar{W} - \frac{4\pi^2\sigma^2}{2\lambda^2}\right) \right\rangle_{S_R} \right|^2 \\ &= \exp\left(-\left(2\pi\frac{\sigma}{\lambda}\right)^2\right) \end{aligned} \quad (2.35)$$

In spite of its widespread use, there is barely any rigorous derivation of this formula which is also known as the *Maréchal approximation* of the Strehl ratio. Its validity has however been proven frequently [53, 54].

In general, an optical system is considered to be diffraction-limited as long as the Strehl ratio is above 0.8 which corresponds to an RMS wavefront error not exceeding 0.075λ .

From formula (2.35) one can derive a useful equation for the effective Strehl ratio when combining several optics with known SR.

We will now use the notation

$$W(x, y) = \vec{W} := \sum_{n,m} c_n^m Z_n^m / \sqrt{N_n^m} \quad (2.36)$$

such that

$$\|\vec{W}\|^2 = \sum_{n,m} (c_n^m)^2 = \sigma^2. \quad (2.37)$$

Assuming an optical system is composed of two smaller subsystems that both introduce respective wavefront errors \vec{W}_1 and \vec{W}_2 , we can write the overall Strehl ratio as:

$$\begin{aligned} SR &= \exp\left(-4\pi^2 \frac{\sigma^2}{\lambda^2}\right) \\ &= \exp\left(-4\pi^2 \frac{\|\vec{W}\|^2}{\lambda^2}\right) \\ &= \exp\left(-4\pi^2 \frac{\|\vec{W}_1 + \vec{W}_2\|^2}{\lambda^2}\right) \\ &= \exp\left(-4\pi^2 \frac{\|\vec{W}_1\|^2 + 2\vec{W}_1 \cdot \vec{W}_2 + \|\vec{W}_2\|^2}{\lambda^2}\right) \\ &= \exp\left(-4\pi^2 \frac{\|\vec{W}_1\|^2}{\lambda^2}\right) \exp\left(-4\pi^2 \frac{\|\vec{W}_2\|^2}{\lambda^2}\right) \exp\left(-4\pi^2 \frac{2 \cos(\theta) \|\vec{W}_1\| \cdot \|\vec{W}_2\|}{\lambda^2}\right) \\ &= SR_1 SR_2 \exp\left(2 \cos(\theta) \sqrt{\log SR_1 \log SR_2}\right) \end{aligned} \quad (2.38)$$

Where we defined θ as the enclosing angle of the aberration vectors \vec{W}_i defined by $\cos(\theta) := \vec{W}_1 \cdot \vec{W}_2 / (\|\vec{W}_1\| \cdot \|\vec{W}_2\|)$.

With that we can investigate the effect that finite field curvature has on the Strehl ratio. As discussed in the previous Subsection, the field curvature aberrations describes defocus that usually scales quadratically with lateral displacement from the optical axis. Therefore the field curvature contribution to the dropping Strehl ratio as a function of the lateral position in the focal plane r is given by:

$$SR \approx SR_0 \cdot \exp(-d^4) := SR_0 \cdot (0.8)^{\frac{r^4}{FOV^4}} \quad (2.39)$$

$$\text{with } d = \frac{r}{FOV} \sqrt[4]{-\log 0.8} \quad (2.40)$$

where the *field of view* (*FOV*) is defined as the distance at which the Strehl ratio drops below 0.8 and the PSF ceases to be diffraction limited.

Finally, the calculation of the Strehl ratio from experimental data follows the formula:

$$SR = \frac{M}{N} = \frac{\frac{I_0}{P}}{\frac{J_0}{Q}} = \frac{\int I(x,y) dx dy}{\int J(x,y) dx dy} \approx \frac{\frac{\max_{i,j \in ROI}(im_{i,j})}{\sum_{i,j \in ROI} im_{i,j} \Delta x \Delta y}}{\frac{\max_{i,j \in ROI}(sim_{i,j})}{\sum_{i,j \in ROI} sim_{i,j} \Delta x \Delta y}} \quad (2.41)$$

where M and N denote the power-normalized peaks of the image and diffraction-limited simulation, such that P and Q correspond to the respective powers and I and J to the intensities. Here an ideal camera with infinitesimal pixel size is assumed. Comments on more sophisticated approximations of the Strehl ratio for measured images can be found in Chapter 3.5. In general, the measured peak intensity I_0 needs to be referenced to the total power P contained in the image. The same is true for the ideal/simulated PSF. For real images the peak will be the maximum single pixel value and the integral can be approximated as the sum over all pixels in a finite ROI of the image (im), multiplied with the corresponding pixel size. It is advantageous to simulate the reference PSF (sim) on the same grid, such that the pixel size cancels.

2.3 2D Tweezer array

In this Section, the working principle and the generation of optical tweezers to trap neutral atoms is discussed. In addition, further details are given on how tweezer arrays can be created using AODs and what needs to be considered when imaging optical tweezer potentials.

In essence, optical tweezers are tightly focused laser beams in which neutral atoms can be trapped in the optical dipole potential [15, 55]. Their generation can be thought of as reversing the high-resolution imaging process. One needs to create a flat wavefront that impinges on a microscope objective to project the tweezers. As for the imaging case, any errors in the plane wavefront before the objective will decrease the tweezer quality and cause the light to focus less tightly. Due to these similarities, most concepts discussed in the context of high-resolution imaging therefore also apply to optical tweezers.

Note that in this work, a terminology is used where "tweezer beam" refers to the laser beam that impinges on the high resolution objective *before* being focused to create the actual optical tweezer.

2.3.1 Dipole potential, trap depth and trap frequency

The mechanism responsible for the optical dipole potential is the frequency dependent *polarizability* $\alpha(\omega)$ of a specific atomic species. When a light field is applied that addresses an atomic transition with energy $\hbar\omega_0$ detuned by $\Delta = \omega - \omega_0$, one can show [55, 56] that the energy of the atomic ground state is shifted by

$$U_{dip}(r, z) = \frac{3\pi c^2}{2\omega_0^3} \frac{\gamma}{\Delta} I(r, z) \quad (2.42)$$

where $\hbar\gamma$ refers to the transition line width, \hbar is the reduced Planck constant and c the speed of light. This formula can be simplified using the polarizability:

$$U_{dip}(r, z) = -\frac{1}{2\epsilon_0 c} \alpha I(r, z) \quad (2.43)$$

with the dielectric constant ϵ_0 . This relationship means that the atoms experience a position dependent potential that can be used for trapping if the light is *red-detuned* from resonance, meaning $\Delta < 0$. It is proportional to the intensity distribution of the light, that allows the experimentalist to realize a variety of geometries for the traps. If tight confinement and robust trapping of the atoms is desired, high intensities and strong localization of the laser beam is needed which can be achieved by focusing it with a high-resolution objective (see previous Chapter). Thereby generated potentials are known as *optical tweezers*.

There exist three main parameters describing the trap geometry for tweezer traps:

1. The **trap depth** refers to the total energy barrier a trapped particle needs to overcome to escape the trap. It is given by $U_{dip}(0, 0)$. In a lab setting the related quantity *relative trap depth* per Watt input power is of particular interest and be calculated to be $U_{dip}(0, 0)/P = -\frac{1}{2\epsilon_0 c} \alpha$.
2. The **radial confinement** given by the trap frequency of the harmonic oscillator that approximates the radial potential via $U_r(r) = \frac{1}{2}m\omega_r^2 r^2$.
3. The **axial confinement** given by the trap frequency of the harmonic oscillator that approximates the axial potential via $U_{ax}(z) = \frac{1}{2}m\omega_{ax}^2 z^2$.

Here m refers to the atomic mass. From purely optical measurements of the tweezer intensity distribution we estimate all three quantities in the following way. The relative trap depth can be computed from its ideal value, simply multiplying with the Strehl ratio:

$$\begin{aligned}
\frac{U_{dip}(0,0)}{P} &= -\frac{1}{2\epsilon_0 c} \alpha \frac{I(0,0)}{\int I(r,z)d^2A} \\
&= -\frac{1}{2\epsilon_0 c} \alpha \cdot SR \frac{\int J(r,z)d^2A}{J(0,0)}
\end{aligned} \tag{2.44}$$

where $J(r, z)$ denotes the ideal diffraction-limited intensity distribution. Similarly, we can give approximations for the trap confinement using harmonic approximation of the potential. In case the potential is described by a Gaussian function, the harmonic approximation is found analytically using the Taylor expansion of the exponential function:

$$U(x) = U_0 \mathcal{G}(x, x_0, w_G) \tag{2.45}$$

$$= U_0 \exp\left(-\frac{2(x-x_0)^2}{w_G^2}\right) \tag{2.46}$$

$$= U_0 \left(1 - \frac{2(x-x_0)^2}{w_G^2}\right) + \mathcal{O}\left(\left(\frac{x}{w_G}\right)^4\right) \tag{2.47}$$

We now obtain the trap frequency normalized to the square root of laser power

$$\frac{\omega_x}{\sqrt{P}} = \sqrt{\frac{2U_0/P}{m} \frac{2}{w_G^2}} \stackrel{(2.44)}{=} \sqrt{\frac{\alpha}{2\epsilon_0 c} SR \frac{\int J(r,z)d^2A}{J(0,0)} \frac{4}{mw_G^2}}. \tag{2.48}$$

Intuitively we can summarize that all trap parameters scale with the peak power as well as the Strehl ratio, while the radial and axial confinement is given by the corresponding resolution of the microscope that generates the tweezer. Therefore, it is required to generate tightly focused laser beams approaching the diffraction limit of light, discussed in Section 2.2.2.

2.3.2 AOD-generated tweezer arrays

To generate 2D tweezer arrays a superposition of multiple tweezer beams is required impinging with different angles on the objective entrance pupil. Each beam will then be focused to an optical tweezer at various positions in the focal plane. To achieve this ensemble of beams we use two *acousto-optic deflectors* (AODs) that generate a 1D and subsequently a 2D array of beams by dividing the input beam into a well defined number of outputs. Figure 2.6 A illustrates the working principle. The AOD can be operated from a computer that communicates with an *arbitrary waveform generator* (AWG) which generates a radio frequency (RF) signal and sends it through an amplifier to the ultrasonic transducer of the AOD.

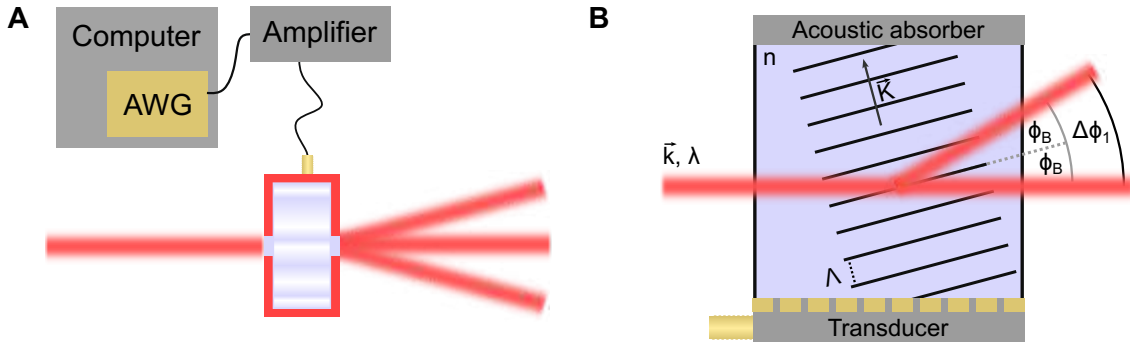


Figure 2.6 – AOD working principle In **A** action of an AOD on a collimated input beam is illustrated including its electronic signal chain. Part **B** is a schematic of the working principle.

A schematic of the deflection process in an AOD crystal is visualized in Figure 2.6 B. Physically, an AOD consists of a crystal in which an ultrasonic wave travels nearly perpendicular to the optical axis. For a single frequency wave, the refractive index of the substrate n is modulated in a sinusoidal pattern by the density variation from the compression wave [57, pp. 357–440]. The light can then diffract from the artificial grating which leads to constructive interference for certain deflection angles

$$\Delta\phi_m = m \frac{\lambda}{n\Lambda} = m \frac{\lambda f}{nv_s} = 2m\phi_B \quad (2.49)$$

where $\Delta\phi_m$ is the deflection angle of the diffracted beam, the integer m refers to the diffraction order, and $\Lambda = 2\pi/K$ is the wavelength of the sound wave with f , v_s denoting its frequency and velocity. The last equality rephrases the angle in terms of the Bragg angle in small angle approximation $\phi_B = \arcsin\left(\frac{\lambda}{2n\Lambda}\right) \approx \frac{\lambda}{2n\Lambda}$. At the same time, the diffracted beam is slightly shifted in frequency according to

$$\omega_m = \omega_0 + m\Omega. \quad (2.50)$$

In this Equation, ω refers to the light and Ω to the sound wave angular frequency. This process can be viewed as small-angle Bragg diffraction off the wavefronts with an additional Doppler shift of the light frequency. A thorough derivation of the interaction of light with sound waves based on diffraction can be found in [48, pp. 674–694]. Another useful and intuitive picture is to view the interaction a photon absorbing m phonons of the acoustic wave. Energy and momentum conservation then also lead to the results above.

To generate an array of tweezer beams multiple frequencies are sent into the AOD that cause the incoming beam to diffract into different first-order Bragg angles whose spacing is given by the frequency spacing of the drive signal. The intensity distribution of the tweezer beam array is usually not completely homogeneous and requires active feedback to the RF amplitudes for balancing.

AODs are generally operated with collimated input light, since that enables homogeneous deflection across the whole wavefront. An example of the output of an AOD for focusing the laser into it can be found in the Appendix in Figure B.3 D. The

diffraction efficiency depends strongly on the order of diffraction, where low orders are generally favored, as well as the acoustic wave amplitude. Furthermore, the relative propagation direction of the acoustic and optical waves as well as their polarization is crucial for phase-matching and thus the coupling efficiency. Phased-array transducers are frequently included in AODs to optimize the phase matching conditions simultaneously for multiple tones within the bandwidth (see [57, p. 411]).

2.3.3 Imaging of optical tweezers

In general, optical tweezers can be imaged by any system that offers large enough resolution to image the smallest features of the tweezer. An intuitive rule of thumb is to ensure that the imaging system has larger NA than the lens that generates the tweezer. In fact, one can even show theoretically, that it is sufficient to use an imaging objective of equal NA as the tweezer-generating objective. We will prove more generally, that imaging an ideal tweezer with an ideal diffraction-limited objective will yield an Airy pattern, that is the larger of the two. We assume that the tweezer-projecting objective has a numerical aperture NA_T , the imaging system has the numerical aperture NA_I , there are no aberrations in the system and the light source is coherent and monochromatic. Let $\mathcal{A}_{NA}(r)$ refer to an Airy pattern in polar coordinates with given NA, and let $S_R(r)$ be a 2D circular aperture function with radius R (comp. Eq. (2.10)), while r denotes the radial coordinate. We calculate the image $I(r)$ as the convolution of the tweezer with the PSF of the imaging system. Since both are Airy patterns that only differ by the NA we obtain:

$$I(r) = \mathcal{A}_{NA_T}(r) * \mathcal{A}_{NA_I}(r)$$

We can now apply a 2D Fourier transform twice and use the convolution theorem to obtain:

$$\begin{aligned} &= FT[FT[\mathcal{A}_{NA_T}(r) * \mathcal{A}_{NA_I}(r)]] \\ &= FT[FT[\mathcal{A}_{NA_T}(r)] \cdot FT[\mathcal{A}_{NA_I}(r)]] \end{aligned}$$

Furthermore, we identify the Fourier transform of an Airy pattern with a circular aperture function, whose radius is given by the NA and proportional to the highest spatial frequencies in image space.

$$= FT[S_{R_T}(r) \cdot S_{R_I}(r)]$$

In the Fourier domain, the product limits the spatial frequencies to those contained in the smaller aperture, while in the object space, the larger Airy pattern governs the convolution.

$$\begin{aligned} &= FT[S_{\min(R_T, R_I)}(r)] \\ &= \mathcal{A}_{\min(NA_T, NA_I)}(r) \end{aligned} \tag{2.51}$$

Since we want to observe the tweezer without being limited by the imaging system this requires: $NA_I \geq NA_T$

This results is a consequence of precise interference of coherent Airy distributions and will break down for aberrations in the system or incoherent light. Therefore, since it is possible, that the imaging objective itself is not perfect, it is useful to choose NA_I slightly above NA_T .

2.3.4 Effect of a Gaussian input beam envelope

Apart from aberrations caused by phase imprints on the tweezer beam, its amplitude distribution is also of great importance for the optical tweezer quality. In particular, the contributions towards the edge of the objective aperture are very important and need to be well-illuminated to obtain small tweezers. This connection is understood best, when using the Fourier transform property of lenses. In this framework, the aperture function that consists of phase and amplitude is Fourier transformed to generate the optical tweezer. Therefore, in case the tweezer beam far from the optical axis is weaker than at its center, high spatial frequency components will be attenuated which results in larger tweezers and worse atom confinement.

The scenario described above frequently occurs under realistic laboratory conditions, since it is usually not feasible to work with flat-top beams and one instead uses Gaussian beams to illuminate the objective. This however, requires the Gaussian beam waist to not significantly exceed the objective aperture size, as otherwise too much of the limited available power is clipped which reduces the trap depth and might also pose the threat of intense stray light on the optical table. Therefore, there exists an optimum between a Gaussian waist that is too small, such that the tweezers become really wide, and a very large beam, where most power is lost. The parameter that governs this transition and that characterizes the optical tweezers in the following chapters is the dimensionless *relative Gaussian beam size* $2w_G/D_O$, where twice of the Gaussian beam waist is compared to the objective entrance pupil diameter.

Note that throughout this thesis, "Gaussian waist" w_G refers to the 1/e value for the electric field of light as manifest in the following representation with radius r and amplitude E_0 :

$$\mathcal{G}(r, E_0, w_G) = E_0 \exp\left(-\frac{r^2}{w_G^2}\right) \quad (2.52)$$

To estimate the impact of a Gaussian envelope on the tweezer size, we realize that there exist close-form solutions to this problem in the limits $2w_G/D_O \rightarrow \infty$ and $2w_G/D_O \rightarrow 0$. Namely:

$$FT[S_{R_0}(r) \cdot \mathcal{G}_{w_G}(r)] = \begin{cases} FT[S_{R_0}(r) \cdot 1] = \mathcal{A}_{NA}(r) & 2w_G/D_O \rightarrow \infty \\ FT[1 \cdot \mathcal{G}_{w_G}(r)] = \mathcal{G}'_{w'_G}(r) & 2w_G/D_O \rightarrow 0 \end{cases} \quad (2.53)$$

where $R_0 = D_0/2$. Here we used the Airy pattern definition in case the Gaussian beam is so large, that is can be described as a plane wave, as well as the well-known

formula for Gaussian beam focusing $w'_G = \frac{\lambda f}{\pi w_G}$, in case clipping on the aperture is negligible when it is much larger than the beam size. As we are interested in optical tweezers in a regime in between those two extremes, numerical simulations are required.

In the following, the results of a simulation are presented, that investigated the effect of an incoming Gaussian tweezer beam on the purely geometric and the trap parameters of optical tweezers. The simulation uses Fourier transform of circular aperture functions with a radius of 20 points, sampled on a 5000×5000 point grid. Finally, the pattern is squared to obtain the intensity distribution. The aperture function additionally has a Gaussian amplitude envelope with variable waist, that is scanned during simulation. Taking the limit of $w_G \rightarrow \infty$ yields the diffraction-limited tweezer, that is used to calibrate distances in the simulation. The waist is sampled in the vicinity of the most relevant region around $2w_G = D_0$.

The outcome of this simulation are summarized in Figure 2.7. In these plots, the dependency of different parameters on the relative Gaussian beam size is analyzed. First, in subfigure A the direct tweezer size increase due to attenuated high-frequency contributions is tested. The broadening was measured by the means of tracking the radial minimum position (argmin) and fitting an ideal Airy pattern (ξ). It is striking that the minima move outwards faster than the center distribution broadening. In fact, the simple Airy fit will be the quantity of interest, since for the actual data analysis ξ will be estimated based on the a naive Airy fit of the broadened pattern, rather than a minimum-finding algorithm. We observe a hyperbola-like shape, that is significantly increasing for relative beam sizes below 1. In direct comparison, the optical power loss is visualized that is caused by clipping of the beam. The effects visible in the trap parameter analysis will be a result of this interplay between tweezer broadening and power loss.

In subplot B, the different trap parameters depth, radial and axial confinement are calculated as discussed in Chapter 2.3.1 and plotted against the relative beam size. For all parameters, only the power transmitted through the aperture was considered, while for the depth, the maximum value and for the confinement, the quadratic approximations were computed. As expected from the considerations in A, there exists a maximum for every curve, that lies close to $2w_G/D_0 = 1$. Furthermore, since the the trap depth depends on the tweezer power like $\sim 1/P$, instead of $\sim 1/\sqrt{P}$ as the trap frequencies do, this curve falls much faster than the trap confinement for larger tweezer beams. Note that for the axial confinement simulation, a 3D tweezer simulation script was used, that uses Fresnel propagation around the focus.

In subplot C, the relative tweezer leakage was computed. This quantity describes, which fraction of the tweezer peak intensity, atoms are subject to, if they are located one or two lattice sites from the tweezer. The inset illustrates the relative position of a diffraction-limited tweezer (green) to two atomic wave packets spaced one (two) lattice site(s).

We find, that the crosstalk is quite large for a distance of one site and is increasing with the tweezer broadening. For ideal optical tweezers, this leakage saturates to 5% of the peak intensity. The tweezer leakage two sites far from center is already significantly lower and bounded by 1%. For decreasing Gaussian beam size, the crosstalk drops further to zero when the first radial minimum reaches the site at about $2w_G/D_O = 0.52$. Finally, in D the Strehl ratio is plotted. Similar to the tweezer size in A, the SR starts to drop significantly for relative beam sizes smaller than 1. The magnitude of this effect is significant and needs to be taken in to account for the experimental data analysis. Following these considerations, the main setup will target optical tweezers that use $2w_G/D_O = 0.94$, i.e. a Gaussian beam diameter of 33 μm . From this simulation we extract the relative tweezer size $\tilde{\xi}_0 := 1.126 \xi_0$ and the maximum Strehl ratio of 0.905 as the appropriate quantities to compare the expected real tweezers to.

For clarity, a few notes on the conventions used in this thesis are summarized before proceeding to the experimental section. The optical tweezers that are optimal, aberration free and generated by a plane wave incident on an objective with a given NA , are going to be referred to as "ideal", "flat-top (input/incoming) beam" or "NA-limited" optical tweezers. The corresponding diffraction limit is denoted as " ξ_0 ". Optimal optical tweezers, that are aberration free but generated using a Gaussian input beam, are called "real", "Gaussian (input/incoming) beam" or "Gaussian (beam/envelope)-limited" tweezers. The apparent diffraction-limited resolution is written as " $\tilde{\xi}_0$ ".

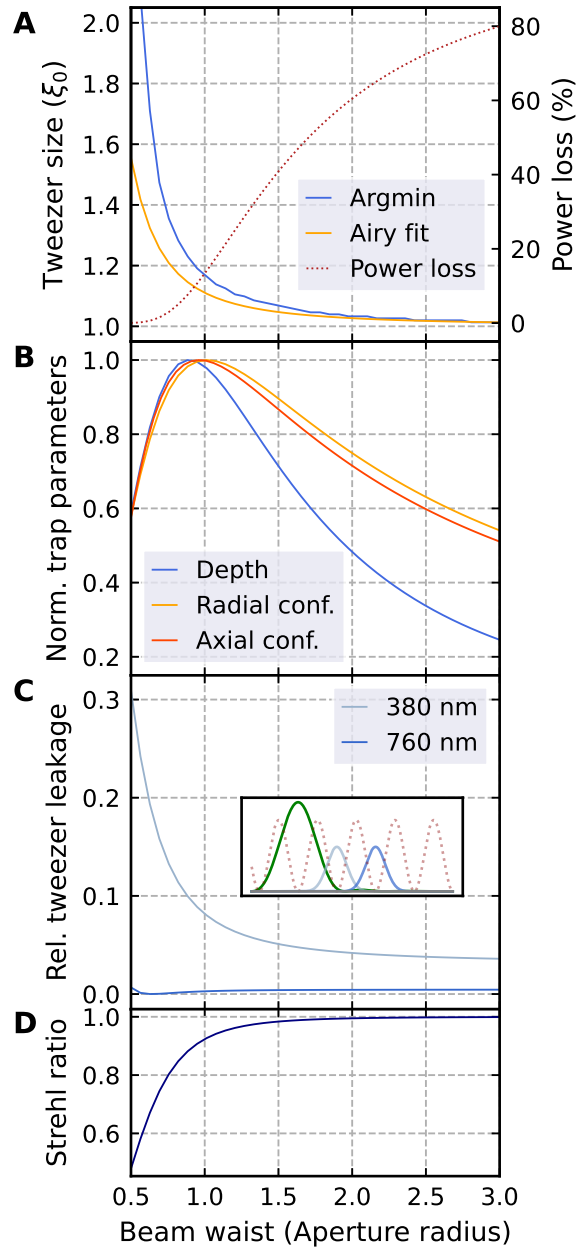


Figure 2.7 – Simulation of optical tweezer parameters for varying Gaussian beam size. In **A**, the tweezer size is plotted, determined using the first radial zero position and by fitting the Airy resolution ξ . It is compared to the power loss due to beam clipping on the aperture. In **B**, different trap parameters are compared, assuming limited input beam power. Part **C** depicts the relative tweezer intensity at different distances from center (shown in the inset) and **D** covers the Strehl ratio.

Experimental results

The main part of this work concentrates on obtaining experimental evidence for the capability of diffraction-limited imaging performance and optical tweezer generation with our high-resolution custom-made objectives¹. In this Chapter the results will be divided into four main sections. The first section provides an overview of calibration measurements for different devices that were used in the experiments shown in the next Sections. Main experimental results on the imaging performance are discussed in Section two, while the following shows measurements on optical tweezer generation. Afterwards, the integration of the optical tweezers in the main lab and first results of trapping atoms are presented. The last part of this Chapter covers technical details which need to be considered when analyzing high-resolution images of point-like sources of light.

3.1 Device calibration

Before the main results are shown, an overview on calibration measurements is presented.

3.1.1 Sub-wavelength pinholes

In order to test the imaging capabilities of the tested objectives, the point spread function needs to be measured. To this end, a small pinhole – ideally sub-imaging-wavelength sized – needs to be imaged. As discussed in Section 3.5.7, the smaller the pinhole, the less sensitive the analysis results will be to uncertainties in actual pinhole size. For the all imaging measurements in this work, a resolution test chart² was used. It consists of a metal frame and the 1x1 cm target chip in its center, which is made of a thin chromium layer on a fused silica substrate patterned by electron beam lithography. The chart offers both, sub-wavelength pinholes and vertical/horizontal stripes with known spacing for magnification calibration. The latter are structures of five vertical and horizontal stripes with a number written next to them referring to the line spacing in units of line pairs per millimeter (lppmm). These stripe patterns

¹Special optics, customized, 54-35-25@399&532-590

²Technologie Manufaktur, TC-RT01

are distributed along the edges of the chart, ever decreasing in size (exponentially) starting at 7.5 up to 3300 lppmm. Measuring point spread functions is made possible by the five pinholes which are located in the center of the chip, each surrounded by four "+"-shaped aiming lines for easier localization. The smallest pinhole is of 250 nm diameter nominally, which is sufficient for accurate PSF measurements. An overview of the offered structure sizes is given in Table 3.1.

Pinhole size (μm)	Aiming line width (μm)	Aiming line length (μm)
4	1100	1
2	550	0.5
1	275	0.25
0.5	137.5	0.25
0.25	68.75	0.25

Table 3.1 - Resolution chart structure sizes

According to the manufacturer, the two smallest pinholes have a diameter tolerance of about 10% which encouraged performing a measurement of the actual pinholes sizes of our product with a scanning electron microscope (SEM) at a neighboring clean room. The results of that measurement as well as a photograph of our resolution chart are shown in Figure 3.1. On top, the image shows the resolution chart with the patterned chip where the largest stripe patterns are still visible by eye. The lower images show two SEM images taken of the 250 and the 500 nm pinholes at 5 kV acceleration voltage. While the 500 nm pinhole exhibits a very round edge, the 250 nm pinhole seems to show stronger edge irregularities. In addition, particularly for the 250 nm hole two edges are visible, one bright one dark next to the actual hole (note that SEM image brightness is correlated to sample curvature). This would agree with a cut cone-like shape of the hole, leading to a larger and a smaller hole radius on the two respective sides. For the imaging properties, the smaller hole is assumed to be relevant. To quantify deviations from the nominal 250/500 nm diameter, the SEM control software allowed for distance measurements (red) which revealed that the 250 pinhole is roughly 10 to 20 nm smaller than expected (about 241x229 nm) and the 500 nm pinhole is 30 nm smaller than expected (about 470x470 nm), which is significant for later analyses. In the upcoming measurements, only the "250 nm" pinhole (now in parentheses since it is smaller actually) was used for imaging tests as the resulting deconvolution will be less sensitive to the actual pinhole size and residual uncertainties compared to the 500 nm pinhole. For the deconvolution, due to technical reasons, a pinhole size of about 240x240 nm is assumed.

3.1.2 Sub-wavelength motion control

High-resolution imaging of sub-wavelength pinholes and optical tweezers with high-NA objectives requires precise axial alignment capabilities for focusing, as the depth of field is usually on the order of a micrometer (see axial diffraction limit in Chapter

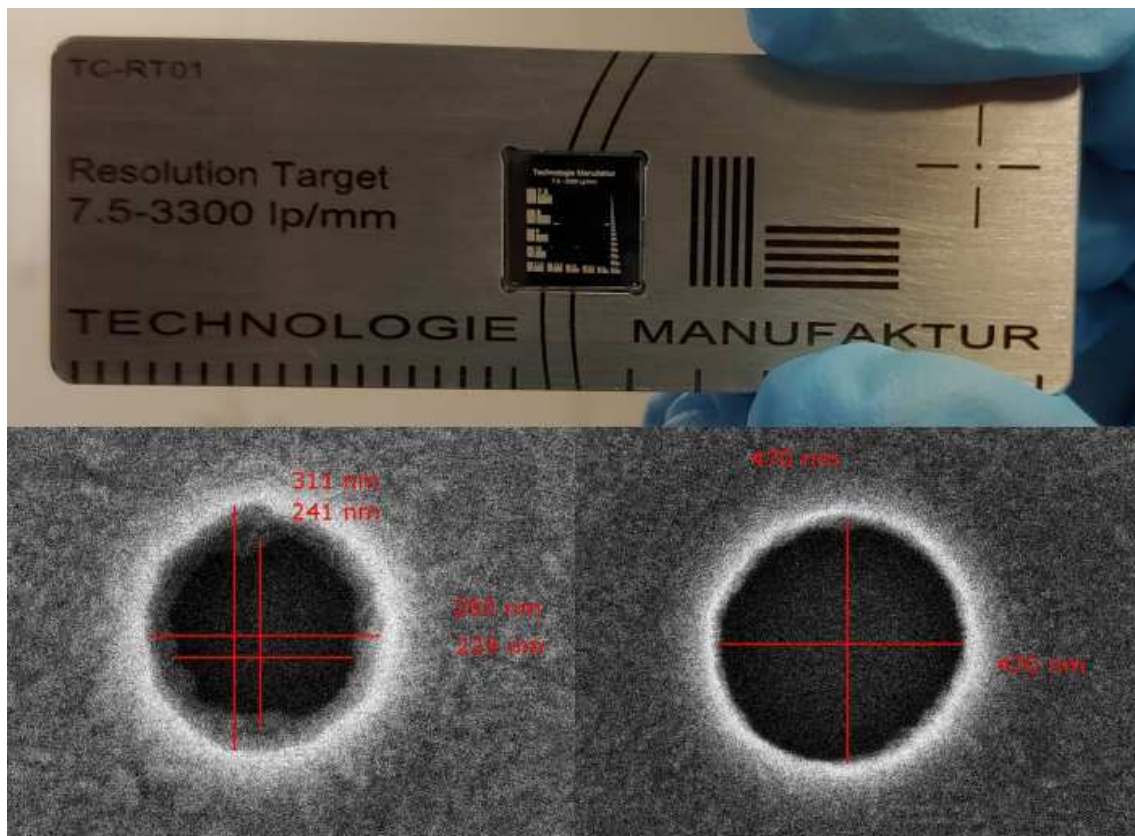


Figure 3.1 – Resolution test chart, picture and SEM images. The upper picture shows an image of the resolution chart depicting the 1x1 cm test plate in the center as well as its metal frame. The stripe patterns at the edges of the chip are visible by eye, the pinholes and aiming lines cannot be seen though. The two lower images show SEM images taken from the used resolution chart with diameter measures in red, the first showing the 250 nm and the second showing the 500 nm pinhole.

2.2.2). To achieve accurate and controlled focusing, in this work open-loop picomotors are used for axial positioning. In general, in objective imaging tests, the target was moved by a single picomotor³ whereas in optical tweezer characterization measurements a commercial high-resolution objective was controlled with a 5-axis motorized stage⁴. All six motors are specified to offer less than 30 nm incremental motion which enables sub-wavelength scanning of strongly focused spots of light.

With the goal of obtaining knowledge of the precise three-dimensional shape of a PSF / an optical tweezer and to ultimately compute expected axial trap frequencies for trapped atoms, images of 2D cuts through the patterns of light need to be taken at numerous axial positions with well-defined spacing. Therefore, the step size of the piezo motors needs to be known exactly. This is however a non-trivial task, since open-loop piezo actuators tend to have strong hysteresis after direction changes, unequal forward/backward step sizes and non-linear behavior when changing the step count,

³Newport, 8321 Picomotor Piezo Linear Actuator

⁴Newport, 8081-M Motorized XYZ θ x θ y Tilt Aligner

meaning moving two steps at once versus translating one step twice in a row does not precisely lead to the same result. In addition, the step size depends on the load to which the motors are exposed to, making accurate predictions challenging.

There are two techniques used in this thesis that allow for precise calibration of the picomotor step sizes. First, one can directly use 3D tweezer/PSF measurements to calculate the expected step size, assuming diffraction-limited operation, with the help of the known axial diffraction limit (see Section 2.2.2). This, however, is susceptible to imperfections since the axial diffraction limit will not hold for aberrated patterns and furthermore it also already assumes what we want to test in the end - if the spot is as small as physically possible. Nevertheless, this method works well as a cross-check for the second method and was applied in Chapter 3.3.3. Second, one can perform an independent interferometric measurement of the picomotor step size. This approach was further pursued in this work to obtain reliable information to later calibrate all focus scans with.

Part A of Figure 3.2 shows the optical setup used for this measurement. It is a Michelson interferometer that consists of a non-polarizing beam splitter cube dividing the incoming collimated beam ($\lambda = 532$ nm) into two arms. Both are retro-reflected, one off a typical highly stable mirror, the other one off a reflecting surface which is attached to a mount which can be moved by the picomotor that is to be tested. Both beams recombine in the beam splitter and exit through two sides of the cube, in front one of which an industrial CMOS camera⁵ is placed. Specifically, the moving retro-reflection mirrors were chosen to be as similar to the final test setup as possible. For the target picomotor, the final target mount (see Figure D.1 B-D) itself was used utilizing the chromium chip of the resolution chart as the mirror. In the case of the commercial objective 5-axis translation stage, the same mount was used, but the objective was flipped to the other side of the thread to keep the load equal, and on its original place, a broadband mirror with negligible weight was attached. All parts were placed as close as possible to one another to minimize mechanical vibration influence. The system was aligned such that the beams are collinear and overlap. Since the measurements are sensitive on a tens of nanometer scale, it was also made sure that all elements are sufficiently relaxed. To prevent background light effects, the lights were turned off during measurement and lens-tubes were attached to the camera to shield potential stray-light.

Each measurement copied the algorithm used for focus scans in the main imaging tests. Naively, these consist of setting up the system slightly defocused, taking an image with the camera, moving a step (or multiple) towards the focus, waiting a few tens of ms due to technical reasons, taking another image and so on until one is on the opposite side of the starting position with respect to the focus position. Then, the direction is changed and the process is repeated, leading to a 2-sided (back-and-forth) focus scan of a PSF/optical tweezer. Having a two-sided scan has the advantages of enhanced statistics, the possibility to avoid foci where the environment strongly affected the measurement quality, and to take advantage of two different picomotor

⁵Allied Vision, Alivum 1800 U-1240m

step sizes. This scheme is repeated with different step counts (moving all at once) per camera image, to account for the variable depth of field among the different objectives/wavelengths used. The waiting times were also varied between 50, 100 and 200 ms. This type of algorithm is compared to a hysteresis compensation procedure. The hysteresis which was observed to be dominant with this type of motor causes strongly changing step sizes after changing the picomotor movement direction. To recover the equidistant step size regime, one first needs to move multiple dozens of steps in the same direction. We therefore implemented an overshoot and recovery part in the algorithm. The compensation algorithm is shown in Figure 3.2 B. The system is prepared such that the point source of light is well-focused, always coming from the positive (referring to the picomotor control, the absolute orientation is irrelevant) side. Then, the algorithm lets to motor move a fixed number of single steps in the same direction, exceeding the distance that should be covered by the scan. It finally changes direction to move the actual compensation steps in the direction of the forward scan. After compensation, usually 200 (sometimes less) images are taken in the positive direction, followed up by another start-up and compensation phase before the final 200 images in the negative/backward direction are taken. Note that a single two-sided focus scan took about 15 minutes per imaging measurement and about 4 minutes for the tweezer test measurements. These times were limited by the synchronous data acquisition speed and by increased image shaking for too high acquisition frequencies.

For good alignment and well collimated beams we expect to observe the beam profile on the camera with a more or less uniform brightness which is very sensitive to gently touching the retro-reflecting mirror mounts. In the ideal case, the intensity on the camera should go down to zero at the minimum corresponding to a contrast or visibility

$$V = \frac{I_{max} - I_{min}}{I_{max} + I_{min}} \quad (3.1)$$

of unity. For a Michelson interferometer operating with light at a given wavelength of λ we expect k full oscillations on the camera for a displacement of the mirror of $\Delta d = k \cdot \lambda/2$, where the factor of two arises from the reflection doubling the optical path. Subplot C in Figure 3.2 shows example interferograms taken with this setup using hysteresis compensation. In each plot the forward and backward scan are highlighted in different color and a third reference measurement is also depicted in grey which was recorded before each measurement without moving the motors. The reference measurement thereby allows us to estimate the degree of mechanical drift right before a given measurement and helps to estimate the error in step size calibration. The three rows show from top to bottom:

1. Target mount picomotor, 1 step per image
2. 5-axis motorized stage, 2 steps per image
3. 5-axis motorized stage, 4 steps per image

To convert these interferograms into usable step size estimates, each trace was first divided into forward and backward parts, then mean subtracted, apodized with a

Hanning window function and finally subjected to a discrete fast Fourier transformation. To convert these spectra that are in units of image frequency to motor (single) step size, the abscissa was scaled with the physical travel distance required observe a full oscillation $\lambda/2$ and thereafter divided by the number of picomotor steps moved between each image in a specific measurement. Thereby the maximum resolvable frequency (Nyquist frequency), that is 0.5 in the inverse image units, is converted to $\lambda/(4n)$, n being the number of motor steps per image. The spectra obtained by this procedure are shown in subfigure D, where comparable measurements are plotted with a similar color. The peak values were retrieved using Gaussian fits (not shown). All hysteresis compensated measurements with the same device, step count per image and different waiting times were averaged to obtain the final results shown in the legends. For the target mount picomotor the different measurements correspond to waiting times of 0.1 and 0.2 s. For the 5-axis stage and 2 steps per image they were 0.1, 0.1, 0.2, and 0.05 s, and for the 4 steps per image 5-axis stage measurement, the waiting times used were 0.1, 0.05 s. The error bar is given by the relative error that arises from an expected systematic drift of half a fringe over 22(40) full cycles for the 1, 2 (4) steps per image scans, plus the standard deviation of the individual measurements corresponding to the statistical error. Gaussian fit errors were negligible (< 0.1 nm). The results are also summarized in Table 3.2. Note the significant discrepancy between forward and backward scans and the difference of about 2 nm between two and four steps per image. Overall the measurement quality is surprisingly good, with relatively low drift and good contrast, making these results quite reliable.

	Forward (nm)	Backward (nm)
Target mount picomotor (step count = 1)	34.8(11)	29.1(7)
Five axis translation stage (step count = 2)	18.1(6)	14.5(6)
Five axis translation stage (step count = 4)	19.7(6)	16.2(2)

Table 3.2 – Interferometric picomotor step size calibration

Finally, plot E shows two further example interferograms without hysteresis compensation for cases 1 and 3.

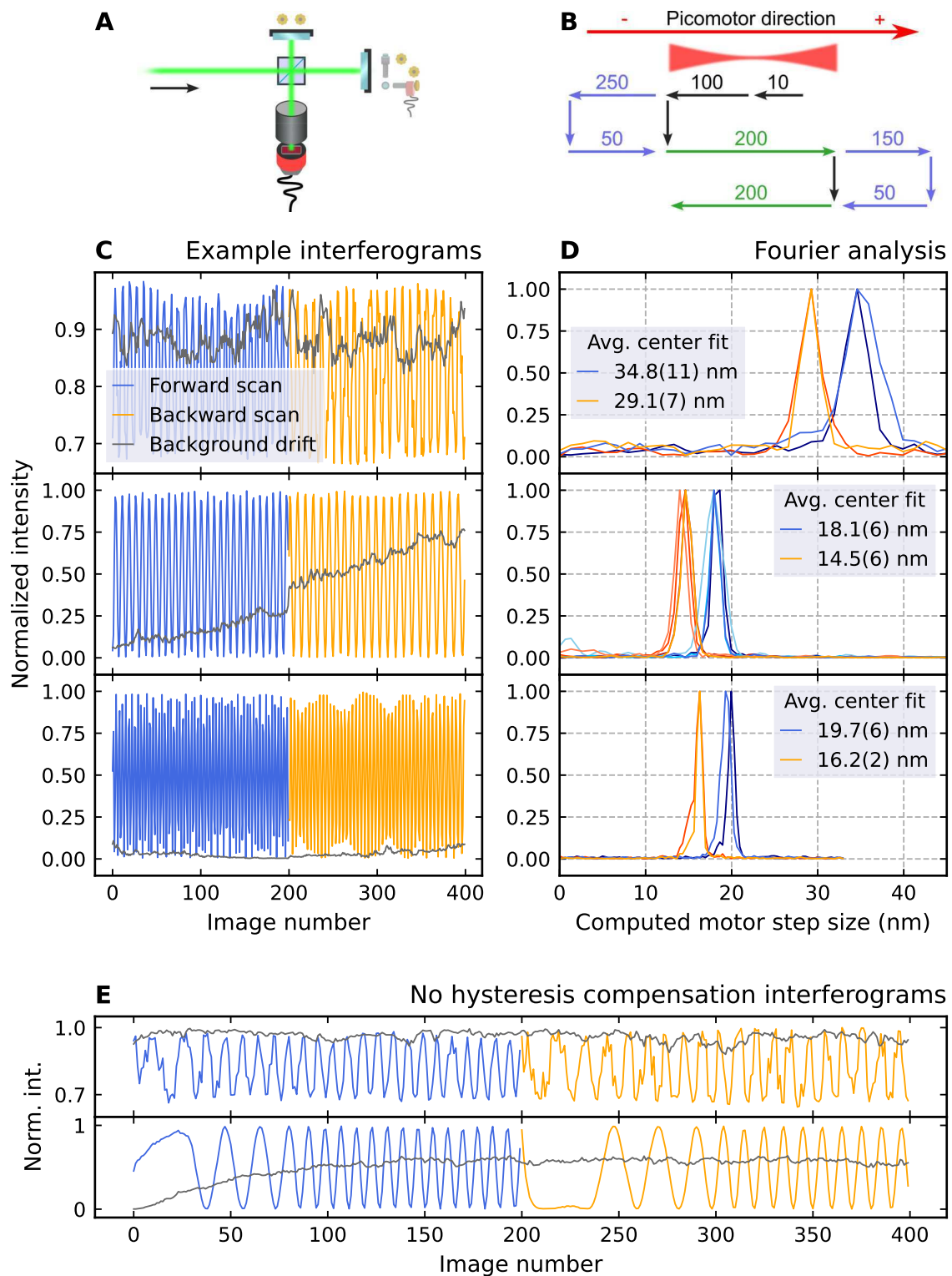


Figure 3.2 – Interferometric motor step size calibration. Subfigure **A** shows the used interferometer setup while subfigure **B** visualizes the hysteresis compensation algorithm. Parts **C** shows example measured interferograms using hysteresis compensation and a background drift curve for reference. **D** covers the Fourier analysis of all comparable measurements re-scaled to the single step picomotor step size. The three rows correspond to the target picomotor at 1 step per image and the 5-axis stage at 2 and 4 steps per image. The given step sizes are retrieved from Gaussian fits of the peaks and averaged over experimental realizations. Subplot **E** shows two examples from the first and third row tests, that did not apply the hysteresis compensation algorithm.

3.2 Showing diffraction-limited imaging performance

The first goal of this work was to verify if our custom high-resolution objectives are diffraction limited and to characterize their point spread functions. The latter will be investigated on the optical axis, in the field of view and for imperfect imaging conditions, involving additional optics in the beam path.

For our main experiment we ordered two custom objectives from *Special Optics* both with working f-number 0.712 and numerical aperture of $NA = 1/(2f/\#) = 0.7022$ [41]. The two objectives will be referred to as *SQM objectives* in the following and to distinguish them, they are labeled according to their packaging as *objective 001* and *objective 002*. Our objectives are specified to be diffraction limited at 399, 532, 552 and 590 nm if placed behind a 6.000 mm fused silica window, that accounts for the glass cell in the main experiment. Furthermore, they are infinity-corrected, consist of multiple AR-coated lenses, exhibits an effective focal length of 24.97 mm, with an entrance pupil diameter of 35 and an exit pupil diameter of 25 mm. It is designed for a working distance of 14 mm which is divided into 1 mm in air, 6 mm in fused silica (glass cell) and 7 mm vacuum to the position of the atoms.

3.2.1 Imaging test setup

In order to achieve this goal, a test setup was prepared that allows for precise measurement of the 3D PSF. The basic setup is reminiscent of the standard imaging system explained in Chapter 2.2.1 and is visualized in Figure 3.3. A legend to all symbols used can be found in Figure 1. Note that the schematic shows two subfigures, both not to scale, the upper show all optical components in the beam path and the accessible degrees of freedom for each mount. The lower displays a linearized version of the setup without mirrors to emphasize the beam size during propagation. In B, the objective is treated as black box system with principal planes indicated by dotted lines similar to the principal and focal planes of the other optics. Paying attention to show the exact number of optics in these schematics is particularly important between the target and camera, since there the imaging will be very sensitive on any wavefront distortions induced by imperfect optics. To this end, for the imaging tests a 2.5 meter linear setup without any folding mirrors was chosen to really measure the objective performance and not be misled by imperfect optics in between. We used two light sources to test the objectives, a 399 nm home-built diode laser (referred to as blue) and a 532 nm 18W Verdi from *Coherent* (referred to as green). Both beams were superimposed on a dichroic mirror to be able to quickly switch wavelength during measurements. After a relatively long propagation distance, useful for accurate alignment, the beam is focused on the test target (Chapter 3.1.1) by a $f = 60$ mm lens. The target is mounted with tip and tilt degrees of freedom as well as 3-axis translation stage of which the axial direction is controlled by a picomotor for precise focusing. The 0.7-NA SQM objectives collect the light transmitted by the chart, which is focused by a $f = 1$ m

achromat doublet lens onto the camera⁶ to complete the imaging process. The sensor chip offers a bit depth of 10 and pixel size of 1.85 μm which allows for sufficient sampling of the PSF during imaging. More specifically, the transverse magnification of this setup is given by the ratio of focal lengths $M_T = f_L/f_O = 1000/24.97 = 40.05$ which leads to an effective pixel size in object space of $1.85 \mu\text{m}/40.05 = 46.2 \text{ nm}$, roughly a tenth of the green diffraction limit. The optics are mounted on a rail to ease alignment reproducibility and the objective and lens mounts are also equipped with tip and tilt and x,y,z translation degrees of freedom. Further notes and images of the mounts used can be found in Appendix D.

As the imaging system is very sensitive on tiny displacements cause by mechanical vibrations of any sort, a few efforts have been taken to stabilize the system. Among those were floating the optical table, shielding the setup with cardboard covers and closing the curtains of the table during measurement. A more detailed discussion on setup stability is found in the Appendix C.2.

Details on alignment can be found in Appendix A, however in short, there are three distinct parameters that need to be adjusted:

1. Tip and tilt
2. x and y (transverse) translation
3. z (longitudinal) translation

The Figures A.5 and A.6 in the Appendix visualize the alignment signals used for each parameter type. The first shows typical back reflections of different optics in a few meters distance that are usually used for angular alignment. This observable is a very reliable signal to optimize on for tip and tilt adjustments. Mostly independent on that, for transverse translation alignment, the transmission through the optics was used and is captured on the auxiliary camera introduced in the previous paragraph. The second Figure shows typical signals on the camera. The Figure A.2 that is also shown and discussed in more detail in the Appendix, contains example focus scans which reveal bad axial symmetry indicating spherical aberrations. For sensitive longitudinal distances (like the camera-tube lens spacing), misalignment will usually create spherical aberrations which can be avoided by iterative axial translation and symmetry checks. Lastly, a useful alignment order is last-to-first element, to always keep the back reflection distance as long as possible.

The alignment accuracies achieved in the imaging measurements are summarized in Table 3.3.

⁶Allied Vision, Alvium 1800 U-1240m

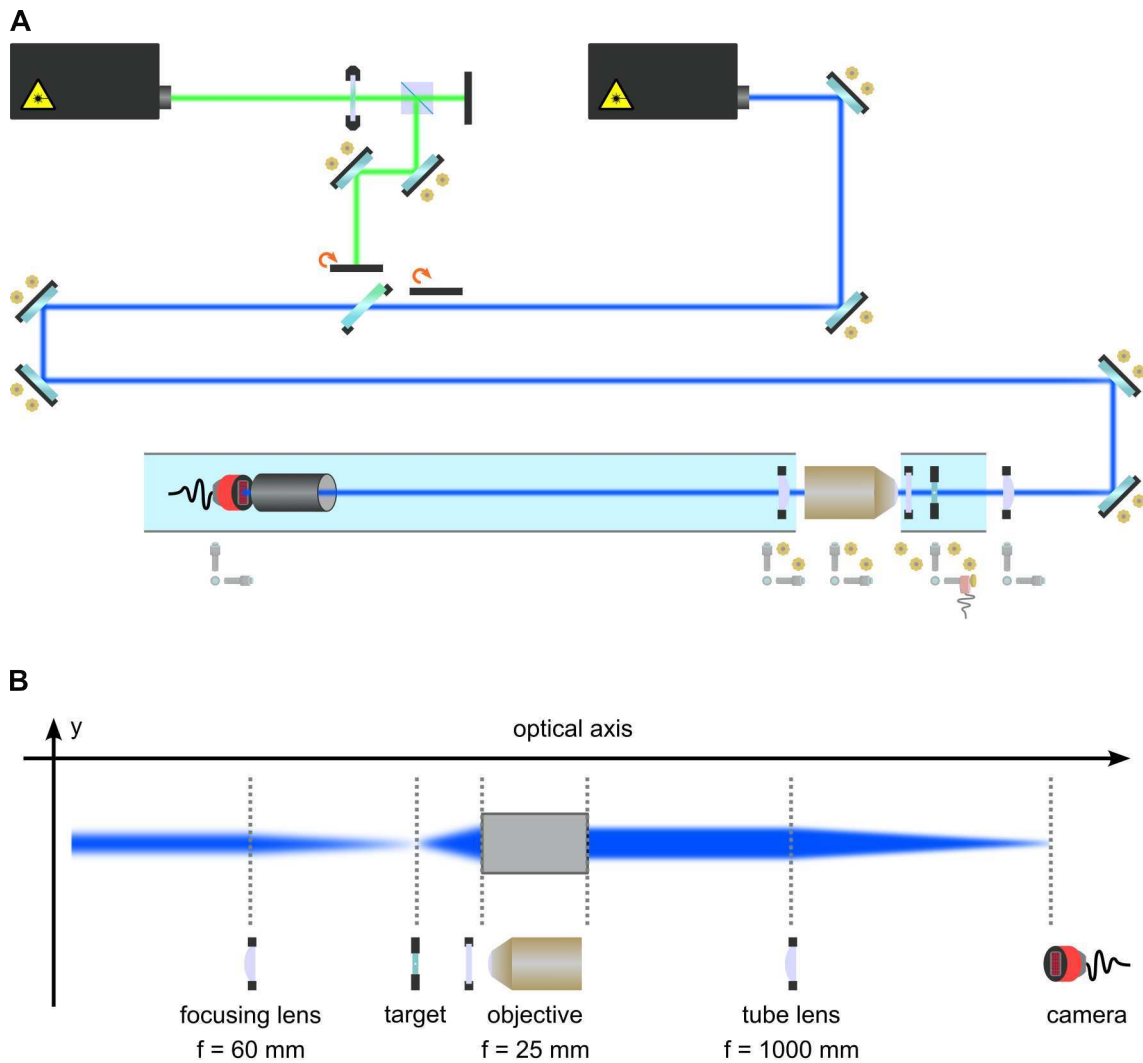


Figure 3.3 – The test setup for imaging measurements with the SQM objectives. In **A** the complete optical test setup for the imaging characterization measurements is shown. This includes all optics and their respective degrees of freedom for alignment. Subfigure **B** depicts a linear version of the setup that omits all mirrors and displays the beam size during propagation. Both illustrations are not to scale.

Component	Tip/tilt	Transverse translation	Axial translation
Target	0.5 mrad	10 μm	30 nm
Glass window	0.2 mrad	—	—
SQM objective	0.5 mrad	20 μm	20 μm
Tube lens	0.3 mrad	40 μm	20 μm
Camera	1 mrad	10 μm	1 mm

Table 3.3 – Alignment accuracies for SQM objective imaging tests

Note that these values pose an upper bound to alignment precision, the actual alignment might be better. Translation values were estimated based on the readings from micrometer screws and ruler measurements, while the angle accuracies were computed from observing the back reflection centering tolerance and dividing the corresponding angle by two to account for the reflection-based angle doubling.

With the alignment strategy presented in the above paragraphs, one is capable of setting most lower-order Zernike coefficients of the imaged wavefront to zero. This works as follows:

1. *Piston*
Set to zero: Imaging is not phase-sensitive.
2. *Tilt x, y*
Set to zero: Image is centered on the camera.
3. *Defocus*
Set to zero: Image is focussed.
4. *Astigmatism*
Non-zero: Difficult to be independently compensated in this setup.
5. *Coma*
Set to zero: Tip and tilt of the glass plate can remove coma completely.
6. *Trefoil*
Non-zero: Not possible to compensate with rotationally symmetric optics.
7. *Spherical aberrations*
Set to zero: Changing axial distances in the imaging setup can remove spherical aberrations.

This means, for this chapter it needs to be kept in mind, that in the test setup we compensate for plenty of aberrations which leaves the objective higher order imperfections (mostly astigmatism and trefoil) to be tested. In the final setup, spherical aberrations and in principal also coma can be compensated in the same way, making this a valid approach. In Chapter 3.4 we integrate the objective in the main setup, where apart from optimal optical alignment, direct compensation of coma inherent to the objectives is not possible since it requires an imaging setup that allows for live-access to the PSF/tweezer quality.

3.2.2 Imaging magnification measurement

To make sure that the anticipated transformation from object to image plane is valid (lenses usually have a tolerance of focal length on the order of 1%), a magnification measurement was performed to confirm the expected 40.05x transverse magnification. To this end, the imaging setup was used to take pictures of the stripe patterns of the resolution chart. The known stripe spacing together with the camera pixel size

allows one to calculate the magnification of the experiment. Figure 3.4 shows the magnification analysis results as a function of investigated stripe pattern size in units of line pairs per millimeter (lppmm).

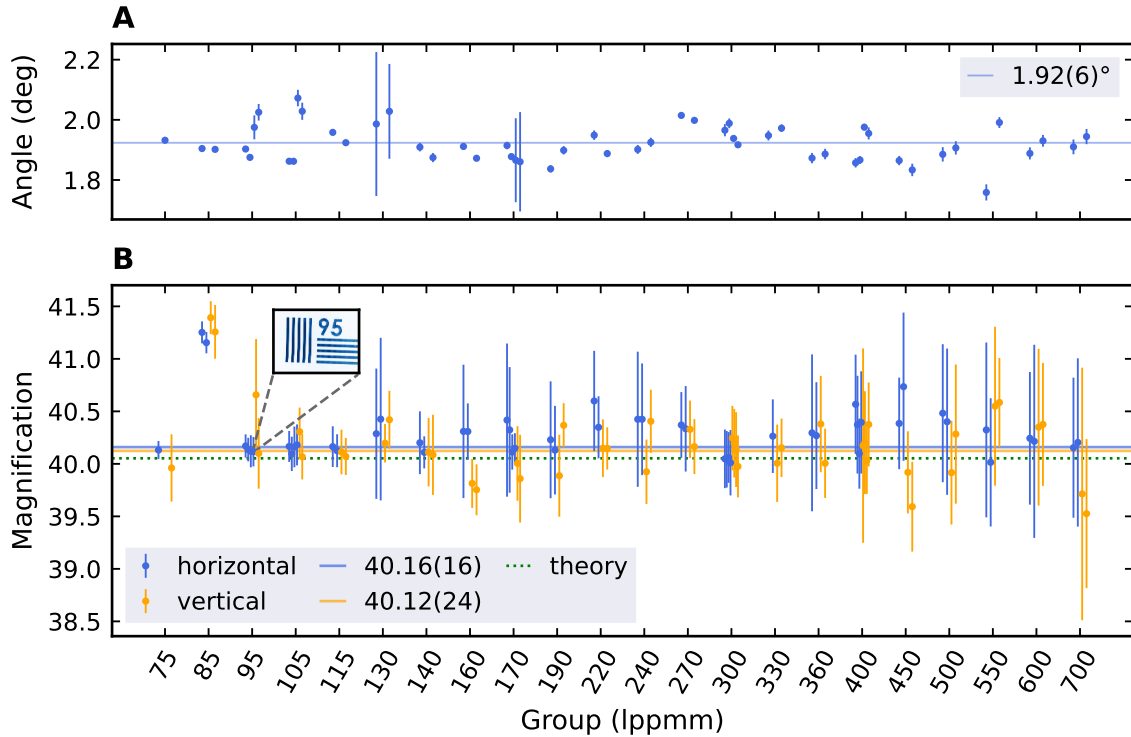


Figure 3.4 – Results from the magnification calibration measurement for the SQM objective imaging tests. Subfigure **A** summarizes the calculated relative angle between inspected structure and the camera. In subfigure **B**, the observed magnifications are shown for the horizontal (blue) and vertical (orange) direction. A variance-weighted average was computed and is shown as solid line for both the horizontal and vertical orientations. It can be compared to the theoretically expected magnification indicated by the green dotted line. The inset at 95 lppmm shows an example image of a stripe pattern. Among all data sets, both images analyzed for 85 lppmm were not included in the final magnification estimate, since they both certainly lie outside of the 6-sigma interval, which indicates that the 85 lppmm structure is not of the expected size.

Subplot A displays the calculated pattern-camera relative angle θ which is 1.92(6) degrees on average. As the magnification is calculated from the spacing along rows and columns of the camera image, this angle is important to account for the $1/\cos(\theta)$ geometrical stretching factor. The angle error bars are computed from the linear fit error from which the angles are retrieved. Subplot B shows the computed horizontal (blue) and vertical (orange) magnification for each image taken. The inset depicts an example image from which one set of horizontal / vertical data points was generated. Some stripe patterns were recorded twice and for a few only horizontal magnification could be calculated due to the image being cut. The error bars are calculated from statistical fluctuations of the magnification within a single image. The variance-

weighted mean has been calculated for this measurement to obtain final magnification values for this setup. The results are a horizontal magnification of 40.16(16) and a vertical magnification of 40.12(24) which agree well with the theoretically expected 40.05 (green dotted line). Note that for these averages, both measurements of the 85 lppmm stripe patterns were dropped, since they lie outside of the sample mean by more than 6σ and probably stem from some manufacturing errors in that specific structure.

3.2.3 Focus scan analysis

We will distinguish single focus scan analyses and multi-scan measurement series evaluations. In the former, a particular focus scan is discussed in detail in two Figures, one concentrating on the physical shape of the PSF, the second depicting all relevant analysis Figures for this scan. In the latter case, only a few condensed key parameters are extracted for each focus scan to compare to other measurements.

The following discussion of observables and analysis parameters also largely applies to the optical tweezer analysis with a few technical caveats (see Chapter 3.5). The analysis concentrates on a few main observables:

1. **Rayleigh resolution (ξ)** from a 2D Airy pattern fit
It represents the main figure of merit to assess whether a PSF is diffraction limited. Furthermore, this quantity is a very direct observable and simultaneously very robust to imaging imperfections due to the nature of fitting.
Applied corrections: Convolution, background, pixel averaging
2. **R^2 value** representing Airy fit goodness
Described by the formula $R^2 = 1 - \sum_i (y_i - f_i)^2 / \sum_i (y_i - \bar{y})^2$, where y_i are the data points, \bar{y} their mean and f_i the fit that is tested, R^2 is a measure for the residue of the fit scaled by the data scatter. This quantity that is also known as the coefficient of determination, exhibits an upper bound of 1 which corresponds to a perfect fit for our model.
3. **Radial $1/e^2$ Gaussian waist (w_r)** from a 2D Gaussian fit
Similar to the Rayleigh resolution, but offers better comparability to different publications. Also, this quantity does not use deconvolution.
Applied corrections: Background subtraction, pixel averaging
4. **Strehl ratio (SR)**
The Strehl ratio is a useful parameter which is closely connected to wavefront errors as discussed in Chapter 2.2.4. Additionally, Strehl ratio is a useful figure to compare the performance of different objectives and can be used to classify PSF measurements as well as to assess optical tweezer quality. Compared to fits, the Strehl ratio is much more susceptible to all sources of experimental and technical errors, which makes it much more challenging to compute meaningful values for experimental images. As a consequence, plenty of rather involved

compensation steps were applied to yield a Strehl ratio estimate that is trustworthy, in particular with respect its error bar.

Applied corrections: Convolution (imaging tests only), imaging infidelities (tweezers only), background, pixel averaging, pixel centering, discretization

5. Axial $1/e^2$ Gaussian waist (w_{ax}) from a Gaussian fit

A 1D Gaussian fit to the axial intensity pattern was used to extract a number describing the axial extent of the PSF. It is also a rather robust quantity that is, however, quite sensitive to uncertainties in the expected picomotor step size.

Applied corrections: Background

Each focus scan measurement, whether it be a PSF or tweezer measurement, was analyzed using the same class-based Python script whose steps will be explained in short in the upcoming paragraph.

1. **Initialization** of the focus scan object. This includes image loading, definition of all parameters, registration of the focus scan shape, image count, brightest images and, if present, saturated images. In case a single pixel is brighter than 1.5 times the second brightest pixel, the brightest pixel will be identified as a pixel defect and will be set to zero (otherwise it can later on be mistakenly identified as very narrow PSF).
2. **Subtracting background.** The background is calculated from the brightest image of each focus since there, most of the light is concentrated in a single spot which helps to distinguish background from signal. To compute the background, the total power contained in a box randomly located outside of the PSF position is investigated. This random location is changed a few thousand times to accurately sample the whole image and to gain statistics. This method simulates the process of picking a region of interest for later analysis in the given picture, of course excluding the area of highest power containing the PSF. The mean and standard deviation of all random positions are then used as the background and background error. Finally from every image in the focus scan the determined background is subtracted, where in case the scan contains forward and backward foci, the largest background is used for subtraction.
3. **Cutting a region of interest (ROI).** For each image the center of mass is identified separately after masking them such that only pixels that exceed 66% of the maximum image brightness contribute with an equal weight of one (this excludes background/noise influence). Then the ROI is cut using the optimal ROI size for the given wavelength and NA, which lies in the sweet spot discussed in Chapter 3.5.4.
4. **Bad image removal.** Before starting with the actual analysis, every image is checked to fulfill a few criteria which classify pictures as suitable for analysis. If an image does not meet these requirements, it will be excluded from analysis. Requirements cover image saturation, images being cut and images not being

well centered in the ROI. Note that during analysis, the program always keeps track of the valid indices to maintain correct axial focus scan distances.

5. **Radial Gauss fits.** The first real analysis step covers the radial Gaussian fits. Those will only be computed for images exceeding 30% of the focus scan maximal brightness, to make sure that an image actually shows a peaked distribution that is similar to a Gaussian. If desired, pixel averaging will be taken into account for the 80% brightest images. For the results shown in this work, for each pixel, the fit averages values on a three times finer grid.
6. **Airy pattern fits.** Similar to the Gauss fits, Airy fits will only be performed for images brighter than 30% of the maximal scan brightness. Pixel averaging and deconvolution are also possible for images with relative brightness larger than 0.8. Similar to the Gaussian case, pixel averaging is incorporated in this work using an oversampling factor of 3. Deconvolution was also performed assuming aperture sizes discussed in Chapter 3.1.1.

The Airy and Gauss fits use six free parameters: transverse position x_0, y_0 , width ξ_x, ξ_y , amplitude A and ellipse rotation angle θ . Depending on the type of analysis, the field or intensity versions of the distributions are used.

The 2D electric field functions used for fitting have the following form:

$$\mathcal{A}(x, y, A, x_0, y_0, \theta, \xi_x, \xi_y) = A \cdot 2 \left(\frac{J_1(\epsilon)}{\epsilon} \right) \quad (3.2)$$

$$\mathcal{G}(x, y, A, x_0, y_0, \theta, w_x, w_y) = A \cdot \exp \left(- \left(\frac{u}{w_x} \right)^2 - \left(\frac{v}{w_y} \right)^2 \right) \quad (3.3)$$

$$\text{with } \begin{pmatrix} u \\ v \end{pmatrix} = \begin{pmatrix} \cos(\theta) & \sin(\theta) \\ -\sin(\theta) & \cos(\theta) \end{pmatrix} \begin{pmatrix} x - x_0 \\ y - y_0 \end{pmatrix} \quad (3.4)$$

$$\text{and } \epsilon = 1.22\pi \sqrt{\left(\frac{u}{\xi_x} \right)^2 + \left(\frac{v}{\xi_y} \right)^2} \quad (3.5)$$

Where \mathcal{A} refers to the Airy pattern and \mathcal{G} to the Gaussian. Note that u and v are variables of the reference frame rotated by θ and displaced by $\begin{pmatrix} x_0 \\ y_0 \end{pmatrix}$. As discussed in Chapter 2.2.2, $J_1(x)$ refers to the Bessel function of the first kind and of order one.

7. **Strehl ratio** computation. The Strehl ratio is computed by dividing the power-normalized maximum image value by the maximum of a power-normalized simulated diffraction-limited PSF following formula (2.41). Since the Strehl ratio is a rather sensitive parameter, several correction steps were applied. While background subtraction affects the numerator only, further refinement steps can be

conducted via the calculated PSF. Optionally, the simulated PSF can be pixel-averaged, centered differently with respect to the pixel grid, convolved with a pinhole of given size or imaging infidelity-corrected in case an optical tweezer is imaged by a separate system. Note that in the case of pixel-averaged imaging measurements, convolution with an aperture function is performed in the oversampled finer grid, because that allows for more precise aperture function sampling (otherwise rounding effects would lead to apertures with diameters of interger multiples of e.g. 46 nm, which is rather coarse). Lastly, all images with brightness lower than 5% of the maximum of the scan will receive a Strehl ratio of zero, to remove outliers caused by noise. This work again used pixel-averaging of three points per pixel and orientation, pixel centering corrections, background subtracted images, discretization corrections, deconvolution and imaging infidelity corrections in the imaging / tweezer test cases.

8. **Axial Gauss fits.** Next, for each focus a 1D Gaussian is fitted to the axial intensity pattern. This pattern is determined by averaging the central 2x2 pixels per ROI in the focus scan, to slightly smoothen out pixel-to-pixel fluctuations. For this step, the different forward and backward picomotor step sizes that have been calibrated in Chapter 3.1.2 were used for correct scaling. The used fit function was

$$\mathcal{G}(x, A, x_0, w, c) = A \cdot \exp\left(-2\left(\frac{x - x_0}{w}\right)^2\right) + c \quad (3.6)$$

9. **Focus position and width** determination. The same 1D Gaussian is fitted this time to the Strehl ratio curve, and for each focus. This leads to two relevant quantities: First, the exact focus position. While the intensity Gaussian fit will find the brightest image only, this procedure allows us to find the image of least confusion, which is particularly relevant for aberrated scans. Second, the waist of the Gaussian fit to the SR enables us to estimate the range over which a particular focus is diffraction limited. This is important for measurement series where every scan needs to be represented by a single number. To obtain this number, several, equally good images in focus need to be averaged, to not restrict the analysis to the best image in an objective, meaningful way that only relies on actual image data. Empirically, the distance $w/13$ was chosen to both sides of the determined focus to average all quantities of interest.
10. **Error computation.** Systematic and stochastic errors of all observables are computed for every image. See the next section for details.
11. Returning a **focus scan summary.** All quantities of interest and their corresponding errors are averaged and returned, to summarize a focus scan in only a few numbers. To maintain statistics, the returns are computed for both foci individually and the averaging used the distance around the focus described two bullet points prior. The quantities summarized for each focus contain:

- The Strehl ratio, with only basic corrections
- The Strehl ratio, with all corrections
- The fitted Rayleigh resolution, both principal axes
- The Airy fit R^2 value
- The 2D Gaussian fit waists
- The axial scan waist and curvature at focus
- The focus position
- The number of images that are averaged for these quantities

For all quantities, except the number of averaged images, the errors are returned as well. Starting with the measured values, weighted averages were calculated for the Airy fits, R^2 , Gauss fits and Strehl ratios, weighted by the individual data point variance. The axial fits, focus position and averaged image count are returned as single numbers. Continuing with the errors, they were either subject to a simple average, or were returned as a single number, according to the mean value procedure. Note that systematic and statistical errors were added differently. Statistical errors were divided by \sqrt{N} , N being the number of averaged images, before adding the systematic errors.

More details on the correction steps can be found in Chapter 3.5. The errors taken in account for the different parameters are listed below.

Quantity	Statistical errors	Systematic errors
Resolution ξ	Fit error	Magnification error
Radial waist w_r	Fit error	Magnification error
Axial waist w_{ax}	Fit error	Picomotor step size error
Strehl ratio	Discretization errors ROI truncation Background Pixel fluctuations	Aperture size error (imaging only) Imaging infidelities (tweezers only)

Table 3.4 – Analysis error sources

Apart from the straight forward fit and calibration measurement errors, the others were calculated under certain assumptions. Starting with the systematic errors, the aperture size errors were estimated by computing the deconvolution two more times for every image, assuming a 10% smaller/larger pinhole. Half the difference of the resulting Strehl ratios was used as the error. The uncertainty induced by not knowing how the tweezer imaging and tweezer generation aberration vectors align, is captured by the formula presented in Section 3.5.8, assuming random orientation of the aberration vectors and 7 dimensions making dominant contributions (corresponding to the lowest order aberrations up to spherical aberrations, assuming the first four Zernike coefficients are vanishing by alignment). Moving to the statistical

errors, discretization errors were estimated using the uncertainty band from Section 3.5.5 and the ROI truncation error simply follows Chapter 3.5.4. To include possible uncertainties of the background subtraction, the standard deviation in the brightness of the randomly sampled patches was used to estimate the effect on the Strehl ratio. In detail, the dependence of the Strehl ratio on correct background subtraction is discussed in Chapter 3.5.3. Lastly, since the Strehl ratio is directly proportional to the intensity of the brightest pixel for the estimate used in this thesis, it is very sensitive to single pixel fluctuations. Accounting for this, an additional relative error is added, which is calculated as the standard deviation of the four brightest pixels divided by the maximum brightness.

3.2.4 Measured point spread functions

With the setup and algorithms presented in the previous Chapters, the point spread function of the SQM objectives was measured and analyzed for 532 nm and 399 nm light. In the following, results will be shown, each for a specific objective and wavelength, while the imaged pinhole from the resolution chart was kept the same, always using the 250 nm pinhole.

Since on the next pages, and also for the optical tweezer analyses, the individual focus scan plots will keep the same structure, a description and explanation of the plot layout will be shown only here, using the very first measurement as an example, while for the others, figure discussion will focus on the experimental results only.

Figure 3.5 summarizes the PSF shape for measurements of SQM objectives 001 (column (a)) and 002 (column (b)) using 399 nm light to image the 250 nm pinhole of the resolution chart. In each column, subfigure A visualizes cuts through both transverse axes in the center of the ROI as a function of position in the focus scan. Here, only forward focus scans are shown. Figure B shows full ROIs taken from the five cuts through the z axis, highlighted by the orange dashed lines in part A. Images in A and B are both depicted in logarithmic scale to enhance the visibility of the faint side-lobes. Along the blue dashed line in Figure A, the 1D on-axis intensity was extracted by averaging the 2x2 pixels in the very center of every ROI. This axial distribution is plotted in subfigure C. Additionally, the axial Gaussian fit (dotted line), corresponding $1/e^2$ waist (gray arrow) and expected axial diffraction limit (green segmented line) are drawn.

One observes that both measurements have relatively good axial symmetry, which can be translated into well compensated spherical aberrations. Furthermore, objective 001 has some residual non-compensated coma to the lower left of the central image in B, while 002 has close to no visible coma. Astigmatism is quite pronounced with objective 001, not only being visible at 350 nm from focus, but also in focus, as clearly visible by the "+"-like shape of the PSF. Objective 002 in contrast shows clear trefoil contributions, indicated by the triangular shape of the PSF in focus. As expected, within the error bars, the axial PSF waist values of both objectives agree well. Note that for objective 001 some problem with the ROI-cutting code occurred, which leads to the sudden jump at about $z = -2 \mu\text{m}$.

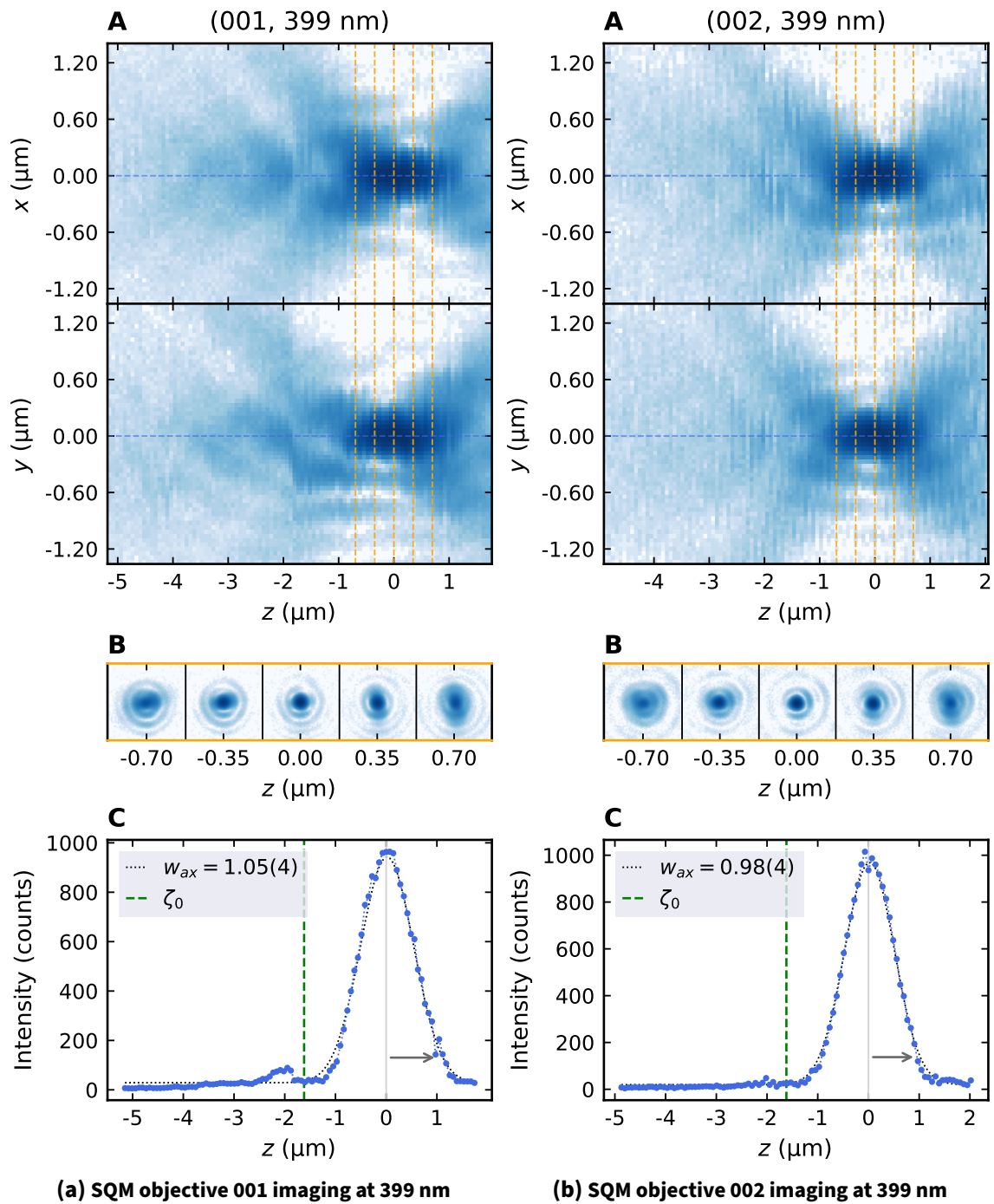


Figure 3.5 – SQM objectives imaging at 399 nm: PSF shape. Columns (a) and (b) show the PSF shape of SQM objectives 001 and 002 respectively, imaging the 250 nm pinhole with 399 nm light. Subfigure **A** shows cuts through the y and x axes through the center of the focus scan, displayed in logarithmic scale. In part **B**, five example images are depicted at different distances from the focus, also shown in logarithmic scale for better visibility of the side-lobes. The cuts from which these images are taken are indicated in A by orange dashed lines. **C** visualizes the axial intensity distribution, as taken from averages over the four pixels in the center of every image. As a guide to the eye, this axis is also shown in A as dashed blue line. The axial Gauss fit is also plotted as dotted line as well as an indication of the expected axial zero crossings (axial diffraction limit ζ_0 , green dashed line). In the legend, the fitted Gaussian waist is given, referring to the $1/e^2$ value, indicated by the gray arrow.

Moving to the analysis, Figures 3.6 and 3.7 visualize the results connected to the PSF shape plots shown on the last page. Starting with subfigure A, the most important - and computationally heavy - data points are plotted as a function of position within the focus scan. We start with the radial resolution in the upper plot, showing not only the fitted Rayleigh resolution ξ_x, ξ_y , but also the waists from the 2D Gaussian fits w_x, w_y . All correction steps mentioned in Section 3.2.3 are applied. Note that the w axis is scaled to theoretically match the Airy fits with the numerical factor $w \approx 0.84/1.22\xi$. Not only the fit parameters are plotted, but also the Airy pattern fit quality in terms of R^2 that is encoded in every data point via its opacity. The green dashed line completes the first plot by indicating the position of the expected diffraction limit for the used wavelength λ and NA given by $\xi_0 = 1.22\lambda/(2NA)$. The lower plot in A illustrates the development of the Strehl ratio across the focus. Two sets of data points are visible, the solid, navy-colored points correspond to Strehl ratio, calculated only using four low-influence correction steps, while the empty, green points have discretization corrections included as well. To give reference, the faint green background highlights the margin in which a Strehl ratio must fall such that the imaging is considered to be "diffraction limited".

Subfigure B displays the best-fit image of the whole scan, meaning that its R^2 value is the highest. To better locate this image with respect to the complete set, a red dotted line is drawn in part A. The 2x3 image array illustrates from left to right the raw data, the Airy fit and the corresponding difference of the former (residue). The two rows offer linear and logarithmic scale, as seen on the colorbars. Finally, part C shows a linear (left) and logarithmic (right) view of azimuth averages of the experimental PSF shown above, as a function of distance to the ROI center. For the azimuth average points at the same unique distance to the ROI center were averaged. In addition, instead of a fit, the ideal, diffraction limited pattern was simulated and averaged around the optical axis. For better comparison, the calculation was repeated twice with (back) and without (gray) including convolution in the simulation. The radial diffraction limit was again included as green dashed line, to provide reference.

The results show clearly that both objectives are diffraction limited even for the shorter wavelength of 399 nm. The resolution curves closely approach the diffraction limit, and the Strehl ratio goes up well beyond the 0.8 mark. As already indicated by the PSF shape Figures, objective 001 suffers from stronger astigmatism compared to objective 002, which is visible in the resolution panel as the axial focus displacement, with an astigmatic difference of about 550 nm (obj. 002 \sim 200 nm). This effect can also be observed in the best fit, whose residue exhibits the characteristic cross-like shape, typical for pronounced astigmatism. The example PSF of objective 002 however, shows trefoil as the main aberration, which is visible as the triangular shape of the PSF in logarithmic view. The azimuth averages for both objectives have very good agreement with the simulation. Only when the zero crossings are approached, the data starts to deviate from the simulation, which is explained by the residual astigmatism and trefoil. Furthermore, in the case of objective 002, one can also note that the calculated PSF, that includes convolution with a pinhole, does indeed better fit the data than the naive bare PSF.

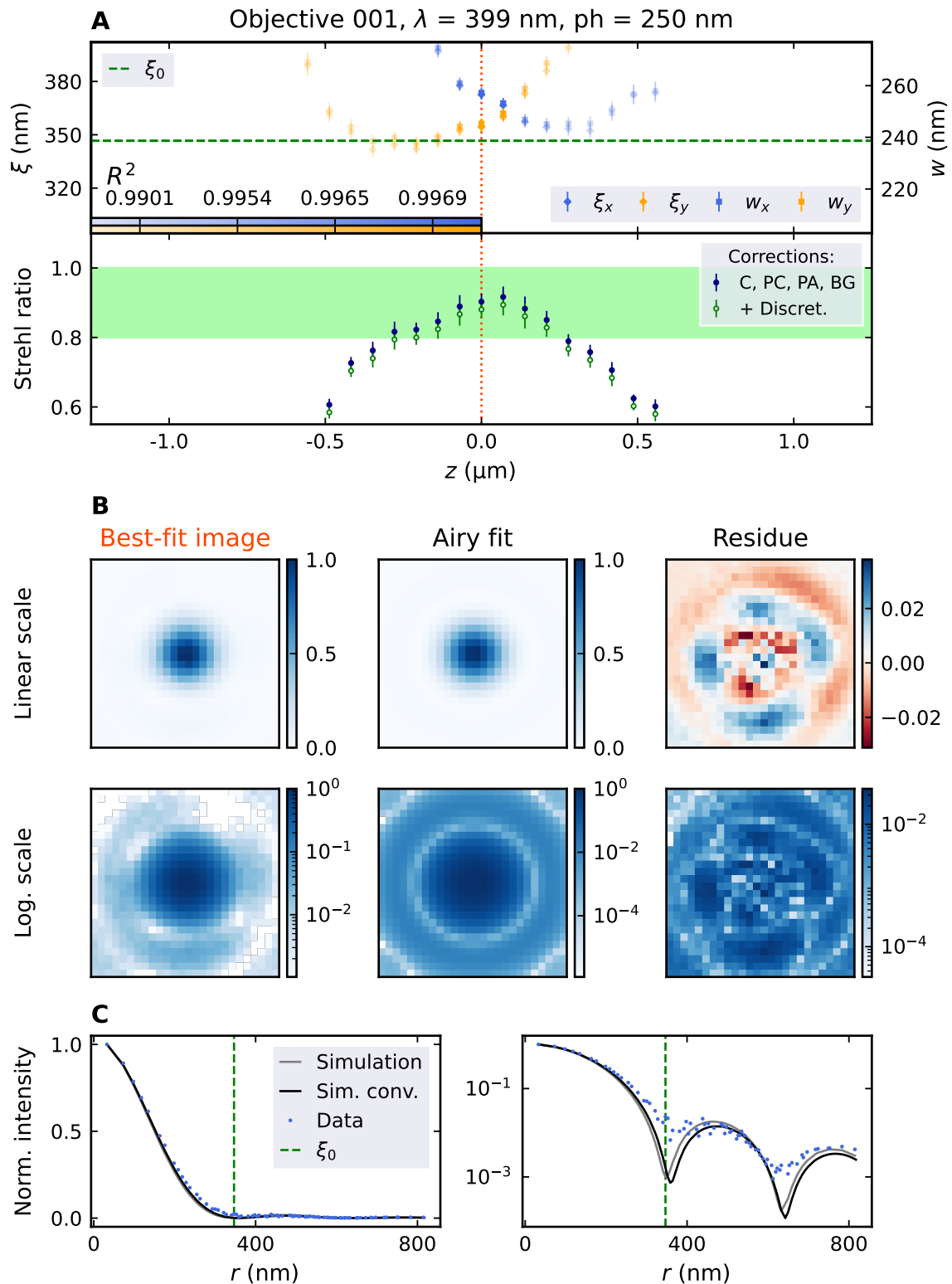


Figure 3.6 – SQM objective 001 imaging at 399 nm: PSF analysis. The main analysis results are summarized in subfigure **A**, starting with the upper plot that shows both the fitted Rayleigh resolution ξ and the waists w from the Gauss fits. For reference, the radial diffraction limit ξ_0 is drawn as well as dashed green line. Lastly, alpha-encoded R^2 values enable one to assess the Airy fit quality for each image. The lower plot displays the Strehl ratio with two different sets of correction steps and the "diffraction-limited" area highlighted in green. Part **B** shows the best R^2 fit of the whole scan, from left to right the image, fit and residue, both in linear and logarithmic scale. To better locate the image in the overall scan, a red dotted line is drawn in **A**. Section **C** shows azimuth averages of the above image and of ideal diffraction-limited simulations with and without convolution. Those are plotted in linear (left) and logarithmic scale (right).

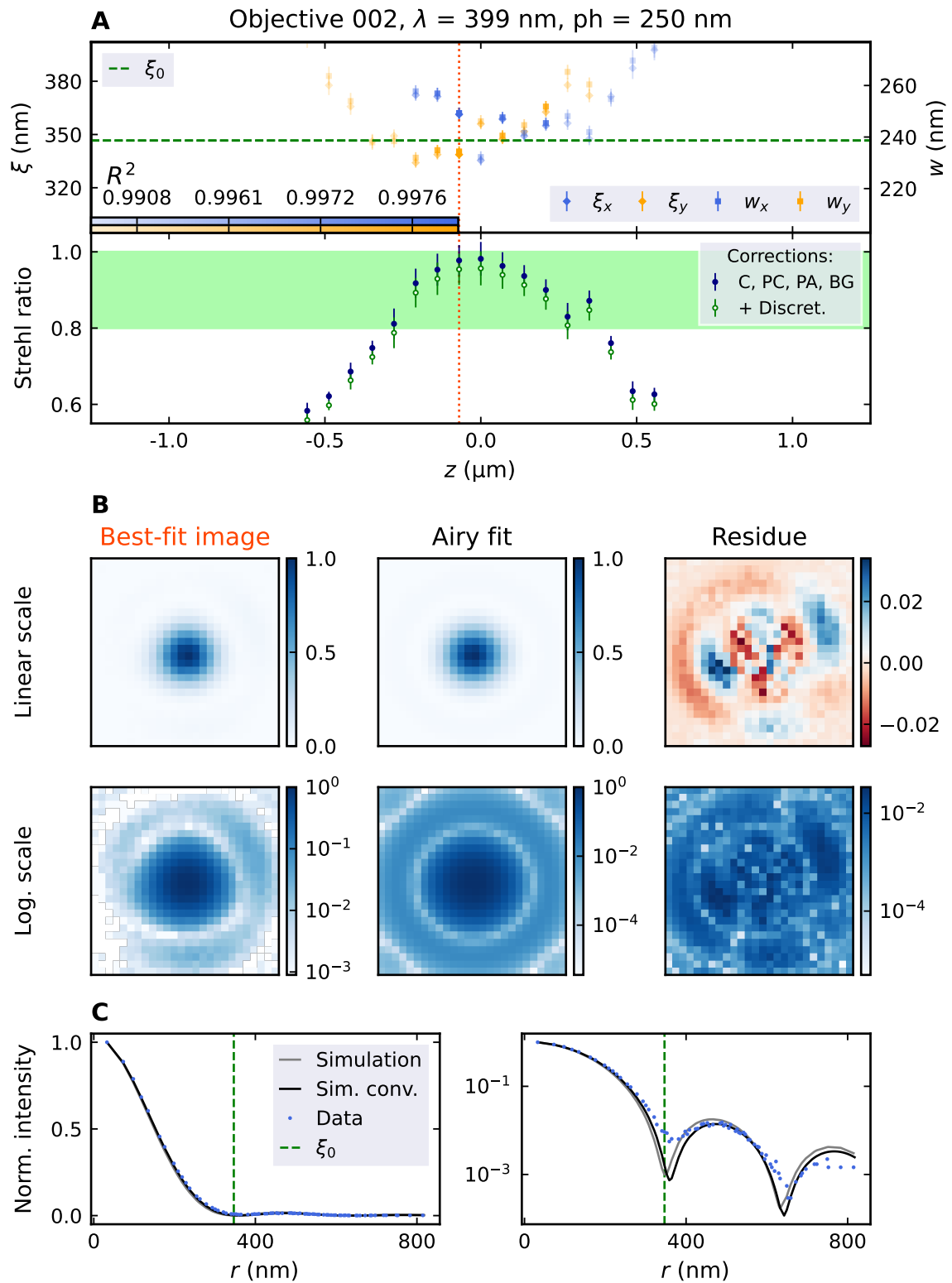
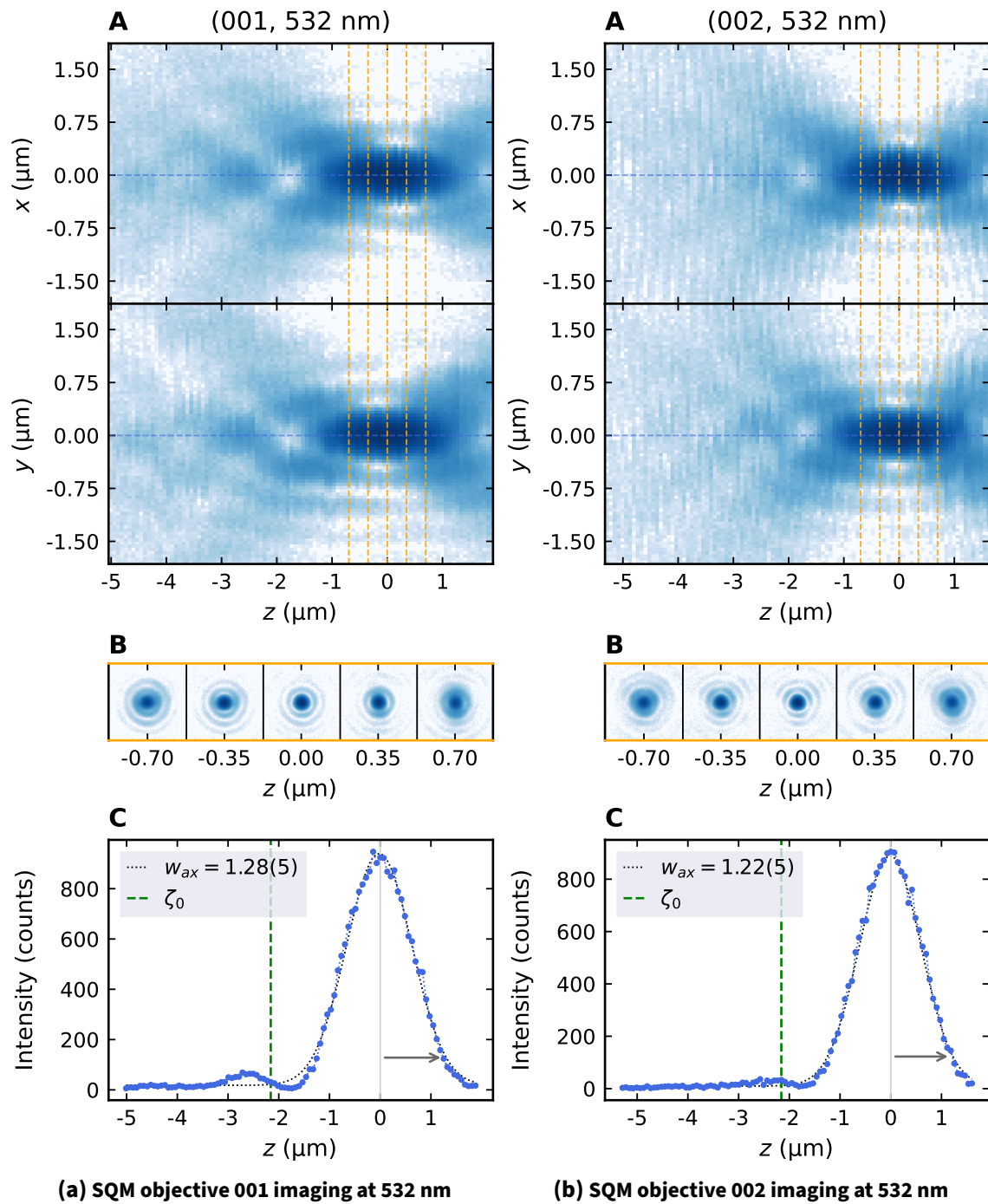


Figure 3.7 – SQM objective 002 imaging at 399 nm: PSF analysis. The Figure has the same structure as Figure 3.6.

Moving to the measurements in the green optical spectrum with the 532 nm beam, we first discuss the PSF shape of both objectives displayed in Figure 3.8. Again, on the left objective 001 and on the right objective 002 are shown. One finds that both scans look very similar, as ideally expected, and show close to no aberrations at first glance. A slight $\pm z$ asymmetry is visible comparing the x and y cuts in subfigure A for objective 001. This is a typical indication of astigmatism which is also confirmed in part B that shows the vertical focus being slightly shifted towards negative z and the horizontal focus in the opposite direction. Nevertheless, it needs to be pointed out that the astigmatism strength is reduced compared to operation of objective 001 in the blue just judging from the images. There is no clear sign of spherical aberrations and coma, which have been effectively compensated. For objective 002 the example images in B again show trefoil, like in the blue light case. Axial fits in C are in very good agreement leading to an axial waist of about $1.25 \mu\text{m}$ on average. Note that the mismatch between expected axial resolution limit ζ_0 and the actual minimum presumably arises from errors in the picomotor step size calibration (3.1.2), which had reduced contrast and stability compared to the five-axis stage calibration.

The analysis of the the green imaging tests confirms diffraction-limited performance for both objectives. Comparing panel A of the Figures 3.9 and 3.10, the astigmatism of objective 001 is found again by the axial focus displacement which is, as expected, weaker for green light compared to the shorter wavelength of 399 nm analyzed before. More specifically, the astigmatic difference is about 450 nm, which is less than the 550 nm in the blue light case. The astigmatic difference for objective 002 is about 200 nm and thereby very similar to the blue light case. Another interesting feature is the resolution discrepancy between the two principal axes of the fit, which is visible for both objectives and is of the order of 20 nm. It is unlikely that an effect of this order of magnitude is connected to ellipticity of the imaged pinhole, which makes this anisotropy an objective property. The Strehl ratio reaches up close to one in both cases, confirming that for green light imaging is less sensitive to imperfections compared to the blue imaging tests where SR only went up to about 0.90 to 0.95. Note that in case of objective 002, and only applying the four straight forward corrections, the threshold of one would be exceeded. This is of course unphysical (assuming wavelength and NA are correct) and lead to investigations into the source of this behavior. As clearly visible in part B, logarithmic scale, plenty of theoretically existing power in the wings is simply set to zero by the camera sensor discretization. Since this will artificially increase the Strehl ratio, the discretization compensation was implemented and explained in Chapter 3.5.5 which reduces the SR again, as indicated by the empty, green points in the plot.

In subfigure B we can see PSFs that are dominated by astigmatism (001) and trefoil (002) mostly recognizable by the symmetry of the residue. Overall, the fit fidelity is quite high (and in particular higher compared to the blue light tests) as the R^2 value in A confirms. Especially the very round PSFs of objective 001 achieved coefficients of determination of up to 0.9995. Finally, in Section C, measurements of both objectives show excellent agreement with the simulated diffraction-limited PSF. Slight deviations near the first minimum can be explained by the aforementioned aberrations.



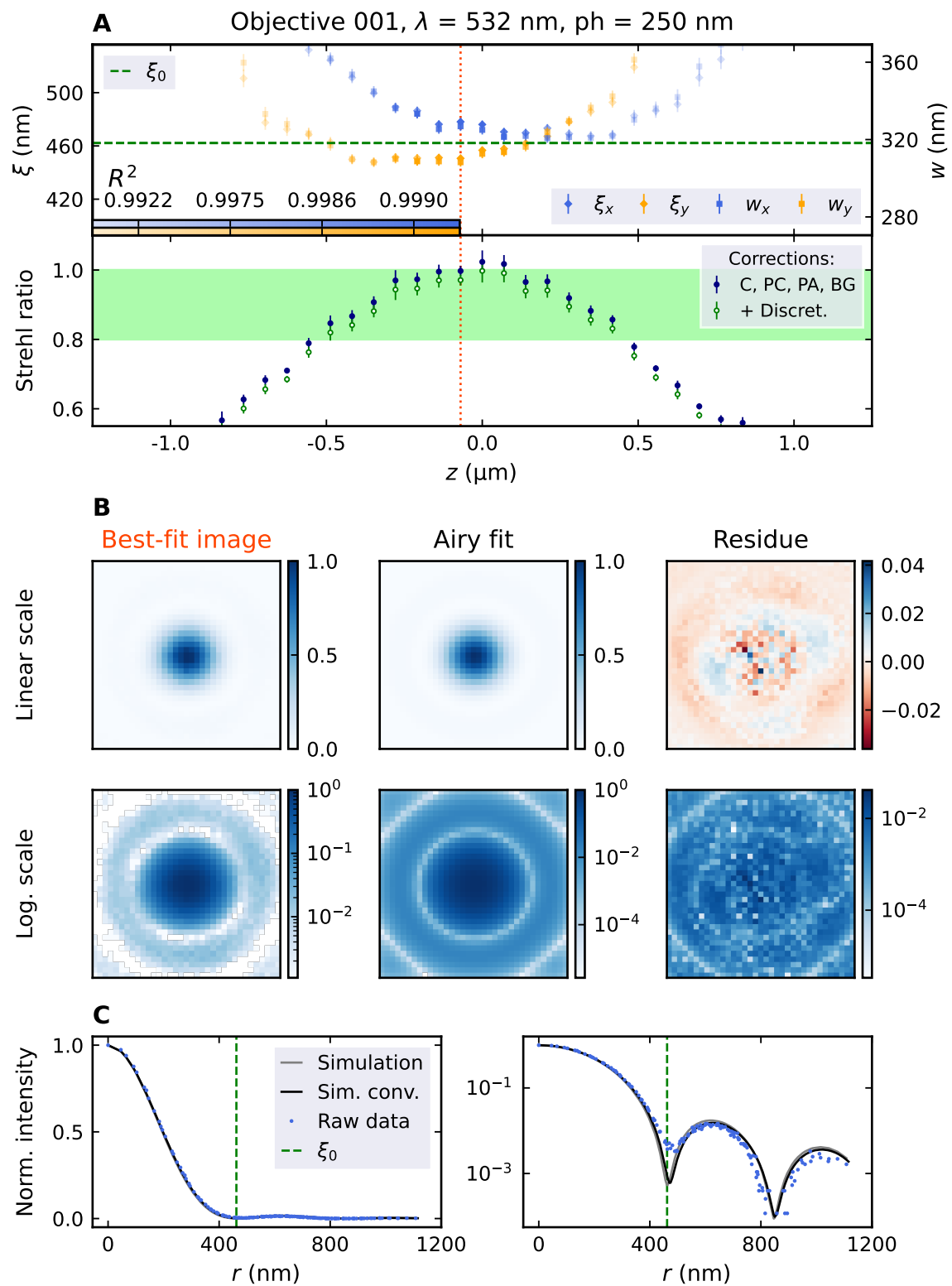


Figure 3.9 – SQM objective 001 imaging at 532 nm: PSF analysis. The Figure has the same structure as Figure 3.6.

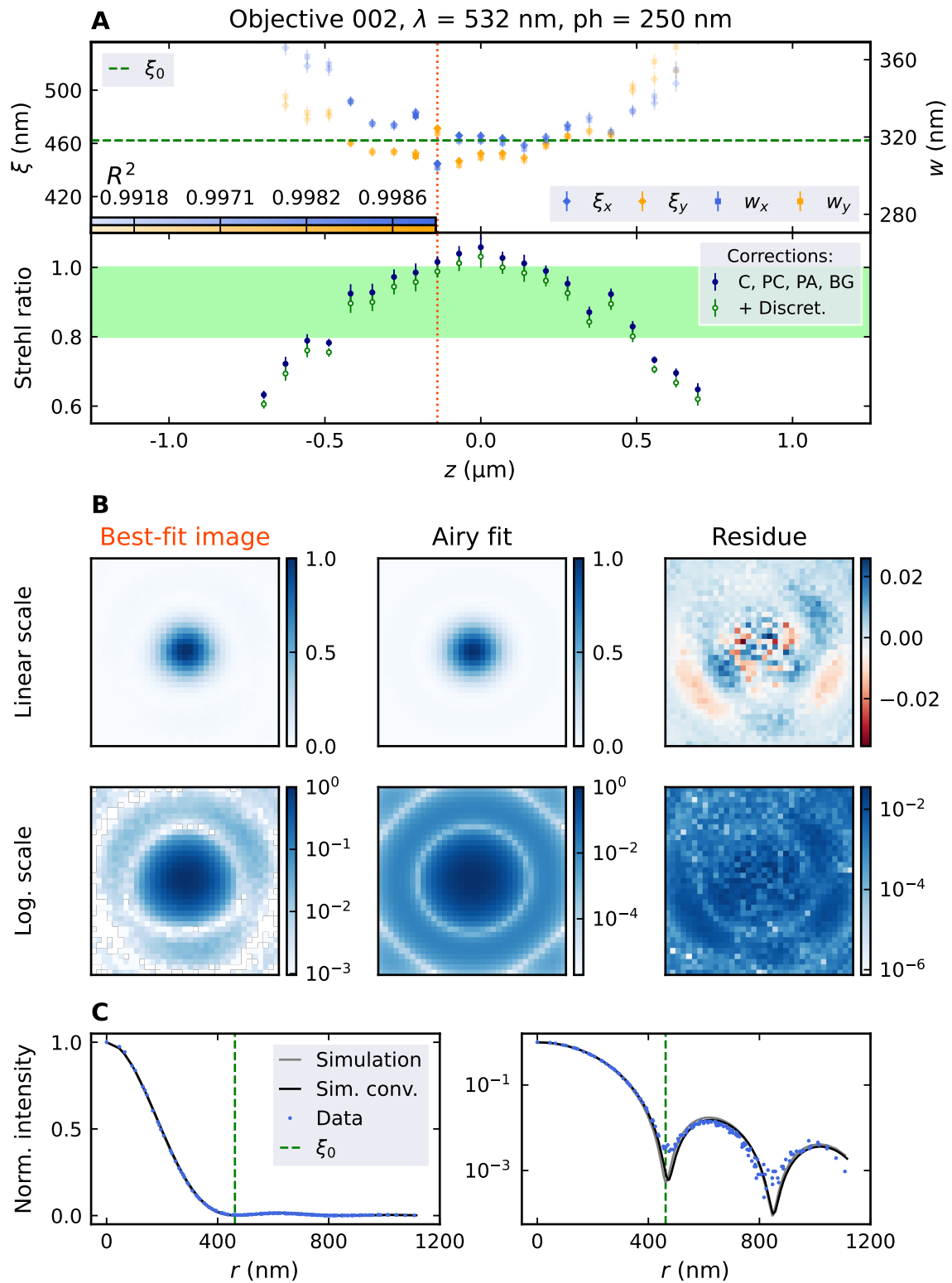


Figure 3.10 – SQM objective 002 imaging at 532 nm: PSF analysis. The Figure has the same structure as Figure 3.6.

To summarize the results shown on the past few pages, the following Tables contain the optimal, expected results if one assumed diffraction-limited imaging, and the measured performance of both objectives for the two tested wavelengths. The experimental quantities shown for each scan are calculated with the procedure explained in Section 3.2.3.

Wavelength	399 nm	532 nm	532 nm
Numerical aperture	0.7022	0.7022	0.9
Rayleigh resolution ξ (nm)	346.6	462.1	360.6
Radial waist w_r (nm)	238.6	318.2	248.3
Axial waist w_{ax} (μm)	1.11	1.49	0.90
Strehl ratio	1	1	1

Table 3.5 – Expected point spread function characteristics

399 nm light	Objective 001	Objective 002
Resolution min, max ξ (nm)	359.4(23), 368.5(24)	347.5(23), 351.6(23)
Radial waist min, max w_r (nm)	248.9(17), 254.5(17)	240.8(17), 243.0(17)
Axial waist w_{ax} (μm)	1.05(4)	0.98(4)
Strehl ratio (with all corrections)	0.877(20)	0.935(25)
532 nm light	Objective 001	Objective 002
Resolution min, max ξ (nm)	454.1(25), 475.2(26)	455.4(26), 459.6(26)
Radial waist min, max w_r (nm)	310.8(19), 324.6(20)	311.5(19), 314.1(20)
Axial waist w_{ax} (μm)	1.28(5)	1.22(5)
Strehl ratio (with all corrections)	0.977(15)	1.002(14)

Table 3.6 – SQM objective imaging test results

As expected from the individual image analysis, both objectives are diffraction limited for each wavelength, according to the Strehl ratio criterion and the fitted Rayleigh resolution that deviates along the major axis by no more than 6.3% (2.8%) for blue (green) light from the diffraction limit. The radial waists agree with this trend. Note that the axial waist is slightly off (especially in the green light case) from the expected values, which is presumably due to imperfections in the interferometric picomotor step size calibration for the target motor.

During this study, plenty comparable measurements of the PSFs have been recorded usually with the same optics but new alignments. To put the example measurements shown on the previous pages into perspective, Figure 3.11 provides an overview to all optimally prepared measurements of the PSF for both objectives and wavelengths. The measurements are divided into wavelength (subfigures A and B) and objective (column) while the measurement number is given on the abscissa. Every section displays the resolution (x and y axis) and the Strehl ratio (basic and all corrections). The expected diffraction limit ξ_0 and the diffraction-limited area for the Strehl ratio

are marked as usual. In case focus scans include two foci corresponding to forward and backward scanning, both will be plotted individually close to their measurement number. Additionally, for every measurement, the best-Strehl ratio image is shown in logarithmic scale. Note that measurements five, six and seven used a glass window different from the one used previously, that should however have the same (nominal) thickness of 6.000 mm. In measurement seven, a different camera⁷ was used.

We find the measurement-to-measurement resolution and Strehl ratio fluctuations do not exceed 5% confirming reproducible experimental conditions. The back and forth foci also agree on a few percent level, which is expected since there basically the same measurement is performed twice within 2 to 15 minutes and changed scan direction. Inspecting the best Strehl ratio PSFs, they share the main features characteristic for the corresponding objective like astigmatism (001) and trefoil (002). Slight variations in side-lobe power illustrates the differences in experimental realization and adds intuition to the slight SR fluctuations. After spherical aberration compensation, the measurements using the different windows still show very similar results. This is not necessarily expected, as the windows required a different spherical aberrations compensation as using same adjustments for both did not work. A different window thickness on the order of 20 μm might explain this observation. Furthermore, using a different camera (that has 3.45 μm pixel size instead of 1.85 μm) did not systematically change the analysis result which can also be a consequence of the sophisticated pixelation effects compensation. Comparing blue to green, one again observes the blue imaging performance to be much more sensitive to aberrations, which is visible in resolution, Strehl ratio and PSF symmetry. Lastly, during measurement six, the camera was mounted differently, explaining the flipped image.

⁷Allied Vision, Alvium 1800 U-240m

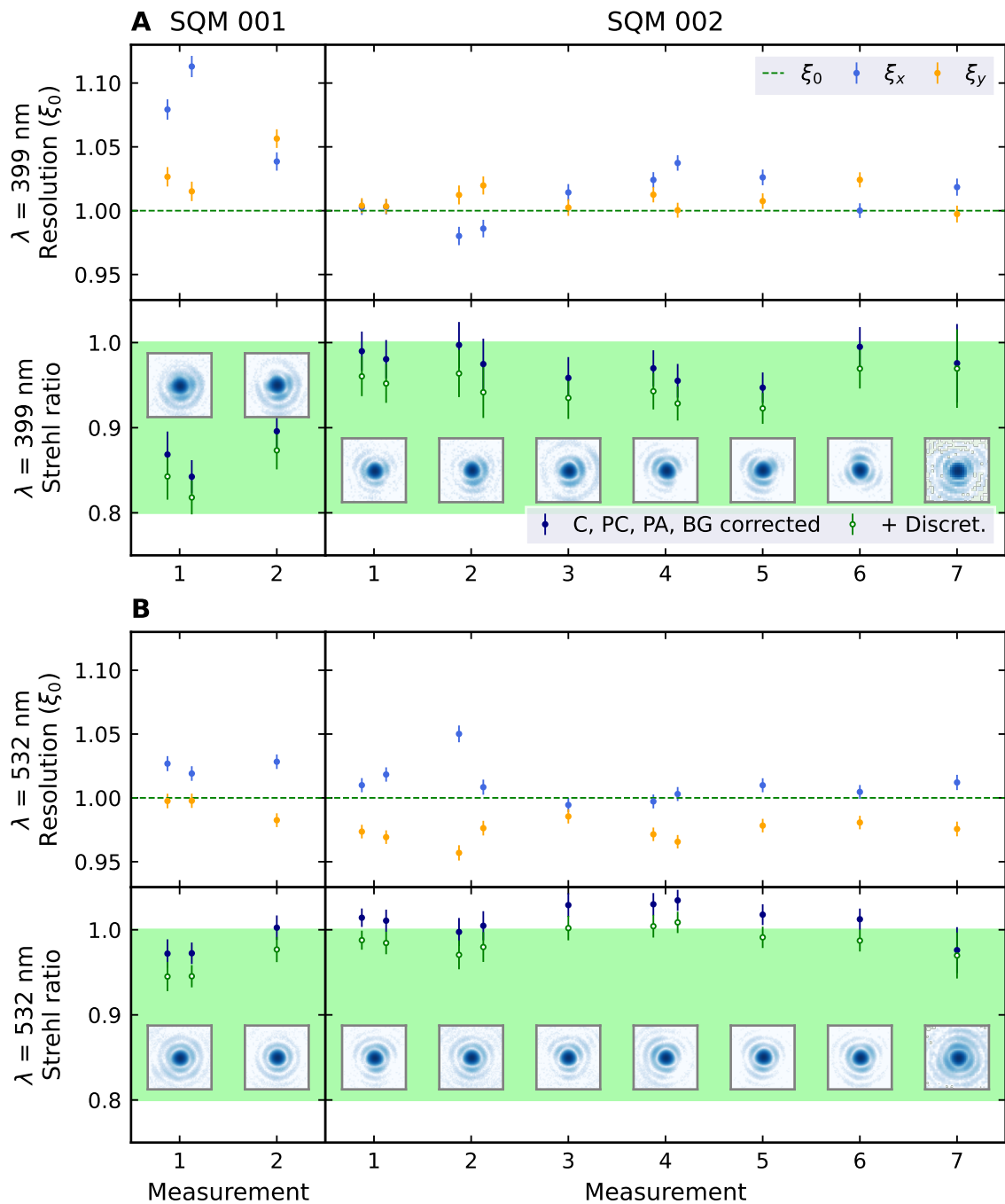


Figure 3.11 – SQM objective imaging - different measurement overview. The two subfigures **A** and **B** show imaging results for 399 nm and 532 nm light, respectively, and for SQM objectives 001 and 002 (left and right column). For each comparable measurement, central analysis figures are plotted. In case an analysis contained two foci, they are drawn next to each other as a data point pair. The fitted x, y resolution is given in terms of the diffraction limit (green dashed line) and the Strehl ratio is visualized below using only convolution, pixel-centering, pixel-averaging and background corrections (navy filled points) and applying all correction steps including discretization (green open points). The area in which an image is considered to be diffraction limited is colored in green. To form a connection between the numbers and the actual image shape, for each measurement the best-SR PSF is displayed as an inset in logarithmic scale.

3.2.5 Field of view analysis

After having confirmed the diffraction limited performance of both objectives for all elements being on-axis (made sure by alignment, see A), the imaging fidelity in the whole field of view (FOV) needed to be tested. Specified by Special Optics, the objective should have a field of view diameter of 100 μm that means diffraction-limited performance within this range. To check this specification, after initial on-axis alignment of all parts, the pinhole was moved in the objective FOV using the micrometer screws of the target mount. Subsequently, focus scans were performed. The reading of the micrometer screws offered a first coarse (on the order of 10 μm) estimate on the new position relative to the FOV center. The latter was kept constant by not moving the SQM objective, camera and lens and was thus fixed to the middle section of the camera picture. The FOV center positioning fidelity is given by the objective transverse alignment accuracy as given according Table 3.3 to be on the order of 20 μm . To compute the distance to the assumed FOV center more precisely, before every focus scan, which was acquired with a reduced data-taking ROI to save space on the hard drive, a calibration image was taken covering the whole camera sensor. For each calibration image, the distance of the PSF to the image/FOV center was determined.

Overall, two of these field of view test measurements were taken, using a different spatial testing grid and different optical alignment. Both measurements were repeated with each SQM objective and both wavelengths of interest, 399 and 532 nm and summarized jointly for all four cases in the following four plots. Since the plot layout is again identical, it will be explained once for Figure 3.12, the others follow analogously.

Starting with subfigure A, fitted Rayleigh resolution ξ and the Strehl ratio including all corrections are shown as a function of FOV position. Square and diamond markers allow one to distinguish x and y fits. The expected diffraction limit ξ_0 is shown as a green dashed line in the upper plot and the corresponding "diffraction limited" region in Strehl ratio is colored in light green in the lower. To visualize the FOV measurements, the 2D plane was cut in different angles and the analysis results are assigned their position on the cut axis relative to the expected FOV center. The inset enables cut-angle differentiation as it shows the FOV cut orientation, distinguished by a color code. The two measurements corresponding to subplots B and C are shown in A as filled and empty symbols. In case a measurement offered two foci in a scan, both foci analysis results are drawn separately.

Giving some intuition on the PSF shape as a function of the position in the FOV, subfigures B and C illustrate the best-SR PSF in log-scale for every FOV position measured. Plot B corresponds to the filled markers in A while C shows PSFs from the empty symbol measurements. On the axes, approximate locations of the images are given, relative to the center image. Note that the individual PSF images are plotted together but distances between and location of individual images are not to scale and are only supposed to give an overview of the measurement shape.

Starting with a few general remarks to the FOV analysis results, we observe that both

objectives do perform according to the specifications and fulfill the diffraction-limited criterion over a broad area. While it is difficult to give an exact number, from the plots it is easy to see that the distance over which the Strehl ratio is not dropping strongly is usually close to 100 μm . Even at 70 μm distance from the optical axis, image performance is still reasonable apart from slight PSF distortion that is barely visible in linear scale images. This is particularly useful for the main experiment, as it is planned to image a 100x100 μm area in which the corners will be about 71 μm from the center. Furthermore, the resolution curves usually do not show a clear trend towards the edges from the FOV, apart from an increased resolution scatter (x vs y), that is typical for coma-like aberrations, and larger error bars. In terms of Strehl ratio, at least for the 399 nm measurements, a clear drop is visible with a plateau in the center. This would agree with the $\exp(-x^4)$ law discussed in Section 2.2.3. For the 532 nm light tests, the Strehl ratio is much less sensitive to FOV position compared to 399 nm, as observed previously in the single focus scan analyses. Imperfect overlap of the Strehl ratio data points for different cut angles, or even slight displacements of the SR maximum, are caused by not matching measurement and FOV center.

In particular, objective 002 again outperforms objective 001 at both wavelengths and still shows the characteristic trefoil in the PSFs images. Note that measurements corresponding to the FOV test shown in C (empty markers) were strongly offset to the right (positive x) from the actual FOV center.

Subplots B and C always show the same trend for the PSFs shape moving away from the optical axis. The first Airy ring swaps towards the center of the FOV creating a pattern that is reminiscent of coma. However, as the opposite side of the PSF shows, outer ring structures remain and the center peak is stretched to the outside, which is in disagreement with typical coma as seen in Appendix F.5. The degree of pattern change is again proportional to the wavelength used. For blue light, the limited-FOV effects play a role already at 30 μm from the center while at this point with green light, barely any effect is visible.

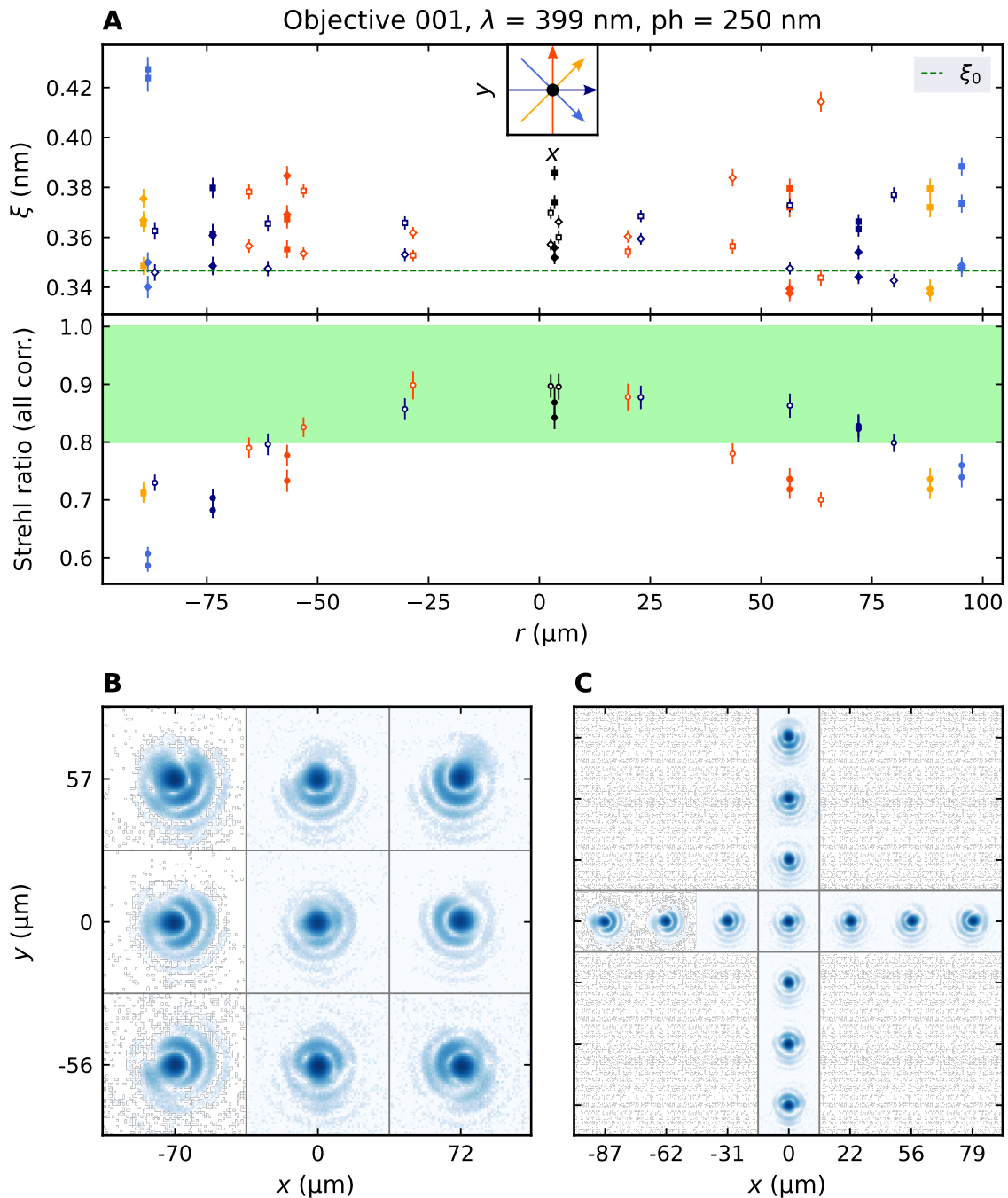


Figure 3.12 – SQM objective 001 imaging at 399 nm - Field of view. Part **A** displays the fitted resolution ξ and the Strehl ratio (using all corrections) as a function of radial distance in μm to the approximate FOV center. Diffraction limit ξ_0 as well as the 0.8 to 1 Strehl ratio band are highlighted. This plot summarizes results from two measurement series, that are distinguished by filled and empty markers. The measurement drawn with filled markers used back and forth focus scans whose two foci are plotted at the same position in equal color. To distinguish different directions within the FOV in this 1D plot, cuts through the FOV at different angles are shown. For every cut axis, data points are plotted according to their position relative to the (expected) FOV center. The axis cut angle is visualized in the inset. Note that x and y airy fits are distinguished by square/diamond markers. Subplots **B** and **C** show stitched-together best-SR PSFs from the FOV corresponding to the filled and empty data points in **A**, in log scale. Their approximate FOV position is marked on the axes.

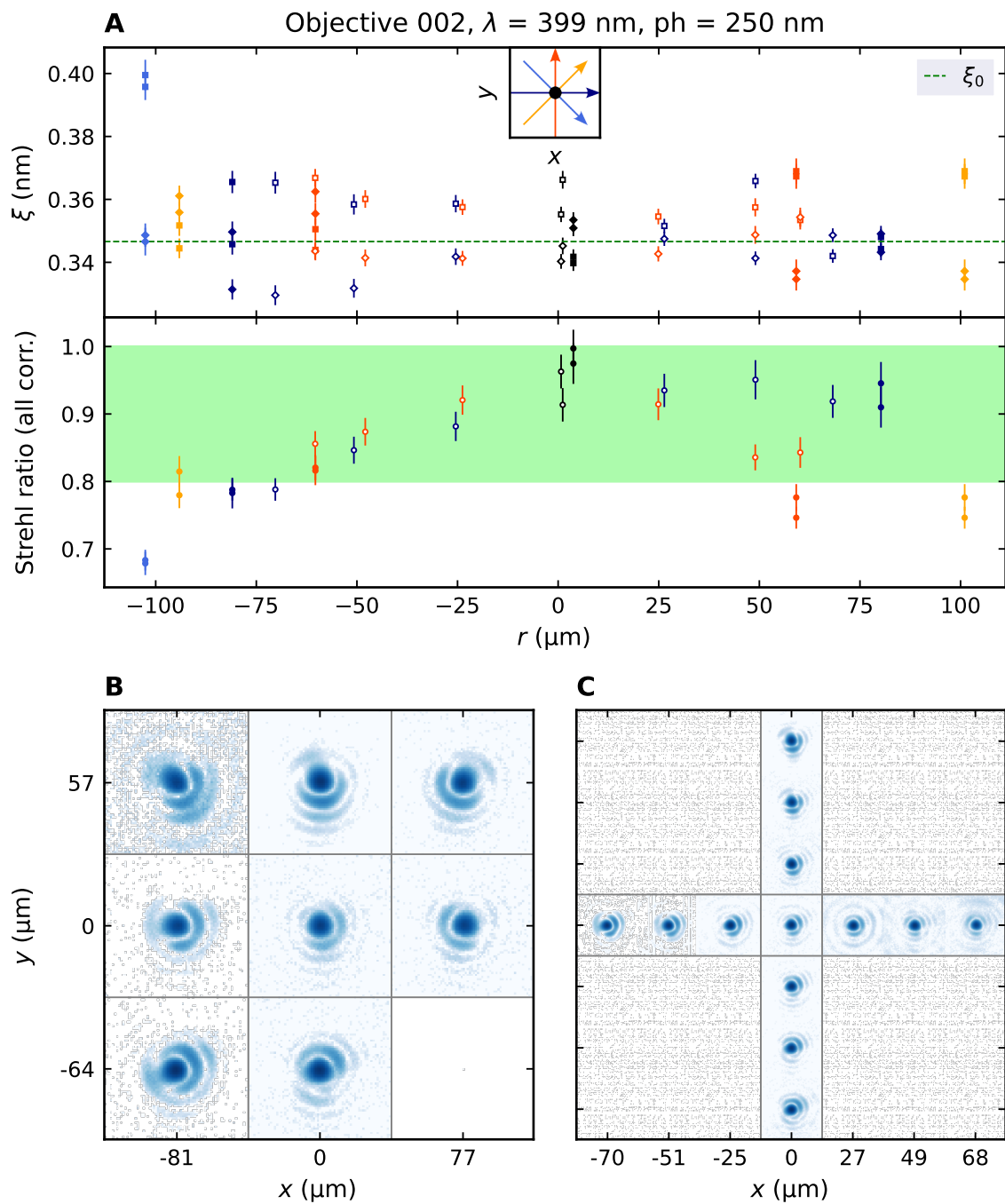


Figure 3.13 – SQM objective 002 imaging at 399 nm - Field of view. The Figure has the same structure as Figure 3.12. Note that the lower right measurement in B was not recorded and is therefore missing.

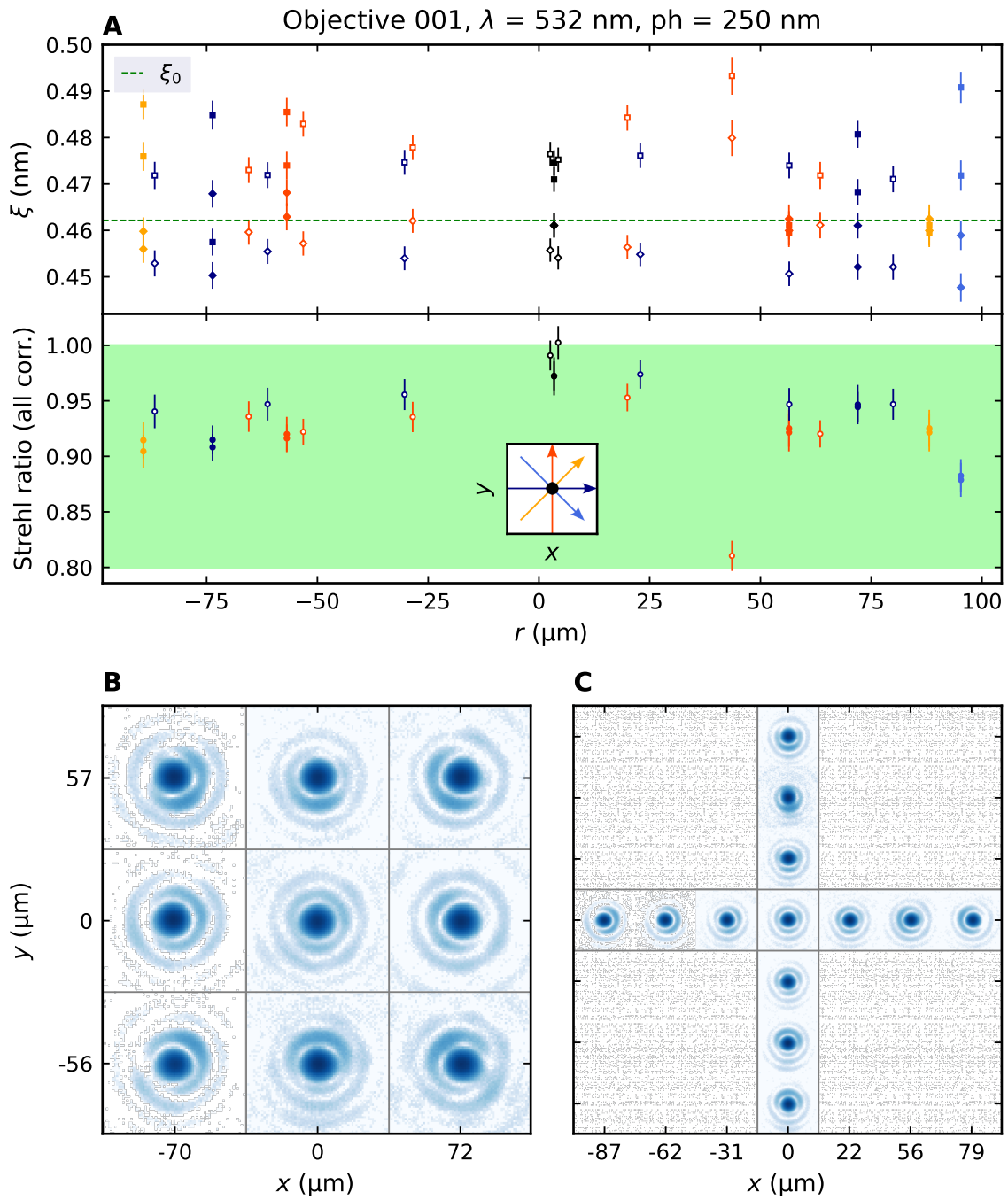


Figure 3.14 - SQM objective 001 imaging at 532 nm - Field of view. The Figure has the same structure as Figure 3.12.

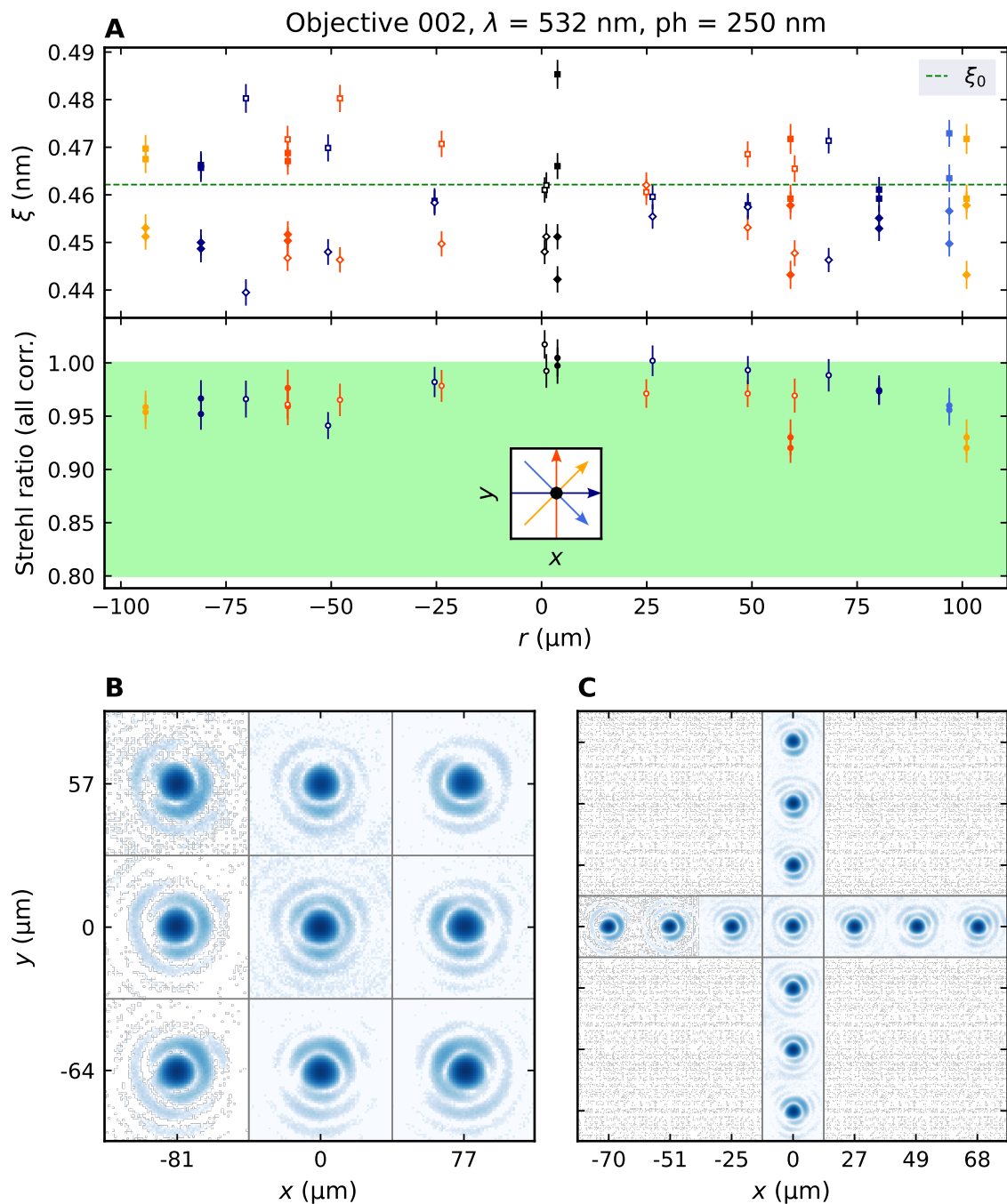


Figure 3.15 – SQM objective 002 imaging at 532 nm - Field of view. The Figure has the same structure as Figure 3.12.

3.2.6 Impact of additional optics on the PSF

After characterization of the objective imaging performance in the ideal case with as few optics as possible in the setup, the influence of additional reflective and transmissive optics on the PSF was tested. In the ultracold atom experiment, the imaging beam

path needs to be folded several times to deal with the limited space on the optical table which requires the beam to reflect off a couple of additional mirrors. Furthermore, to superimpose different laser beams on the same axis, dichroic mirrors need to be placed in the imaging beam. Because the imaging quality (as well as the tweezer projection) relies heavily on uniform wavefronts across large apertures, we decided to investigate the influence of these additional optics systematically. To this end, optical test setup measurements, as well as interferometric measurements of the optics surface flatness using a Zygo interferometer were performed.

For the optical test setup measurements, mostly the same layout was used as shown in Figure 3.3. Transmissive optics were placed in a 45° angle with respect to the optical axis in the imaging beam. Note that the resulting transverse shift of the imaging beam (on the order of 1-2 mm) only created a tiny displacement of the image on the camera and no visible aberrations, which is why this effect was usually not compensated. For reflection, a mirror was centered on the imaging axis and turned to an angle of incidence of 45° . The tube lens and camera were moved accordingly. For all test measurements described in this section, objective 002 was used, that intrinsically has less astigmatism compared to 001.

We noticed, apart from phase front contributions that can be corrected by alignment and refocusing (like defocus and tip and tilt) the most pronounced aberration introduced is astigmatism. This is not surprising, since any (even isotropic) curvature of the mirror surface (which could be compensated by re-focusing), will be squeezed across the horizontal to a width $1/\sqrt{2}$ of the original width. This now anisotropic curvature is precisely the required phase contribution for astigmatism that leads to different focal lengths for the horizontal and the vertical planes.

Figure 3.16 A displays results from surface flatness measurements using a Zygo interferometer. Tests of two different mirrors are shown: On the left, an elliptical two-inch mirror with broadband coating⁸ and on the right a three-inch mirror with the same coating⁹. The measurements show a colorbar encoding the surface flatness as well as peak-valley (PV) and root-mean-square (RMS) values. The program also offered expected PSF shapes assuming a plane wavefront impinges on the tested optics. In the lower left corner of each image, this PSF is shown. As expected by the large anisotropic curvature of the elliptical mirror, the expected PSF suffers from strong astigmatism as the striking cross-like shape confirms. For the three-inch mirror, the imaging quality is nearly perfect in this test, apart from defocus aberration which is not compensated here. However, if turned by 45 degrees, astigmatism will arise here as well as the test setup measurements show. Note that the reference wavelength λ was 633 nm.

The main observable that is compared in the test setup analysis is the astigmatic difference, which is proportional to the astigmatism magnitude. Thereby, it is also connected to the Strehl ratio and resolution of a scan. Overall, about 40 individual test measurements with additional optics (and without as reference) were conducted and analyzed. Of those, a relevant selection is averaged and shown in B. The analysis was

⁸Thorlabs, BBE2-E02

⁹Thorlabs, BB3-E02

performed as follows: For every measurement the scan was analyzed as usual, but restricted to 1D ROI cuts instead of full 2D ROIs. To this end, ROIs were cut along x and y going through the center of every image. Afterwards, a 1D Strehl ratio equivalent, Airy fits and the other quantities are computed for the two 1D cuts individually. From these 1D analyses, the astigmatic difference is computed by subtracting and scaling the two 1D cut focus positions. The focus position is computed in three ways:

1. **Strehl ratio Gaussian fit.** Like in the 2D case, a Gaussian is fitted to the Strehl ratio curve. This is very insensitive to noise, however, in the 1D case, the SR as a function of image number is slightly skewed making this fit function not optimal for peak finding.
2. **Strehl ratio weighted average.** Here, the Strehl ratio was used to calculate a weighted average of the image number, where high SR locates the focus position. While this approach has the advantage of being very direct and requiring a minimum of assumptions, it is also very sensitive to noise in the low-SR off-focus regions.
3. **Maximum R^2 region.** The region of maximized coefficient of determination is found by a optimizing for the position of a 10 image wide window over which values are averaged.

All three approaches usually give qualitatively similar results with a scaling factor in between them which motivates to average them to obtain a more condensed measure.

In order to resolve the principal axes of the astigmatism, the analysis above was repeated with different cut angles. Thereby, angles will be used for analysis where the cuts lie close to 45° rotated with respect to the astigmatism planes which will lead to a vanishing observed astigmatic difference, followed up by a sign change when rotating further. The resulting sinusoidal shape of the observed astigmatic difference as a function of cut angle can be viewed in part B of Figure 3.16. The shown results are averaged over analysis method, foci and comparable measurements, while the error bars show the standard deviation of the averaged measurements. Note that the astigmatic difference is probably not accurate on a 5% level, but shows a good overview of the differences between optics and the order of magnitude of the astigmatism.

The results are divided into measurement with green (532 nm, left) and blue (399 nm, right) light and different measurement sets are visualized using different colors and markers as shown in the legend. The optimal case of an astigmatic difference of zero is indicated with a green solid line. The visualized measurements contain reference measurements, where no additional optics were placed in the imaging test setup, tests using dichroic mirrors¹⁰ transmitting 399 nm and reflecting 532 nm light, reflection tests with three- and two-inch broadband mirrors and a two-inch elliptical mirror.

¹⁰Optoman, 70x50x6 mm

In addition, for one dichroic mirror reflection measurement astigmatism compensation was attempted. Zygo measurements of the the elliptical and the three inch mirror are shown in A.

Overall, different astigmatism magnitudes and phases are visible. The dominant angle contribution seems indeed to be along the horizontal/vertical axes of the setup, which is favored by the 45° angle of the additional element. Reference traces show a low, but non-zero astigmatic difference, which is larger for blue light, as expected.

We find that the dichroics we wanted to implement in the main setup exhibit too strong astigmatism to be used, both in transmission as well as in reflection. Note that in transmission the astigmatism is weaker, even though the used wavelength was shorter. This can be explained by refraction at two surfaces, assuming they have similar curvature which partially cancels the aberration. In comparison, in case of reflection off a curved surface, the optical phase imprint corresponds to the bare surface curvature enhanced by a factor of 2, accounting for the optical path doubling due to reflection.

Noticeably, it is possible to (partially) compensate for astigmatism by only using horizontal translation degrees of freedom. The main parameters that helped reduce the astigmatism is translating both tube lens and objective horizontally to a 2.6 cm total relative displacement, while the target was moved to the edges of the objective FOV. One needs to be aware that this procedure presumably adjusts existing astigmatism contributions of the other elements to cancel those of the dichroic. Initial alignment and FOV properties might change with this compensation.

The two and three inch mirrors show astigmatism that is of slightly different phase, and generally much weaker than for the dichroic. Especially the three inch mirror performs well in this test, by approaching the reference curve in the green light case. The worst mirror tested was the elliptical two inch mirror. Its astigmatic difference exceeds even the dichroic by 200 nanometers and should not be used in the high-resolution imaging application.

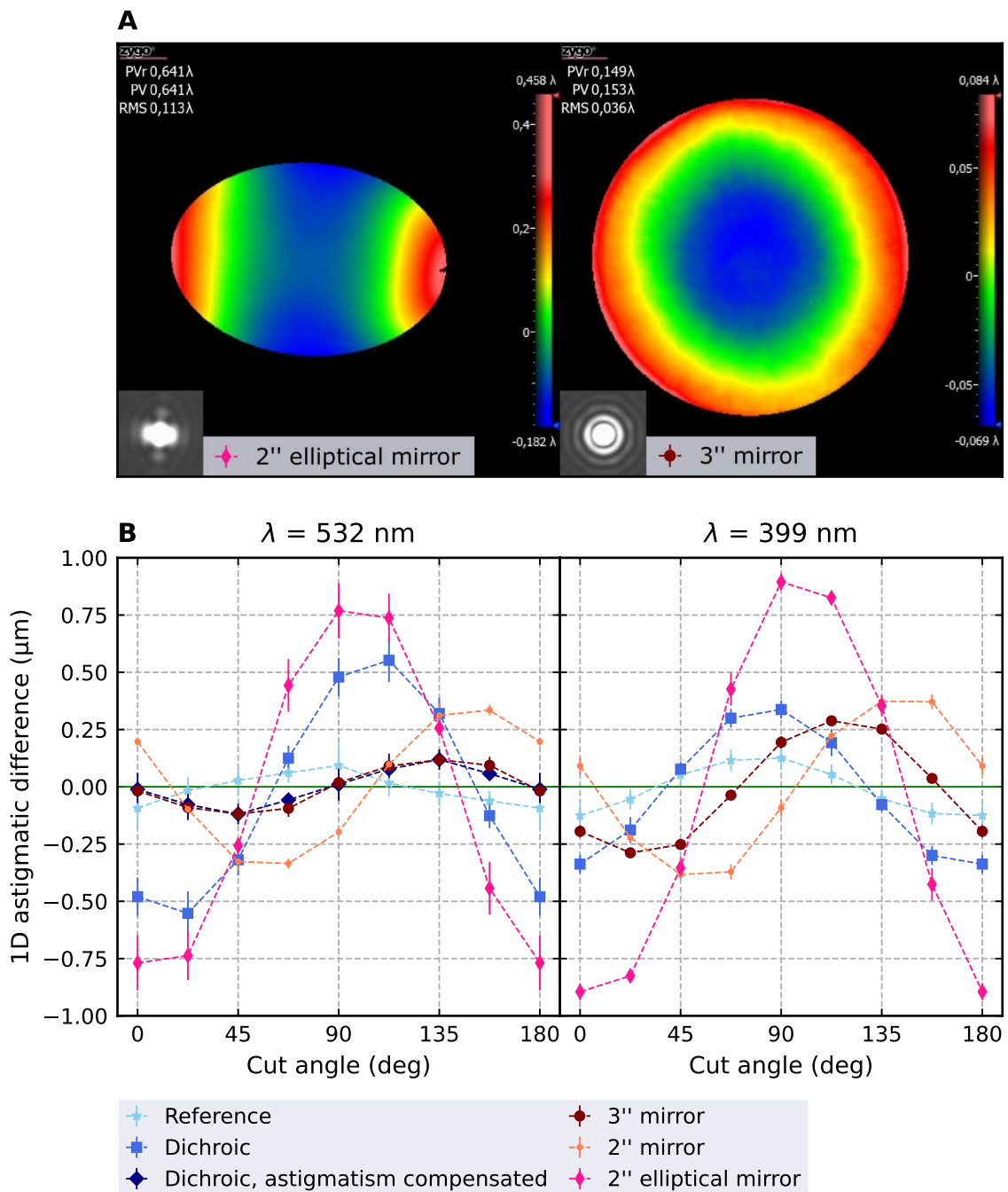


Figure 3.16 – Additional optics imaging tests. In subplot **A**, two mirrors whose effects are quantified in **B** are analyzed with a Zygo interferometer with respect to surface flatness. The topography map is shown as well as PV and RMS measures. Note that the reference wavelength is 633 nm. In the lower left corner, a simulated PSF is shown, assuming the measured phase imprint. Part **B** depicts a summary of test setup measurements in green (left) and blue (right) with different optics added to the imaging path (see legend). The plots show the astigmatic difference calculated from two orthogonal 1D cuts through the center of the PSF. The angle at which the cuts were selected is changed across the horizontal axis, which affects the observed astigmatism. With this overview, the astigmatism magnitude and plane rotation angle can be extracted.

3.3 Showing diffraction-limited tweezers

After having tested the imaging capabilities thoroughly in the previous Section, we now focus on the second goal of this thesis, which is to investigate the optical tweezer-generation with the SQM objectives and to create 2D tweezer arrays.

To measure the optical tweezer intensity distribution, we use a high-resolution imaging setup incorporating a commercial 0.9 NA microscopy objective¹¹ which is going to be referred to as the *Nikon* objective. It is infinity-corrected, has an effective focal length and working distance of 2 mm, and is specified to be diffraction limited in the visible range. Since optical tweezers can be thought of as the reverse process of high-resolution imaging, many aspects of the measurements and analyses are very similar to the PSF characterization in the previous chapter.

3.3.1 Tweezer test setup

The full tweezer test setup is depicted in Figure 3.17. Similarly to the previous setup visualization in Figure 3.3, two subfigures are shown. While the upper concentrates on accurate representation of all optics on the table including available degrees of freedom, the lower is more simplified to highlight tweezer beam propagation. Note that both figures are not to scale and a legend explaining all symbols is shown in Figure 1. To not lose overview, all lenses, waveplates and AODs will be referred to according to their order of appearance starting from the fiber outcoupler, and for lenses a preceding distance will indicate their focal length (e.g. AOD #2, 100 mm lens #3 := L3 etc.).

The light source on top of part A is the same Verdi laser used in the previous Chapter, except this time it was coupled into a photonic crystal fiber¹² (PCF) after attenuating its power using waveplates and polarizing beam cubes. This is done to reproduce the conditions of the main experiment as accurate as possible while also cleaning the beam shape. It is important to place a waveplate before the fiber to align the light polarization to the principal axes of the photonic crystal. The light is coupled out by a $f = 60$ mm outcoupler¹³ and collimated to a waist that was measured to be approximately 1.65 mm. It was checked using Gaussian beam propagation that any collimator lens positioning errors up to 1 mm would not create significant changes in the beam size or wavefront curvature. The collimation was verified quantitatively with a beam profiler and suggests about 0.2 mm coupler positioning mismatch. After the outcoupler, a half-wave plate and a polarizing beam cube allow us to further attenuate the beam, which was necessary because optical tweezers focus light so tightly that the imaging camera is easily saturated. Next, due to the polarization dependence of the diffraction efficiency of AODs¹⁴, another half-wave plate is placed.

¹¹Nikon, CFI TU Plan Apo EPI 100x/0.90 A, $\infty/0$

¹²NKT Photonics, LMA-PM-15

¹³S+K, 60FC-T-4-M60L-01

¹⁴Pegasus optics, AA.DTSX-400-xx

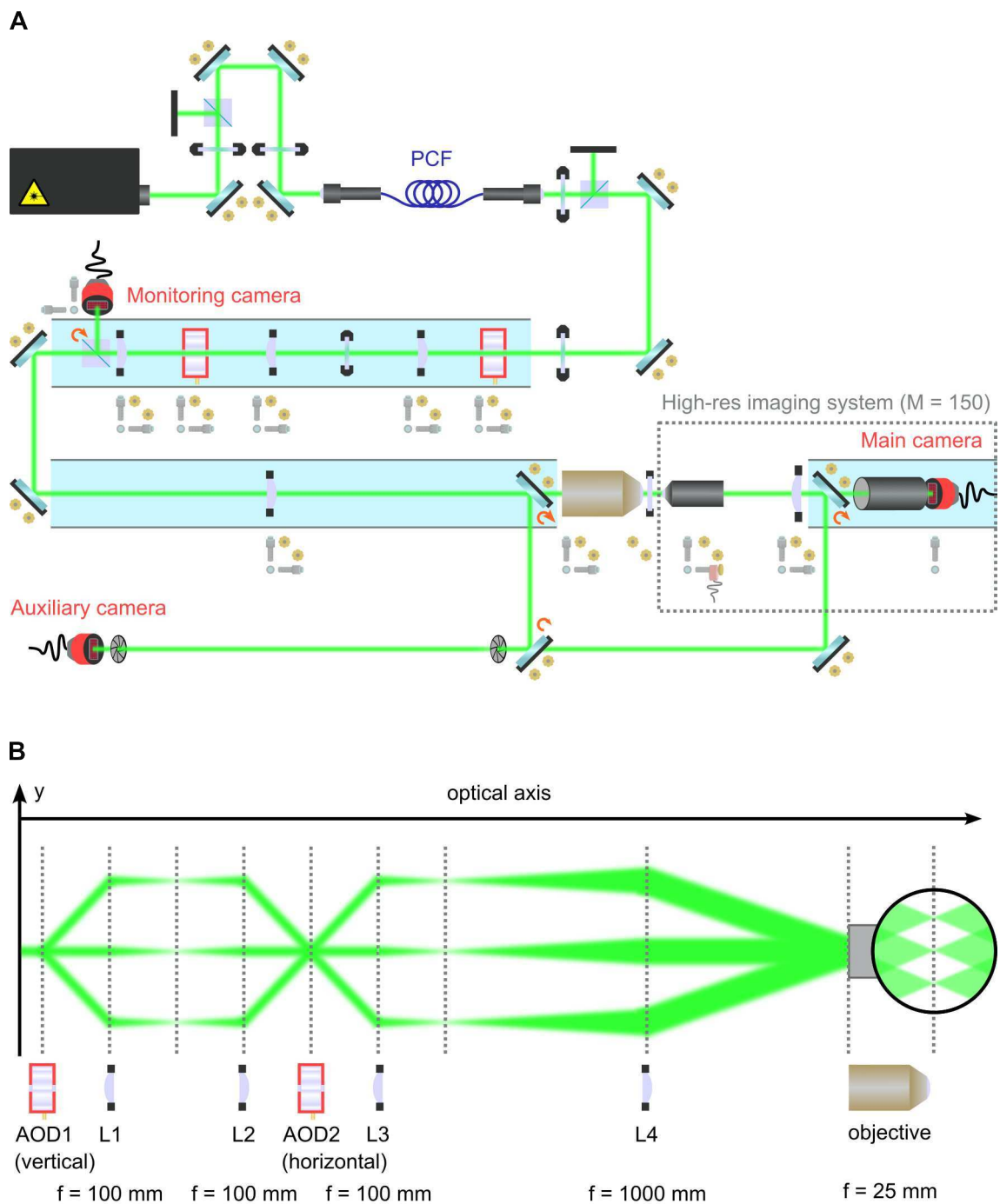


Figure 3.17 – The optical test setup for tweezer array measurements. The Figure has the same structure as Figure 3.3.

Now follows the tweezer beam array generation. The first AOD (AOD #1) will deflect the beam in the vertical direction, while the second AOD (AOD #2) is rotated by 90 degrees and controls the horizontal angle. Both AODs are driven by the amplified

output of a AWG card¹⁵. The center of AOD #1 is imaged into the AOD #2 in order to guarantee that all rays leaving AOD #2 emerge from the same point on the optical axis. This way the number of rows and columns are controlled by AOD #1 and AOD #2, respectively, including the respective spacing. The imaging 1:1 telescope is composed of two $f = 100$ mm visible achromat lenses (L1 and L2) in a $4f$ configuration. Note the third half-wave plate within the telescope needs to rotate the polarization by 90 degrees before the light impinges on AOD #2. The following set of three lenses can be understood in two ways. We can group the first 100 mm achromat lens (L3) with the $f = 1000$ mm achromat lens (L4) to form a 1:10 telescope which magnifies the tweezer beams by a factor of 10. This increases the effective/used NA of the SQM objective which then focuses the collimated beams to form optical tweezers. Second, we can imagine that lens L3 creates the optical tweezers in its focus, but only with limited confinement owing the low NA. The L4-objective pair can then be interpreted as a 40:1 telescope, effectively reversing the imaging measurements from the last chapter. This telescope then images and demagnifies the already generated tweezers by a factor of 40, leading to the final the final optical tweezers. This last view is also essential to understand the purpose of the beam cube that comes after lens #3. The cube can be placed if required and reflects the focused tweezer beams onto a camera¹⁶. Such a *monitoring* camera, which is mounted on a 3 axis translation stage, allows us to view the optical tweezers before they are projected by the objective. This helps with AOD alignment, tweezer power balancing and cross checking if the array appears correct in shape. It is important to emphasize that the camera and cube combination must be mounted compactly for this task, such that the tweezers can be focused without the need of additional optics while also enabling very robust and direct measurements.

After the SQM objective, a glass cell mock window is placed in order to have the tweezers projected through. They will form in a distance of roughly 7 mm from the glass window, before their light is collected by the Nikon objective that is part of the high-resolution imaging system. Together with a 300 mm tube lens, the tweezers are imaged onto the *main imaging* camera¹⁷ with an expected magnification of 150. The CMOS camera has a pixel size of 3.45 μm and bit depth of 12, and is again protected against stray light with a lens tube. Furthermore, most optics are placed on rails to ease axial alignment and improve reproducibility. Finally, to achieve the most precise translation alignment of all parts, two flip mirrors are placed before the SQM objective and in front of the main camera, thereby redirecting the beam through two irises that are spaced more than a meter. After the last iris, an *auxiliary* camera¹⁸ allows one to check the transmitted beam pointing which is connected to the transverse positioning of the optics.

While detailed notes on how to align this system from scratch are summarized in the Appendix B, lens alignment is in essence the same as described in Section 3.2.1.

¹⁵Spectrum Instrumentation, M4i6631-x8

¹⁶Allied Vision, Alvium 1800 U-240m

¹⁷Allied Vision, Alvium 1800 U-240m

¹⁸Allied Vision, Alvium 1800 U-1240m

Part B illustrates the main optical tweezer beam propagation from the outcoupler to the atom plane. Relevant refractive optics of the above Figure are also shown and labeled there, however, mirrors and alignment assistance paths are not depicted. Note that for individual tweezer beams collimated and focused sections alternate exactly opposite to the collective tweezer beam propagation behavior. This illustrates the importance of the distances between optical elements, and hence why they are needed to be carefully calibrated.

As discussed in Chapter 2.3.2, the AODs require a superposition of sinusoidal RF signals with distinct frequencies, also referred to as tones. The generation of these signals and the corresponding electronic setup is the same as depicted in Figure 2.6. A computer controls an arbitrary waveform generator (AWG) card¹⁹, whose output is amplified before it is fed into the AODs. Monitoring the tweezer power either on the main or the monitoring camera, a closed feedback loop enables iterative intensity balancing. The homogenization algorithm is based on tweezer power proportional reduction of the individual RF tone power.

3.3.2 High-resolution tweezer imaging

To assure that the Nikon imaging of the optical tweezers is itself diffraction-limited and aberration-free, the imaging setup was tested after every tweezer setup change separately. To this end, a test configuration that resembled the usual tweezer generation setup was prepared without the 1:10 telescope, SQM objective and glass window. In case the AODs and the 1:1 telescope part of the setup was already installed, the beam transmitted at the AOD center frequency was used to test the imaging setup. Instead of the SQM objective creating an optical tweezer, the resolution chart test target was placed in front of the Nikon objective. The setup is illustrated in Figure 3.18 identically to Figure 3.17. Measurements and analysis are completely analogous to the ones described in Section 3.2. The following measurements all used $\lambda = 532$ nm light to image the 250 nm pinhole of the resolution chart.

We begin with the magnification calibration procedure. The test measurements were recorded and analyzed exactly as described in Subsection 3.2.2 and are shown in Figure 3.19. Note that a total of three different magnification measurements were performed, after every tweezer setup rebuilding. Those three measurements, are shown as columns in the plot. Overall, the magnification is very close to the expected 150 with fluctuations on the sub-percent level. The determined magnification values were used for the analysis of every test with the corresponding setup. A representative Nikon imaging test is shown on the next pages. In Figure 3.20, the shape of the PSF is shown in similar ways as previously in Figure 3.5a for the SQM objectives. A two-sided focus scan was recorded this time, since the Nikon objective depth of field is so short that there are only a few images sampling the in-focus region even for a single picomotor step per image. With two foci per scan, the statistics are enhanced and they are depicted as two columns.

¹⁹Spectrum instrumentation, M4i6631-x8

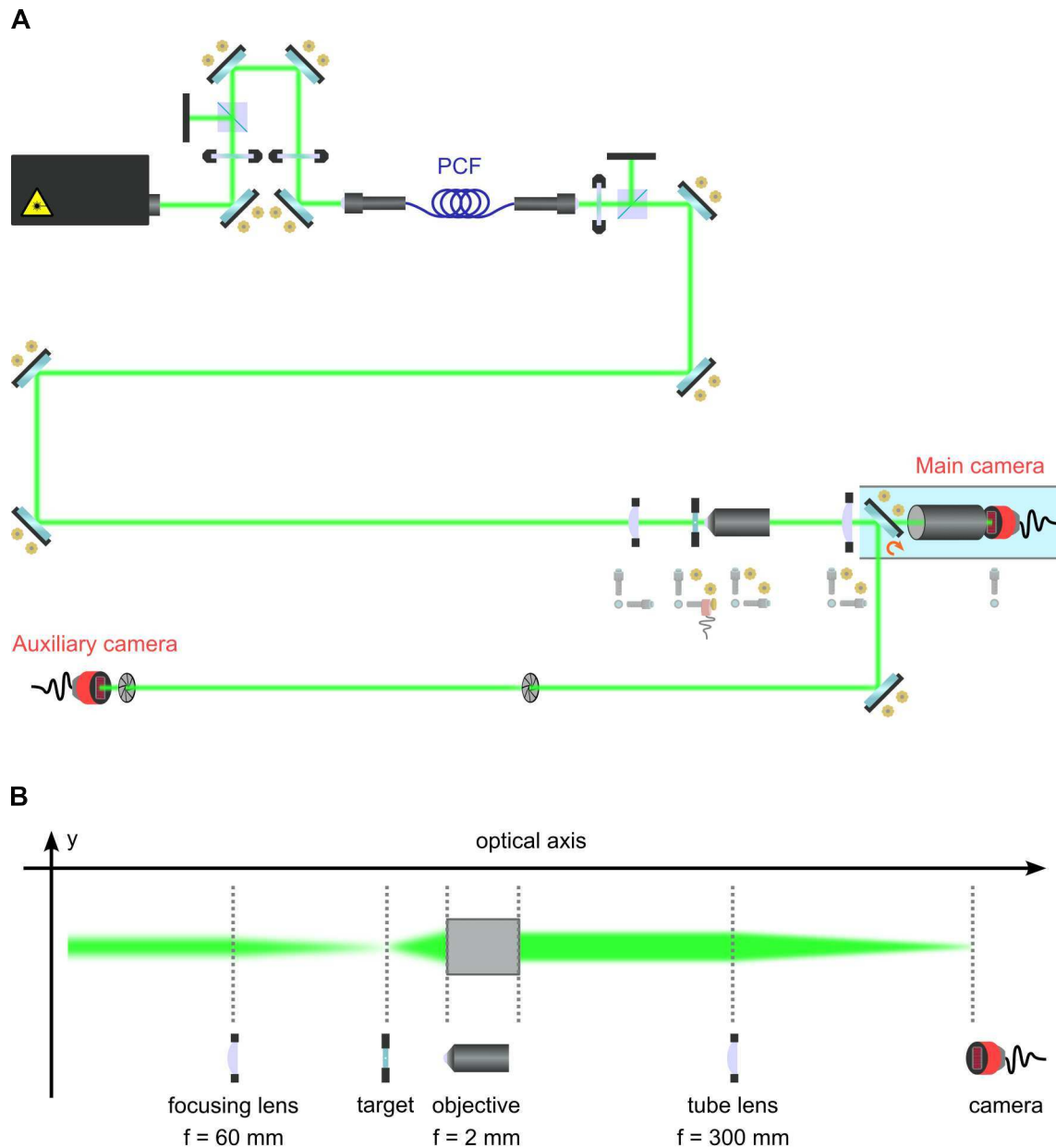


Figure 3.18 – The imaging characterization test setup for the Nikon objective. The Figure has the same structure as Figure 3.3.

The PSF shape looks very close to ideal and is well sampled on the camera. Comparing it to the SQM imaging measurements with an effective pixel size of 46.25 nm, the pixel size here is $3.45 \mu\text{m} / 150 = 23 \text{ nm}$. There is still some residual coma visible with rings being more pronounced to the top and a center maximum that is slightly compressed vertically. This is already much better than a previously tested objective²⁰ which was barely diffraction limited, having a worse coma, and was then replaced by the current one.

²⁰Nikon, CFI TU Plan Apo BD 100x/0.90 A, $\infty/0$

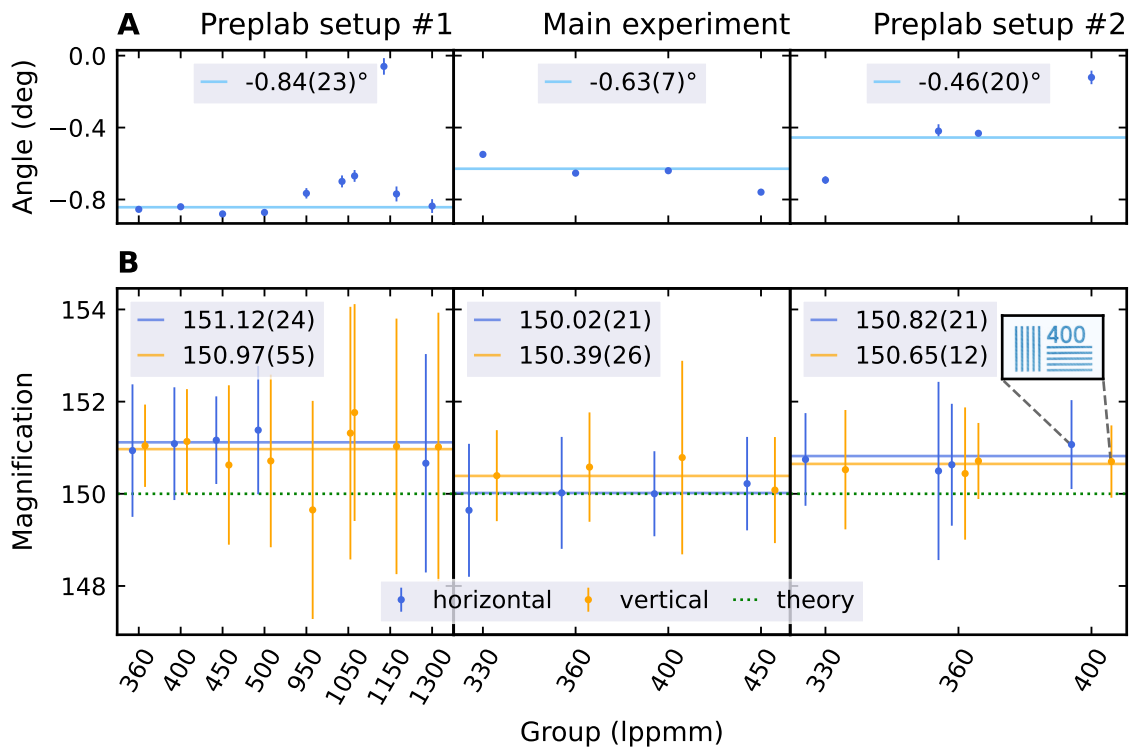


Figure 3.19 – Results from the magnification calibration measurements for the Nikon objective imaging tests. The Figure has the same structure as Figure 3.4, however it uses three columns corresponding to the different magnification measurements at slightly different magnification values.

The analysis results shown in Figure 3.21 are similar in layout to the SQM objective analysis in Figure 3.6, but with an additional column for the second focus in part A. Starting with this panel, the ellipticity of the PSF is clearly visible as ~ 30 nm discrepancy between ξ_x and ξ_y . While the vertical resolution is even slightly below the expected diffraction limit, the horizontal resolution is significantly worse. To avoid aberration effects like the ones mentioned in Section 3.3.2, the NA was chosen well above the tweezer-generating NA. Nevertheless, the Strehl ratio is still very close to the optimal 1.0 as expected for a commercial objective which is not corrected for a glass plate in between. Subfigure B illustrates that the PSF is indeed very close to a perfect Airy pattern, except the above-mentioned coma that is clearly recognizable in the residue. Lastly, part C shows that the azimuth averages agree almost completely with the simulation, apart from the minima where the images are limited by noise and the broadening along the horizontal. Note that in the logarithmic view, one clearly observes the convolved simulation fitting the data better than the simple simulated PSF. To conclude, the Nikon 0.9 NA objective is diffraction limited according to the Strehl ratio and fitted resolution, and it furthermore creates a PSF that is very symmetrical and only minimally aberrated.

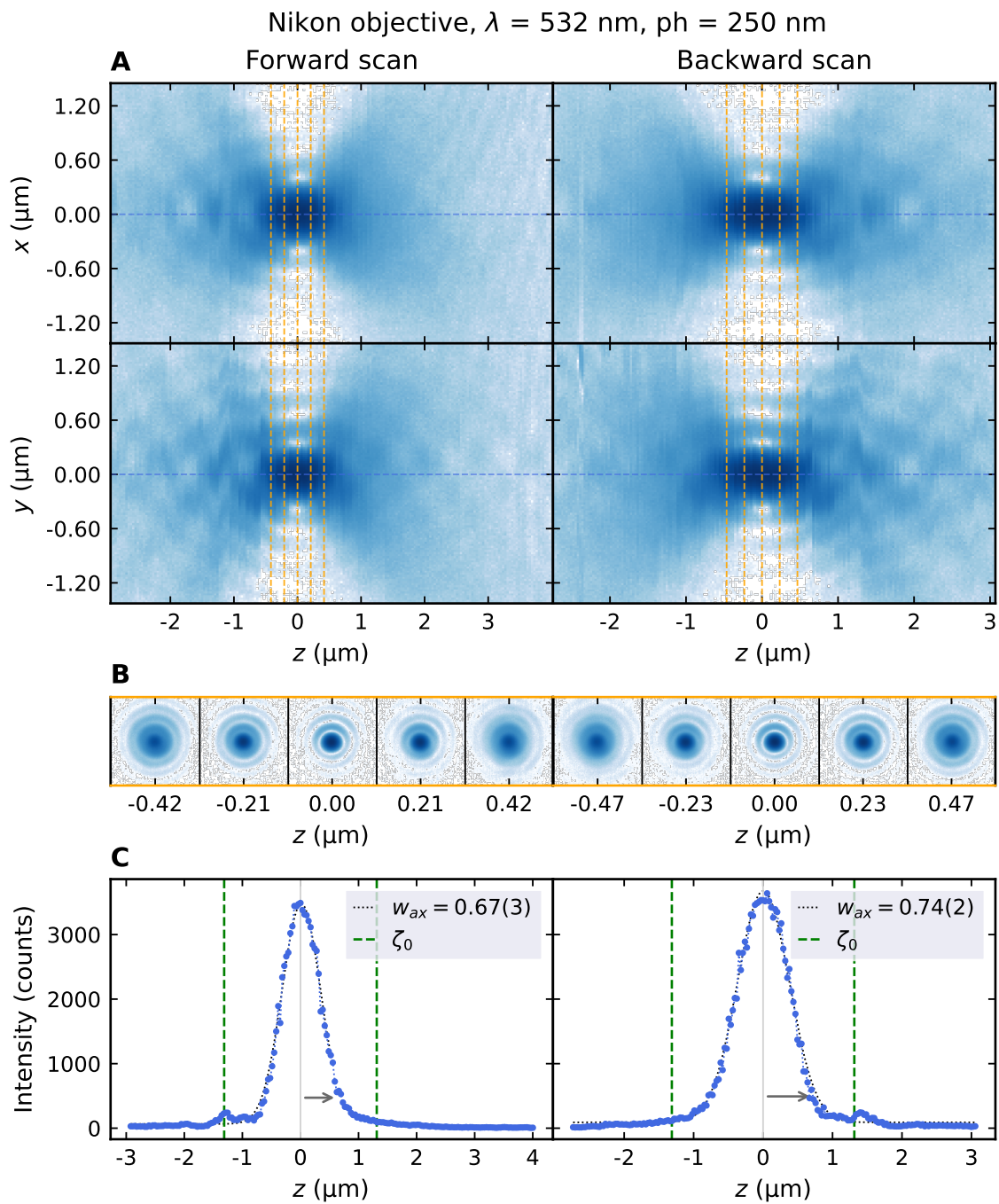


Figure 3.20 – Nikon objective imaging at 532 nm: PSF shape. The Figure has the same structure as Figure 3.5a, with an additional separation into two columns corresponding to forward and backward scan.

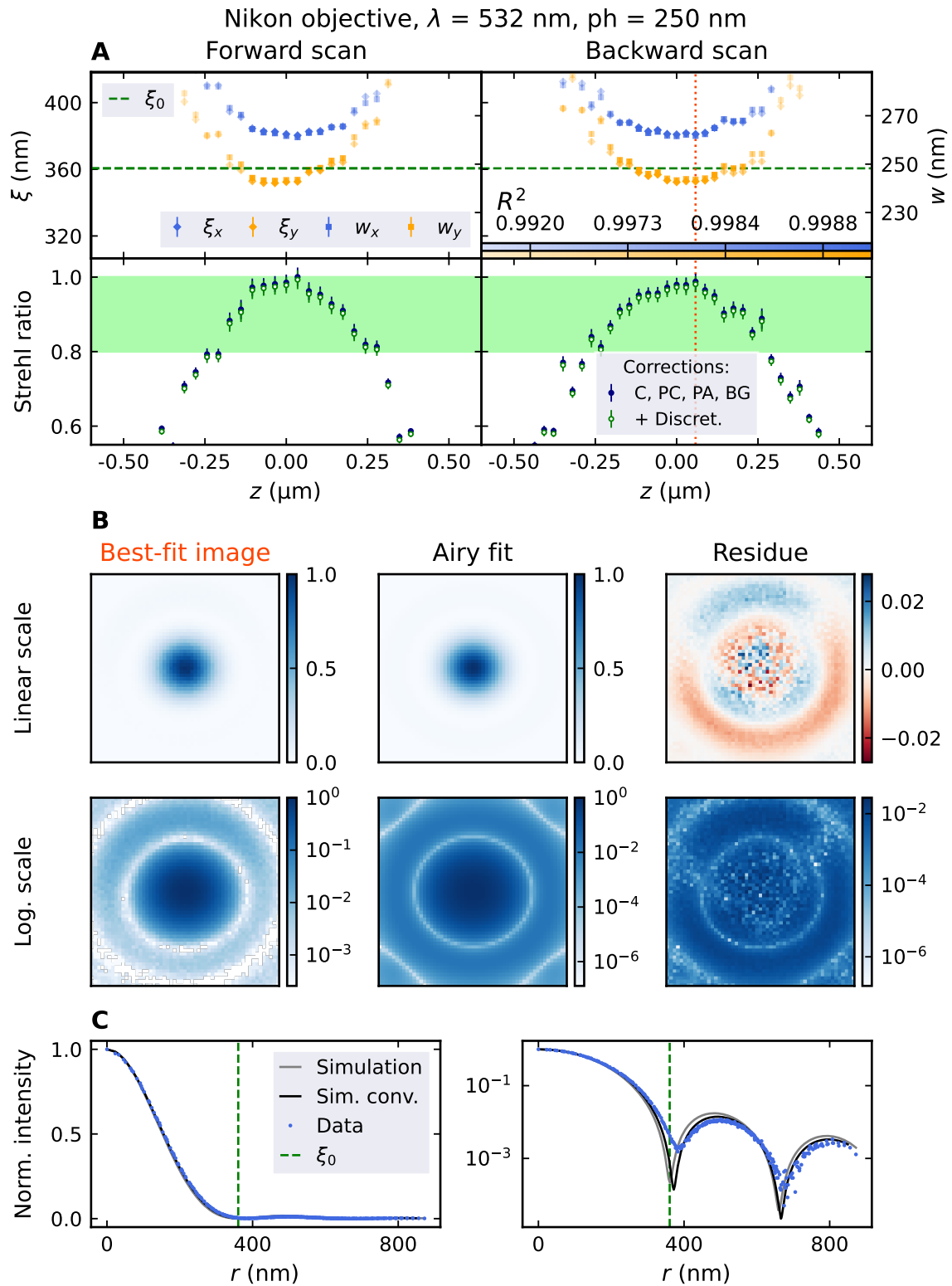


Figure 3.21 – Nikon objective imaging at 532 nm: PSF analysis. The Figure has the same structure as Figure 3.6, with an additional separation into two columns corresponding to forward and backward scan.

To quantify the alignment reproducibility and to assess imaging performance for the different tweezer measurements shown in the next sections, a Nikon imaging quality overview was generated. Figure 3.22 displays the analysis results of all final Nikon imaging tests that were conducted prior to optical tweezer measurements. As in the previous Figure, resolution and Strehl ratio are shown again as a function of the measurement date (yy/mm/dd). Additionally, best-SR PSFs are depicted at the bottom of the Strehl ratio plot in logarithmic scale. Note that the asterisk indicates the only measurement where the setup has not been realigned since the last reference measurement. There are always two points (of the same kind) plotted horizontally offset for every date, corresponding to the two independent foci of the measurements.

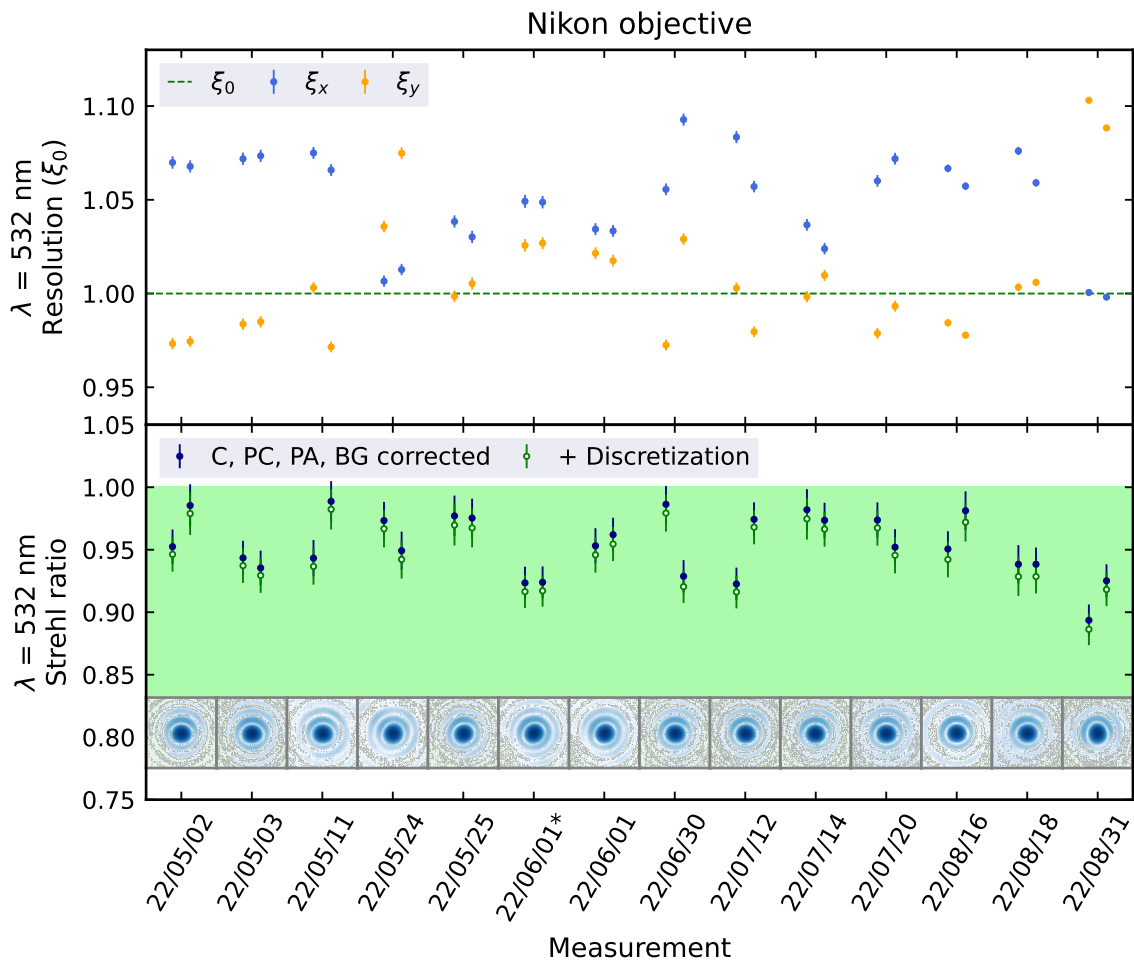


Figure 3.22 - Nikon objective imaging: different measurement overview. The Figure has the same structure as Figure 3.11.

One can notice the significant spread in Strehl ratio and resolution, both between two foci and among the different dates. This could be attributed to the low image count in focus, making it a rather stochastic process whether a top Strehl ratio image was included. In addition, unlike the SQM objective imaging tests, the setup was neither shielded against air currents nor was the table floating, which potentially added

to the overall imaging system noise. Apart from that, the imaging performance is overall very high, with Strehl ratios never falling below 0.9 and resolutions always lying on the diffraction limit for the vertical while not exceeding a 10% increase in the horizontal. The best PSFs agree with this observation, however, there are a few in which the central peak looks deformed. In particular, the last measurement exhibits a strongly stretched shape in the vertical direction which was observed in all eight reference measurements, including after three realignments that day. It is possible that, after using the objective extensively for several months, some lens internally moved slightly thereby changing the PSF.

To estimate the required alignment precision that minimizes aberrations of the Nikon objective, short test series were performed where the objective was tilted and translated in a controlled way. In Figure 3.23 the test results are shown in A while subfigure B depicts the corresponding best-Strehl ratio PSFs. Horizontally, the plots are divided into two columns which correspond to the tilt and transverse translation of the objective (left), and a short FOV test (right).

Starting with the results on the alignment sensitivity on the left side, it is worth mentioning that the values given on the horizontal axis are only estimates. They were calculated geometrically with coarsely known calibration constants linking the adjustment screw revelations with stage movement. Overall, the PSF abruptly deteriorated near the 120 μm translation mark. Presumably, this threshold should rather be 70 μm and corresponds to the actual field of view edge (compare Chapter 3.3.9). This identification is probable due to the sudden nature of the imaging quality drop, which hints towards an abrupt hard-aperture cutoff within the objective that was also reported in the just-referenced Chapter. All PSFs look close to identical below such threshold, which is expected for highly aberration-corrected commercial objectives within the FOV, so up to milliradian tilt of the objective alone did not have an effect on the imaging. The "flatness" of the focal plane is also apparent in the right column, where no particular difference can be observed between the center of the FOV and 30 μm out of center. Lastly, one might have noticed that the overall PSF ellipticity changed between the left and the right column. That is because the measurement on the left was performed much later than the measurement on the right, such that the PSF change of the 31st of August already occurred (see Figure 3.22).

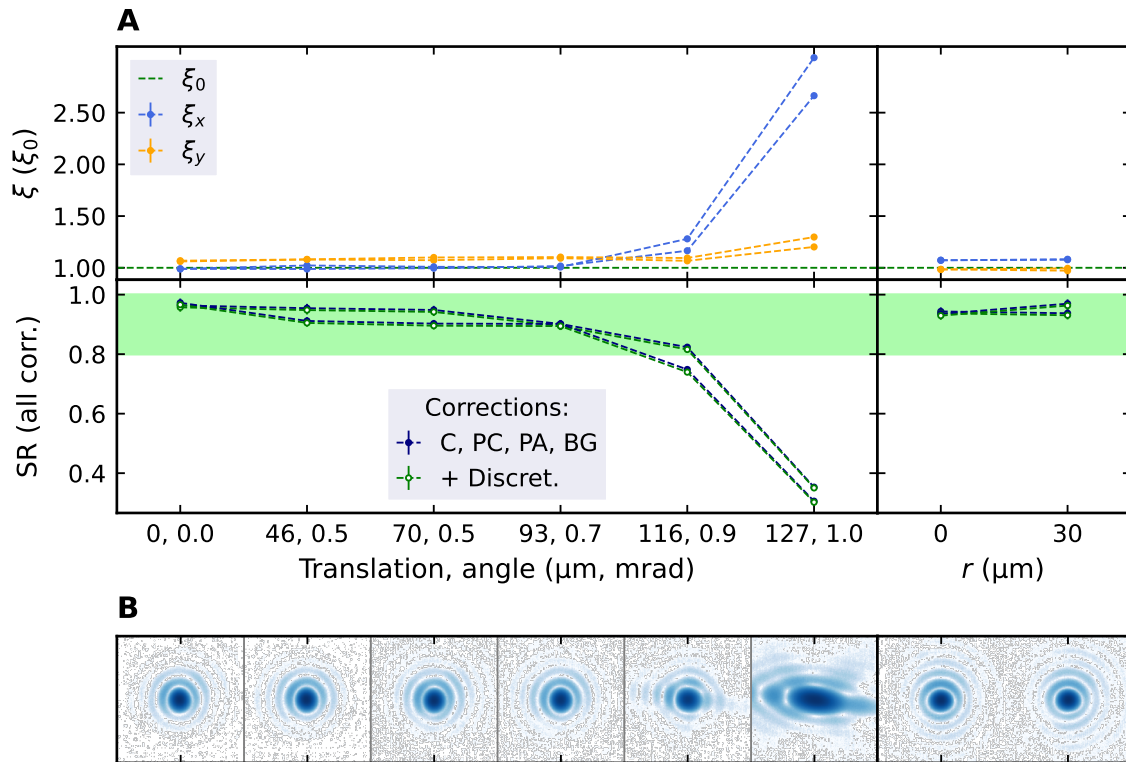


Figure 3.23 – Nikon objective imaging: alignment and FOV tests. The sensitivity of the Nikon objective angle alignment (left column) and a FOV test (right column) are shown with respect to analysis results in **A** and best-SR PSFs in **B**. In the alignment section, the Nikon objective was tilted and translated as indicated by the estimated distance and angle pairs on the horizontal axis. Since these values were calculated using coarse estimates linking revelations of the adjustment screws with actuator displacement, they may be inaccurate. Only two positions in the FOV, the center and about 30 μm displaced, are tested. The plots in A use the same conventions as described in Figure 3.6.

3.3.3 Single tweezers

After preparing the optical test setup and characterization of the high-resolution imaging, optical tweezers were generated and are shown in the following section. As discussed in Section 2.3.4, the size of the Gaussian input beam impinging on the SQM objective strongly determines the minimum achievable optical tweezer extent. The tweezer beam size, referring to twice the Gaussian waist, that is used in the main setup is 33 mm as in the test setup. This leads to an input beam size relative to the objective entrance pupil diameter of $2w_G/D_O = 0.94$ that lies close to the optimum of 1 which was determined in the aforementioned Section. To test the ideal, plane wave case, tweezers were also generated with a 220 mm incident beam size, which is much larger than the 35 mm pupil diameter of the objective. These beam sizes are calculated from the measured beam size after the outcoupler and theoretical telescope magnifications. For the tests shown in this section, both AODs and the 1:1 telescope were absent to isolate the expected tweezer-generating performance of the objective

alone. All measurements were performed using a $\lambda = 532$ nm laser beam and five picomotor steps per image.

Optical tweezer measurements and analysis results are shown in the following pages for both SQM objectives. Since tweezer generation can, to some extent, be thought of as reversed high-resolution imaging, the data analysis is analogous to that explained in Chapter 3.2.3. In addition, there are important differences in the data analysis steps for the Strehl ratio. As in these measurements optical tweezers are imaged, there is no need for deconvolution, which is dropped for all data points. Nevertheless the imaging itself might artificially decrease the observed tweezer fidelity and is accounted for in the green, open circle data points as explained in Section 3.5.8. Because this compensation exhibits a rather large uncertainty, the error bars are significantly larger than without considering this effect.

The analysis plot layout is nearly identical to the plots explained in Section 3.2.4 except they comprise of two columns for the forward and backward scans and the convolution simulations in the azimuth averages are omitted. We will not identify a focus scan as the 3D shape of a point spread function, but it will instead be the 3D shape of an optical tweezer that – in theory – looks perfectly identical to the PSF. However, imperfections of the optics generating the tweezer beam and different components used in the optical setup will create differences that one can observe comparing the imaging and the tweezer measurements. To comment on the symbols used, ξ will no longer be the Rayleigh resolution with the physical meaning of resolving power, since that is not intuitive in the context of tweezers. It will instead represent the fitting quantity that purely describes the radial distance to the first zero crossing of an Airy pattern, since those are still fitted to the optical tweezers.

Starting with the incoming tweezer beam size of 220 μm , the twice the Gaussian waist to objective aperture relation ($2w_G/D_O$) is 6.28. This is far in the Airy pattern limit of formula (2.53) and should thus create an ideal optical tweezer. To enhance the beam diameter to the desired 220 μm , an additional telescope is added before the 1:10 telescope; it consists of a $f = -75$ mm concave lens and a $f = 500$ mm achromat doublet, both of which are not shown in Figure 3.17. This leads to a total beam magnification of 66.6 that increases the 3.3 mm beam diameter after the fiber to 219.8 mm in front of the objective.

The tweezer shape of objective 001 is visualized in Figure 3.24. While the shape is very clean and mostly absent of irregularities, slight spherical aberrations that were not perfectly compensated are still visible. As expected for number 001, astigmatism is also clearly visible in the cuts along z , as well as in the example images with fixed axial position. The axial resolution limits shown in C agree well with the actual minima, which can be attributed to more reliable picomotor calibration measurements for the five-axis motorized stage as opposed to the target single picomotor case.

In the plot 3.25 A, we again find diffraction-limited performance both via resolution and Strehl ratio. Even without accounting for imaging imperfections, the SR is 0.9 or better which indicates that the tweezers are indeed very close to the optimum. Furthermore, the fit panel shows a large distance between both foci of about 850 nm, which is much larger than the astigmatic difference of about 450 nm reported in the

imaging tests. The example tweezer in 3.25 B also shows this astigmatism as the plus-like main peak symmetry visible in the logarithmic scale image or, even more clearly, in the linear residue. In C, The data points lie very close to the simulation with the exception of the Airy zeros, where the astigmatism and residual spherical aberrations limit the contrast.

Moving to objective 002, the tweezer shape is shown in Figure 3.26 which is similar to the one of objective 001, except that spherical aberration compensation worked better and that the astigmatism appears to be weaker. Not surprisingly, the observed trefoil in the imaging section is also visible in the optical tweezer images in 3.26 B. Subfigure C again shows very good agreement of the expected axial resolution limit ζ_0 with the z-cut intensity minima. Note that in the first focus, a few images were saturated and consequently not included in the axial Gaussian fit.

The saturated images have also been excluded from the analyses to avoid invalid data points. This caused the gap visible in Figure 3.27 A. Nevertheless, analysis results of the second focus also show diffraction-limited tweezer generation for objective 002. The R^2 and SR are slightly better than for objective 001. That fact that the SR error bar is smaller close to focus, is a consequence of the imaging imperfection compensation. In case an image has a Strehl ratio close to or slightly above 1, the correction-error approximation is not well-defined anymore and leads to very narrow error bars. As expected from the imaging tests, the astigmatic difference is also reduced compared to objective 001 to only roughly 400 nm, which is much more than the 200 nm in the imaging case. The reason for the enhanced astigmatism in both tweezer cases is presumably the asymmetric surface curvature for the 45° mirrors after lens #3. This hypothesis would also agree with the astigmatic axes aligning well with the reflection plane. For the imaging tests, in contrast, the whole relevant setup was built on a line without any additional mirrors. It is possible that the -75:500 telescope also contributed to the astigmatism, as both lenses had fewer tunable degrees of freedom which reduced the alignment precision. Subfigure B nicely shows the trefoil property of objective 002, which reduces the fit quality as visible in the residue. This trefoil also deteriorates the overlap of the azimuth average with the simulation in C. Fortunately, apart from the minima, the tweezer size and side-lobe power do not seem to be strongly affected by this aberration.

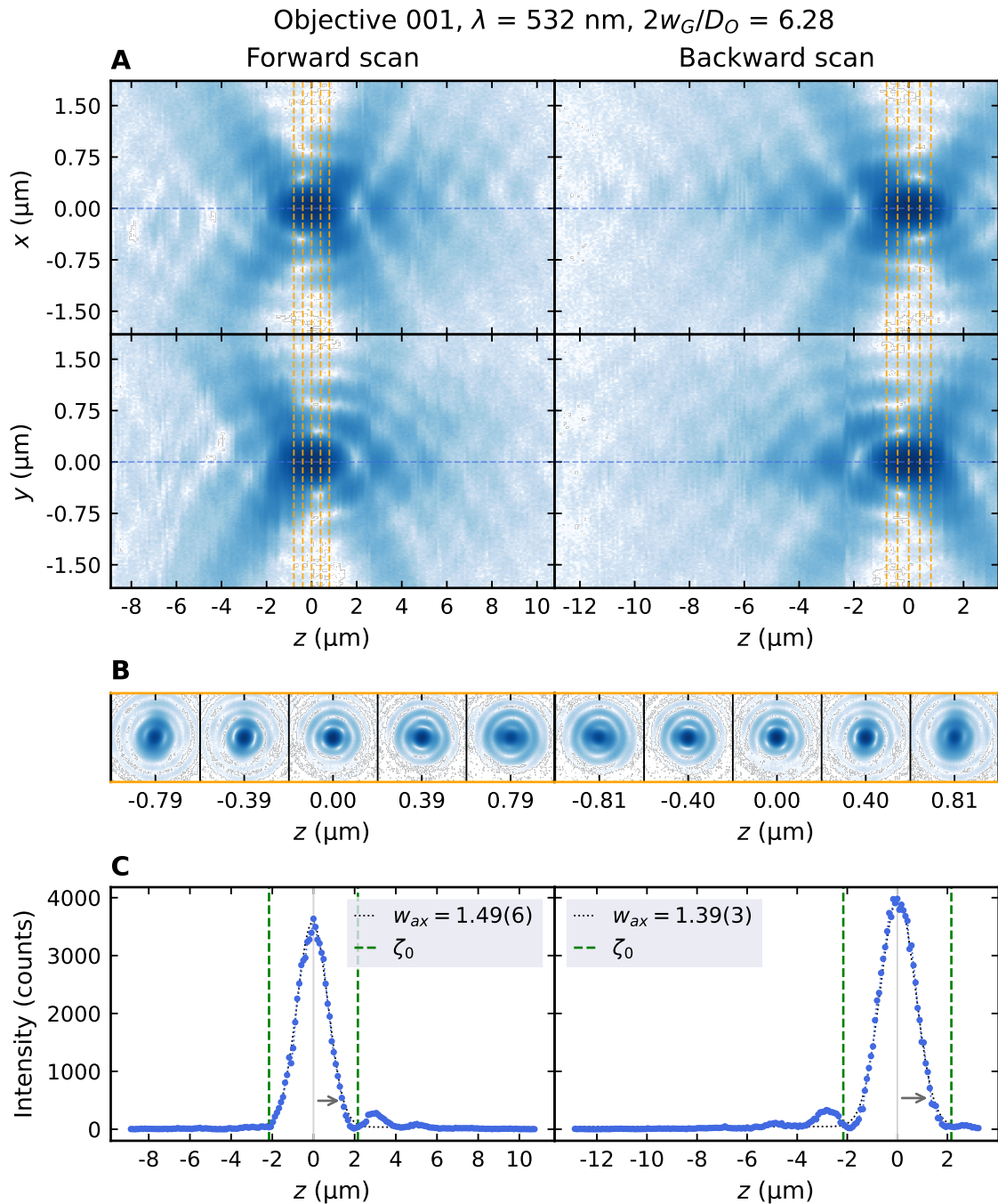


Figure 3.24 – Single tweezer measurement, no AODs, 220 mm incoming beam, objective 001: Tweezer shape. The columns represent the tweezer shape for the forward and backward focus scans, respectively. Subfigure **A** shows x-z and y-z cuts of the 3D scans, fixing the third axis to the center of the ROI and displayed in logarithmic scale. In part **B**, five example images are depicted at different distances from focus and plotted in logarithmic scale for better visibility of the side-lobes. The cuts from which these images are taken are indicated in A with orange dashed lines. **C** visualizes the axial intensity distribution, as taken from averages over the four pixels in the very center of every image. As a guide to the eye, this axis is also shown in A as a dashed blue line. The axial Gauss fit is also plotted as a dotted line, as well as an indication of the expected axial zero crossings (axial diffraction limit ζ_0 , green dashed line). The fitted Gaussian waist, referring to the $1/e^2$ value, is given in the legend and indicated by the gray arrow.

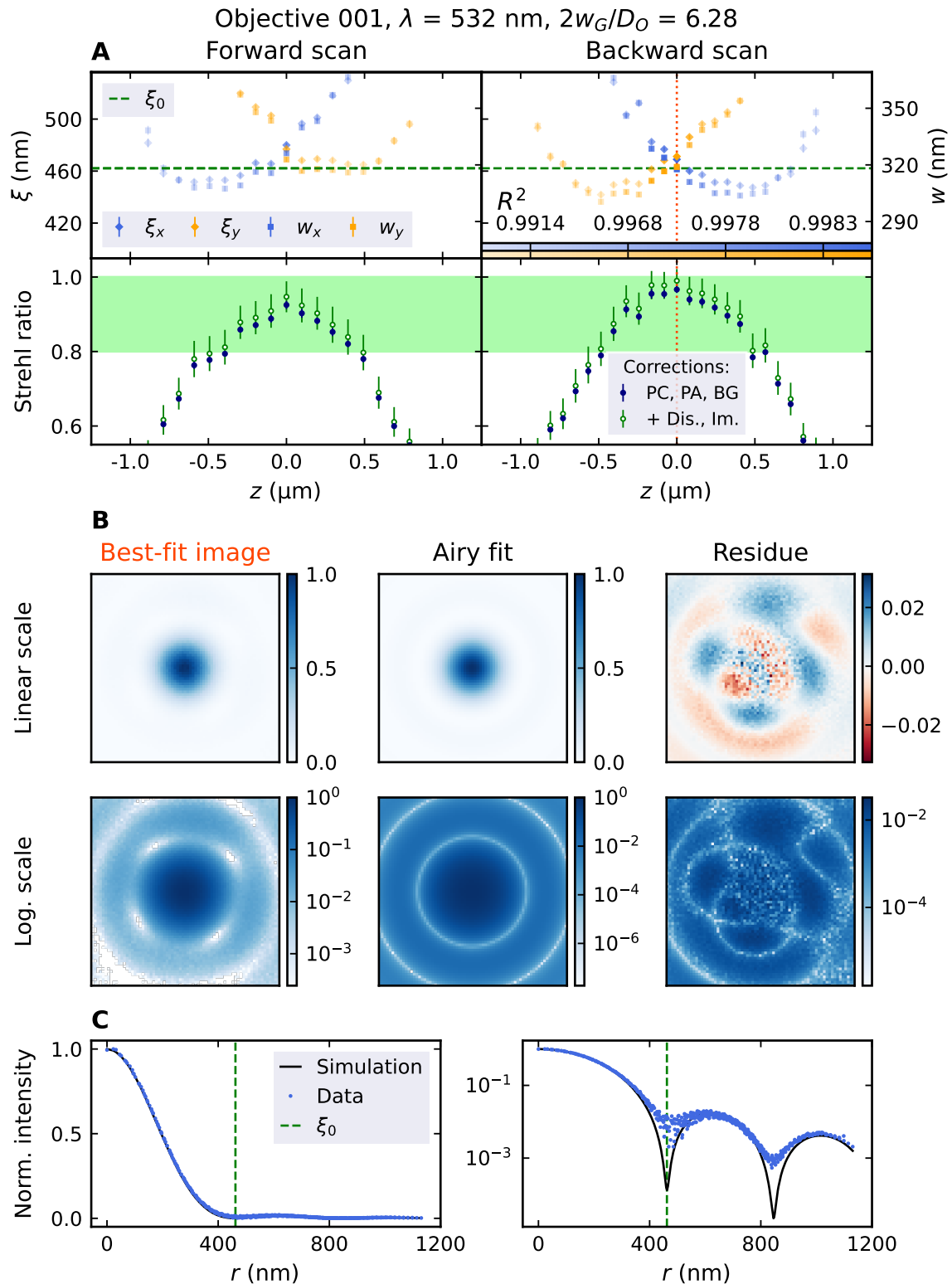


Figure 3.25 – Single tweezer measurement, no AODs, 220 mm incoming beam, objective 001: Tweezer analysis. The main analysis results are summarized in subfigure **A**, starting with the upper plot that shows both, the fitted Rayleigh resolution ξ and the waists w from the Gauss fits. To provide reference, the radial diffraction limit ξ_0 is drawn as a dashed green line. Lastly, alpha-encoded R^2 values enable one to assess the Airy fit quality for each image. The lower plot displays the Strehl ratio with two different sets of correction steps and the "diffraction-limited" area highlighted in green. Part **B** shows the best R^2 fit of the whole scan from left to right the image, fit, and residue, in both linear and logarithmic scale. To better locate the image in the overall scan, a red dotted line is drawn in **A**. Section **C** shows azimuth averages of the above image and of ideal diffraction-limited tweezer simulations in linear and logarithmic scale.

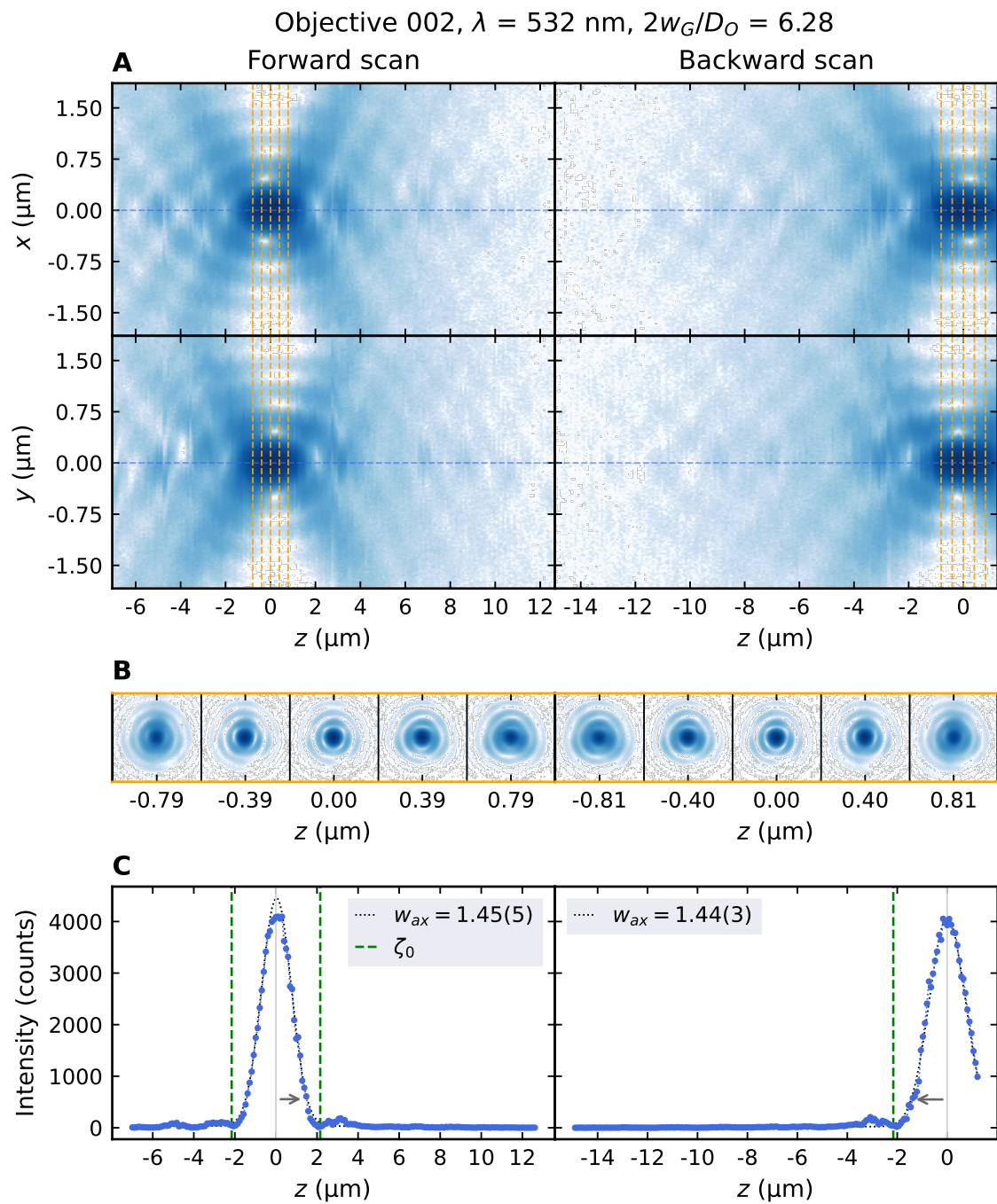


Figure 3.26 – Single tweezer measurement, no AODs, 220 mm incoming beam, objective 002: Tweezer shape. The Figure has the same structure as Figure 3.24.

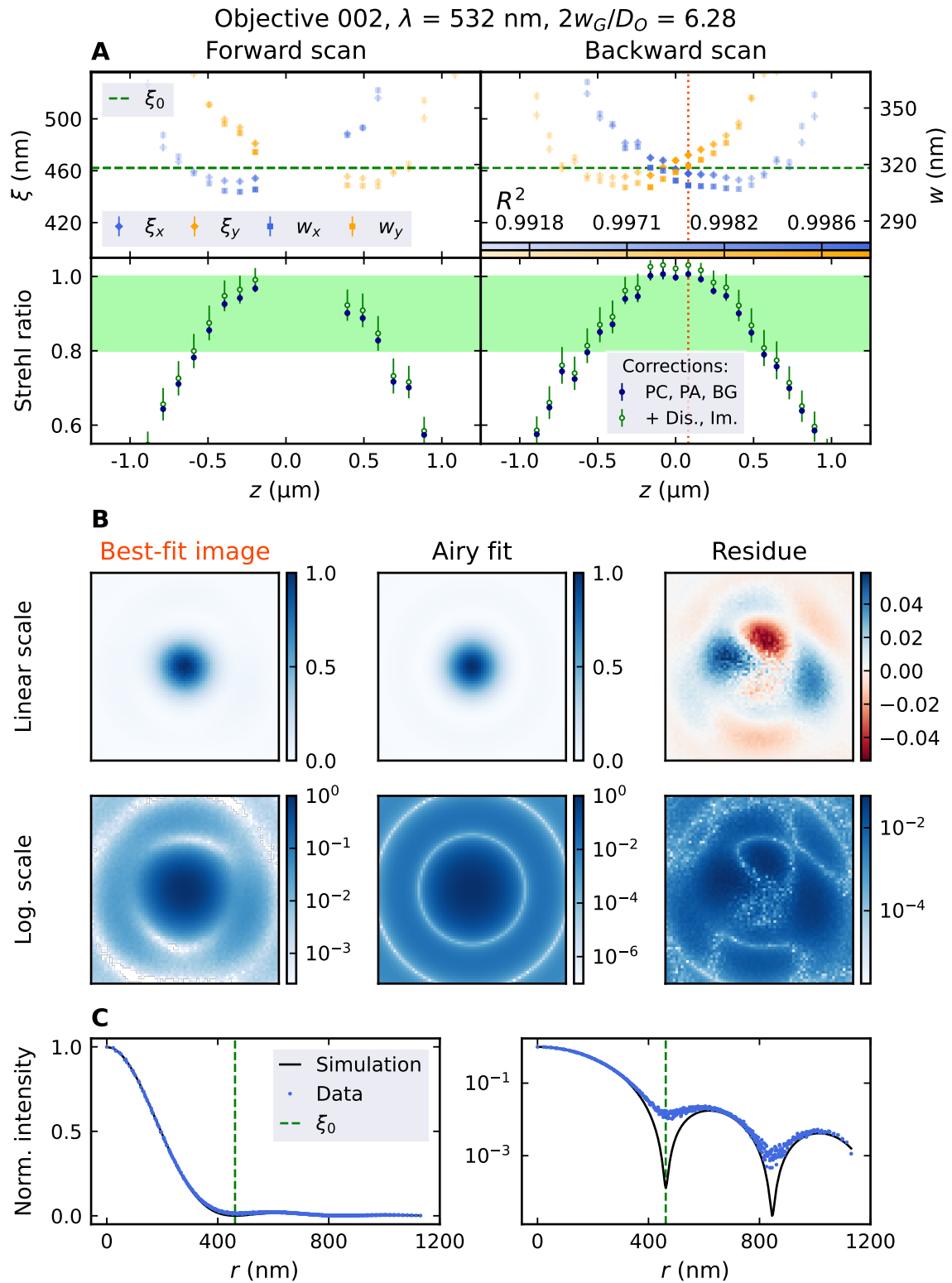


Figure 3.27 – Single tweezer measurement, no AODs, 220 mm incoming beam, objective 002: Tweezer analysis. The Figure has the same structure as Figure 3.25.

Since the axial distributions are fitting reasonably well with the expected axial zero crossings and the tweezers are in fact diffraction limited, we compared the measured picomotor step size with an estimate calculated from the axial focus scan shape. To this end, the axial Gaussian waist was scaled with $1.22/0.84$ to obtain the zero position. This assumes the axial distribution to be similar to a cut through an Airy pattern, and uses the waist-to-resolution relation for a Gaussian approximation of an Airy peak. By comparison with the theoretical axial zero crossing $2\lambda/NA^2$, a step size is computed. The following table compares the measured and computed step sizes for the Newport five-axis translation stage (z -direction), with a picomotor step count of five steps per image.

	Forward (nm)	Backward (nm)
Interferometric calibration (4 steps)	19.7(6)	16.2(2)
Objective 001	19.58(16)	17.27(14)
Objective 002	20.14(14)	16.71(15)

Table 3.7 – Computed five-axis translation stage picomotor step sizes from tweezer analysis

Within the error bars, both the interferometric measurement and the calculation agree well in the forward direction. For backward scans, there is a discrepancy which might arise from a slight change in the backward step size between the calibration and the tweezer measurements. However, such mismatch is not covered by error bars does not exceed 5%.

Table 3.8 summarizes the "flat top" input beam tweezer measurements where, since both foci are treated as independent, meaningful measurements, only the best single focus is displayed for each objective. Following the derivations in Section 2.3.1, the trap parameters that can be expected for 174-Yb, given the measured tweezer characteristics, were calculated, assuming a polarizability of $-12.13 \text{ hHz W}^{-1}\text{cm}^2$ and are shown in the lower two sections. To compute these quantities, only the Strehl ratio values that have been corrected for pixel averaging, pixel centering and background were used. The first section summarizes purely optical properties of the tweezers, while the second and third respectively give trap parameters in units of Hertz and Kelvin.

The remainder of this Subsection discusses the tweezers generated with a more realistic, smaller input beam with 16.5 mm waist, making the relative beam size parameter $2w_G/D_O = 0.94$. The same beam size is used in all further tweezer measurements of this thesis, including those in the main experiment. Compared to the previous analyses, the expected size and Strehl ratio of the tweezers changes from the fact that the incoming wavefront has a Gaussian envelope; this is accounted for by applying the results from Subsection 2.3.4. The "diffraction-limited" region in the Strehl ratio plot is scaled by 0.905, the maximum achievable Strehl ratio. The lower SR bound is similarly scaled to maintain its proportion in the entire range. Simultaneously, the ideal NA-limited diffraction limit ξ_0 is replaced by $\tilde{\xi}_0 = 1.126 \cdot \xi_0$, which is the expected increase in ξ when fitting an ideal tweezer created by a Gaussian input beam with a

	"Flat top" beam tweezers	Objective 001	Objective 002
Tweezer shape	Rayleigh resolution ξ (nm) Radial waist w_r (nm) Axial waist w_{ax} (μm) Strehl ratio (all corrections)	468.9(14), 475.6(14) 317.9(10), 322.3(10) 1.39(3) 0.97(3)	460.9(13), 469.6(14) 311.3(10), 317.4(10) 1.44(3) 1.024(15)
Trap (Hertz)	Trap depth U_0 ($\frac{\text{h}\cdot\text{GHz}}{\text{W}}$) Radial trap frequency ω_r Axial trap frequency ω_{ax} Frequency units ($2\pi \cdot \frac{\text{MHz}}{\sqrt{\text{W}}}$)	6.35(3) 2.664(11), 2.701(11) 0.871(7)	6.68(3) 2.775(11), 2.829(12) 0.865(8)
Trap (Kelvin)	Trap depth U_0 ($\frac{\text{k}_B \cdot \text{mK}}{\text{W}}$) Radial trap frequency ω_r Axial trap frequency ω_{ax} Frequency units ($2\pi \cdot \frac{\text{k}_B \cdot \mu\text{K}}{\text{h} \cdot \sqrt{\text{W}}}$)	304.7(15) 127.9(5), 129.6(5) 41.8(4)	320.5(16) 133.2(6), 135.8(6) 41.5(4)

Table 3.8 - Single tweezer results: "Flat top" input beam

perfect Airy pattern. With these adjustments, the new size limit is physically meaningful and the Strehl ratio values can be assessed with respect to the bound given by the optimal tweezer that is generated by a Gaussian beam. Lastly, there is an additional simulation in the azimuth average plots, which includes the Gaussian shape of the beam impinging on the objective.

Starting with objective 001, the tweezer shape is shown in Figure 3.28. As subfigures A and B display, perfect spherical aberration compensation was not achieved. One side of the focus is always more diffuse than the other that has larger fringe contrast. This is especially visible in the axial cut shown in C, where the center-oriented side exhibits more pronounced axial peaks. Due to performing worse than objective 002, this objective was intended to be used in the main setup and these measurements were not retaken with improved spherical aberration compensation. Astigmatism is visible as in previous measurements. As a consequence of the Gaussian input beam envelope, the overall tweezer shape looks much more smeared out and the minima are less pronounced. The white stripes at the bottom of subfigure A originate from images too close to the data-acquisition ROI boundary, thus ending up cutout and filled with zeros during data analysis. These features are also visible in the shape plot of objective 002.

The analysis results of the focus scan are shown in Figure 3.29. The main differences to the previous scan that used a 220 mm input beam are overall reduced Strehl ratio, increased total size, and reduced contrast at the minima. The characteristic

astigmatism of objective 001 prevailed in this measurement. Nevertheless, according to the adjusted criteria for an incoming beam with a size of 33 mm, the tweezers are still diffraction limited. In subfigure C one finds how the Gaussian input beam significantly changes the expected tweezer size. The data and the simulation match quite well, even though aberrations prevent the minima from having good contrast. The measurement side lobes are remarkably more intense than those of the simulation, which is presumably due to the added aberrations.

Figure 3.30 shows the shape of the tweezer generated by objective 002 that used a Gaussian input beam. While the axial symmetry is close to perfect aside from some slight astigmatism, coma could have been compensated more efficiently. Proceeding to the analysis results in plot 3.31, this scan is as diffraction limited as the one recorded with objective 001 even though both foci are quite different this time. Note that in the forward focus there was one image excluded from analysis due to camera saturation. The typical trefoil shape is found again in subplot B, while subplot C shows similar agreement of the data with the Gaussian beam tweezer simulation as in the previous analysis plot. In contrast to objective 001, the minima are approached much more closely and the side-lobe power does not exceed the simulation. This is attributed to the fact that, apart from the trefoil preventing the first minimum to be reached in subplot C, the spherical aberrations are perfectly compensated this time and therefore suggest to explain the outer rings containing much more power than expected in the case of objective 001.

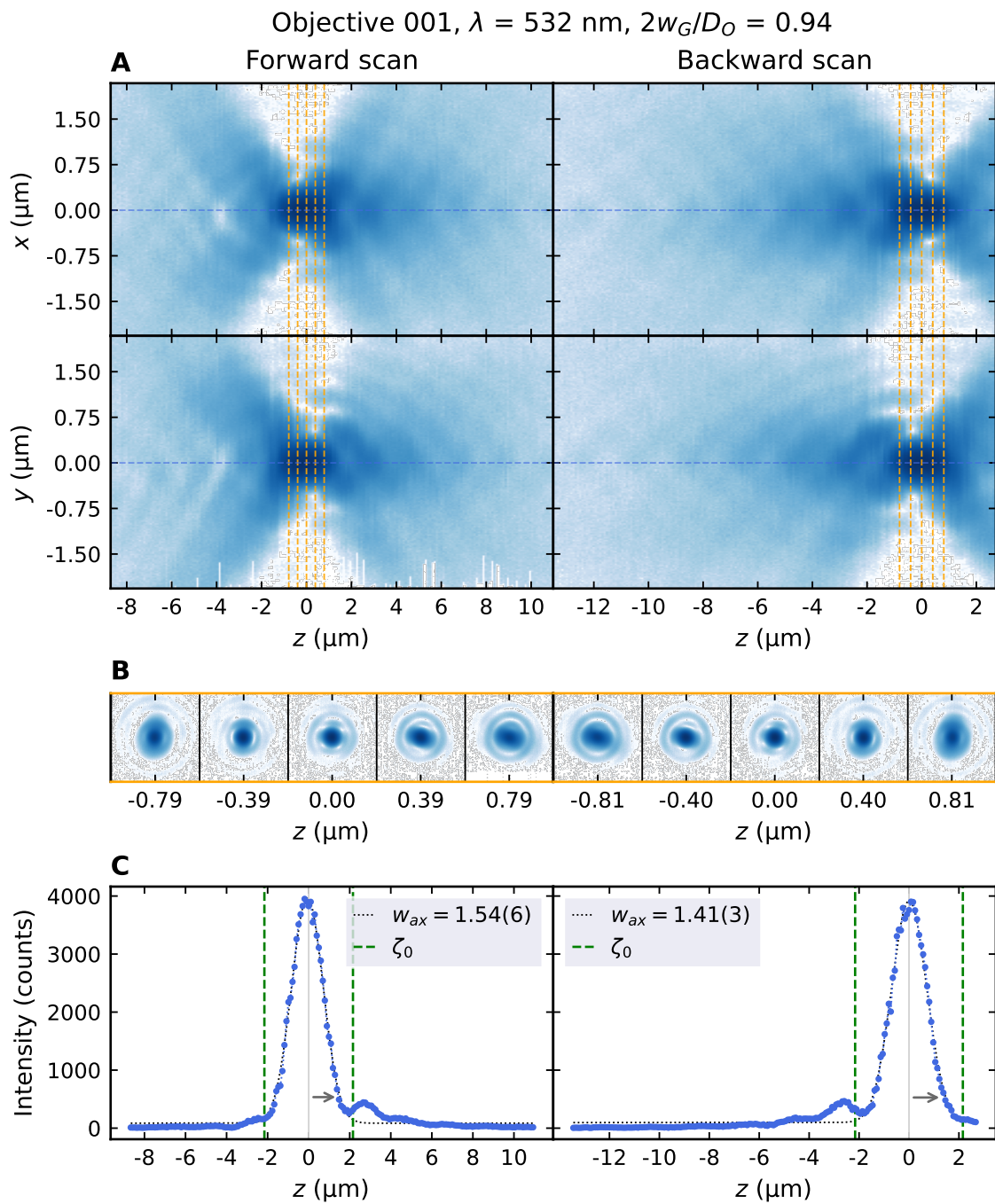


Figure 3.28 – Single tweezer measurement, no AODs, 33 mm incoming beam, objective 001: Tweezer shape. The Figure has the same structure as Figure 3.24.

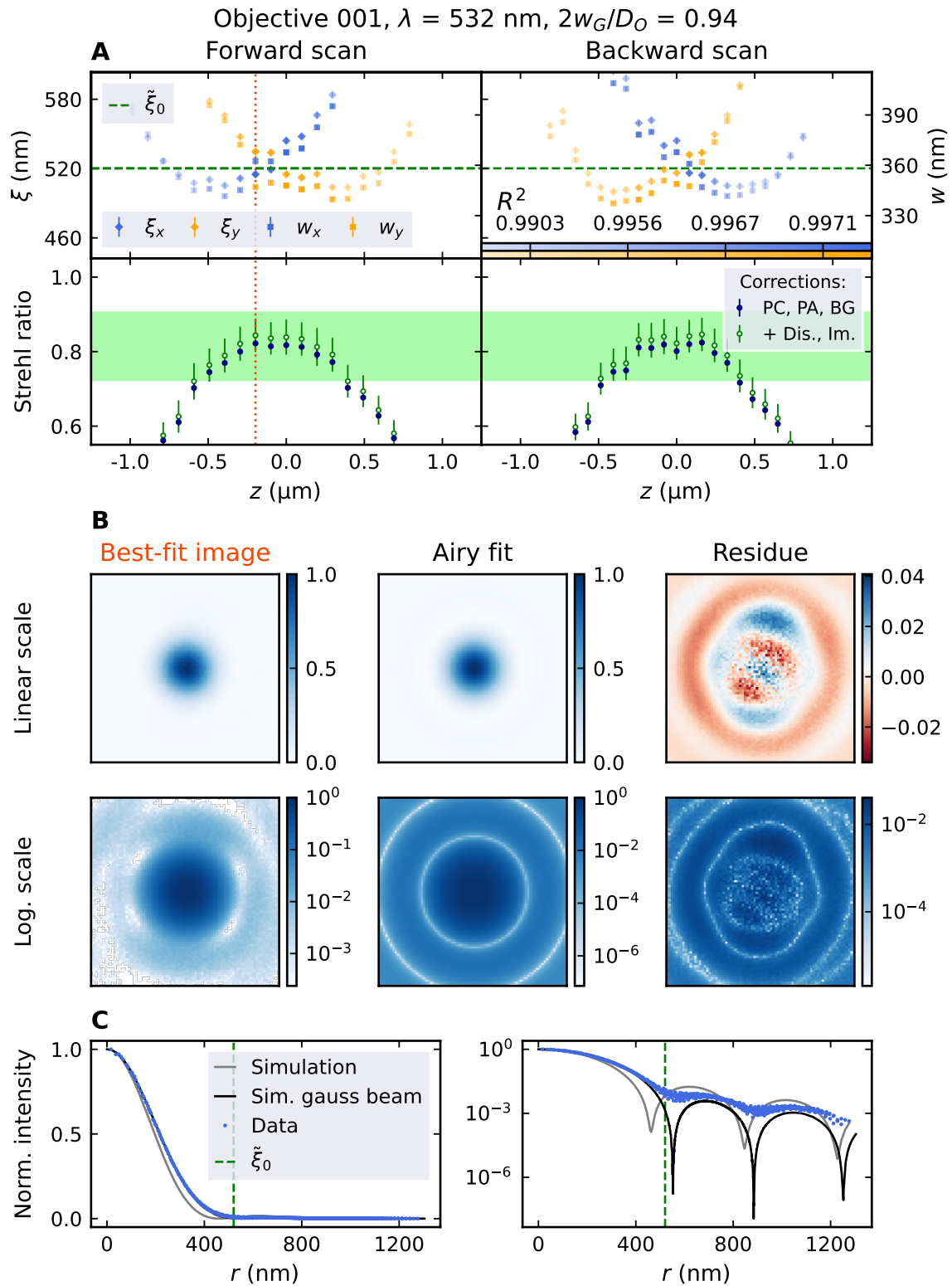


Figure 3.29 – Single tweezer measurement, no AODs, 33 mm incoming beam, objective 001: Tweezer analysis. The Figure has the same structure as Figure 3.25 with an additional simulation in subplot C accounting for the Gaussian input beam shape. The diffraction limit references in subplot A are adjusted to the larger ideal tweezer size.

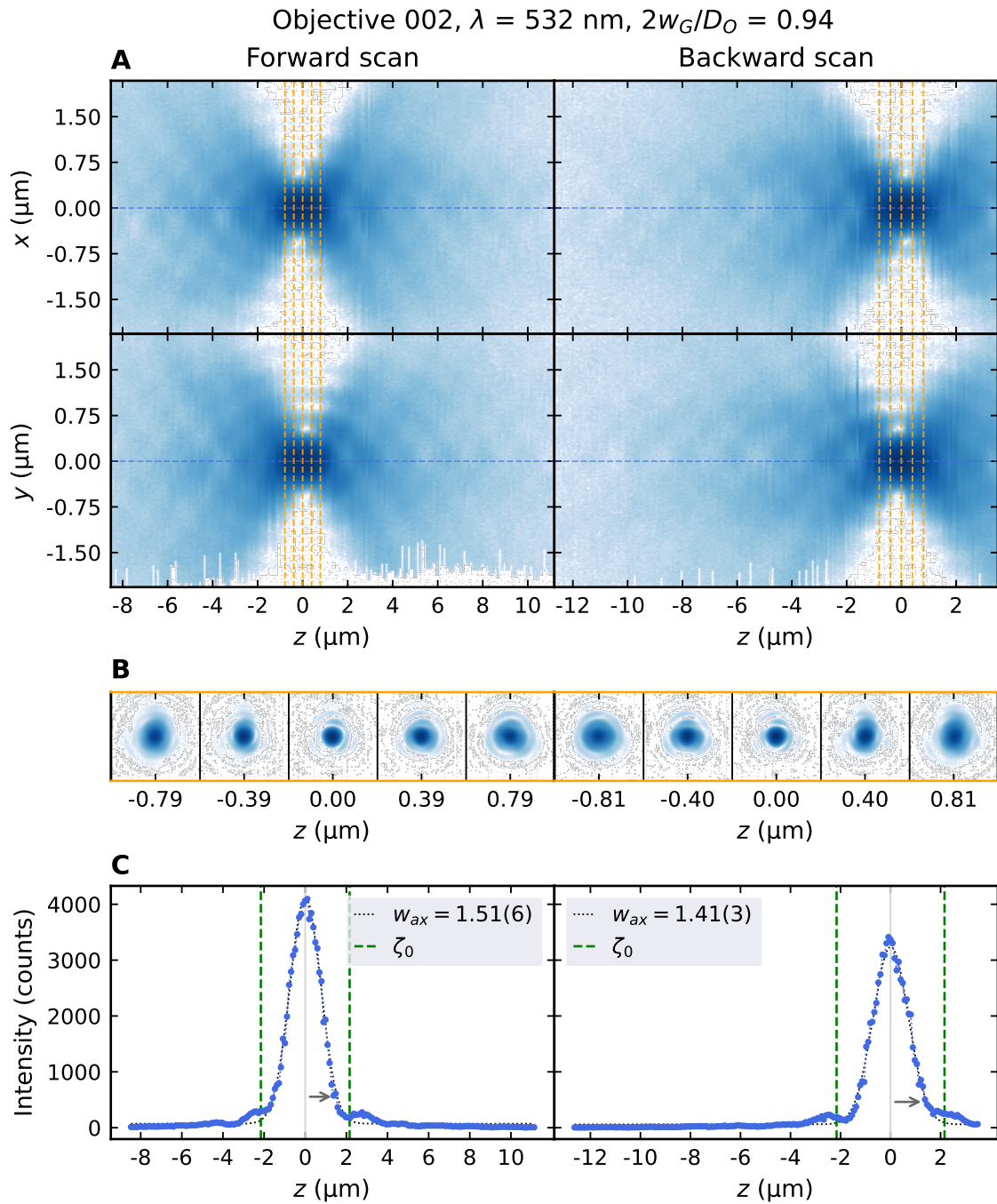


Figure 3.30 – Single tweezer measurement, no AODs, 33 mm incoming beam, objective 002: Tweezer shape. The Figure has the same structure as Figure 3.24.

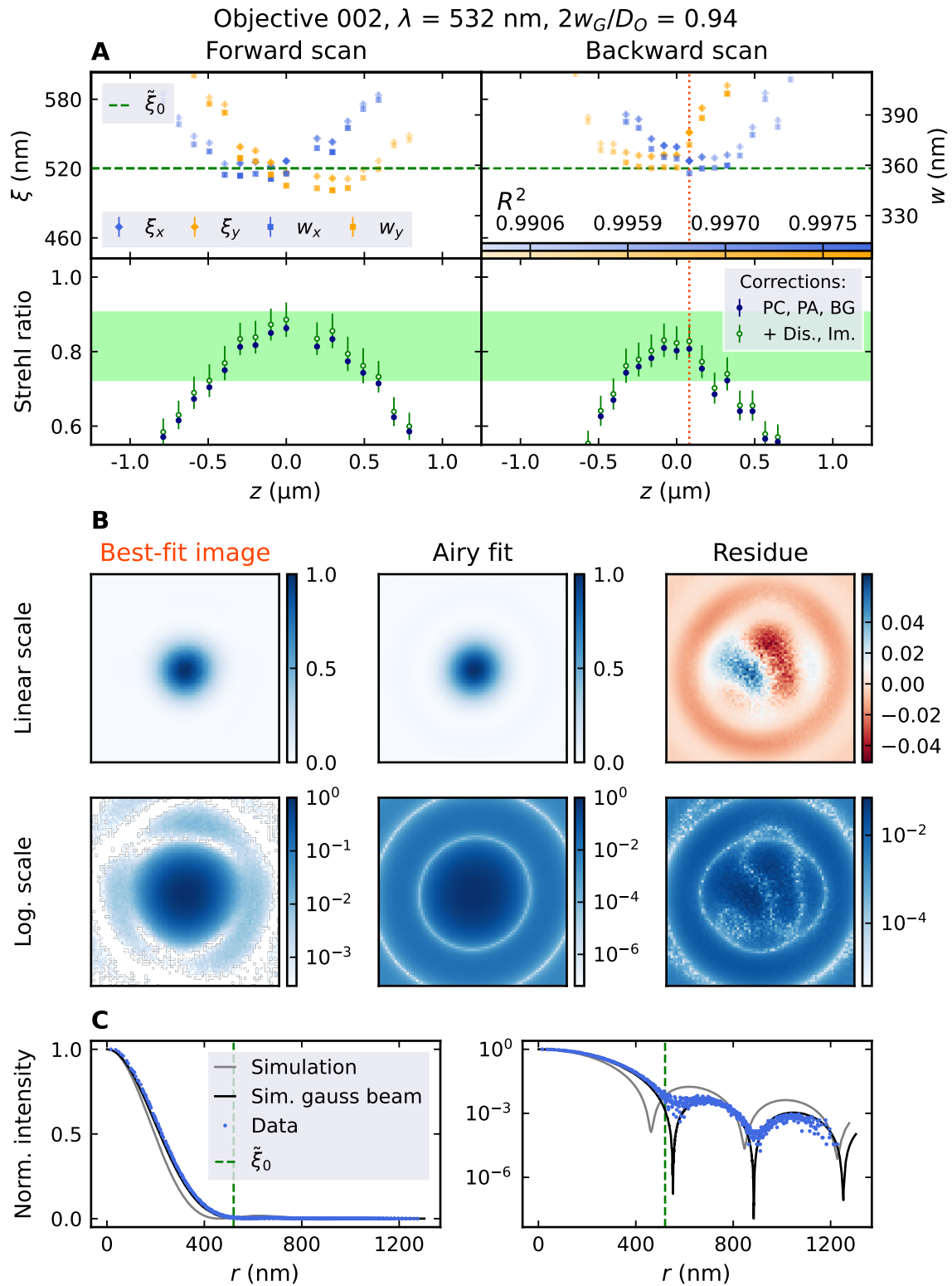


Figure 3.31 – Single tweezer measurement, no AODs, Gauss beam, objective 002: Tweezer analysis. The Figure has the same structure as Figure 3.25m with an additional simulation in subplot C accounting for the Gaussian input beam shape. The diffraction limit references in subplot A are adjusted to the larger ideal tweezer size.

As with the "flat-top" input beam case, the tweezer generation performance was again summarized in the following table, this time for the measurements with a Gaussian incoming beam. From top to bottom, the three sections summarize the tweezer shape, the trap parameters in units of Hertz, and the trap parameters in units of Kelvin.

	Gaussian beam tweezers	Objective 001	Objective 002
Tweezer shape	Rayleigh resolution ξ (nm)	523.6(16), 530.7(16)	518.2(16), 530.7(16)
	Radial waist w_r (nm)	347.5(10), 365.7(11)	349.5(11), 358.5(11)
	Axial waist w_{ax} (μm)	1.54(6)	1.51(6)
	Strehl ratio (all corrections)	0.84(4)	0.86(4)
Trap (Hertz)	Trap depth U_0 ($\frac{\text{h}\cdot\text{GHz}}{\text{W}}$)	5.453(22)	5.579(26)
	Radial trap frequency ω_r	2.176(8), 2.290(8)	2.246(9), 2.303(9)
	Axial trap frequency ω_{ax}	0.731(7)	0.755(7)
	Frequency units ($2\pi \cdot \frac{\text{MHz}}{\sqrt{\text{W}}}$)		
Trap (Kelvin)	Trap depth U_0 ($\frac{\text{k}_B\cdot\text{mK}}{\text{W}}$)	261.7(11)	267.8(13)
	Radial trap frequency ω_r	104.5(4), 109.9(4)	107.8(4), 110.5(4)
	Axial trap frequency ω_{ax}	35.1(4)	36.3(3)
	Frequency units ($2\pi \cdot \frac{\text{k}_B\cdot\mu\text{K}}{\text{h}\cdot\sqrt{\text{W}}}$)		

Table 3.9 – Single tweezer results: Gaussian input beam

3.3.4 Single tweezers with two AODs in the beam path

With the full setup, including both AODs and the 1:1 telescope, the optical tweezers can be moved in the FOV and 2D arrays can be generated. The impact of changing to the complete setup described in 3.3.1 is investigated in this Subsection. The set RF voltage was swept to check for any tweezer quality change due to nonlinear effects in the AOD crystal. For this and the following FOV measurement, objective 002 and two picomotor steps per image are used. The latter increases the statistics and accuracy of the computed scan parameters compared to the single tweezer measurements in 3.3.3, which used five picomotor steps per image.

Results are shown in Figure 3.32, where the RF voltage is scanned within the range rated for a single tone (from 80 to 230 mV) and the results on the tweezer are checked. Subplot A shows the Airy fits and Strehl ratio as in the previous plots and subplot B displays the corresponding best-Strehl ratio tweezers in logarithmic scale. We observe no clear trend in any direction, and the analysis fluctuations seem to be connected to measurement uncertainties and instabilities. We conclude that:

1. The RF voltage has no significant impact on the tweezer quality.
2. The resolution and Strehl ratio do fluctuate naturally on a (max-min) level of about 10 nm and 0.05, respectively.
3. Now including the AODs, two arc-like structures emerged and can be observed around the tweezers intersecting in the center and rotated by 90° with respect to each other. These structures can also be observed by eye in the focus of the tweezer-generating lens L3, see Figure B.3 F in the Appendix. The arcs brightness were observed to scale with RF power and points in an ellipsoidal shape towards higher and lower order AOD diffraction peaks. The physical origin of these is unknown, however, since the brightness scaling of these arcs does also affect the transmitted first diffraction order, the relative arcs-to-tweezer brightness remains approximately constant. This explains why we cannot see any relative brightness difference of the images in subfigure B.

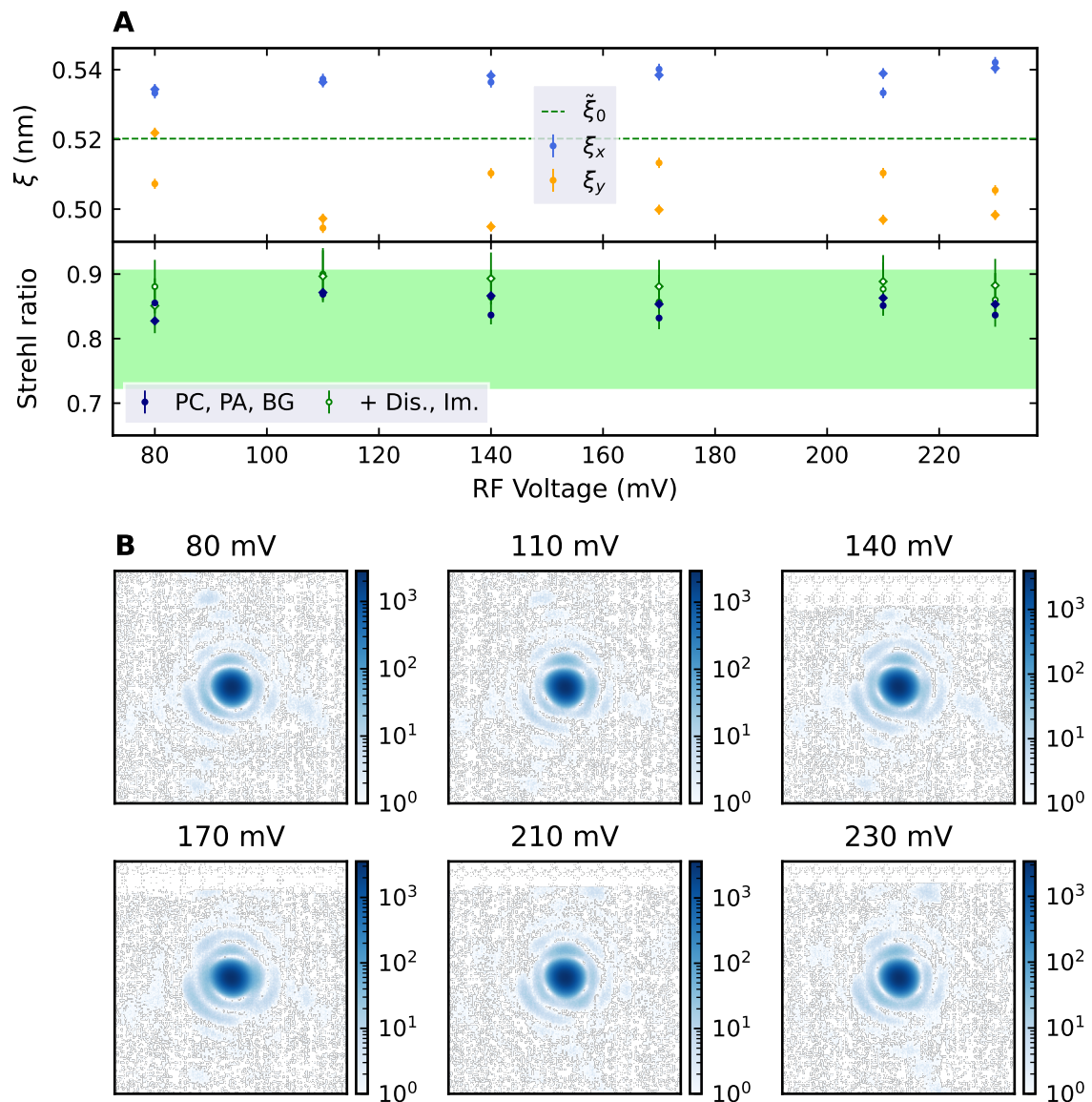


Figure 3.32 – Single tweezer measurement as a function of RF voltage, 2 AODs, 33 mm incoming beam, objective 002 In **A**, the fitted tweezer size ξ , and the Strehl ratio was plotted against the RF drive voltage to check if there exists a correlation between them. Correspondingly, in **B** the best SR tweezer images are shown for the respective RF voltage in logarithmic scale.

3.3.5 2D tweezer arrays and field of view

After having confirmed diffraction-limited performance in the full setup, the two AODs are used to generate 2D tweezer arrays used to test the whole FOV of the SQM objectives. In the following, tweezer arrays of six rows and eight columns are created with 2.17 MHz RF frequency spacing between neighboring tones, which corresponds to a $4.44 \mu\text{m}$ tweezer spacing in the atom plane. These numbers were used for the following reasons:

1. The spacing is large enough such that neighboring tweezers, including the arcs discussed in the previous paragraph, do not overlap which would skew the analysis results.
2. A 6x8 tweezer array with the chosen spacing fits well on the camera sensor in the image plane, without the risk of tweezers being cut.
3. For the FOV measurement, a 100x100 μm square had to be sampled to already test conditions of interest for the ultracold atom experiment. Taking twelve measurements at different positions in the FOV of 6x8 tweezer arrays shaped in three columns and four rows, enables us to measure 24x24 optical tweezers covering an area of 102x102 μm . Using these numbers, almost the whole bandwidth of the AODs is tested (precisely: 49.91 MHz out of 50 MHz).

The field of view measurements were only taken with objective 002 and tweezer balancing was applied as described in 3.3.1. A typical in-focus image of such a tweezer array, taken from the FOV measurement discussed in the next pages, is depicted in Figure 3.33.

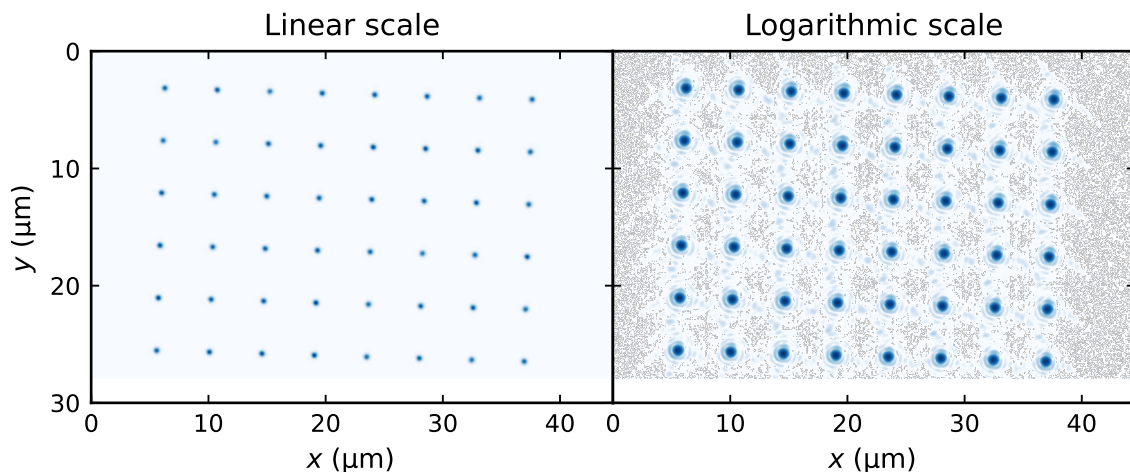


Figure 3.33 – Example image of a 2D 6x8 optical tweezer array. The raw camera image is shown in linear (left) and logarithmic (right) scale. It is taken from position "5" of the FOV measurement series, therefore the center of the FOV is approximately located in the center horizontally and half a tweezer spacing below the bottom row.

The image is shown in linear and in logarithmic scale on the left and right, respectively. The slight angle between array and camera could theoretically be easily compensated by turning the AODs. Inspecting the linear scale image, one finds that the tweezers look nearly identical and are arranged in a regular grid. In the logarithmic scale, however, slight differences between the tweezer side-lobes are visible.

The results of the main tweezer FOV test are discussed in the next pages. As mentioned above, a 24x24 tweezer square grid was prepared in 4x3 patches containing 6x8 optical tweezers each. The tweezer spacing is 4.44 μm , resulting in an explored

area of $102 \times 102 \mu\text{m}$ in the FOV. Back and forth focus scans were taken for every measurement. Apart from testing the FOV with this measurement, it also provides statistics on fluctuations of the optical tweezer quality in this kind of focus scan measurement, as well as information on the reproducibility and stability when comparing to forward and backward scans of the same optical tweezers. The twelve measurements were recorded in approximately a four-hour period. As a quick reference to the correct sector in the FOV test, the following table labels all measurements:

	Row (x axis)		
	1	2	3
	4	5	6
	7	8	9
Col (y axis)	10	11	12

Table 3.10 – FOV measurement labeling

Figure 3.34 starts with showing the best-Strehl ratio images, in logarithmic scale, of every individual optical tweezer in the whole FOV test for the forward scan only. The picture is stitched together using a display ROI size that maintains the correct distances between the tweezers. While the distances are to scale also between arbitrary tweezers, the relative positioning of the 24×24 images might be a few pixels off. Another effect based on this is the image looking square, even though all twelve individual measurements were slightly rotated, as seen in Figure 3.33. Furthermore, different regions in the image show stronger and weaker arcs around the tweezers. This effect is due to non-uniform overall tweezer brightness among the measurements; for example measurement 10 in the lower left corner was close to camera saturation and thus made more details visible.

All tweezers look overall similar, with the center peak appearing to be of equal size and only differing by the side-lobe shape. Most strikingly, the change in PSF towards the edge of the field of view observed in Subsection 3.2.5 seems to be reversed towards the outside. In the extreme case of the four tweezers at the very edges of this image, the tweezer shape is observed to be strongly distorted and elongated in the radial direction. The distortion of such outermost tweezers is not introduced by the SQM objective generating them, discussed in Subsection 3.3.9, but rather by the FOV cutoff of the Nikon objective being reached. Because of this, the 4 outermost tweezers are not taken into account in the following discussions. In this measurement, the tweezer position was changed to gain insights on the SQM objective while the Nikon was not moved for any measurement so as to keep its alignment quality the same. Therefore, this is a very precise measurement of both, the Nikon FOV diameter, that appears to be about $2 \times 70 \mu\text{m}$, and the SQM FOV centering quality with respect to the Nikon FOV, appearing to be well centered judging from the symmetric distribution of the four worst tweezers in the corners.

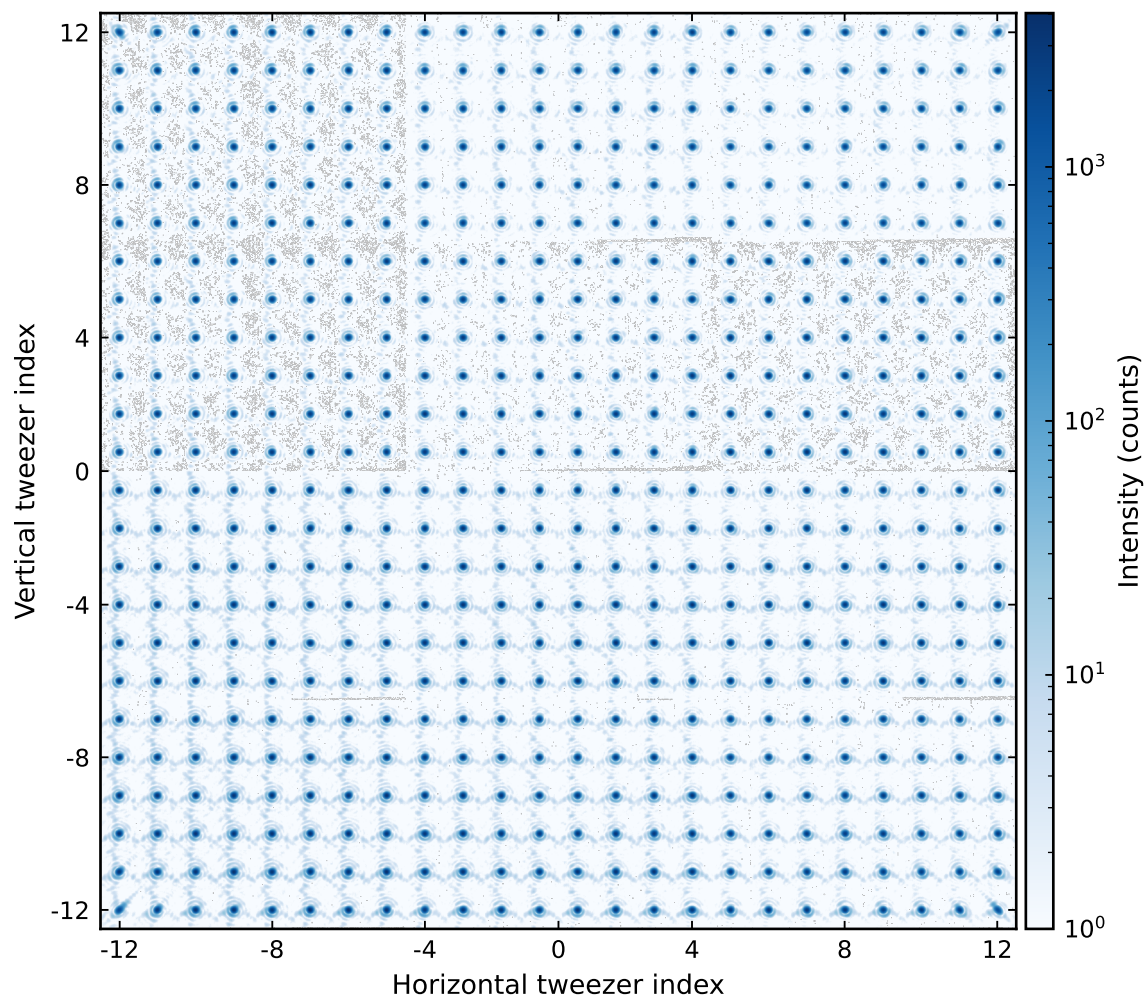


Figure 3.34 – Optical tweezer FOV measurement: complete image The complete FOV measurement is displayed as one image showing the best-Strehl ratio image for every individual tweezer. The images, in logarithmic scale, are taken from the forward scan only. The data is taken from twelve different 6x8 tweezer array measurements mapping the whole FOV. A display ROI has been cut, of the same size as the tweezer spacing in the measurement, for every tweezer. This means that the image shown is not one picture, but a collage of all individual images cut such that the composite plot has the real dimensions. On the axis, the tweezer index is labeled and the overall extent of the array is 102x102 μm .

The following plots present the analysis results of all 576 tweezers in different ways. The quantities of interest are listed below.

1. **Tweezer homogeneity.** For each individual measurement, the relative tweezer power was compared to obtain insights in the tweezer homogeneity, the success of the balancing code and possible correlations of the tweezer intensity with the other quantities.
2. **Strehl ratio.** The Strehl ratio including all corrections is computed as well.

3. **Resolution.** The tweezer "Rayleigh resolution" ξ , or the size of the tweezer measured from the center to the first radial zero, using an Airy pattern for fitting. Usually given in units of ξ_0 , the expected or ideal tweezer size. To condense the ξ_x and ξ_y resolution values into a single data point, both fit values were averaged.
4. **Fit fidelity R^2 .** The goodness-of-fit of the above Airy fits.
5. **Field curvature.** This aberration, as explained in Subsection 2.2.3, describes how the focus position varies within the field of view and is usually parabola shaped. Since the measurements always observed 48 tweezers simultaneously for the same position of the Nikon objective, this quantity is now accessible. However, since the focus position varies strongly between different measurements, the twelve separate field curvature patches need to be connected by adding the correct offset. This was done assuming a parabolic field curvature shape and fitting the offset parameters by maximizing the overlap with an arbitrary fitted 2D parabola.
6. **Axial tweezer waist w_{ax} .** The fitted axial Gaussian waist is also measured, as it governs the out-of-plane confinement of the optical tweezers.
7. **Distortion.** This aberration describes the effect of non-uniform local magnification in the image. As a result, distances between our tweezers would change across the field of view, even when the angles of the beams impinging on the objective are uniformly distributed. This effect was measured by determining the position of every tweezer averaged over a few well-focused images in a particular focus scan.

The first and most intuitive way of presenting the analysis results is via 2D heatmaps that show the values for every tweezer in the FOV. In Figures 3.35 and 3.36, the aforementioned quantities are displayed in eight subplots for the forward and backward tweezer measurement, respectively. Each subplot shows a 24x24 pixel representation of the FOV measurements with the colorbar quantifying the analysis shown.

Subfigure A starts with the homogeneity in units of relative tweezer power, normalized separately for each of the individual measurements. While there still is room for improvement, currently most tweezers lie in between 80 and 100% normalized power. In subfigure B, we observe a slight reduction of the Strehl ratio towards the corners, which is on the same scale as the overall fluctuations within the FOV. The achieved Strehl ratios are in good agreement with the theoretical limit of 0.905, staying in the diffraction-limited regime throughout the whole FOV. Continuing with the resolution plot in subfigure C, a similar pattern is observed as in the Strehl ratio heatmap and correlations between these two are investigated more thoroughly later in Subsection 3.3.6. The tweezer size is given in units of the adjusted diffraction limit ξ_0 that takes into account the Gaussian input beam size. We find that almost all tweezers are not larger by more than 5% of the expected diffraction limit, which is perhaps the most important result of this thesis. In addition, there is a visible correlation between relative

tweezer brightness and Strehl ratio, or resolution. This behavior is also investigated in more detail in 3.3.6. The fit fidelity in subfigure D is essentially only detecting the corners as being very different from an Airy pattern, most other tweezers are approximated well by the Airy pattern.

The field curvature shown in plot E follows the expected parabolic shape; the accuracy in its centering and radial symmetry confirms a good alignment. Apart from the 4x3 outermost tweezers, this field curvature is caused by the SQM objective as discussed in more detail in Subsection 3.3.9. The axial tweezer size displayed in part F is distributed quite evenly, aside from having the same twelve outliers in the corners as previous plots. A few measurements exhibit a global shift compared to the others, possibly caused by slightly fluctuating picomotor step size between them. Subplots G and H depict the horizontal and vertical distance between the tweezers. Since the measurements are distributed over three columns and four rows, white vertical and horizontal lines indicate the regions where no spacing could be computed. The overall range of tweezer distance fluctuations is less than 3%, or about 100 nm, and it is neither distributed randomly nor does it follow typical "barrel" or "pillow" distortions. Instead, we observe a linear trend precisely along both tweezer array axes, with almost the same magnitude. It appears as if the RF tone frequencies would not increment in uniform 2.17 MHz steps, but rather with a small quadratic contribution leading to a linear increase in distances. Up until today the cause of this systematic effect remains unclear.

Comparing the first and second focus, the plots are highly similar in the fluctuation-dominated subfigures like the Strehl ratio, tweezer size, and the distortion heatmaps. This indicates that the visible fluctuations have a significant contribution of systematic tweezer-to-tweezer variations, instead of being pure measurement noise. In addition, the values also agree relatively well, which suggests that the tweezer quality can be assessed up to a given certainty with these focus scans.

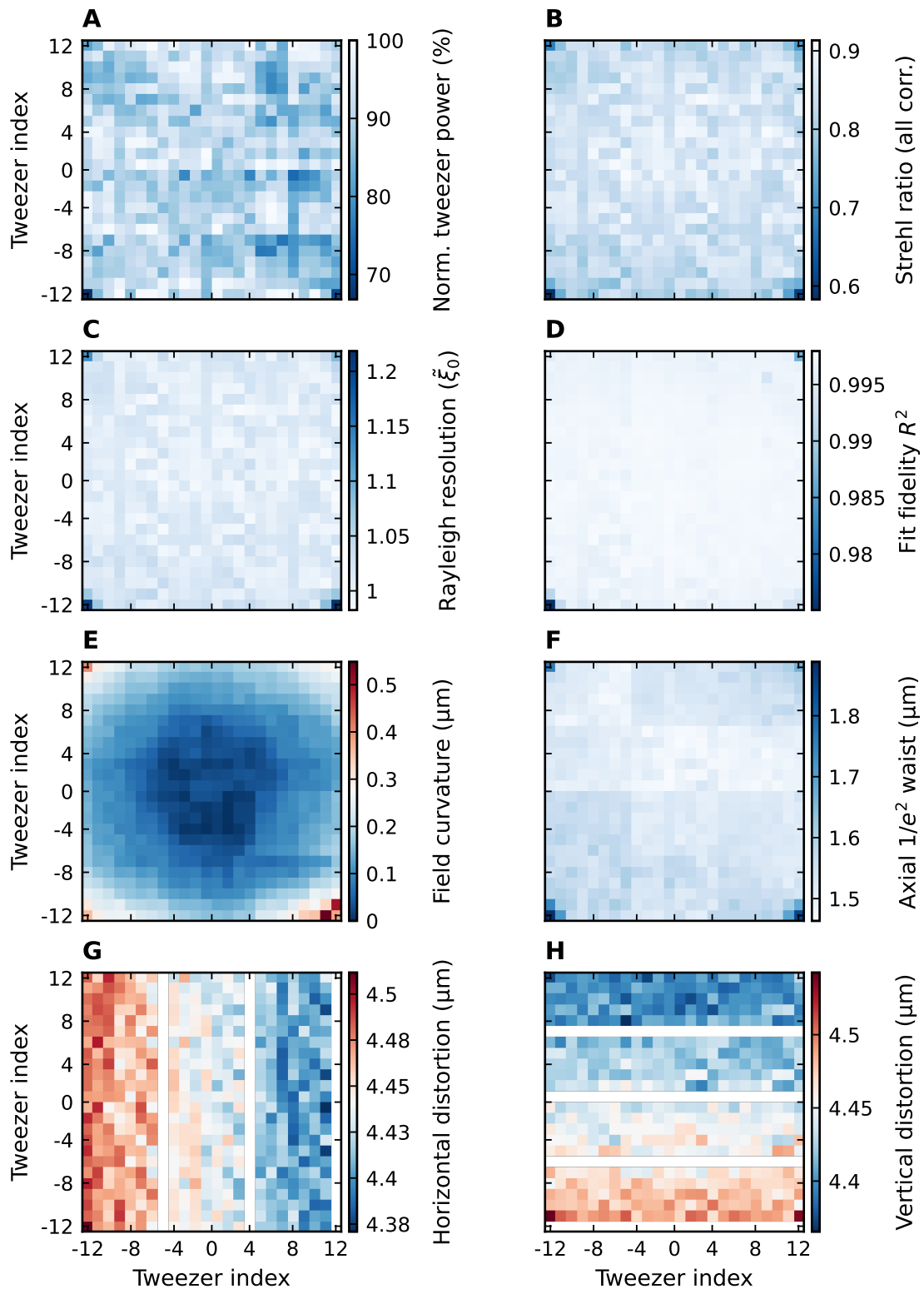


Figure 3.35 – Optical tweezer FOV measurement: analysis heatmaps, forward scan The FOV measurement results are displayed in 24x24 pixel heatmaps, showing the quantities of interest as a function of tweezer index. Colorbars are plotted to quantify the heatmaps. Shown are the tweezer power balance in **A**, the Strehl ratio including all correction steps in **B**, the average tweezer size in units of ξ_0 in **C**, the Airy fit fidelity in **D**, the field curvature or relative axial focus position in **E**, the axial tweezer waist in **F**, and the horizontal and vertical tweezer distances in **G** and **H**, where white lines correspond to unavailable information due to the segmented nature of the FOV scan. Note that the 12 outermost pixels were already affected by the Nikon imaging FOV boundary and were not be counted while assessing the SQM objective performance.

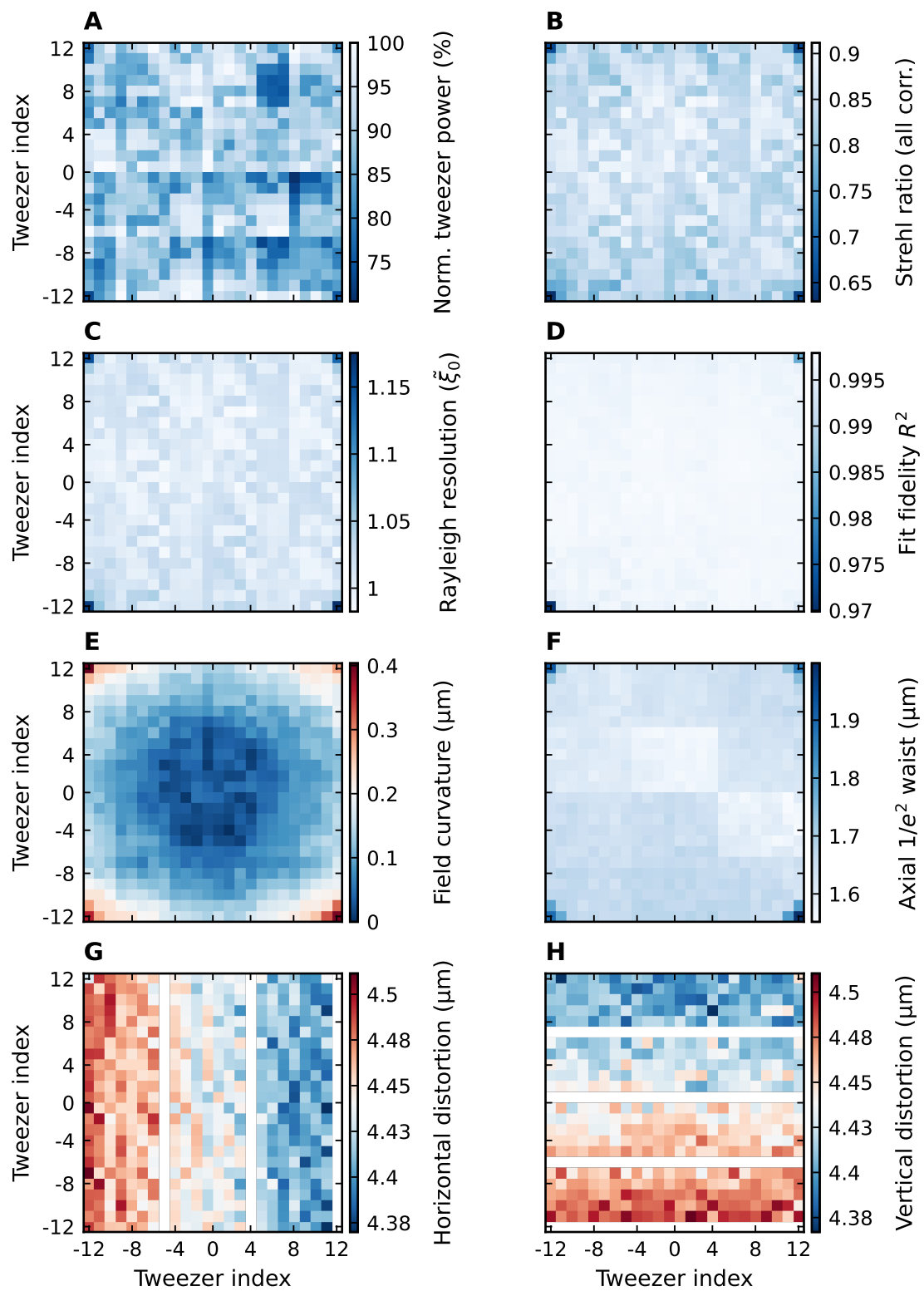


Figure 3.36 – Optical tweezer FOV measurement: analysis heatmaps, backward scan The Figure has the same structure as Figure 3.35.

Figure 3.37 shows histograms quantifying the plot more effectively. Both forward and backward scans are shown in one figure, respectively as blue and orange bars, and the four tweezers in the corners were excluded from analysis to allow for a clearer visualization that is less skewed by Nikon imaging effects. In A we find that the power fluctuations lie indeed mostly between 80 and 100 %, and that both recorded foci agree quite well. The latter is true as well for the Strehl ratios in B. We also see that the Strehl ratios are nicely distributed between 0.8 and 0.9, with a small tail towards 0.75 mostly due to the eight remaining edge tweezers. The resolution histogram in C is even narrower, only ranging from about 0.99 to 1.03 ξ_0 , showing that, compared to the Strehl ratio, the resolution is a rather insensitive measure that is robust in the presence of weak aberrations. In D, the outliers are the most striking feature having R^2 values very far from the central tweezers peak. The field curvature histogram in E, exhibits a smooth tail corresponding to the greater distances from FOV center. Also for this plot, both foci appear to agree very well within the fluctuations. This is not the case for F, which is the only histogram where the two scan directions notably differ. In theory, the picomotor step size calibration should counteract any differences in the axial size measurements, however, there might still be a residual error of about 10% arising from non-ideal step size reproducibility of the mount. In other words, the step size in this particular measurement series was different from the step size which was measured during the interferometric calibration. The individual single tweezer focus scans shown in Figure 3.28 also show this discrepancy. A mismatch of the same magnitude in E can be observed upon close inspection, although it is harder to spot due to the overall larger distribution. Finally, G and H show histograms that are in accordance with the linear trend observed in the previous Figure, visible by the plateau region in the center. The overall magnitude of the tweezer position deviations is apparent in these plots and reads 0.1 μm .

The accurate centering within the FOVs of both objectives motivates interpreting the results as a function of the radial coordinate. Such azimuth averages were computed for the first six quantities of interest shown in Figure 3.38, where again the four outermost tweezers are excluded. In subplot A, we find no correlation between brightness fluctuations and radial distance. However, the Strehl ratio in subplot B shows a curvature towards larger radii which, apart from the fluctuations, does look like a second or fourth order polynomial. Note that for this plot, as well as for the next subfigures, the last data point is already affected by the Nikon imaging FOV and should therefore not be interpreted as a feature of the FOV properties from the SQM objective. While the average Strehl ratios in subplot B are located within an 0.80 to 0.88 interval, the tweezer size is much more homogeneous within the FOV as suspected from the previous plots. In subplot C, the resolution lies between 1.00 and 1.02, and slightly rises towards the FOV edges. The fit quality in subplot D displays a similar trend, dropping fit fidelity towards larger radii, which is caused by the enhanced side lobe observed in the full FOV Figure 3.34. The eight tweezers affected by the Nikon FOV contributed to a fit fidelity significantly worse than the others. Such discontinuity in R^2 also represents a way to identify tweezers affected by the imaging process. Plots A, B, C and D all show a strong similarity between both scan directions

as, overall, the curves lie on top of each other and the irregularities also show mostly the same trend. This hints towards sub-structures arising due to physical differences in the tweezers, instead of purely stochastic measurement or tweezer noise, where we would not expect any correlation between the foci. The field curvature in subfigure E appears much smoother compared to the other plots and resembles a parabola. Comparing both scans, we notice slight opposite sign differences in the center and towards the outer region of the FOV. Altogether, this leads to a larger field curvature for the forward direction than for the backward, which is on the order of 10%, and agrees with the axial scaling mismatch observed in F for the axial waist. While there is only a minute FOV effect for the axial tweezer size of a few percent, the focus discrepancy and the Nikon FOV impact are much more significant.

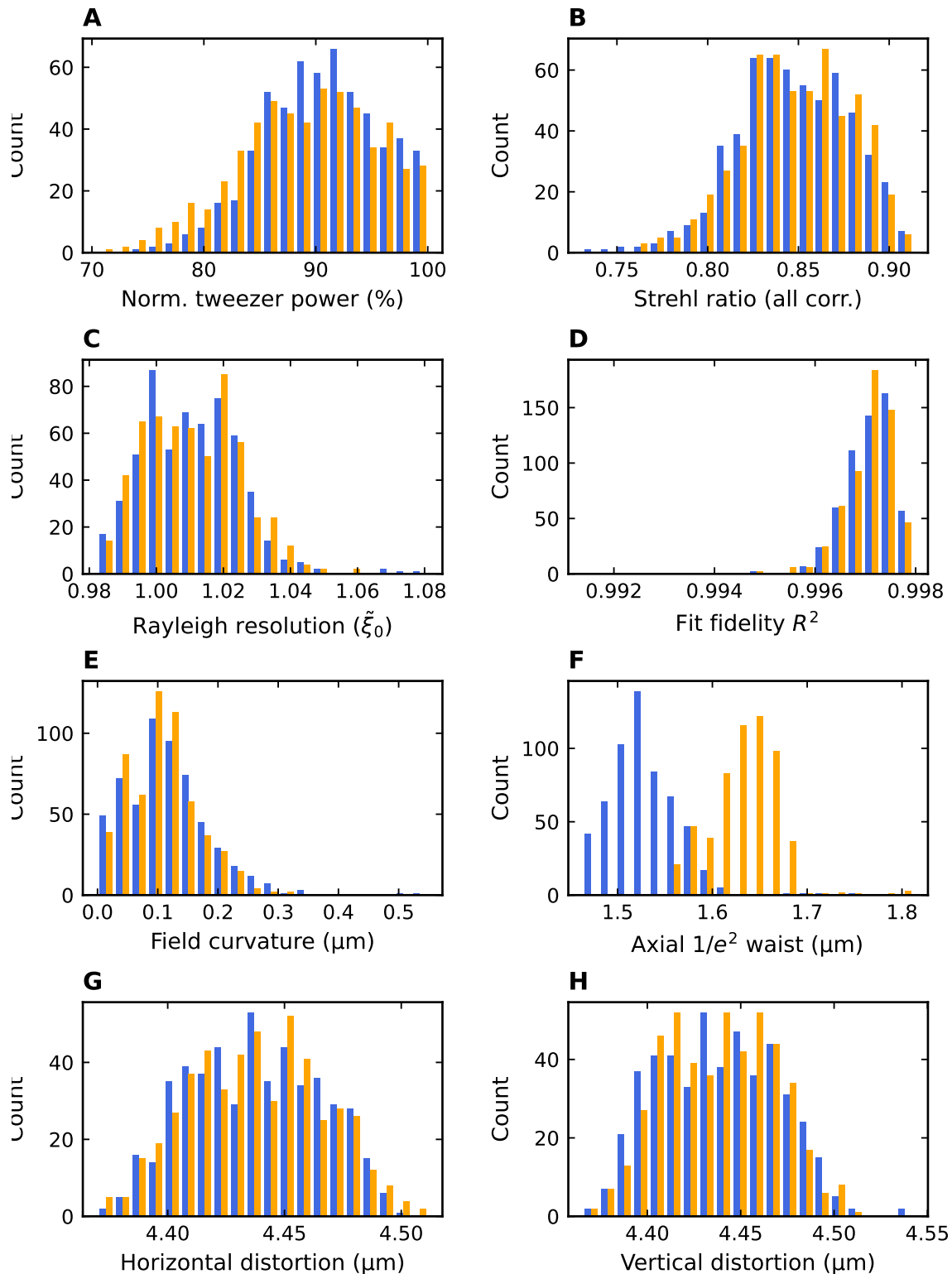


Figure 3.37 – Optical tweezer FOV measurement: histograms The FOV analysis results shown in Figures 3.35 and 3.36 are visualized in histograms displaying the forward scan (blue) and the backward scan (orange). Note that the four corner tweezers were excluded as they were deteriorated strongly by the Nikon FOV edge. The remaining eight outermost tweezers were included in the histograms, but are also affected by the Nikon FOV boundary.

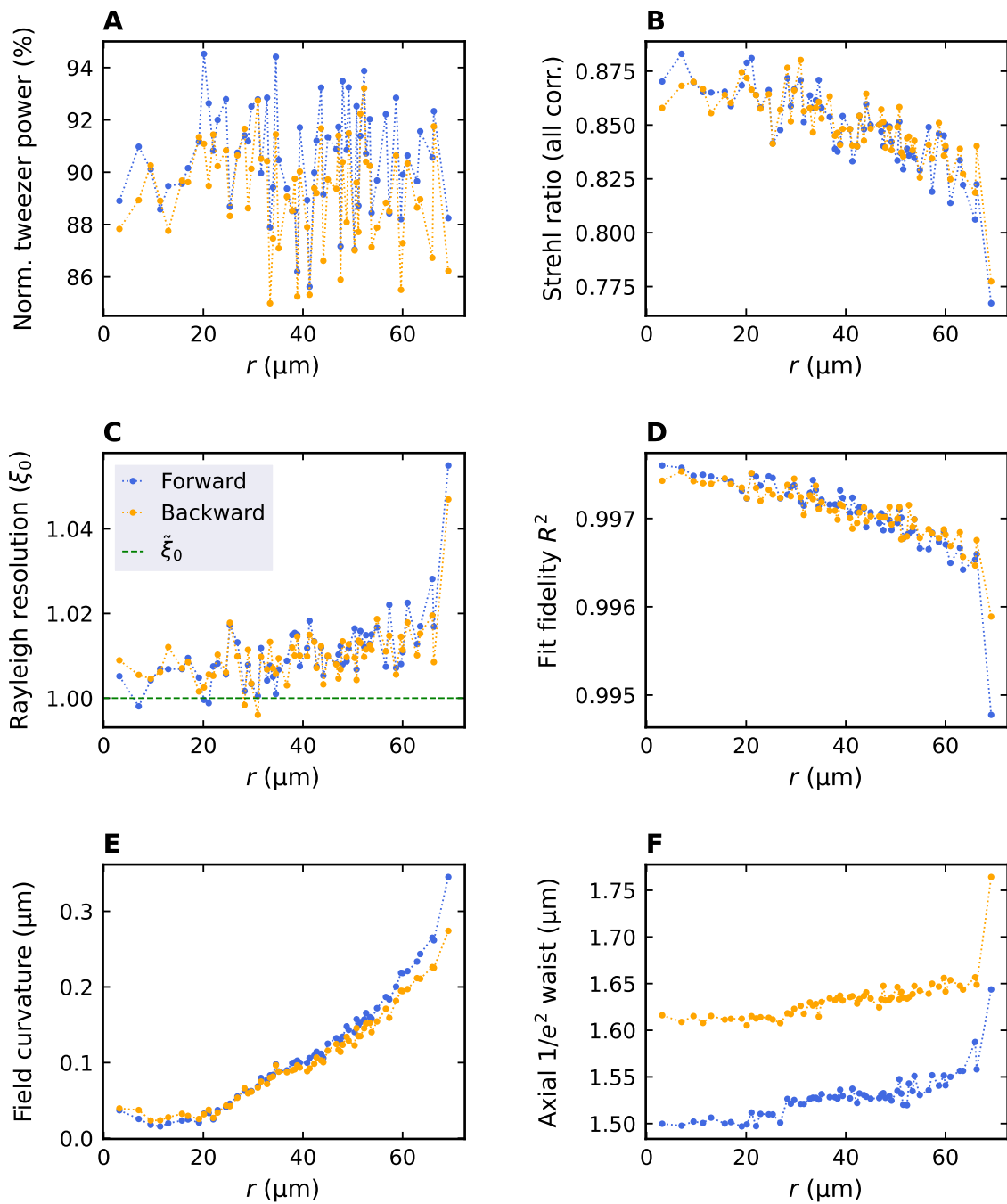


Figure 3.38 – Optical tweezer FOV measurement: azimuth averages The FOV analysis results are grouped as a function of radial distance to the FOV center. These azimuth averages are only shown for the quantities displayed in subplots A to F from Figure 3.37. Both foci are included in this visualization, where blue corresponds to the forward and orange to the backward scan. As for Figure 3.37, the 4 corner tweezers were excluded. The last data point is also affected by the Nikon FOV, but was not removed.

3.3.6 Tweezer statistics and correlations

In this Section, we will take a closer look at statistical fluctuations of individual tweezers, the correlation between tweezer brightness and bit-depth of the camera on the Strehl ratio, as well as the relation between Strehl ratio and tweezer size.

Different measurements are analyzed in Figure 3.39, they all display the Strehl ratio as a function of the "effective bit-depth" of the sensor. In this context, effective bit-depth refers to the dynamic range of the camera that is used. It can be reduced by artificially reducing the bit-depth in the camera settings or via attenuation of the light impinging on the sensor. Both approaches were used and are visualized in the Figure. Finally, the tweezer FOV measurement is also displayed, correlating the power of each tweezer with its Strehl ratio. All measurements used the same camera that offers a bit-depth of 12, which corresponds to a maximum count of 4095.

On the left side of the figure, a single-tweezer measurement series using the FOV setup was acquired, gradually decreasing the camera exposure from 3 to 0.4 milliseconds, to imitate the effect of a weaker laser beam. Attenuating the laser beam itself was decided against, since the precision of the available attenuation wheel and wave-plates was not high enough. This is not an issue, since effects that were to be tested are based on data acquisition and analysis, instead of actual laser power induced nonlinearities, and the laser power in the setup was always less than 2 mW. The plot shows the Strehl ratio, with the basic and the more advanced correction steps, as a function of the maximum tweezer intensity referenced to a green background indicating diffraction-limited operation. From this plot, we identify two main behaviours of interest. First, the Strehl ratio only changes noticeably for very low intensities, below 300 counts, which experimentally indicates that there is effectively no effect on the observed SR for changing brightness compared to overall fluctuations. Apart from that, the same tweezer was imaged several times without any changes in the setup over a total duration of 80 minutes. The information we obtained on statistical fluctuations and its differences between forward and backward scans are depicted in the plot as diamonds and squares, respectively. For the same focus scan direction, the fluctuations appeared to be on a 0.01 to 0.02 level, while between the forward and backward directions, a significant systematic difference of up to 0.04 Strehl ratio was observed. The reason for this difference remains so far unclear. However, both focus scans being valid and separate measurements of the same tweezer justifies restricting to the better measurement when characterizing the tweezer quality.

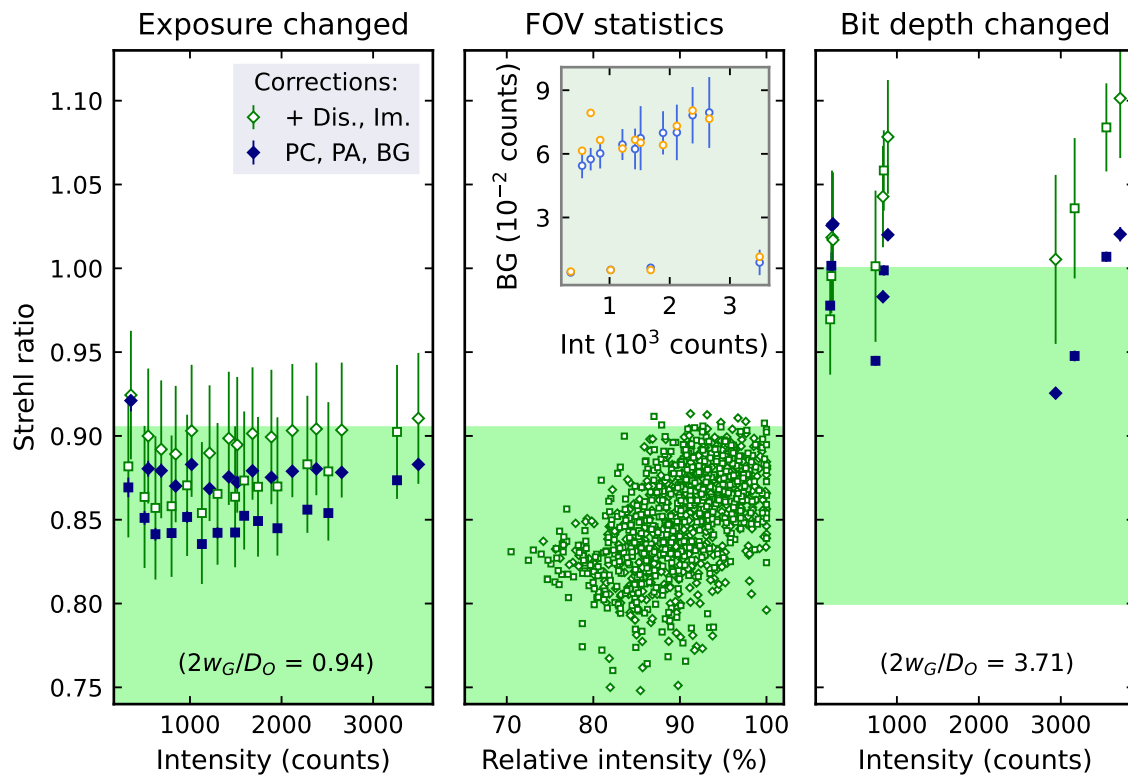


Figure 3.39 – Investigations on the correlation between tweezer Strehl ratio and power. The leftmost plot contains measurements where the same single optical tweezer is imaged for different exposure times of the camera, displaying the corresponding Strehl ratio as a function of maximum tweezer intensity with both few and all corrections steps applied. The green background corresponds to the diffraction-limited region, and the diamond and square markers distinguish between forward and backward scans. The center plot shows the correlation of Strehl ratio (all corrections) with tweezer power for all tweezers from the FOV measurement for both scan directions. The inset depicts the estimated measurement background as a function of tweezer brightness of in the left plot, calculated with a sophisticated (blue) and a simple (orange) algorithm. Finally, the rightmost plot is similar to the leftmost, but it includes six measurements using three different camera bit-depth settings.

The FOV measurement is again displayed in the center plot, this time to correlate the individual tweezer brightness with its Strehl ratio. More specifically, tweezer brightness refers to the tweezer power in a small analysis ROI relative to the other tweezers in a 6×8 measurement. All 576 tweezers are shown, including both scan directions as diamonds and squares. We find a clear correlation between relative intensity and Strehl ratio. Nevertheless, the distribution around that correlation is quite broad, indicating that there are still other parameters involved that contribute to the SR and brightness. The inset shows a background analysis of the measurement in the left column. Here, the calculated average background in 10^{-2} counts is shown as a function of tweezer maximum intensity. The random sampling algorithm and a very simple algorithm, respectively labeled with blue and orange circles, were tested to compute the background. The first is used in all analyses and agrees relatively

well with the simple implementation, while the latter averages the outer regions of an image and shows stronger fluctuations. As expected, the background rises with increasing tweezer power. However, for reasons yet to be known, some images had a nearly vanishing background which also increased with the exposure time.

For the subfigure on the right, a single tweezer was imaged six times using the 8, 10, and 12 bit-depth camera settings in a test setup with different lenses and $2w_G/D_O = 3.71$. All measurements and both scan directions are shown as in the first subfigure. Interestingly, the individual measurements did fluctuate a lot compared to the first column. This may be explained by the measurement conditions, which were worse compared to the first two plots as the setup was rebuilt with different optics and without the custom-built mounts, also making it challenging to extract relevant information. Nevertheless, we find a slight increase in observed SR for the lower bit-depth while at the same time the discretization compensation strongly reduces the SR in the green points.

To conclude, there exists a correlation between Strehl ratio and tweezer power which is not related to data acquisition and analysis errors as shown in the first plot. Most likely, this correlation is neither caused by the brightness, nor by the Strehl ratio but because of the tweezer quality in the first place. This would presumably suggest the causal connection between a high-quality tweezer that is usually strongly peaked and thus brighter than other tweezers, leading to a simultaneously higher Strehl ratio. But since the 2D arrays are not entirely homogeneous, the brightness fluctuations caused by the AOD will randomly affect the power of different tweezers and cause a broadening of the distribution.

Continuing with further analyses, we also investigated the correlation of the calculated Strehl ratio with the fitted tweezer size ξ . The result in Figure 3.40 shows the Strehl ratio using all corrections as a function of corresponding Airy fit size ξ for all tweezers from both scan directions of the FOV test. The green background indicates the diffraction-limited region. We observe a very narrow correlation that lies on a straight line, which was fitted to obtain the approximate linear relationship: $SR = -2.1\xi + 2.97$.

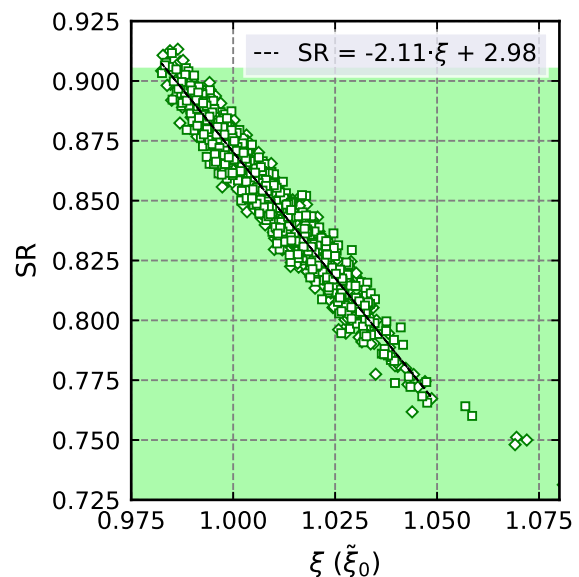


Figure 3.40 - Correlation between tweezer Strehl ratio and resolution. For every tweezer in the FOV test, the forward and backward scans are represented as diamonds and squares. The fully corrected Strehl ratio is plotted and linearly-fitted as a function of fitted tweezer resolution, and the green background corresponds to the diffraction-limited area.

3.3.7 Angle alignment sensitivity

In this section, we discuss the alignment sensitivity of different optics based on systematic test measurements that monitor the tweezer quality. To this end, single tweezers and 2D tweezer arrays were created and imaged for different misalignment severity of three optics. The optics tested include the 100 mm lens L3, the 1000 mm lens L4, and the glass window. The tip and tilt degrees of freedom were changed in order to systematically test misalignments, starting from the well-aligned case, by marking positions on the adjustment screws of the mounts and using known revelation-to-tilt calibrations.

To begin L3 and L4 were tested in the main 2D tweezer array setup by creating the usual 6x8 arrays at FOV positions 8 and 12 in order to distinguish its center and edge effects. The results for the 100 mm lens #3 are summarized in Figure 3.41 and similarly to Figure 3.38 it also shows azimuth averages of the measurements. Although in this case the measurements only include quadrant 8 and 12 (see Table 3.10), which is visible by the small gap in the radial distributions. Different color-coded turning angles of the lens are plotted on top of each other. In subfigure B, a colorbar connects the data point colors with the turning angle of the lens, ranging up to 60 milliradians. To better understand what is happening while turning, the two insets in C and D display the very corner of measurement patch 12 for 0 and 60 milliradian turning in logarithmic scale.

While we do not see any deterioration of the tweezer quality around the Nikon FOV center, a clear effect at the edge of the it is visible that is visible in nearly every subplot. The only quantity appearing rather insensitive to optics tilt is the field curvature. This behavior is also observed in the insets, where the tweezers in the corner become even more elongated and stretched towards the FOV center. The curves also appear noisier than the original FOV azimuth average plot, as two out of twelve measurements provide much less data points to average out stochastic fluctuations.

Moving on to the alignment sensitivity analysis of the 1 m lens, the results are depicted in Figure 3.42. This test only included region 12, the corner of the accessible FOV, since the optics proved insensitive around the FOV center in the previous measurement. In this case, we find a strong impact from tilting the lens by angles much smaller than 60 mrad. While the outermost tweezers are already sensitive to misalignments of 10 mrad, even the tweezers lying well inside the FOV were greatly affected by tilts exceeding 35 mrad. This behavior can be observed from the Strehl ratio, tweezer resolution, fit fidelity and the axial waist, whereas the field curvature is again fairly insensitive. Remarkably, there appears to be no radial dependence of the tilt susceptibility, and all tweezers lying far enough from the edge of the FOV are equally affected. As expected from the geometrical projection, the main aberration seems to be astigmatism, as visible in the insets of D.

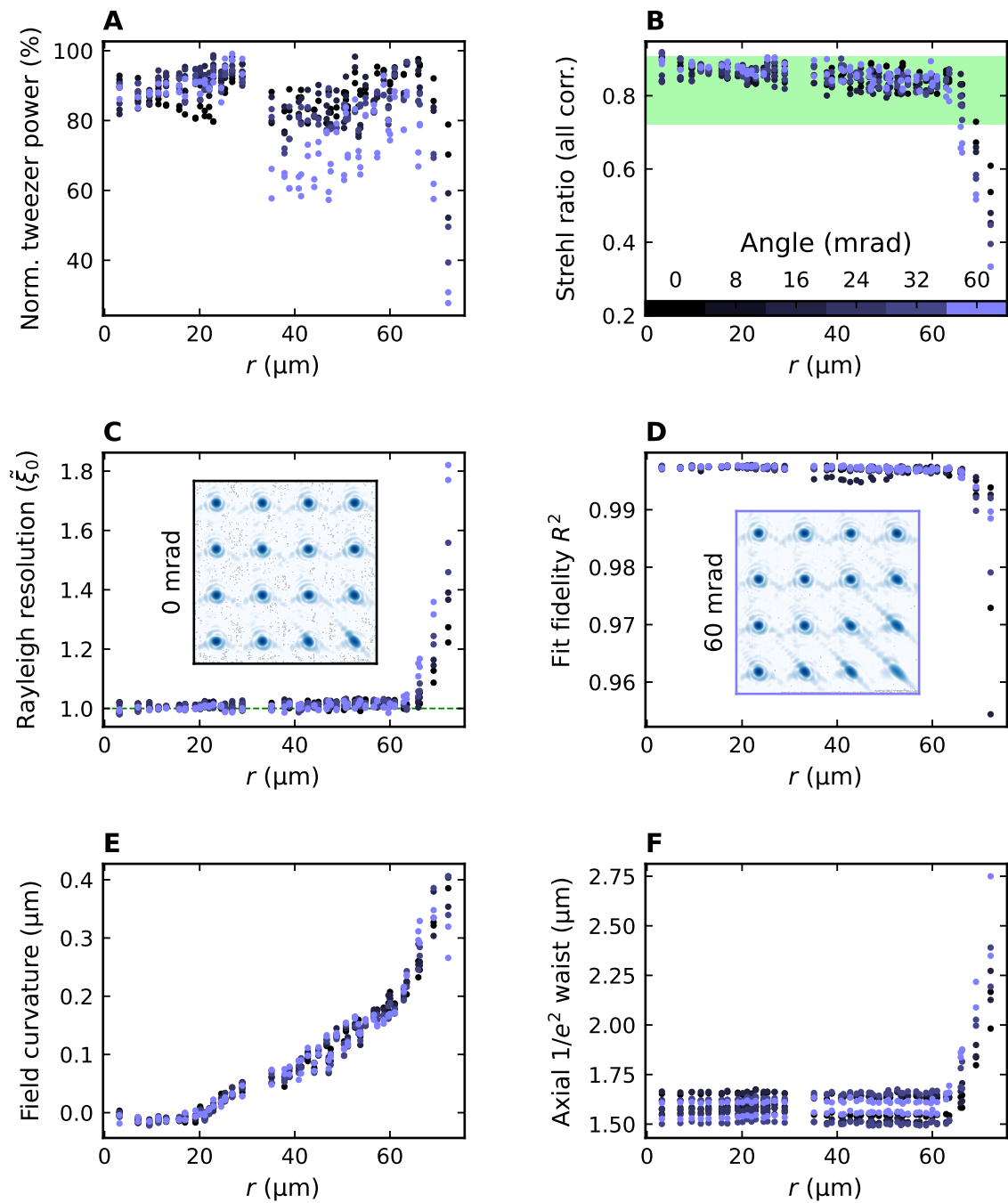


Figure 3.41 – Alignment sensitivity test: 100 mm lens #3. This Figure shows 6x8 2D tweezer array measurements at two positions in the FOV (8 and 12, see Table 3.10) for a variety of tilt angles of the 100 mm lens #3. It is similar in overall layout to Figure 3.38, but with a color-coded tilt angle explained via the colorbar in B, as well as the two insets, displaying example images in logarithmic scale, from the 0 and 60 mrad tilt measurements at the boundary of the FOV.

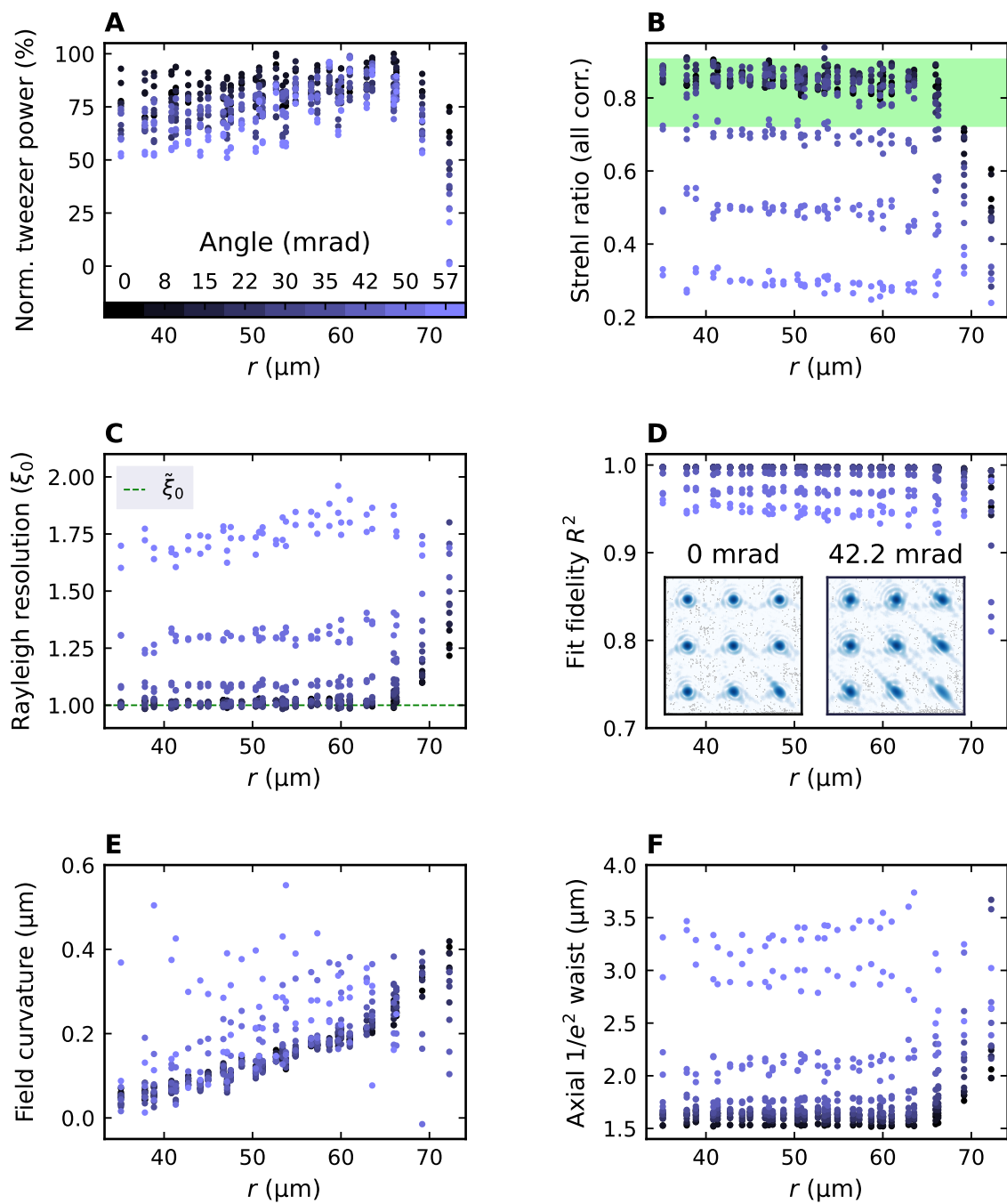


Figure 3.42 – Alignment sensitivity test: 1 m lens. The Figure has the same structure as Figure 3.41, but only position 12 in the FOV was tested.

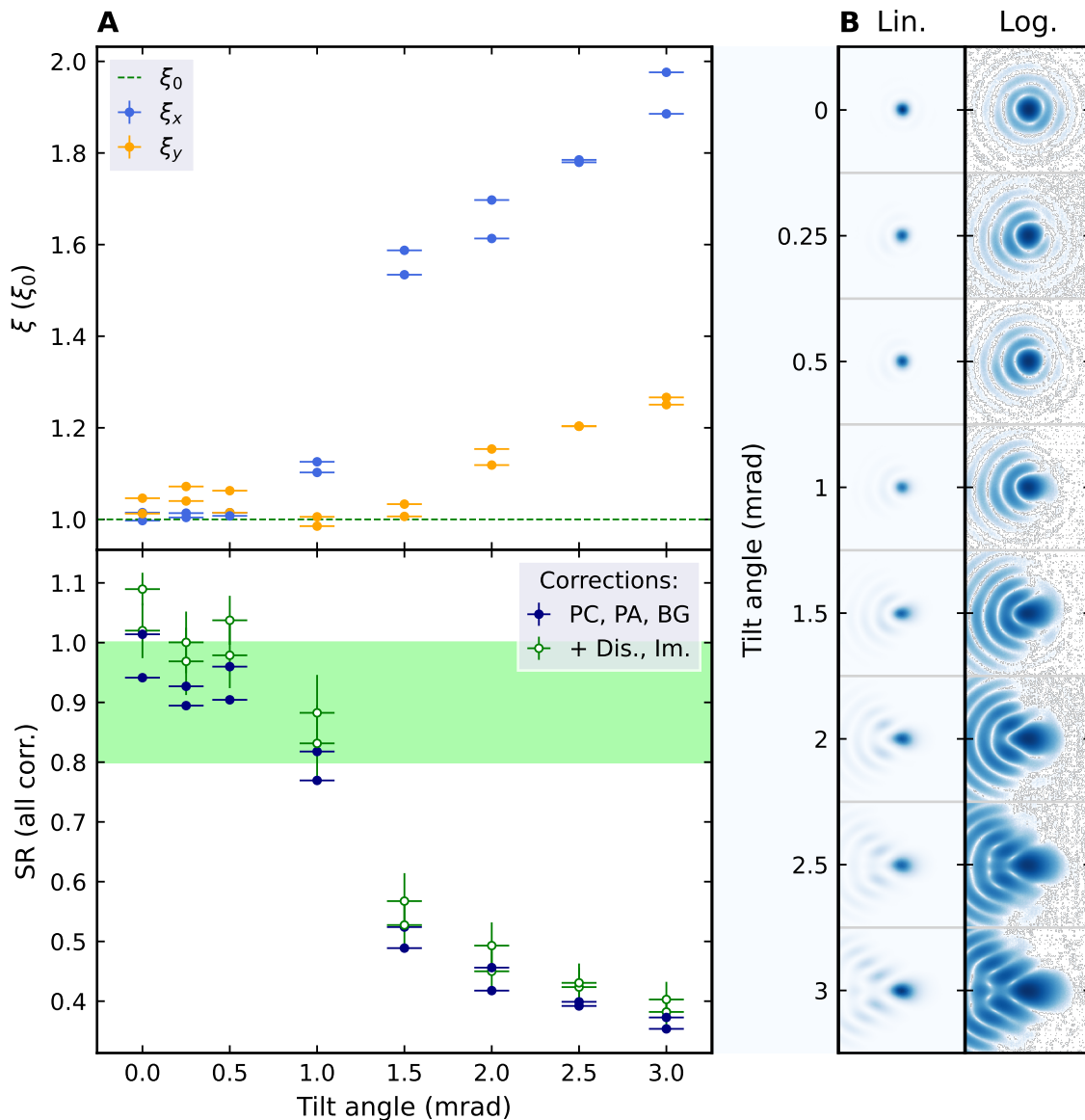


Figure 3.43 – Alignment sensitivity test: glass window. This Figure illustrates the impact of glass window tilt on the observed tweezer quality. In subfigure **A**, the x and y resolution and Strehl ratio with two different types of correction sets are plotted as a function of tilt angle. For comparison with the tweezer shape, part **B** displays the best-SR tweezer image in linear and logarithmic scale for every tilt angle.

Finally, the impact of tilting the glass window, for which our custom objectives are corrected for, is tested. A single optical tweezer was generated, without AODs and 1:1 telescope in the beam path. To avoid being limited by the Gaussian envelope, two telescopes are combined to magnify the tweezer beams from a width of 1.3 mm to 130 mm, leading to a relative beam size of $2w_G/D_O = 3.71$. The results are summarized in Figure 3.43. Subfigure **A** shows the observables tweezer size ξ (ξ_0) and the Strehl ratio with two correction sets, for back and forth scan directions, as a function of window tilt angle. It is clear that this is the highest sensitivity element in the setup,

since the Strehl ratio drops significantly for a misalignment of only 1 mrad and the resolution in the y-direction rapidly increases. In B, we find linear and logarithmic scale images of the best-Strehl ratio picture for all tilt angles. The tweezers suffer from severe coma for tilt angles larger than 0.5 mrad, where in addition to the emerging side-lobes, the horizontal size increases strongly whilst, the vertical is less affected by the coma. In case the actual tweezer shape is of particular relevance, one already observes asymmetric diffraction rings for tilt angles as small as 0.25 mrad.

3.3.8 Impact of different optics in transmission

In the main experiment, the tweezer beams need to pass at 45° through a non-polarizing beam splitter²¹ (NPBS) and a dichroic mirror²² (DC). To quantify the aberrations introduced by these types of optical elements, a NPBS and DC were selected from a variety of identical elements. Both were glued by one corner in order to minimize strain from the curing glue, the dichroic with UV glue, and tested in the optical test setup (see Figure 3.44). While they were chosen based on the best performance in Zygo surface flatness measurements, it is still necessary to characterize the magnitude and type of aberrations that can be expected when passing the tweezer beams through the optics. Note that here, the optics were centered as well as possible on the optical axis and rotated so as to have an incidence angle of 45° with respect to the incoming tweezer beams. While a transverse beam displacement by the optics should be negligible, e.g. 1-2 mm compared to the 33 mm Gaussian beam width, a slight horizontal displacement of the tweezers was observed with both optics. The shift was on the order of $4\ \mu\text{m}$, or one tweezer spacing, and attempts at compensating it were not made.

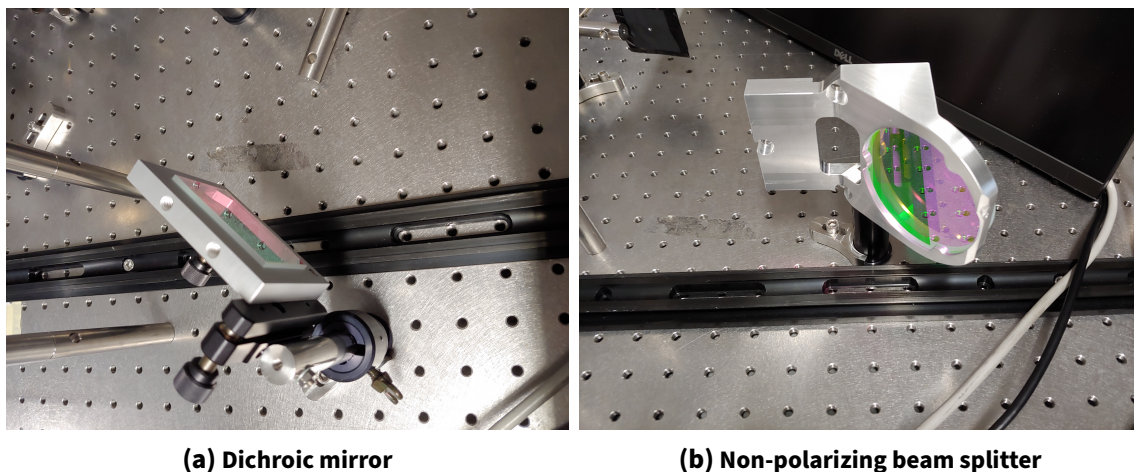


Figure 3.44 – Optical elements tested in the 2D tweezer array setup. The pictures show the dichroic mirror on the left and on the right the non-polarizing beam splitter.

²¹UFI $\varnothing 3'' \times 12.7\ \text{mm}$

²²Optoman 60x40x7 mm

For the test measurements, 6x8 tweezer arrays were generated in two areas in the FOV; in the region 3 and at the central 6 rows of the combined areas 5 and 8 (compare Table 3.10 for orientation). This allows us to investigate changes to the tweezers symmetrically around the FOV center and at the corner. The resulting radial plots for all observables are shown in Figure 3.45, where both focus scan directions are plotted as diamonds and squares, and the DC and NPBS measurements are compared to a reference measurement, without the test optics in place. For the reference measurement, only the forward scan was successfully recorded. The tweezer lying furthest from the FOV center was excluded from analysis, as it is mostly affected by the limited Nikon FOV. In the center regions there are no significant differences visible between the three cases. Followed by the NPBS, the DC performs the worst according to the resolution and Strehl. However, this order swaps when inspecting the edge of the FOV, where the NPBS starts to have worse tweezer quality and the dichroic similar tweezers as the reference measurement. The insets, showing the 9 outermost tweezers, might be misleading, since the most stretched tweezer is found in the reference measurements instead of in those involving the test optics. This apparent benefit to the tweezer quality comes from the horizontal tweezer shift, described in the previous paragraph, which reduces the impact of the Nikon FOV in the case of thicker optics. That also explains why the NPBS looks even better than the dichroic just judging from the extreme tweezer image. In fact, when viewing the tweezers lying inwards, the NPBS tweezers look much more deformed than those of the reference measurement.

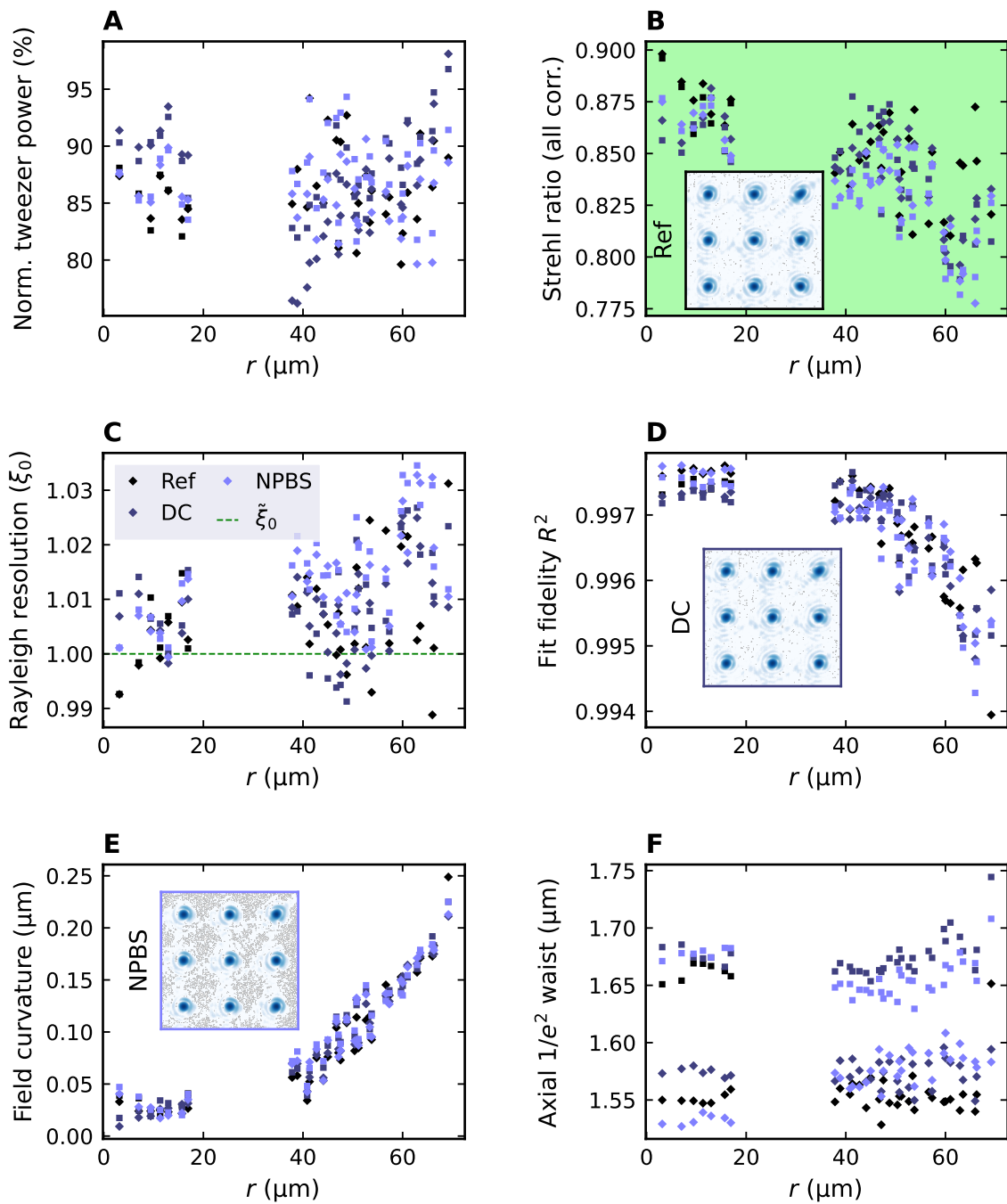


Figure 3.45 – Tweezer arrays in the FOV with optical test elements in transmission. In this Figure, the impact on the tweezer quality of transmitting the tweezer beams through a dichroic mirror (DC) and non-polarizing beam splitter (NPBS) is investigated. The individual elements are tested compared against a reference measurement. The analysis results are shown in a similar fashion as in Figure 3.41 while the diamond and square markers distinguish the scan directions.

3.3.9 Impact of the imaging FOV limit

As observed in all previous tweezer FOV tests, the 4 to 12 outermost tweezers were disproportionately worse than the surrounding ones. This effect was found to be caused by the edge of the Nikon imaging FOV. Within the center of the FOV, commercial high-NA objectives like the one we used exhibit minimal field curvature and barely any changes to the PSF as observed in the short FOV test in Figure 3.23. However, when the regime is approached where the imaging quality drops, commercial objectives tend to use a hard-aperture that enables to physically restrict the observation area to the FOV of the objective. This hard cutoff also explains the rather abrupt change in PSF when tilting and translating the Nikon objective found in the above mentioned Figure.

In Figure 3.46, a systematic test was performed with a 6x8 tweezer array at position 3 in the corner of the SQM FOV. It compares the original all-objectives-on-axis alignment, where the camera was moved to reach the off-axis image, with a measurement where the SQM objective was moved to position the tweezer array in the center of the Nikon FOV. This was accomplished by fixing the camera position to the optical axis and moving the SQM objective until the tweezers that were generated at position 3 appear at the center of the camera image. Note that translating the objective is not an issue here, since the roughly 30 μm displacement is three orders of magnitude smaller than the incoming tweezer beam size. The resulting quantities of interest are plotted as a function of the radial coordinate with insets showing the most extreme tweezers. This time, all tweezers were included in the radial plots and we found that the three outermost tweezers now have a quality that is far better than before, even approaching Strehl ratios and resolution of the inner tweezers. There seems to be a global shift in Strehl ratio and fit quality indicating that there must have been a small impact from the Nikon FOV in all tweezers, not only those at the boundary, of roughly 0.04 SR. The insets also show that the tweezers at the edge now look way more homogeneous than before compensation. Lastly, subfigure F contains another inset which shows a raw, linear-scale and overexposed camera image of the 6x8 array which was moved directly on the border of the Nikon FOV. This image highlights a very abrupt cutoff near the Nikon FOV boundary, where no more tweezers will be formed after the outermost ones.

Overall, this measurement justifies excluding the outermost tweezers from the previous analyses and confirms that our objective will be able to sufficiently generate diffraction-limited optical tweezers, even up to $\sqrt{2}\cdot 50\ \mu\text{m}$ from the center of its FOV.

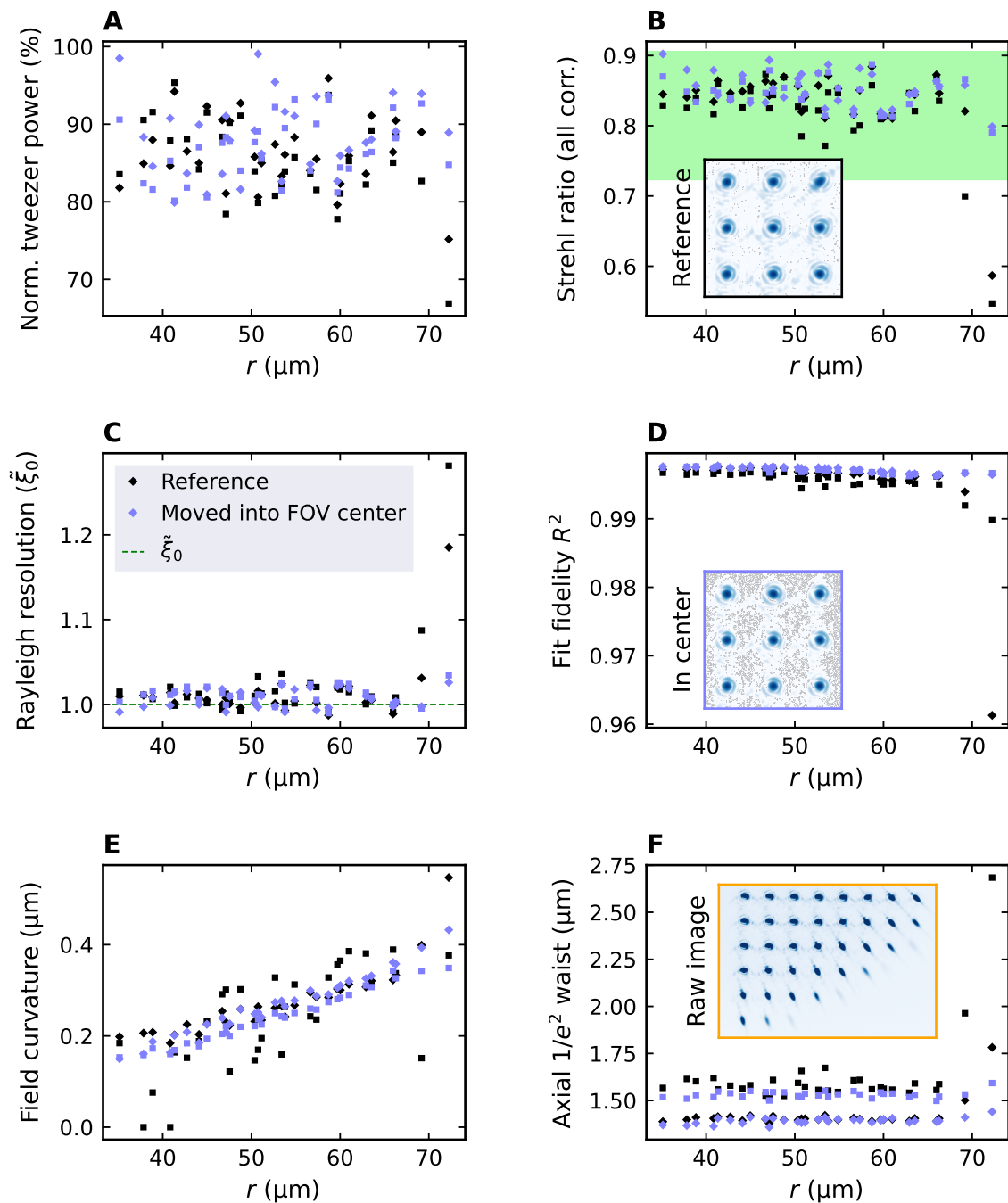


Figure 3.46 – Impact of the imaging FOV limit on the tweezers. The FOV limit impact of the Nikon imaging system on the tweezer quality is shown in this Figure. Two data sets are compared, both showing 6x8 optical tweezer arrays generated at the very edge, position 3, of the SQM objective FOV. The SQM objective was moved in one of the measurements to center the tweezer array on the imaging axis. In addition to the plot structure in Figure 3.41, the inset in F depicts a linear-scale, overexposed image of a 6x8 tweezer array projected right on the Nikon FOV border.

3.4 Integration into the main experiment

After thoroughly testing and characterizing both objectives with respect to their high-resolution imaging and tweezer-generating performance, the tweezer setup was transferred into the main lab to be integrated into the experiment. We carefully selected all (dichroic) mirrors that will face imaging or tweezer beams larger than a centimeter in diameter after several surface characterization measurements with a Zygo interferometer and including results from chapters 3.2.6 and 3.3.8. In addition, the lenses and AODs that were used in the test setup were all carried over and integrated into the main setup. Due to a manufacturing error of our SQM objective 002, it did not fit the custom objective mount that was designed for the experiment. Therefore, we switched to objective 001 for the following measurements, and our main lab in general, even though it performed slightly worse.

This chapter includes the setup in our main experiment, results from the main lab tweezer test setup and the first signal of imaging individual atoms in optical tweezer arrays.

3.4.1 Tweezer array and high resolution imaging setup

The layout of our main experimental table showing the vacuum system, the experimental chamber and all optics that belong to the high-resolution imaging and tweezer array setup are shown in Figure 3.47. This figure is based on a CAD drawing of the whole vacuum setup, depicted in gray, including the atom source, Zeeman slower, 2D MOT and main experimental chamber with the glass cell and magnetic field coils. The outline of the breadboards that offer access to the glass cell and the Zeeman slower are also shown in gray. The main parts relevant for this work are all mounted on the table surface, below the breadboards. The optics are drawn to-scale and so are the laser beams, where blue represents 399 nm imaging light and the green stands for the $\lambda = 532$ nm tweezer beams. All lenses that are displayed are achromats, referenced using their focal length in millimeters.

The first few optical elements are all the same as in the test setup, starting with the fiber outcoupler in the bottom right corner that collimates the 532 nm beam which exits the PCF, we have used the same parts from the optical test setup. Next, there is a half-wave plate followed by a polarizing beam splitter cube (PBS) which are used to attenuate the beam and clean the polarization after the fiber. In the following, a beam sampler (BS) plate reflects a tiny portion of the intensity onto a photodetector for intensity stabilization monitoring. After two more mirrors for alignment, another half-wave plate allows us to match the polarization of the light to the sound wave propagation axis inside the first acousto-optic deflector. As in the test setup, the 1:1 telescope images the center of the first AOD into the second AOD to guarantee that all tweezer beams share the same distance from focus. The third waveplate rotates the light polarization by 90 degrees such that the diffraction efficiency of the second AOD is optimal. The AOD is followed up by a PBS which cleans the polarization once again with the waveplate playing the role of adjusting the transmission through the

cube. The last 100 mm lens then focuses the beam into the first out of two folding mirrors that deflect the beam towards the opposite side of the optical table. During that path, the beam expands before it impinges on the $f = 1$ m lens which collimates the beam again. From this lens, like in the test setup, there is another meter until the first principle plane of the SQM objective that is reached after the beam passes two more 3-inch folding mirrors (Zygo and test setup tested, see Chapter 3.2.6) as well as an dichroic mirror (tested with Zygo and in Chap. 3.3.8). Between the dichroic mirror and the objective, there is another 3-inch broadband mirror (Zygo tested) which has an angle of 45° towards the table surface to reflect the beam upward. After the 45° mirror, the beam travels through the NPBS, that was tested with the Zygo and in Chapter 3.3.8 with the optical test setup, which is needed to shine in the vertical MOT beam, until the tweezer light finally reaches the objective which projects it into the glass cell (compare Figure 2.1).

In case atoms are trapped in the tweezers and resonantly excited with 399 nm light, they will scatter photons that are collected by the objective and sent back the same way where the tweezer beam came from. When impinging on the dichroic however, the light is reflected instead of transmitted and after reflecting off two more 3-inch mirrors (Zygo tested), it is focused onto a scientific camera²³ by a $f = 500$ mm achromat lens, completing the imaging setup.

In addition to those main light pathways, there are two more smaller parts of the setup that need explanation. First, as in the optical test setup, an additional branch enables us to monitor the tweezer beams, before they are demagnified by the 1m lens - SQM objective system. This allows us to perform tweezer intensity balancing algorithms based on this purely optical signal, as well as to check the tweezer array shape and regularity. To this end, the leakage light transmitted through the very first folding mirror is collected by a 3:2 telescope that images the large tweezers, created by the 100 mm lens #3, onto the monitoring camera²⁴. Secondly, to ease aligning the different beams on top of each other, as well as to create a fixed reference for later comparison, an additional 532 nm reference is installed close to the dichroic mirror. Note that the tweezer beam, the reference beam and an additional 399 nm beam from the top of the glass cell that travels towards the camera, are all overlapped (see Table 3.11 for the accuracies).

²³Hamamatsu Photonics, ORCA-Quest qCMOS Camera

²⁴Allied Vision, Alvium 1800 U-240m

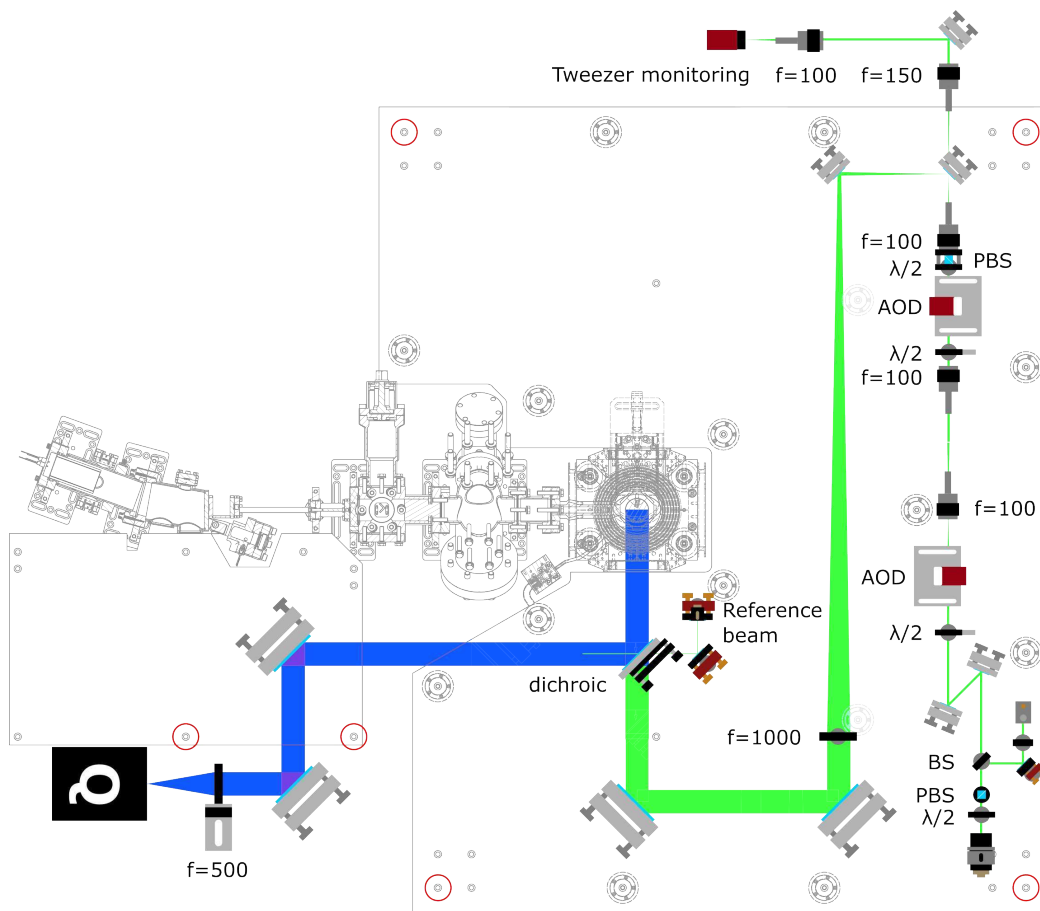


Figure 3.47 – Schematic of the main lab optical tweezer and high-resolution imaging setup.

This figure shows a CAD schematic of the vacuum system of the experiment with to-scale drawings of the approximate positions of all optics on the main experiment table, that are used for the 532 nm 2D optical tweezer arrays and the 399 nm high-resolution imaging. All lenses that are shown are achromats, referenced by their focal length in millimeters.

All axial calibrations from the previous test setup were measured and recreated in the main lab. Note, however, that these well-calibrated distances were determined for objective 002, so it was not clear whether they would also work for objective 001. In fact, the 1 m lens position had to be adjusted by a few centimeters following the results from the test measurements in the main lab that showed significant spherical aberrations in the beginning. The alignment strategy of the tweezer beam setup mostly remained the same as described in detail in Appendix B. Nevertheless, due to limited access to the relevant optics and restricted viewing possibilities on the detector cards, the alignment quality was lower compared to the previous test setup.

3.4.2 Tweezer test setup results

We built another optical test setup in the main lab, to characterize the tweezer quality in the (almost) final setup and to test the final alignment strategies. To this end, the high-resolution tweezer imaging path was rebuilt with the Nikon objective and SQM objective 001. To integrate this setup on the main table, the optical tweezer beams were picked off with two additional 2-inch broadband mirrors right before the dichroic mirror (compare Figure 3.47). We can compare the new test conditions to the tweezer test setup used in the previous chapter, as well as the final setup anticipated in the main experiment. Beginning with the original optical test setup we find the following differences (compare to Section 3.4.1):

1. The AODs are mounted on different holders that are rotated about the optical axis to match the horizontal optical lattice directions.
2. The 1:1 telescope as well as the 100 mm lens #3 are placed on custom lens mounts that only offer an axial translation stage to reduce the number of degrees of freedom. On the other hand, this made accurate alignment much more challenging.
3. After the 100 mm lens #3, two folding mirrors are placed. The first is positioned in focus and its leakage light is used to tweezer monitoring.
4. The 1 m lens is mounted without any accessible degrees of freedom after clamping. As a result, accurate alignment of this lens was much more challenging.
5. The overall alignment of all parts was less accurate, since due to the different breadboards, pillars and other elements on the main table, accessing the optics and also observing relevant back reflections was harder.
6. There are two (final) 3-inch broadband mirrors used to fold the beam that were not present in the previous setup (except the astigmatism tests). Furthermore, two 2-inch mirrors were added that redirect the beam into the test setup.
7. The tweezer imaging setup did not consist of an auxiliary camera for transverse alignment, such that that the Nikon imaging might have slightly worse alignment.
8. The alignment strategy of the SQM objective was different, which is described in more detail in the following.

There were also a few differences to the final tweezer setup on the main table. Among those are:

1. The two 2" mirrors needed to redirect the beam into the test setup. This could lead to an overestimate of the expected astigmatism of the optical tweezers, as all 6 mirrors from the 100 mm lens #3 up to the objective all reflect in the same (horizontal) plane.

2. The SQM objective test setup mount is used (see Appendix D) instead of the custom mount from the final configuration. This way, the objective was more susceptible to slow drifts after initial alignment that presumably affected alignment fidelity as discussed later.
3. The glass window in front of the SQM objective for testing is identical in terms of specifications (apart from not being AR coated) but is physically different from the window on the bottom of the glass cell. Because of this, the spherical aberration compensation in the atom measurements could be slightly off.
4. Effects of transmission through the NPBS and the dichroic mirror, as well as the reflection of the 45° mirror that sends the beam towards the glass cell from below, are not tested. Nevertheless, the NPBS, dichroic and 45° mirror were all extensively tested and performed reasonably well. In case the dichroic and 45° mirrors cause astigmatism, due to the orientation of their plane of reflection, it does not necessarily need to add up with existing astigmatism, but it can possibly also partially cancel it.
5. There is no high-resolution optical tweezer imaging in the final configuration.

Since the alignment in the final configuration does not offer access to the same signals and parameters that the previous proof-of-performance tests offered, different optical alignment approaches were used. Most notably, first, the transverse alignment of the objective with the transmission of a reference beam will not be as accurate as viewing existing tweezers with a camera and translating the objective accordingly. However, since the MOT has a rather large extent and both the MOT and the objective can be moved quite reproducibly, sub-0.5 mm alignment was not important. An alignment tool was built (see Figure 3.48 part (a)) that enabled centering of the objective entrance pupil on the reference beam with an accuracy of about 1 mm. However, since this transverse objective alignment was way too inaccurate for the magnification of the Nikon imaging setup, for these test measurements the translation was adjusted with the help of the tweezer image on the camera. Second, for the angle alignment the objective itself needs to be tilted, since tip and tilt of the glass cell is of course impossible. Previously, the glass window was always adjusted to precisely remove all coma visible in the tweezers, which was much more accurate than tilting the objective itself, which might be connected to a slight drift of the objective mount after touching the adjustment knobs. Here, we needed to make sure that the objective mount had settled before aligning with the adjustment knobs by optimizing the back reflection overlap with the incident beam (see Figure 3.48 part (b)).

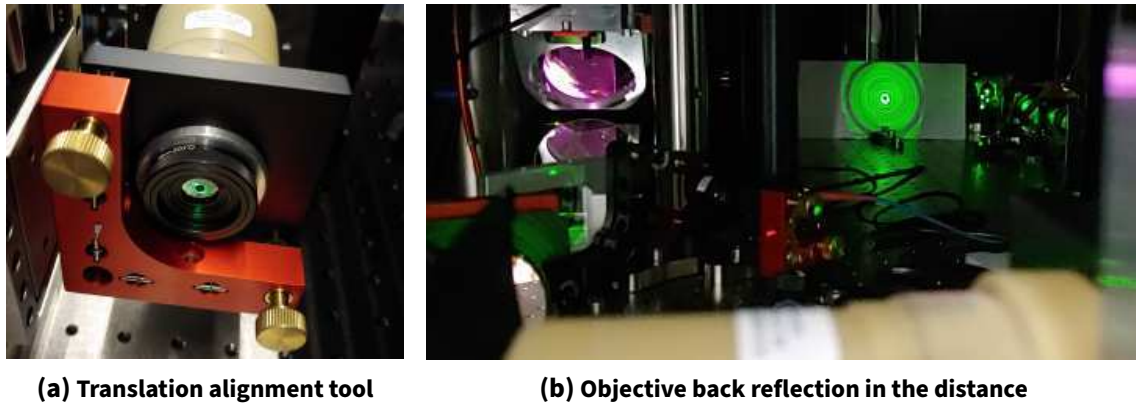


Figure 3.48 – Alignment signals of the main lab tweezer test setup. On the left one finds the alignment tool used for translation alignment that consists of an iris screwed into the objective mount and on the right, for angle alignment the back reflection is observed about two meters in the distance.

An example tweezer that was generated with this main lab test setup is shown in Figure 3.49 with the corresponding analysis in Figure 3.50. In the figure displaying the tweezer shape, we find relatively good axial symmetry which indicates only weak spherical aberrations. The astigmatism is surprisingly low and comparable with the one observed in the original test setup in Figure 3.28. Some coma is also observed in part B that could be the internal coma of the objective, which is not accounted for in the alignment procedure. The axial waist fits also look reasonable with the same discrepancy that was already observed several times in the optical tweezer measurements.

In the analysis figure, we find that the tweezer is still diffraction limited, even though the Strehl ratio is borderline in case the Nikon imaging has not deteriorated the tweezer quality. In addition, in A we observe similar astigmatism as in the previous characterization and close to no indication of coma (like $x - y$ asymmetry in focus). Section B shows overall good quality, apart from the slightly asymmetric fringe in the log-scale image. Since this setup was not perfectly dark, a much stronger background can be observed in part C in the logarithmic scale image. The overall tweezer shape however, does agree well with the simulation.

With the main lab test setup we also calibrated the distance of the optical tweezers for a given RF spacing in 2D array measurements. This is required to provide reference for the spacing of the atom arrays in later fluorescence images.

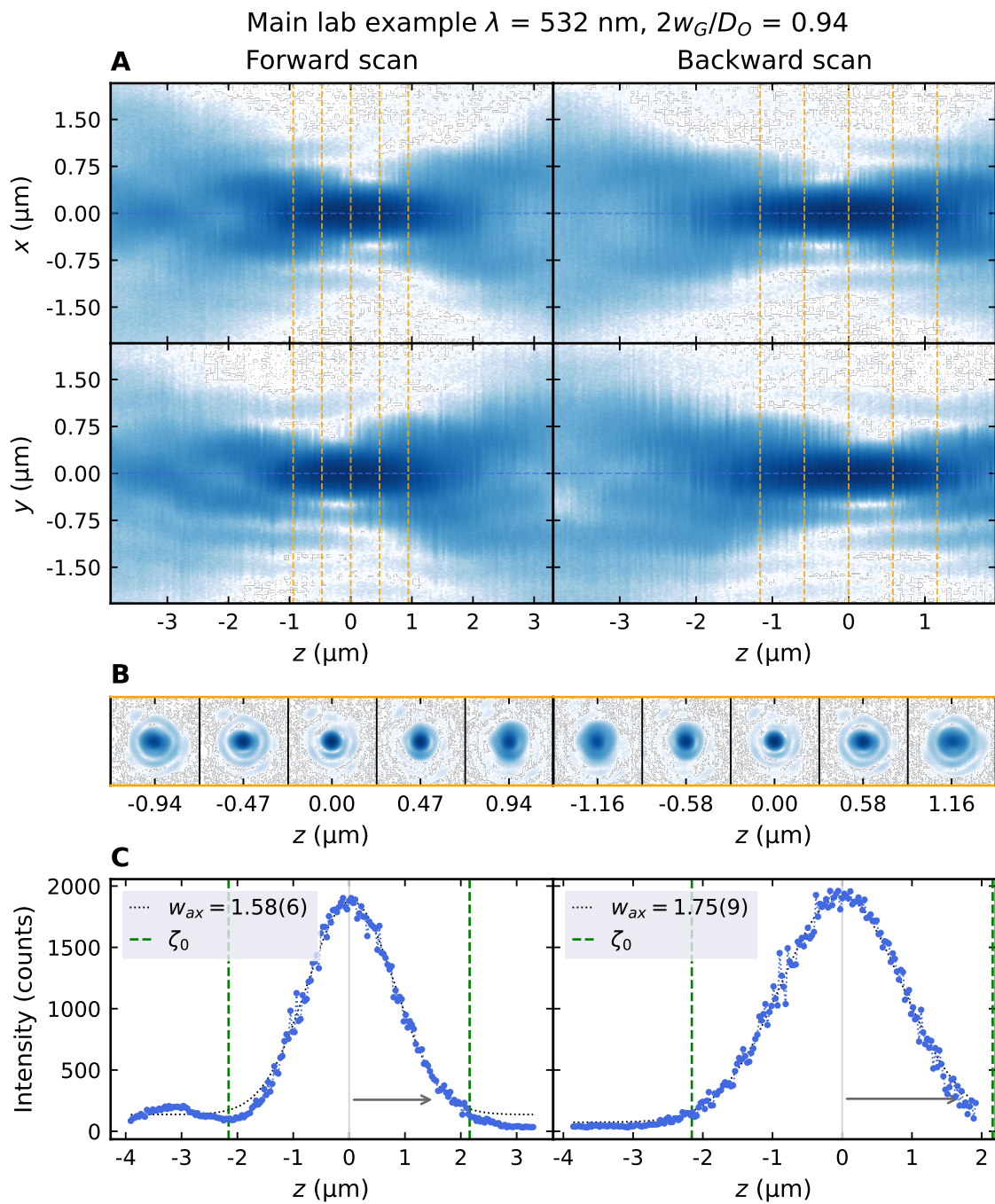


Figure 3.49 – Single tweezer, main lab test setup, objective 001: Tweezer shape. The Figure has the same structure as Figure 3.24.

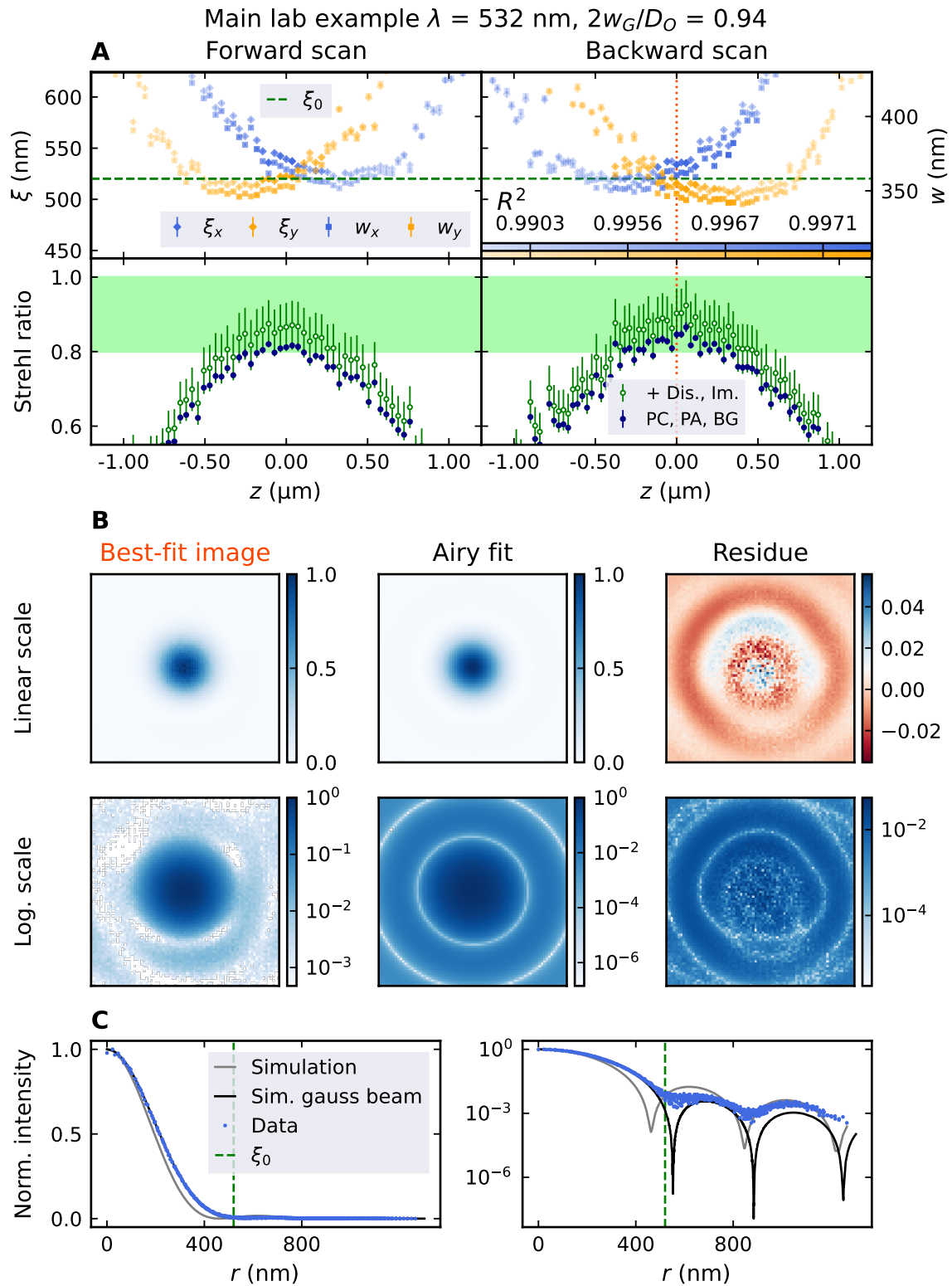


Figure 3.50 - Single tweezer, main lab test setup, objective 001: Tweezer analysis. The Figure has the same structure as Figure 3.25.

To build some intuition on the new alignment sensitivity and the corresponding results, plenty of tweezers have been generated and measured with subsequent mis- and re-alignment of the objective. Providing statistics, the main results of these attempts are presented in Figure 3.51. Overall, it appears to be possible to reliably align the SQM objective only relying on the back reflection and using the test setup mount, to achieve diffraction limited tweezers. Furthermore, the tendency of the coma lobe that is visible for some measurements to be oriented towards the lower right could be a systematic effect that arises from either objective-internal coma, or reproducible drifts of the mount. The latter have definitely been observed when measuring right after mounting the objective and caused the bad images in measurements 1-5. When waiting for several hours and making sure to only exert minimal pressure on the objective mount during alignment, reproducible tweezers with only small coma contributions can be generated.

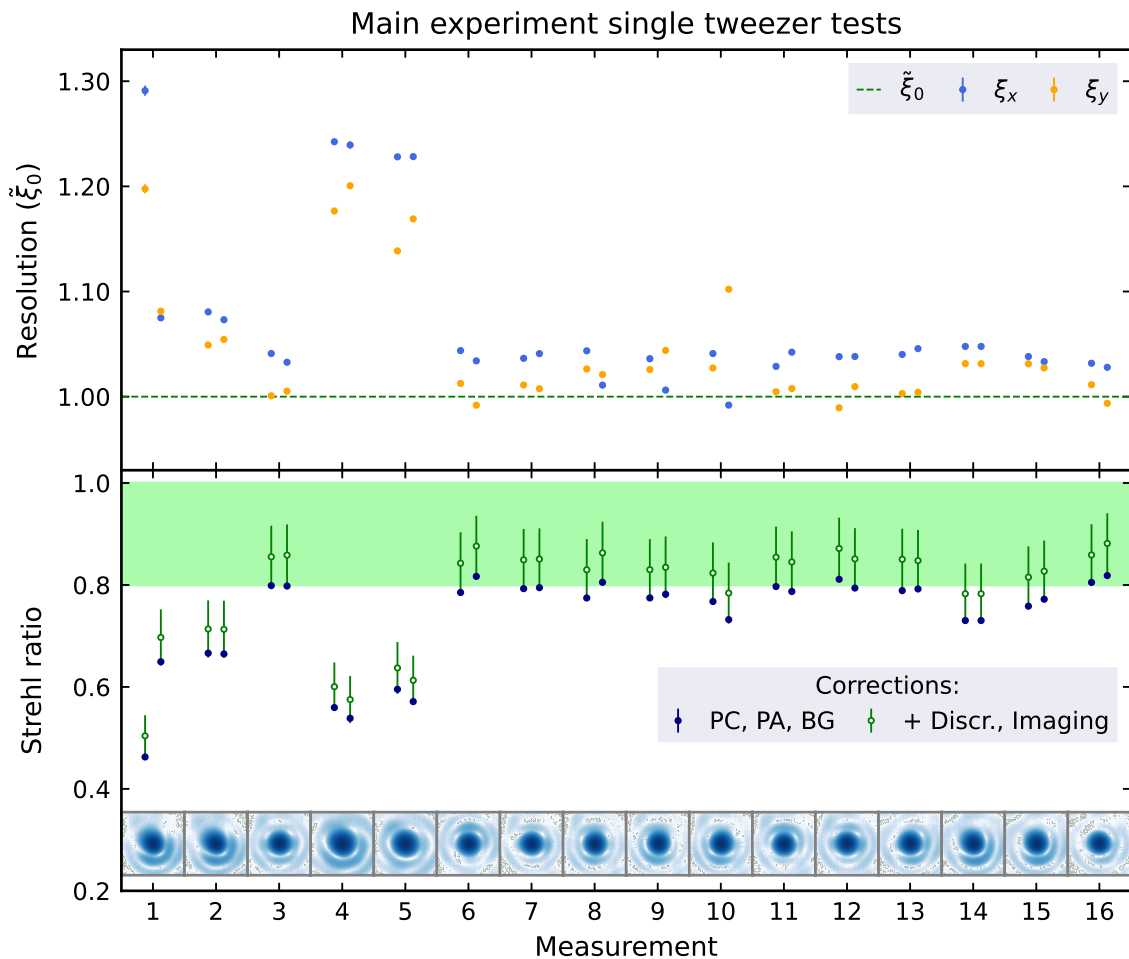


Figure 3.51 – Single tweezer alignment statistics, main lab test setup, objective 001. The Figure has the same structure as Figure 3.11.

3.4.3 Imaging single Yb atoms in optical tweezer arrays

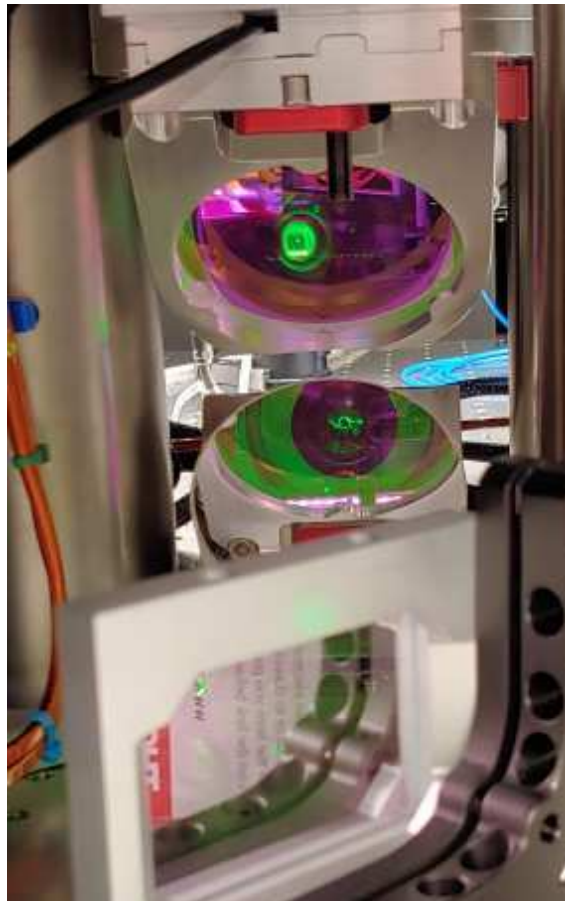
After diffraction-limited tweezer generation was confirmed also for 6 folding mirrors in the beam path and reduced access for alignment, the final configuration was prepared. In general the alignment strategy on the main optical table was the same as for the test setup. However, since the glass cell obviously cannot be moved, the relative alignment of its surface to the objective needs to be aligned completely by tip and tilt of the objective. As there is no way of checking the alignment quality on tweezer images like for the test setup, we used the practice from the main table optical test setup to align the objective only based on its back reflection. Notable differences to the general alignment strategy for 2D tweezer array setups (as discussed in detail in Appendix B) are listed below:

1. There are precisely two conditions that fix both the position and the angle of the optical axis of the main tweezer beam. The first condition is the position of the ultracold atomic cloud contained in the MOT, that needs to be hit by the tweezer array and thereby fixes the **position of the objective**. In practice, this was done using a 399 nm "blowout beam" from the top of the glass cell. It was aligned onto the MOT via kicking out as many atoms as quickly as possible from the trap (observed by absorption imaging from the side) and by entering the glass cell normal to its surface. By centering the objective mount with an iris to that blue beam (or more precisely, to a beam that was overlapped with the blowout beam), the translational degree of freedom is fixed. The centering tool with the iris can be found in part (a) of Figure 3.48. Note that due to the macroscopic extent of the MOT and the possibility to slightly shift its center using the magnetic field coils, centering fidelities of ≈ 1 mm are sufficient to obtain a first signal.
2. Secondly, the angle of the optical axis is defined by the glass cell. To this end, the tweezer beam needs to be aligned perpendicular to the bottom window of the cell, to be able to later minimize the **objective-glass cell relative angle**. Note, though, that this task is not trivial, since the back reflections of the cell that are used for the angle adjustment of the beam are not unambiguous. In fact, there are in theory four reflections off the glass cell, one for each surface of both windows. In our case we found that the single windows have a negligible relative angle of their two surfaces, but the angle between the windows themselves turned out significant. We observed two back reflections of the cell, with an angle of about 2 mrad measured in a distance of 2 meters. If the reference beam is aligned to the wrong back reflection, the objective and bottom window will not be parallel but enclose an angle of 2 mrad. As the analysis in Figure 3.43 showed, this will already suffice to have unusable optical tweezers, such that this distinction is essential. We dealt with this task by scanning the tweezer beam angle while observing the behavior of the back reflection. Thereby, one is able to isolate the first reflection from the second one, as the second reflection moves a slightly larger distance than the first. In addition, there is a point where both reflections will overlap. At this point upper and lower window back reflec-

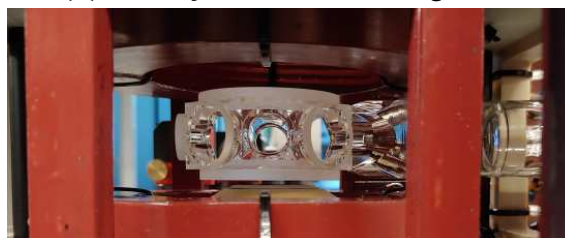
tion will swap position. The outer reflection always belongs to the window that is hit second. Simultaneously, the tweezer beam needs to be aligned on top of the blue reference beam, to fix the transverse position.

3. After initial alignment of the tweezer beam on the glass cell, and centering of the objective mount with respect to the blowout beam, the iris was removed from the mount and exchanged by a mirror. With that an **objective mount angle pre-alignment** is performed, to make sure that it is already very close to optimal. This process was iterated a few times with translation adjustments with the iris tool.
4. As denoted in Figure 3.47, we included a $\lambda = 532$ nm **reference beam** that is transmitted through the dichroic perpendicular to the tweezer beam. This additional beam provides reference in case some mirror was moved unintentionally and it can also help with the imaging beam alignment.
5. Furthermore, the inclusion of the **NPBS** that is transmitted before the tweezer beam impinges on the objective needs to be considered for alignment. As the NPBS causes a lateral displacement of the beam, adjustment of the objective position needs to occur with the NPBS in place. Conveniently, as the beam was already centered on the objective mount without the NPBS, after its inclusion, the 45° mirror can be moved by a translation stage to exactly account for the NPBS shift. The travelled distance was about 4 mm. After alignment, the translation alignment tool needs to be removed again such that the NPBS has to be removed as well paying special attention to not touch the 45° mirror (see Figure 3.52 (a)).
6. The **dichroic mirror** that was tested like the NPBS in Chapter 3.3.8 needs to be placed in the tweezer beam path before beam alignment, which limits accessibility to the NPBS/objective. The angle of the dichroic is adjusted based on the 399 nm top beam that was previously overlapped with the tweezer beam.
7. Most lenses have **reduced degrees of freedom** compared to the optical test setup, to avoid drifts and instabilities in the main experiment. Thereby, all degrees of freedom were effectively coupled, which made the alignment much more challenging.
8. As the 1:10 telescope widens the beam to 35 mm, this is too large to observe helpful back reflections. We therefore **temporarily removed the telescope lenses** from their mounts, while ensuring that this process does not alter the lens alignment.
9. Finally, the **objective was aligned** by centering it with an iris attached to its mount and the NPBS in place. This process as seen through the 45° mirror is depicted in Figure 3.52 (a). After successful translation, the NPBS is removed to take out the alignment iris and is reinserted afterwards. Afterwards, the final

objective tip-tilt alignment was conducted. Using the picomotor actuators in the custom objective mount, the relative angle of the objective to the reference beam was optimized by viewing the objective back reflection, similar to part (b) of Figure 3.48. Even though the objective centering with respect to the tweezer beam might have changed slightly as a consequence of the angle fine-tuning, this effect should be negligible compared to the extent of the MOT.



(a) Final objective translation alignment



(b) Glass cell with objective

Figure 3.52 – Images from the integration of the SQM objective into the main experiment. The top image illustrates how the alignment tool was used to center the objective on the reference beam by viewing it through the NPBS on the 45° mirror. In the foreground, the dichroic mirror can be seen. At the bottom a photograph is depicted that shows the glass cell with the objective below.

The final result with the SQM objective 001 facing the bottom of the glass cell is shown in Figure 3.52 (b). The following table summarizes the achieved alignment accuracy of all relevant components in the final setup.

Optical element	tip/tilt (mrad)	translation, lateral (mm)	Notes
Tweezer beam to glass cell	0.23	—	Main beam
Ref. beam to tweezer beam	1.0	—	($\lambda = 532$ nm)
Top beam to tweezer beam	1.3	—	($\lambda = 399$ nm)
100 mm lens #1	1.7	1	
100 mm lens #2	2.3	0.2	
100 mm lens #3	2.0	0.2	
1 m lens	0.22	0.8	angle vertically off by 0.4 mrad (fixed mount), lens is 1 mm too low
1:1 telescope collimation	—	—	with beam profiler over 140 cm distance
1:10 telescope collimation	—	—	~ 10 mm axially
Objective	~ 0.5	≤ 1	

Table 3.11 – Main experiment alignment accuracies

After setting up and aligning the high-resolution fluorescence imaging path according to schematic 3.47, the tweezers were shot into the MOT to trap Yb-174 atoms. We obtained a first signal by absorption imaging from the side, only creating a single tweezer in the center of the FOV, with its size artificially increased by removing the 1:10 telescope. In combination with a rather long time of flight (15 ms) and optimized MOT position, trapped atoms were visible and maintained captured for up to 50 ms TOF. In fluorescence, it was also helpful to artificially reduce the NA by closing a 3-inch iris in the beam path and to increase the tweezer beam power to about 400 mW. The cooling beam induced photo-association processes where pairs of two atoms undergo a list-assisted collision and subsequently leave the trap [58]. This mechanism ideally only leaves singly and unoccupied tweezers and is therefore the common process to trap single atoms. To increase the imaging time and thus the signal to noise ratio of the images without quickly blowing out the atoms, simultaneous cooling was essential.

After optimization a summary of current results is shown in Figure 3.53. Here, we generated a 5x5 optical tweezer array, with 5 MHz (~ 10 μ m) spacing, 1.25 V RF voltage and approximately 9 mW laser power per tweezer. The images A to C display fluorescence images of atoms trapped in the aforementioned array, in linear scale. We observe statistic loading of the different tweezer sites, which is indicative of a low average number of atoms per tweezer, that approaches 0.5. Moreover, the images of the atoms seem to be close to diffraction limited, however quantitatively, this is hard to tell due to the currently rather small magnification of 20 that was used to ease finding the tweezers in the first place (relative pixel size is $PS/\xi_0 = 45\%$). In

subfigure B, an inset shows a zoom-in on an atom to illustrate the degree of pixelation. In subplot D, 200 individual images were averaged which resulted in a regular 5x5 array with relatively homogeneous tweezer brightness that indicates similar loading probabilities. This image is identical to the one shown previously in the introduction.

For a more quantitative analysis, the brightness was summed for the 25 individual tweezer sites. Repeating this for all 200 images lead to the histogram that is depicted in E. We find a rather narrow peak just above zero counts that corresponds to background light found in empty tweezers. Centered at 200 counts, there exists a well-separated second peak that has a symmetric, Gaussian-like shape which corresponds to the tweezers that are filled by atoms. The fact that this peak is very symmetric and fairly narrow compared to its mean value, without any secondary peak visible is indicative that indeed single atoms are trapped in the optical tweezers.

This figure wraps up the experimental results of this thesis. In the next chapter, we will discuss the sources of technical uncertainties and countermeasures to systematic errors in the image analysis.

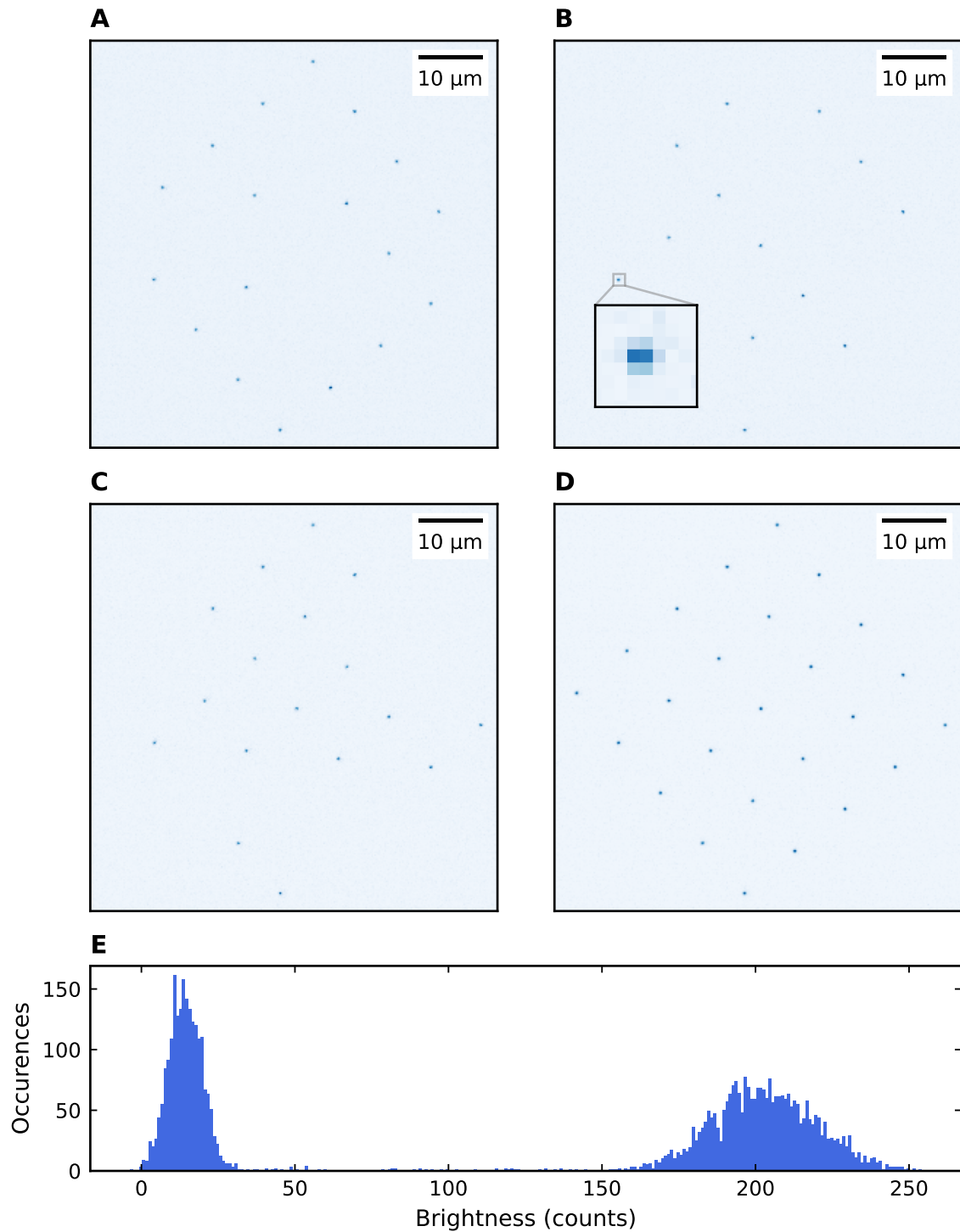


Figure 3.53 – Fluorescence images of trapped ytterbium atoms in a 5x5 optical tweezer array. In the pictures **A**, **B** and **C**, individual single shot fluorescence images from atoms in a 5x5 optical tweezer array are displayed in linear scale. A scale bar is depicted to provide reference, and part B also contains a zoom-in into the picture. In **D**, pictures from 200 individual runs were averaged. Statistics of those can be found in **E**, where the summed brightness per tweezer site is determined and visualized as histogram.

3.5 Technical details for data analysis

In the following Section, we will discuss different effects that impact PSF/optical tweezer measurements and the corresponding data analysis. The Chapter presents experimental observations and discusses theoretical considerations complemented by simulations to better understand the mechanism behind and to estimate the impact of various error sources.

All effects described in the following, disregard the other effects if not noted otherwise. So the pixel averaging Section will not take into account the pixel centering etc. This is also a physical assumption, since these "interactions" are second order corrections and can thus be neglected, assuming they are much smaller than the individual effects (see Section about pixel centering in the presence of pixel averaging).

For simpler terminology, in the following Sections the magnification will be set to one, that means "pixel size" will refer to the extent of a camera pixel in object space.

3.5.1 Pixel centering

First we discuss the effect of pixel centering (PC) errors. This error source only applies to the Strehl ratio computations, since the Airy fits offer degrees of freedom that deal with translation of the patterns. For the Strehl ratio however, the reference pattern is always computed centered on a discrete grid, which at first does not allow us to account for changes in translation of the analyzed peak. But this poses a problem, since for finite pixel size, the position of the peak governs the maximum value that is extracted for the Strehl ratio, according to Equation (2.41). This becomes more clear in Figure 3.54, where the inset in B compares the two most extreme cases where a Peak is aligned onto a pixel center (left) and centered on a pixel corner (right). Both images are shown in linear scale which allows one to visually observe the brightness differences of pixels in both cases.

This PC error can easily be compensated by adjusting the reference Airy pattern of the Strehl ratio computation accordingly. To this end, the center of mass is computed in a special, smaller ROI around the center of the peak, which allows us to estimate on which pixel the pattern is centered on. Subfigure A illustrates this algorithm by depicting an experimental PSF image with the determined center, indicated by a gray cross, next to the simulated Airy pattern for the Strehl ratio determination, that is translated by the corresponding distance. This was repeated for two example images from a $\lambda = 399$ nm imaging measurement, that are close to the two centering-extremes shown in B. Note that this compensation will be meaningless for sufficiently small effective pixel size (below $0.05\sqrt{2}\xi_0$). In that case, the centering algorithm will fail, as the flatness of the peak maximum in combination with measurement/pixel noise, makes finding reasonable peak center estimates very hard.

In order to determine the magnitude of this error, a simulation was conducted, that computes the ratio of the SR in the two most extreme centering cases (2 to 1). Note that this estimate shows the worst-case error, many experimental images will be less affected by this effect. As mostly the peak value is of interest for this simulation, choosing a rather small 20x20 pixel ROI size enabled us to save computation time. We will distinguish two curves, one with and the other without the pixel-averaging correction described in more detail in the next section. Not surprisingly, without pixel averaging, the curve just follows the Airy pattern shape. This motivates to scale the pixel size axis by $\sqrt{2}\xi_0$ such that the

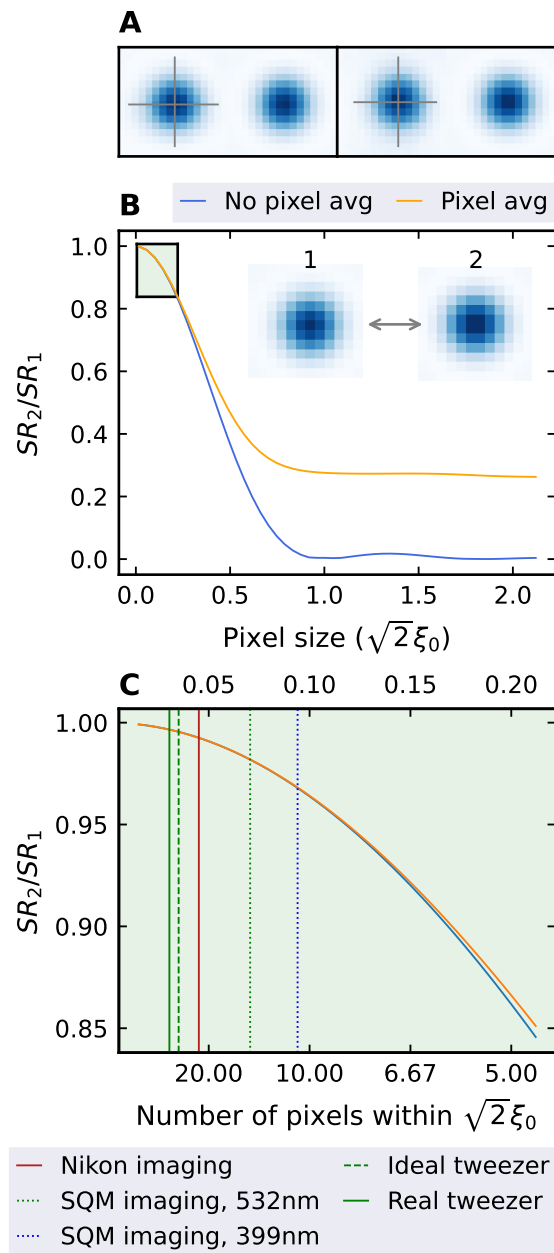


Figure 3.54 - Pixel centering simulations. In panel **A**, crosses indicate the center of mass of two measured PSFs. To their right, the simulated reference is shown that is used for Strehl ratio estimation. In **B**, the worst-case relative change in SR is plotted for various pixel sizes, with or without pixel averaging. The inset in B shows the two extreme centering cases 1 and 2. In **C**, a zoom-in into B is displayed, with vertical lines indicating typical parameters in this work.

minimum is found at a relative pixel size of 1. Here, the $\sqrt{2}$ takes into account that the two extreme cases that are considered in this simulation are displaced diagonally. With pixel averaging (oversampling factor $o = 20$, see next Section), the integration over the pixel size leads to saturation of the change in Strehl ratio. This occurs once the relative pixel size exceeds 1, such that in case 1 (2), single pixels effectively contain all (a quarter) of the patterns power.

While it is instructive to discuss the pattern for relative pixel sizes beyond 1, in practice we are more interested in smaller pixel sizes. To this end, the highlighted area in the top left corner in B is zoomed into in subplot C. While there is still the pixel size given on the top axis, the bottom axis is given in the corresponding number of pixels within $\sqrt{2}\xi_0$, which is a more intuitive quantity in this pixel size regime. Additionally, vertical lines indicate typical relative pixel sizes, that can be found in this work. In this regime, we find close to no change to the PC error caused by pixel averaging which is in accordance with the argument presented earlier that error "interactions" are usually of higher order and thus negligible. The overall magnitude of the PC effect ranges up to 4% in the 399 nm imaging case, which is a significant contribution, while the tweezer measurements hardly exhibit any deterioration.

In this thesis, we always corrected for pixel centering errors in measurement analysis.

3.5.2 Pixel averaging

The second aspect that is discussed is pixel averaging (PA). This phenomenon describes that sharp features in an image can be washed out or broadened, in case the pixel size becomes comparable to the typical length scales of structures in the image. It is based on the working principle of camera sensors that, in simplified terms, are just arrays of very tiny photodetectors that will absorb photons that impinge on their pixel surface and return a voltage proportional to the total number of collected photons. As a consequence, each pixel has its own finite spatial resolution over which it can detect light. Finer sub-structures will be averaged over such that they get lost. Part A of Figure 3.55 illustrates this loss of resolution visually. The continuous intensity distribution (here a narrow Airy pattern) is averaged by every pixel, which results in the recorded intensity pattern deviating from the original distribution in particular for regions with strong curvature. Positive (negative) curvature will lead to an increase (decrease) of the brightness recorded, such that all together, this leads to an apparent broadening of peaked structures. This visual argument leads to the conclusion, that for strongly pixelated images, one needs to move away from the perception of pixels as point-like detectors, towards treating them as extended sensors that average over an area.

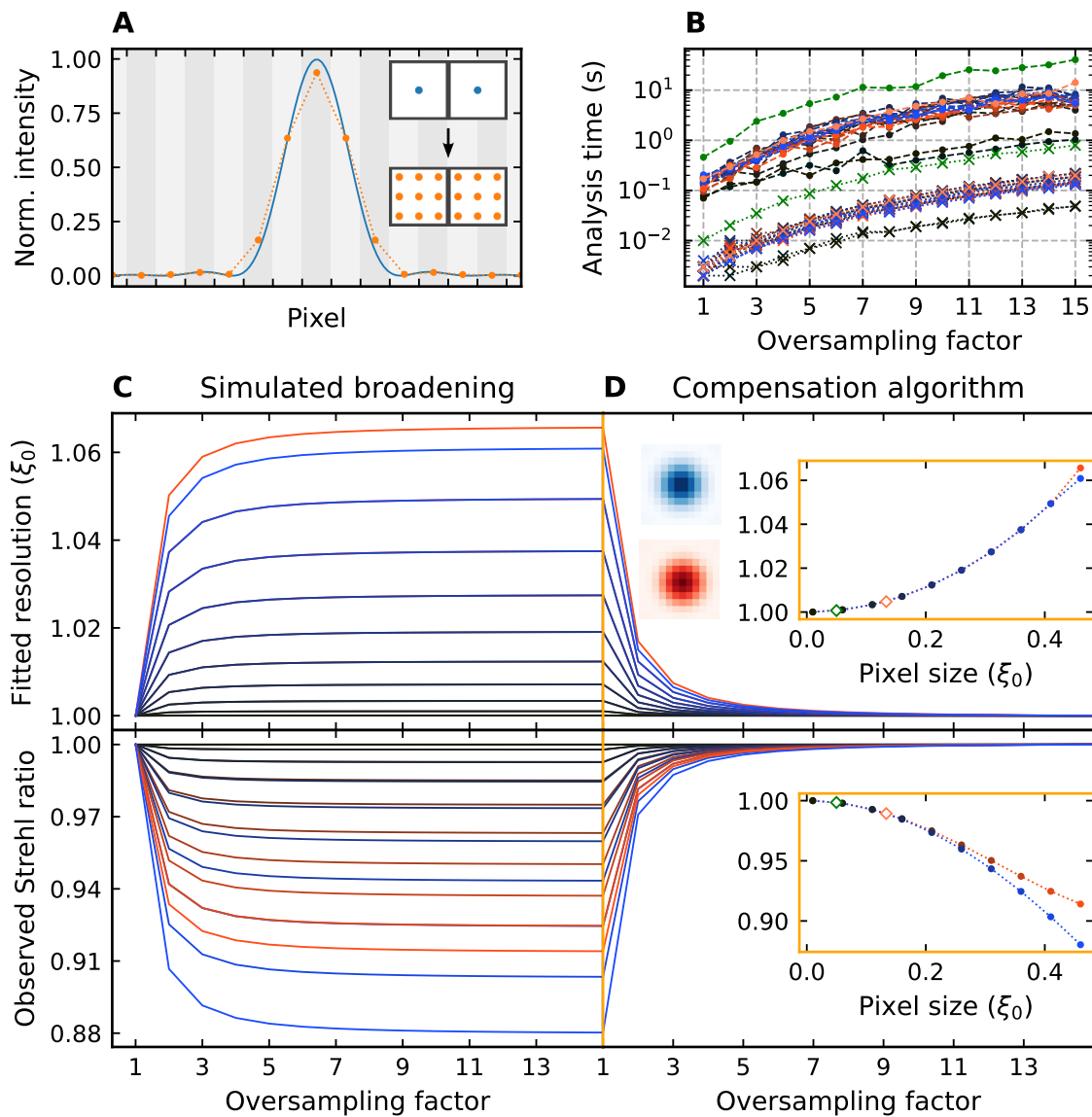


Figure 3.55 – Simulation of the effect of pixel averaging on the Strehl ratio and resolution. Subfigure **A** shows an illustration that visualizes the effect of pixel averaging on an Airy pattern, while the insets show the positions in pixel space where a naive and a pixel-averaging data evaluation would sample a function. In **B**, for all simulations and experimental data evaluations from the following subplots, the Strehl ratio computation time (crosses) and the Airy fitting time (points) is shown as a function of the oversampling factor used in the compensation algorithm. In the subplots **C** and **D**, the impact of pixel averaging on fitted resolution and observed Strehl ratio is shown. The different curves correspond to variable pixel size (brightness) and centering of the pattern relative to the pixel grid (color). In particular, **C** describes how PA influences the results when not accounting for it in the analysis as a function of the oversampling factor. In subfigure **D**, a fully pixel-averaged Airy pattern ($\sigma = 15$) is analyzed while applying PA compensation with varying oversampling factor. The insets in **D** depict cuts through the plots at the orange line, which enables one to assess the PA effect as a function of pixel size. In addition, the insets also contain two data points from experimental images, that illustrate the relative change due to PA compensation.

If we want to incorporate PA into a model function that describes the intensity distribution of a peak, we can follow the procedure shown in the inset in part A. The concept is to evenly sample the area occupied by one pixel, before averaging over it, instead of just computing a single value for the pixel center. This approach was followed in this work and will be referred to as *oversampling*. The *oversampling factor* o is the number of function evaluations along each axis of the pixel, leading to a total increase of function calls of o^2 , compared to without pixel averaging. It is important to note, that the points needs to be sampled homogeneously over *all* pixels, meaning that one needs to avoid double counting values at the pixel edges, or any sort of uneven accumulation of points, that would weight certain areas more than others. One should rather sample as depicted in the illustration, such that the point spacing is the same also between two pixels.

In the case of Airy pattern fitting and Strehl ratio estimation for high-resolution imaging and tweezer generation, we expect that as a consequence of camera pixel averaging, the fitted resolution becomes larger and the Strehl ratio drops. To better understand this process, we simulated the broadening starting from ideal Airy patterns, that were "observed" by sensors with a particular pixel size. The results from subsequent naive Airy pattern fits, as well as Strehl ratio calculations are summarized in subfigure C. This simulation was repeated under different conditions: The oversampling factor o was varied along the horizontal axis. Furthermore, the simulations were conducted twice, for the two most extreme pixel centering cases which are indicated by the images shown in the insets in D. This parameter can be differentiated by the color (bluish or reddish) of the curve. Lastly different relative pixel sizes are encoded in the brightness of a curve such that darker means smaller pixel size. At the position indicated by the orange vertical line, a cut was extracted, that depicts the impact of pixel averaging for 15-fold oversampling and as a function of the relative pixel size. It is visualized in the inset plots on the right. We find that the broadening induced by pixel averaging is already close to maximal for an oversampling of only 3. Furthermore, the effect strongly depends on the pixel size in a parabola-like dependence. For a pixel size that is 20% of the diffraction limit, we observe that the Airy pattern exhibits an apparent broadening of about 1.5%. Simultaneously, because of this, the Strehl ratio drops to below 0.975, which is a significant change. Comparing the two pixel centering extreme cases, there is close to no difference for the fitted resolution, however, for larger pixel sizes the corner-centered case seems to be clearly more sensitive to pixel averaging.

In the second half of the lower plot, labeled with D, the reverse process is studied. This means, that a pixel-averaged Airy pattern was generated with 15-fold oversampling, which is then analyzed using PA-corrected fitting and Strehl ratio determination. To compensate for PA, the fit function simply uses a pixel-averaged version of the Airy pattern and the Strehl ratio references the data to a simulated Airy pattern that is pixel-averaged as well. The oversampling factor for compensation is kept a free parameter in the analysis code. The Strehl ratio implementation assumes it makes no difference whether the data is processed to remove the pixel averaging and then compared to an ideal Airy pattern (normal SR definition), or whether the data is directly referenced to

a pixel-averaged Airy pattern (this assumes a linear relationship between the SR pre- and post compensation, that should be fulfilled for typical relative pixel sizes). We find that with the PA compensation, the ideal Airy pattern is completely recovered from the simulated pixel-averaged data, in the limit of a large oversampling factor. This curve is surprisingly symmetric to the broadening on the left side and also requires only an oversampling of 3 until more than 90% of the PA error is compensated.

Note that for these analyses correct pixel centering is accounted for, and it is assumed that the light detection surface is equal to the complete pixel area. The latter is not strictly true for real cameras, but only concerns very high oversampling rates where the edges of the pixel are explored as well.

The PA compensation demonstration depicted in D is the optimal case where the full effect can be removed. In reality however, the images contain noise and aberrations which might reduce the impact of PA correction. In order to test the pixel averaging compensation effect with real data, two diffraction-limited example images from a $\lambda = 399$ nm imaging measurement (coral empty diamond) and a flat-top incoming beam tweezer (green empty diamond) are analyzed and displayed in the insets in D. Shown is the relative change in resolution/Strehl ratio when not applying compensation compared to applying PA compensation with $o = 15$. While the effect for the well-sampled tweezer measurement with a relative pixel size of 5% is barely visible, the blue imaging measurement with relative pixel size of 13% shows an increase in resolution and a drop in SR by more than 1% due to pixel averaging. Overall the observed PA magnitudes for the experimental images show very good agreement with the simulated curve.

Finally, in subfigure B the scaling of the analysis time with the oversampling factor is depicted, calculated from the simulations in D. The color coding is the same as used in D, the points refer to the Airy fits and the crosses to the Strehl ratio with PA compensation. In general we find that, as expected, the Airy fits take much longer than the Strehl ratio computation, and using a small oversampling factor will also be beneficial with respect to the computation time. In particular, the black curves that display analysis without PA compensation lie significantly lower than the others. In contrast, the experimental analyses lie well above the other curves. Overall this rapid scaling of the analysis time with the oversampling factor motivates choosing it as low as possible while still compensating the majority of the effect.

Therefore, in all analyses shown in this thesis, pixel averaging compensation with an oversampling factor of 3 is performed. An exception are the Nikon PSF characterization measurements that only used $o = 2$ due to their already low degree of pixelation.

3.5.3 Background noise

For images that suffer from strong stray-light effects, background noise can quickly become a problem. In particular the Strehl ratio is very sensitive to a non-zero image background, since it depends on the numeric integral of the images that scales quadratically with the ROI size r (see Chap. 3.5.4) as well as the precise peak value

[59]. Considering the formula (2.41) for the Strehl ratio calculation, the background light contribution can be easily estimated, as it will only affect the measured numerator M via the transformation $I(x, y) \mapsto I'(x, y) = I(x, y) + BG(x, y)$, where $BG(x, y)$ refers to the 2D distribution of background light on the camera sensor. With that we find the relative Strehl ratio error:

$$\begin{aligned}
\frac{\Delta SR_{BG}}{SR} &:= \frac{SR' - SR}{SR} = \frac{\frac{M'}{N} - \frac{M}{N}}{\frac{M}{N}} = \frac{M'}{M} - 1 = \\
&= \frac{\frac{I'_0}{\int I'(x, y) dx dy} - 1}{\frac{I_0}{\int I(x, y) dx dy}} = \frac{\frac{I_0 + BG_0}{\int (I(x, y) + BG(x, y)) dx dy} - 1}{\frac{I_0}{\int I(x, y) dx dy}} = \\
&= \frac{1 + \frac{BG_0}{I_0}}{P_r + \overline{BG} r^2} \cdot P_r - 1 = \frac{\frac{BG_0}{I_0} - \frac{\overline{BG} r^2}{P_r}}{1 + \frac{\overline{BG} r^2}{P_r}} = \\
&\approx \left(\frac{BG_0}{I_0} - \frac{\overline{BG} r^2}{P_r} \right) \left(1 - \frac{\overline{BG} r^2}{P_r} \right) = \\
&= \frac{BG_0}{I_0} - \frac{\overline{BG} r^2}{P_r} + \mathcal{O} \left(\left(\frac{\overline{BG} r^2}{P_r} \right)^2 \right) \tag{3.7}
\end{aligned}$$

Here we assumed a square ROI with size r , image peak intensity I_0 , image power contained in the ROI P_r and we defined accordingly the quantities BG_0 as the background value at the image peak and $\overline{BG} = \int BG(x, y) dx dy / r^2$ as the average background.

After approximation of the denominator to first order in $\overline{BG} r^2 / P_r$, we can extract the error in the low background limit. Interestingly, depending on the ratio BG_0 / \overline{BG} , background can lead to both, over- and underestimation of the Strehl ratio in case the background brightness at the peak of the image is large or small. The second determining quantity is the size of the region of interest r . If one assumes a homogeneous background, as soon as the ROI is larger than the nearly flat plateau region of the observed peak, the negative term will always be strictly greater than the first, leading to an underestimate of the Strehl ratio.

The error derived here was used for the focus scan analyses by calculating the error for the calculated background uncertainty at a given ROI size.

3.5.4 Region of interest size

During all previous discussions we assumed that restricting ROIs for the focus scan processing is sensible and will not affect the analysis results. For the radial Airy and Gauss fits this is also very accurate, since as long as the main peak is not cut at the edges, the fitting algorithms will yield an accurate result with low uncertainty. However, for the Strehl ratio computation this is not so clear. Naively, restricting the SR analysis to a certain ROI size is sensible, as long as the same ROI size is cut for the reference PSF evaluated for the normalization. This already avoids significant deviations by excluding the same area and thereby power in the side lobes for both the image and the simulated pattern. In principle, this SR estimate is already something different from the actual Strehl ratio, but if one assumes the experimental image and simulation agree well enough, there should exist a monotonous mapping between the real Strehl ratio with infinite ROI and the approximate SR using a finite ROI. In the limit of high objective performance, such that both images are close to geometrically *similar*, i.e. they scaled versions of one another, this mapping is linear and the Strehl ratio calculated from a ROI is even identical to the real SR. However, for aberrated PSFs and tweezers this approximation fails which raises the question whether the calculated Strehl ratio of the imperfect shape is affected by the ROI size differently, than the reference pattern which would create an error in the SR.

We can estimate this effect by assuming that the image and the diffraction-limited simulation are slightly geometrically *dissimilar*. We begin by observing that this discussion only concerns the integrated powers:

$$\frac{\Delta SR_{ROI}}{SR} := \frac{SR' - SR}{SR} = \frac{\frac{M'}{N'} - \frac{M}{N}}{\frac{M}{N}} = \frac{\frac{I_0/P'_r}{J_0/Q'_r} - \frac{I_0/P_\infty}{J_0/Q_\infty}}{\frac{I_0/P_\infty}{J_0/Q_\infty}} = \frac{\frac{Q_r}{P_r}}{\frac{Q_\infty}{P_\infty}} - 1 =$$

Where P_r and Q_r represent the power inside a ROI of size r , while P_∞ and Q_∞ denote the total power of the respective pattern. Next, we identify $P_r = P_\infty - p$ and $Q_r = Q_\infty - q$ to find:

$$= \frac{\frac{Q_\infty - q}{P_\infty - p}}{\frac{Q_\infty}{P_\infty}} - 1 = \frac{\frac{p}{P_\infty} - \frac{q}{Q_\infty}}{1 - \frac{p}{P_\infty}} \sim \left(\frac{p}{P_\infty} \right)^2 \quad (3.8)$$

Assuming second order dissimilarity in the sense of $\frac{q}{Q_\infty} = \frac{p}{P_\infty} + c \left(\frac{p}{P_\infty} \right)^2 +$ higher orders. Numerical simulations²⁵ indicate that the constant factor c is approximately 2, which leads to the final result for the relative ROI or truncation error:

²⁵Zemax, OpticStudio

$$\frac{\Delta SR_{ROI}}{SR} = 2 \left(\frac{p}{P_{\infty}} \right)^2 \quad (3.9)$$

where $\frac{p}{P_{\infty}}$ is the relative discarded power, that is calculated in the analysis from the simulated Airy patterns for a given ROI size.

Apart from estimating the truncation error, the size of the image used for analysis should not be taken randomly, but based on a systematic considerations. One needs to balance two limits: On the one hand, a ROI that is too large will be extremely sensitive to background fluctuations, as this scales quadratically with the ROI size. In addition the overall signal to noise ratio will be bad, which affects most analysis quantities. On the other hand, cutting the images too closely around the main peak has the obvious disadvantage of discarding too much information. This is described by the error estimated in the previous paragraph. To find the optimal size for the analysis ROI, an empirical approach is pursued, in which two representative focus scan measurements were analyzed for a variety of ROI sizes. First, in Figure 3.56 results are shown for a flat-top input beam tweezer measurement and an imaging measurement. Both measurements are diffraction-limited and were generated by objective 002 with $\lambda = 532$ nm light. The imaging measurement had a substantially larger background than the tweezer, which is important as in this Figure both analyses were repeated with and without applying background subtraction. In addition the bit depth of the imaging measurement was limited by the camera to 10 instead of 12 bit for the tweezer measurement.

In subplot A, the logarithmic normalized intensity of the images is plotted against the distance from the center. The data is compared to a simulation that is shown in black and fits the experimental points within two diffraction limits from the center. In this plot, the behavior of the different measurements for larger radii is of central interest. We find that the tweezer curve matches the simulation well, even up to $5\xi_0$, where the data points start to be limited by the dynamic range of the camera sensor. As expected for this measurement, background subtraction makes close to no difference. However the imaging measurement does not fall below 10^{-3} for larger distances from the center, which indicates a strong non-zero background. Still, there are small peaks visible also for the imaging measurement, that emerge from the background level. In the background subtracted curve, those peaks are visible much more clearly and agree both in location and roughly in magnitude with the simulation. This analysis shows, that both the camera sensor dynamic range, as well as reducing the background are essential for accurate PSF/tweezer images, that also provide information past the second diffraction ring. In case of the imaging measurement, it is important that the ROI size is chosen to not include contribution past the second side-lobe, as these sections will be dominated by noise. Lastly, we find that for both measurements in particular for the tweezer images, the data is systematically below the simulation. This effect arises from the camera digitization and discretization effects, that are discussed in more detail in Chapter 3.5.5.

A more quantitative investigation of the region of interest impact is shown in part B. For all four measurements, the most relevant analysis quantities as well as the computation time are plotted for different ROI sizes. The first subplot shows the total power contained in the ROI normalized to the total image power after background subtraction, for the brightest image in the focus scan. We find the characteristic strong increase for small ROIs, where the major contribution from the central peak is being integrated. Beyond that ROI size a plateau is visible that belongs to the first radial zero, with a final clearly visible increase that is connected to the first diffraction ring. For the tweezer image, even a second plateau can be found, before the power increases to the final level. From this behavior it is apparent that the optimal ROI size that includes most power, but does not extend farther should end somewhere close to the second radial minimum plateau. Another striking feature is the strong increase in power for the imaging measurement that was not background subtracted when approaching larger ROI sizes. In fact, this curve is well described by a parabola, as expected for a homogeneous background. A quadratic fit, that is plotted in black yields a background of 1.06, using the relation $P_{r \rightarrow \infty} \approx P_{\infty} + \overline{BG} r^2$. This background also agrees well with the one calculated during analysis that is 1.09(5). Even though it is possible to compensate the background effect by subtraction, it is sensible to choose a ROI that minimizes the contained background such that its relative power is below 10^{-1} . This way, the impact of errors in the background subtraction is kept low.

The Strehl ratio as a function of ROI size is very unstable especially for smaller ROIs. This highlights the differences between ideal and measured Airy patterns, that mostly come into play starting from the first radial zero, where we observe a sudden drop in the Strehl ratio for all images. For larger ROI sizes, the Strehl ratio still changes slightly even for the background subtracted measurements. This could have different reasons, however, they all share that for these large distances from the PSF/tweezer center, noise and errors dominate those contributions. In the case of not correcting for the background in the imaging measurement, we find significant under estimation of the Strehl ratio that follows a Lorentz shape according to formula (2.41). Fitting the curved part of the data with $SR(r) = SR_0 / (1 + \overline{BG} (r - r_0)^2)$ yields a Strehl ratio ideally without impact from the background of 0.998. The fit is shown in the figure as black dashed line. From this subplot, we would prefer to use a ROI size that lies close to the first plateau after including the first side-lobe. This guarantees that one covers aberrations that appear in the first radial minimum, without extending too far which would lead to strong contributions of bad signal-to-noise rings. Furthermore, choosing a ROI size, that lies in a plateau of the Strehl ratio would provide greater robustness against small fluctuations in Airy pattern size.

The Airy fits are shown in units of the diffraction limit ξ_0 and horizontal, and vertical fit axes are distinguished by using vertical and horizontal line segments as markers. As expected, we observe that the fitted resolution is much less sensitive to the ROI size and to background subtraction compared to the Strehl ratio. Apart from slight deviations in the beginning, fit fluctuations are on a 10^{-3} level. To summarize for these fits, any ROI size that is larger than $3 \xi_0$ will work.

The fit fidelity has a similar behavior, however, since the difference of fit and image are of importance, the strong-background image loses R^2 with increasing ROI size. The curve follows the Strehl ratio in terms of the pattern at smaller ROIs. Like with the resolution, any ROI size above $3 \xi_0$ will be sufficient.

Finally, the last panel shows the computation time in logarithmic scale (desktop PC, code was not runtime-optimized at this point) for the focus scan analysis. Only pixel averaging, pixel centering and background subtraction corrections were included, and both Gaussian and Airy fits were performed. For the same relative ROI size, the larger magnification in the tweezer imaging setup nearly doubles the pixel count compared to the imaging measurements, leading to strongly increased analysis time. One finds that the computation time also rises significantly with increased ROI size.

After taking into account the behavior of all relevant quantities for varied analysis ROI size, it was decided to use the relative ROI size $3.5 \xi_0$ for all NA-limited measurements in this work, which is indicated as the solid, gray vertical line in subfigure B.

Since it is not clear if this behavior can be transferred to the optical tweezers that were generated using a Gaussian input beam, as they have a shape that is fundamentally different from the NA-limited Airy pattern, this analysis was repeated. We used a representative measurement taken from the single tweezer measurement series with objective 002 and an input beam with $2w_G = 33$ mm. The result is shown in Figure 3.57 that is structured in the same way as the previous. Note that the apparently thicker simulation curve is caused by a low-amplitude oscillatory pattern on the signal, which is an artifact of the discrete Fourier transform sampled on a finite grid, that was used for this simulation (see Figure 3.59). We find that the data looks fairly similar to the previous analysis and chose the analysis ROI size $3.94 \xi_0 = 3.5 \tilde{\xi}_0$ for the same reasons as explained in the preceding paragraphs.

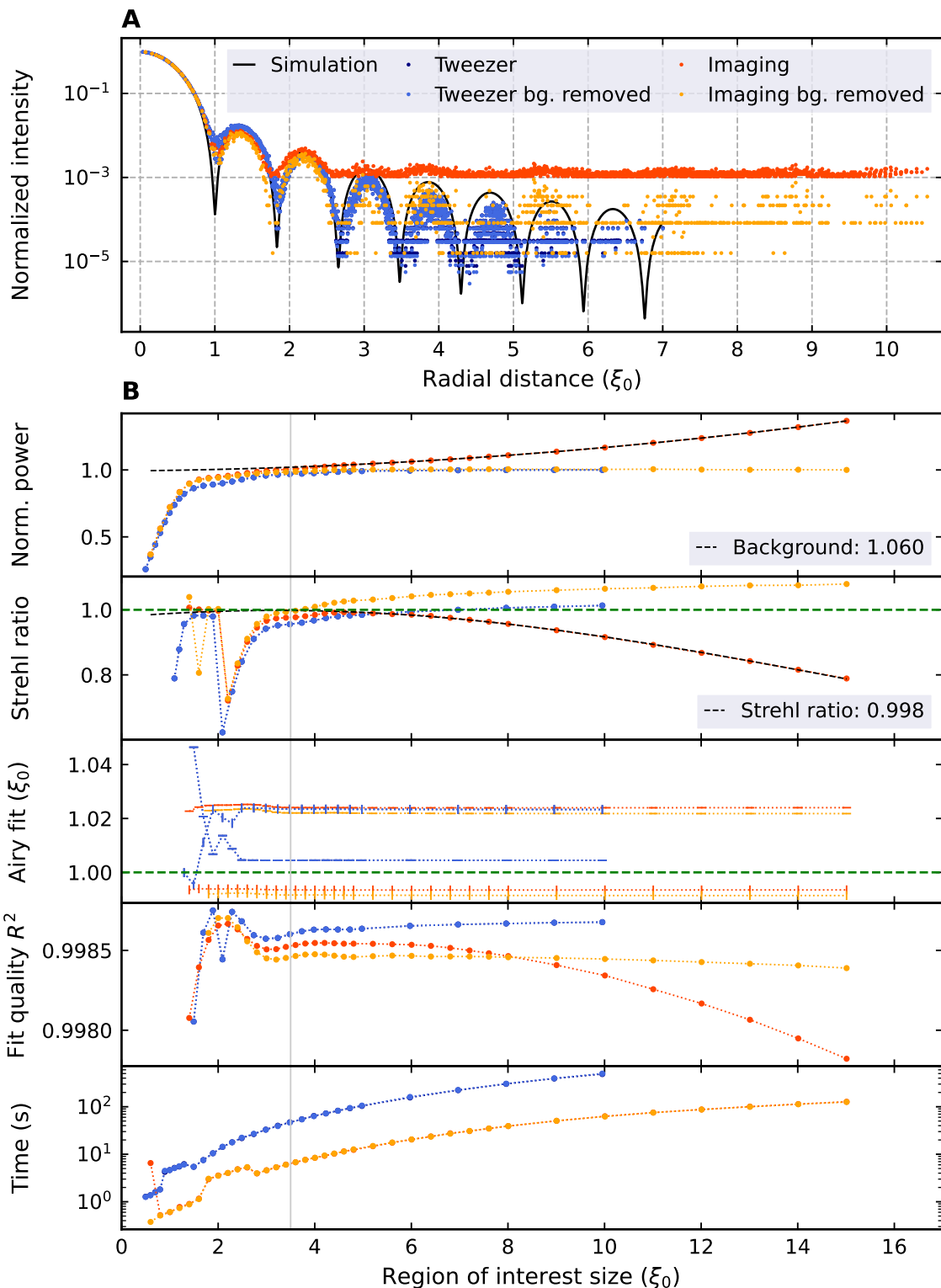


Figure 3.56 – Analysis results for variable ROI sizes for different NA-limited 532 nm measurements. In this figure a representative imaging and tweezer beam measurement are analyzed, that are both close to the NA-given diffraction limit ξ_0 . The measurements are compared with and without background subtraction and are shown as azimuth averages in **A**, where they are compared to a simulation, and with their analysis results in **B**, which were computed for a variety of ROI sizes. A parabolic and Lorentz fit of the imaging measurement results without background subtraction are shown in the normalized power and Strehl ratio plots as dashed black lines. The ROI size that is used for all analyses in this work is indicated by a gray vertical line.

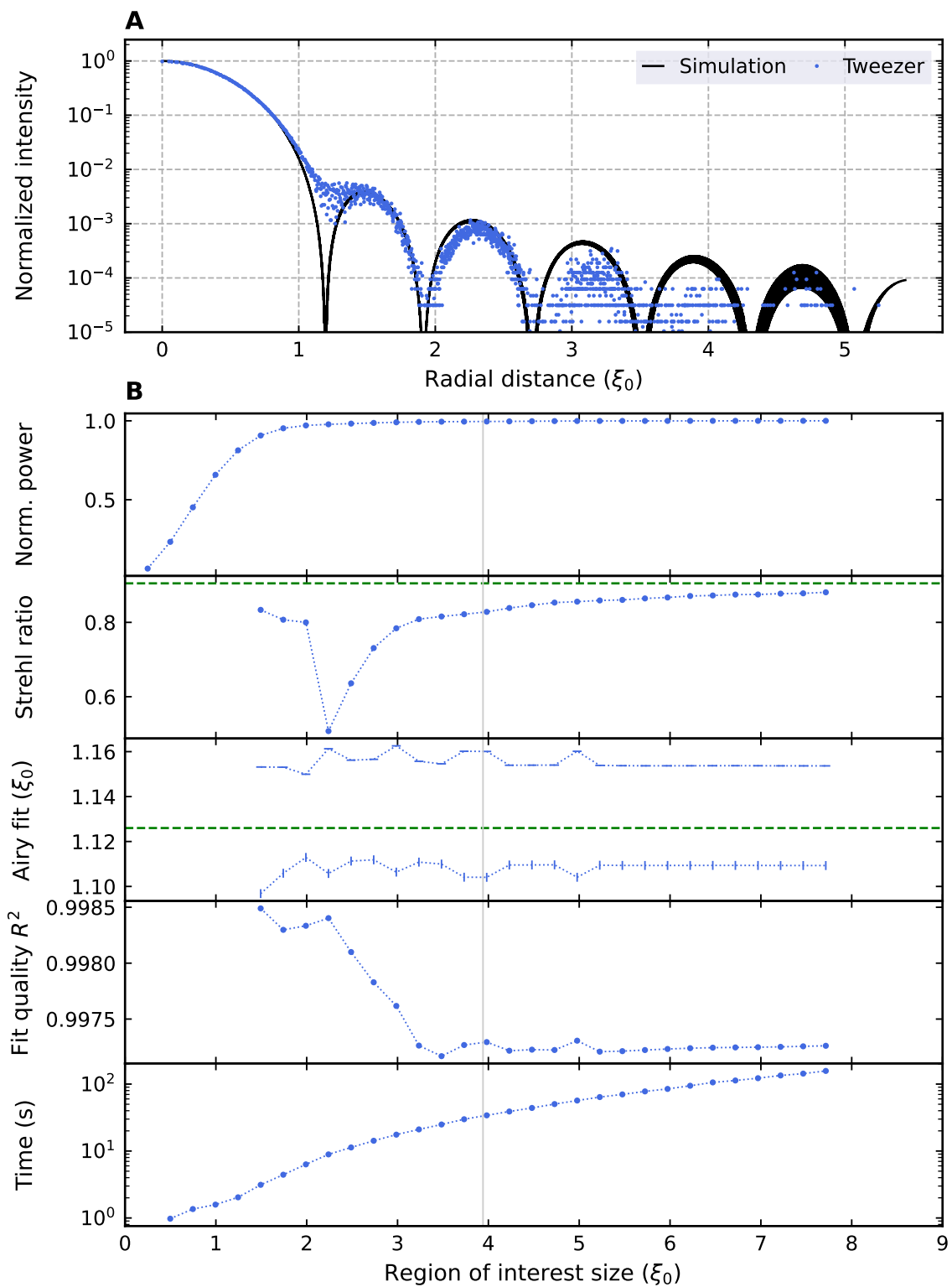


Figure 3.57 – Analysis results for variable ROI sizes for a Gaussian beam tweezer measurement. This figure has the same structure as Figure 3.56, however it shows an optical tweezer measurement that used a Gaussian input beam.

3.5.5 Discretization

As briefly addressed in the previous section, we are able to observe discretization effects from the camera sensor, that lead to lower side-lobe brightness than expected (compare Figure 3.56 A). This is a systematic effect that leads to an overestimate of the Strehl ratio, since power in the wings is missing. To better understand and ultimately compensate this effect, simulations were conducted to recreate this behavior.

The results from those investigations are summarized in Figure 3.58. In A we were able to recreate a distribution that looks very similar to the one observed in Figure 3.56 A. It is compared to the ideal and continuous Airy pattern on which the discretized version is based. Apart from having chosen the simulation parameters identical to the experimental conditions, there were three additional assumptions used to imitate the camera sensor (in order of application to the ideal curve):

1. **Poissonian counting noise** was added to every pixel to recreate the random nature inherent to real measurements.
2. **An additional threshold** was included to account for the strong underestimation of intensity in the wings, that cannot be solely explained by pixel rounding. Up to this threshold, any intensity is ignored and not counted to the output of the simulated pixel. Physically, this assumption makes sense in a simple photo diode picture, that is subject to dark current. Because of this, the pixels need to exhibit a threshold that prevents measuring the dark current.
3. **Pixel rounding.** More specifically, rounding down, is assumed to recreate the characteristic integer-valued output that a camera sensor produces. In addition, the physical assumption is made, that the brightness of a particular pixel needs to exceed a certain integer before returning that value, which is implemented by the *floor* function.

There were two free parameters (mean Poissonian noise and the threshold value) that were optimized by hand to match the curve from the measurement. The main difference to the experimental data is that this simulation does not contain any sort of aberrations, leading to data points precisely approaching the radial zeros of the ideal Airy pattern. Apart from that, the simulated data looks very similar to the experimental results, as it also shows the reduced brightness in the wings, as well as some randomness and the discretized "levels" far from the center of the structure. In B this is even more obvious, as the two pictures show the images from which the azimuth averages were computed in A in log-scale. We immediately find that most of the structure past the first three rings is lost by the discretization as well as a broadening of the radial zeros. Comparing the lower picture with the ROIs shown in the Figure 3.8 we observe good agreement.

To quantify the SR overestimate due to this effect, the Strehl ratio was computed systematically for a range of ROI sizes. As the effective dynamic range of the image is of crucial importance for the impact of this effect, the simulation was repeated by

varying the Airy pattern intensity from 100 to 4100 counts. The resulting change in Strehl ratio can be viewed in subfigure C, where the left side shows the Strehl ratio as a function of ROI size color coded for different brightness, while the right side displays a cut through the previous plot revealing the dependence on intensity.

Starting on the left side, we find the error having positive sign as expected and increasing towards larger ROIs. This is explained by a gradual accumulation of missing power with every diffraction ring. If inspected closely, one notices the wiggly shape of the different curves, that is caused by the Strehl ratio increase being most pronounced near the radial minima. Here, it also pays off to use an analysis ROI size, that lies on a plateau, to be less sensitive to deviations from the ideal tweezer size. Furthermore, one finds a striking dependence of the Airy pattern brightness that is shown in more detail in the cut on the right side. To remain consistent, this cut is taken from the position corresponding to the actual relative ROI size, that is used in the data analysis in this thesis and is highlighted by an orange dashed line. We find the Strehl ratio increase to be inversely proportional to the Airy pattern intensity. Note that the severity of this trend is on the order of about 1.3% for moderately well illuminated images at 2000 counts, while for a high effective dynamic range exploiting the full 12 bit, the error is only slightly above 0.6%. To estimate the sensitivity of this estimate on the manually chosen parameters described above, the simulation was repeated with 10% in- and decreased parameters. The resulting tolerance is visualized as shaded region. To systematically compensate for the overestimate, the mean of the three curves (min, optimal, max), as well as half of the difference of the 10% tolerance curves are fitted with the result:

$$SR(BR) = 1 + \frac{27}{BR + 77} \pm \frac{5.8}{BR + 286} \quad (3.10)$$

where BR stands for the Airy pattern maximum brightness.

Since the Gaussian beam-limited tweezers have a significantly different shape compared to the ideal tweezers/PSFs, this analysis was repeated using simulated Airy patterns that are created with an incoming Gaussian beam relative size of $2w_G/D_O = 0.94$ as used for the measurements in this work. The simulation is shown in Figure 3.59 and is qualitatively identical to the previous. Notable differences include slightly different numerical values as well as fits, and an apparently broader simulation in A, that is a consequence of the wiggles visible at the outer minima of the upper image in B. The latter is caused by discretization/finite size artifacts from the discrete Fourier transform. The new fits used in the main analyses for compensation and the error bars are:

$$SR(BR) = 1 + \frac{0.72}{BR - 30} \pm \frac{0.045}{BR - 88} \quad (3.11)$$

The fact that in this case, a slightly different fitting function is used, does not have any physical motivation and only had the purpose to obtain a more accurate fit, that can be used for compensation in the analysis program. For the NA-limited

and the Gaussian-limited discretization figures, the simulated data in part A, used well-illuminated images with maximum brightness of 3991 (3984) counts, to be comparable and to resolve side-lobes properly.

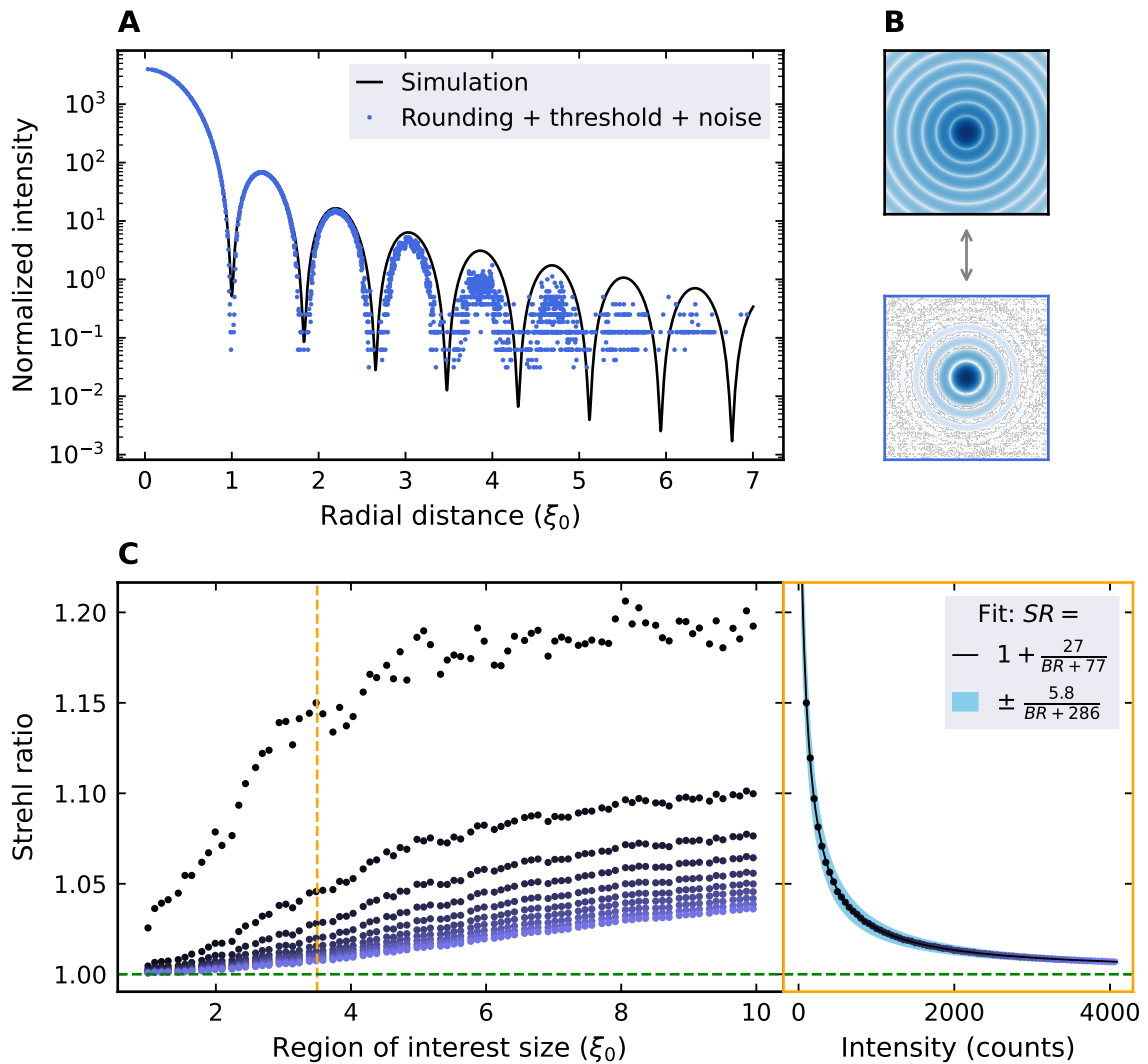


Figure 3.58 – Simulation of the discretization effect for NA-limited Airy patterns. In part A, azimuth averages are shown, comparing an ideal Airy pattern with simulated data, that is generated from the ideal pattern by adding noise, applying a threshold and rounding off all values. The corresponding two images are displayed in part B in logarithmic scale. In subfigure C the Strehl ratio is plotted for the simulated data as a function of relative ROI size and for different image brightness. The image maximum intensity is color coded and unraveled in the right part of the figure, that shows a cut through the curves on the left at the orange dashed line. An error range is displayed as well which is computed from adjusting the parameters that created the simulated data by 10%. Fits of the SR as a function of intensity as well as of the tolerance are given in the legend.

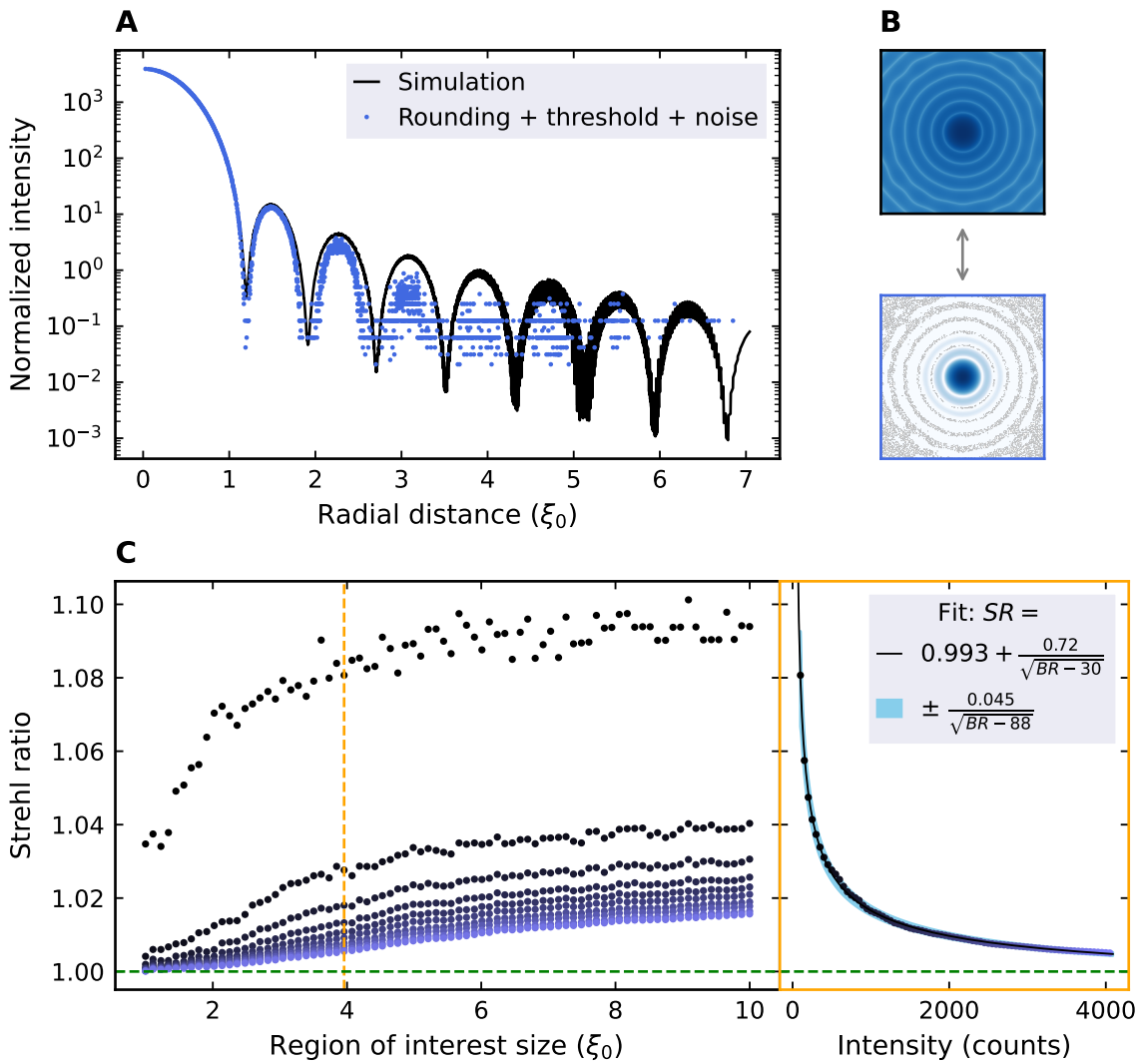


Figure 3.59 – Simulation of the discretization effect for a Gaussian beam tweezer. This figure has the same structure as Figure 3.58, however it shows an optical tweezer measurement that used a Gaussian input beam.

3.5.6 Tweezer overlap

The arcs found in the tweezer images from measurements that included both AODs, like in figures 3.32 or 3.33, could potentially affect neighboring tweezers and alter their analysis results, in particular their Strehl ratio. However, as observable in the respective plots, these wings are very weak and will never reach into a $4 \times 4 \xi_0^2$ box around the tweezer center. Therefore, this effect is neglected in this analysis.

3.5.7 Convolution

Another significant effect that only concerns imaging measurements, is the impact of finite-sized pinholes, acting as point sources. In reality, this is of course not true, and

the proper way to deal with extended sources like a 250 nm pinhole, is to convolve the structure with the point spread function, as discussed in Chapter 2.2.2. This convolution needs to be taken into account when analyzing imaging measurements where the pinhole has a comparable size to the PSF, since in general, it leads to a smearing out of the intensity distribution.

While there exists no closed-form solution of this problem, the limiting cases are known. For tiny pinholes, the convolution will recover the original PSF (the ideal case for high-resolution imaging) while in the case of a very large hole, the diffraction effects will be negligible and the image will look like the circular aperture. In reality though, the image will lie in between those two extremes, and needs to be computed numerically.

The process of compensating the effect of convolution, which is also known as deconvolution, is a well-known problem of signal reconstruction, with plenty of solution approaches ranging from least squares fitting, Wiener deconvolution [60], the Lucy Richardson algorithm [61], direct inversion to only name a few. In our case, we used a simple fitting approach, where the convolution is implemented in the fitting model.

A thorough analysis of the magnitude and compensation of this phenomenon is presented in Figure 3.60. In subfigure A, we illustrate the impact of convolving a PSF with a small pinhole on the observed intensity distribution. To this end, azimuth averages are depicted in both, linear and logarithmic scale. The curves shown are the unperturbed PSF, as well as its field and intensity 2D convolution (note that the dimensionality plays an important role due to the radial symmetry). Each of them is normalized to contain the same power, and was generated assuming parameters typical for this work, a NA of 0.7, a $\lambda = 532$ nm light source and a pinhole diameter of 240 nm. For sub-wavelength pinholes it is adequate to assume spatially coherent light and thus to convolve the aperture function with the electric field PSF rather than with the intensity PSF. It is crucial to emphasize that this decision has a very strong effect on the impact of the convolution. Since convolving with the intensity PSF can only lead to a broader distribution, the convolution will usually grow significantly in size, while destructive interference in the field-case will, to some extent, prevent the convolution from broadening as strongly. As expected, we find significant broadening for the intensity convolution while the field convolution only slightly grows in size. Interestingly, the characteristic zeros, that are visible as dips in the logarithmic view, have completely vanished in the intensity convolution case. As a consequence of the broadening with fixed total power, the "peakedness" drops which will be observable in reduced Strehl ratio.

Panel B shows a simulation of the effect that convolution has on the observables resolution " ξ " and the Strehl ratio. To this end, a diffraction-limited (field) PSF was convolved with a circular aperture function, sampled on a 400 (200) pixel grid with a pixel size of 1% (2.5%) of ξ_0 for the SR (resolution) simulations. Note that the computation time of a 2D convolution scales *quartic* with the 1D pixel count, that limits the maximum ROI size which is important to smoothly sample the effect of changing aperture size, due to discretization. Since the pixel size is well below 10% of the diffraction limit, no pixel averaging was performed.

The SR plot, shows the relative drop in Strehl ratio compared to the ideal PSF without convolution, as a function of aperture size in units of ξ_0 . Typical relative pinhole sizes for different measurements presented in this work are shown as vertical lines, including 399 nm and 532 nm imaging tests with our 0.7 NA objective, and imaging measurements with the commercial 0.9 NA Nikon objective and 532 nm light, all imaging the "250 nm" pinhole (see legend). In addition, a zoom into the most relevant small-pinhole regime is displayed for clarity. We find that for the 0.9 NA objective and the 399 nm imaging tests, the expected SR error is already on the order 1.5% and thus significant.

The resolution scales similarly with the aperture size as the Strehl ratio. Shown are two graphs, that show the fitted resolution ξ of a diffraction limited PSF convolved with a circular aperture. The first (blue) naively assumes a simple airy-pattern fit function, while the second curve (orange) shows the fitted resolution when convolution with a known aperture size is included in the fit function. As for the Strehl ratio, an inset shows a zoom of the small pinhole regime. At the relative apertures used in this work, the underestimate of the resolution is about 1 to 2%, however, if compensated, this effect is eliminated in this simulation. Still, one needs to keep in mind that this is a simulation without aberrations and noise, such that this complete compensation will probably not be reached in the actual data analysis. The result of compensating the convolution in the Strehl ratio case is not simulated, as the SR will always be 1 trivially.

In both plots in B we find the characteristic two limits for small and large pinholes. For pinholes much smaller than $0.5 \xi_0$, the resolution closely approaches 1, as if there was no convolution to begin with. On the other side, for large pinholes, the change in convolution size becomes proportional to the pinhole size increase, indicating that a regime is entered, in which the image is basically scaling strictly with the pinhole size and PSF/interference effects stop playing a significant role.

Lastly, subfigure C shows the fitted resolution of measured example images using the deconvolution fit, as a function of the assumed aperture size. Two different example images recorded using 399 nm light were analyzed, one using the 250 nm pinhole, the other imaging the second smallest pinhole available on the target, the 500 nm pinhole. The resolution values given, are the mean of the x and y fits. The nominal aperture sizes with the official 10% tolerance are shown as vertical lines with a surrounding shaded region. Note how the sensitivity of the retrieved resolution on knowledge of the aperture size becomes significant for a large pinhole size. This behavior makes it unfavorable to image pinholes with a size on the order of the diffraction limit. That is why, for this work, we decided to restrict our measurements to the 250 nm hole only. Despite for clarity referring to the pinhole as the "250 nm pinhole", the analyses in this thesis assumed a pinhole size of about 240 nm, as measured in Chapter 3.1.1.

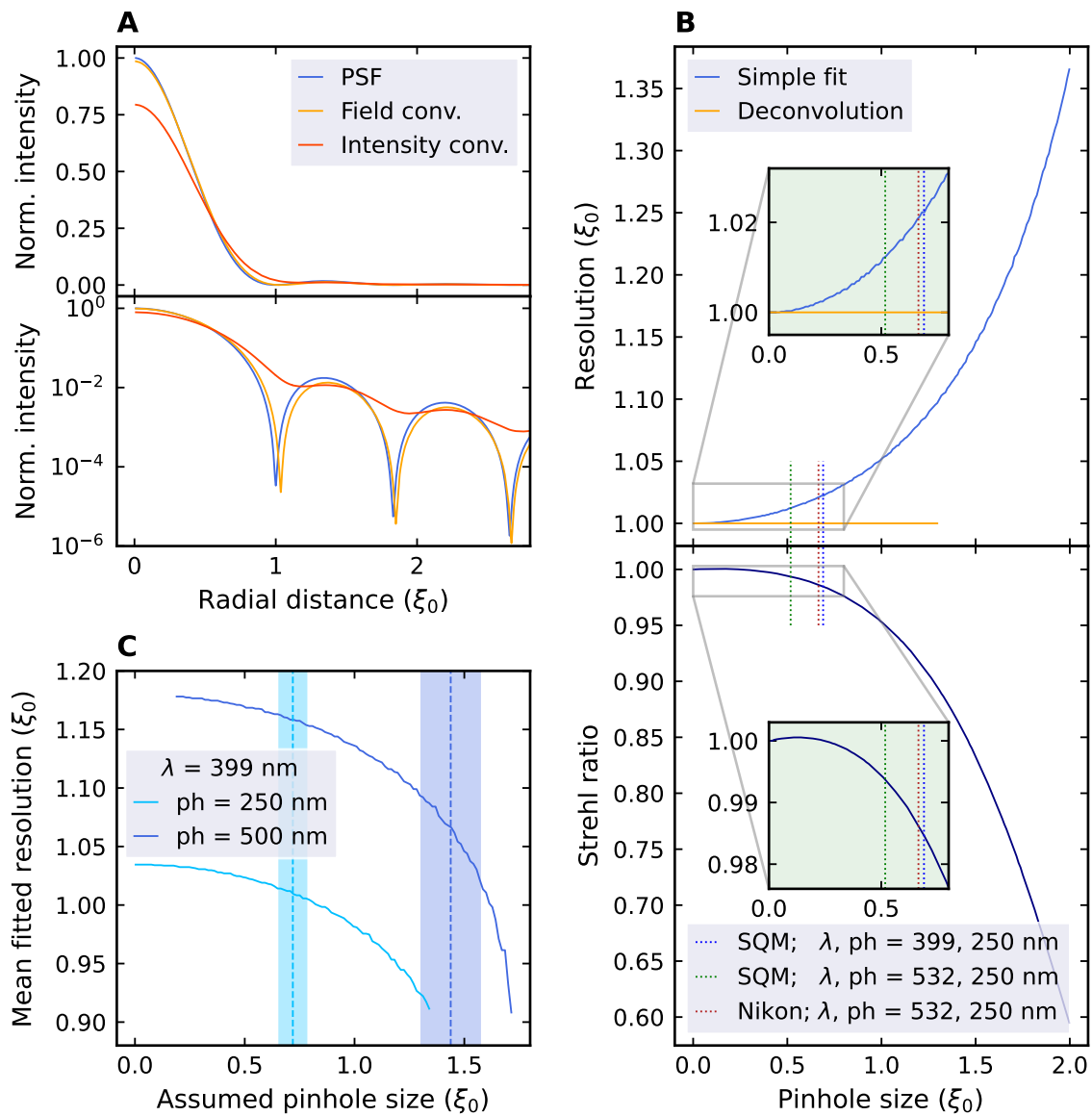


Figure 3.60 – Discussion of the impact of convolution with a finit-sized pinhole on the fitted resolution and Strehl ratio. In subfigure **A**, a typical diffraction-limited PSF is illustrated in comparison to the same ideal PSF, that was convolved in field and intensity with a finite-sized circular aperture. The patterns are displayed as azimuth averages in linear and lograithmic scale. Part **B** shows the apparent increase in PSF size and drop in Strehl ratio as a function of the pinhole size. Insets zoom into the most relevant regions that correspond to imaging sub-wavelength pinholes. To provide reference, vertical dotted lines indicate typical relative pinhole sizes in this work. In addition, the simulated effect of deconvolution on convolved ideal PSFs is displayed in the resolution plot as the orange line. Subplot **C** shows the fitted resolution, calculated using the deconvolution fit, for two example images of the 250 and 500 nm pinholes, that were recorded with $\lambda = 399$ nm light. In addition, the nominal pinhole size as well as the official diameter tolerance is drawn as vertical dashed lines and colored bars.

Deconvolution, as discussed in the previous paragraphs, is performed for all analyses in this thesis, assuming circular pinholes with a radius of 240 nm, sampled on grids that are a factor of 3 more dense, than the natural grid of the measurement. This help to increase the precision/smoothness with which the convolutions can be calculated. As an example, green light measurements that have an effective pixel size of 46 nm, will be able to simulate the aperture width as 230 nm without and as 245 nm with the increased density.

3.5.8 Tweezer imaging imperfections

In the realistic case, that the high-resolution imaging setup for the tweezer tests is not perfect, it will itself introduce wavefront errors that add with already present errors from the tweezers. Thereby, instead of testing the tweezer quality on its own, one observes an artificial decline in performance caused by the measurement setup. In our case, as seen in Chapter 3.3.2, the Nikon exhibits some slight, yet existing coma, that might have systematically affected the tweezer quality. As it is rather involved to precisely calculate the additional error from the Nikon objective, we will present an estimate in this chapter, that predicts the most probable trend, however, with a rather large error bar. Note that this effect is only calculated for the Strehl ratio. Systematic effects on the resolution are ignored for this work.

To take this effect into account, we recall the SR-combination formula from Chapter 2.2.4. We have access to the observed Strehl ratio of tweezers, that includes the SQM objective as well as the Nikon imaging setup. This "complete" Strehl ratio will be referred to as SR_C . Furthermore, calibration measurements of the Nikon objective imaging give access to the isolated Strehl ratio of the imaging system SR_I . We calculate the Strehl ratio of the optical tweezers SR_T by:

$$SR_C = SR_T SR_I \exp\left(2 \cos(\theta) \sqrt{\log SR_T \log SR_I}\right) \quad (3.12)$$

$$\Leftrightarrow SR_T = \frac{SR_C}{SR_I} \exp\left(-2 \cos(\theta) \sqrt{\log SR_T \log SR_I}\right) \quad (3.13)$$

Where θ is the angle enclosed by the normalized aberration vectors. This result only implicitly determines SR_T , such that we need to make further simplifications. To proceed, three assumptions will be made to end up with a stochastic prediction for the bare tweezer Strehl ratio.

1. **Truncating Zernike expansion.** The number of Zernike polynomials that add relevant contributions is limited. More specifically, the first four elements (Piston, x , y tip and tilt as well as defocus) are assumed to be zero by good alignment and focusing of the tweezer. Furthermore, only the first 7 aberrations are considered to have non-negligible impact, as higher order aberrations usually appear less pronounced. Those comprise of x/y astigmatism, x/y coma, x/y trefoil and spherical aberrations.

2. **Independent setups.** The tweezer-imaging and -generating setups are treated as individual black box systems that imprint a certain phase on an incoming wavefront. Both systems are independent and not correlated. The latter is particularly relevant, since if in both setups the same type of lens built by the same manufacturer was included (which is not the case), the probability increases that aberrations add constructively. This would delegitimize the probabilistic approach.
3. **Maximal aberration ignorance.** There exists maximal uncertainty on the aberration vector orientation. Therefore, the pointing of every aberration vector is treated as a random variable that is uniformly distributed on a d -dimensional hypersphere.

With these approximations and the definition $\cos(\theta) := \vec{e}_a \vec{e}_b$, we can compute relevant statistical properties of $\cos(\theta)$.

$$\begin{aligned}
\langle \cos(\theta) \rangle_{P(\vec{e}_a, \vec{e}_b)} &= 0 & (3.14) \\
\langle \cos(\theta)^2 \rangle_{P(\vec{e}_a, \vec{e}_b)} - \overset{=0}{\langle \cos(\theta) \rangle_{P(\vec{e}_a, \vec{e}_b)}^2} &= \langle (\vec{e}_a \vec{e}_b)^2 \rangle_{P(\vec{e}_a, \vec{e}_b)} \\
&= \left\langle \sum_{i,j} e_a^i e_b^i e_a^j e_b^j \right\rangle_{P(\vec{e}_a, \vec{e}_b)} \\
&\stackrel{3.}{=} \left\langle \sum_{i,j} \delta_j^i e_a^i e_b^i e_a^j e_b^j \right\rangle_{P(\vec{e}_a, \vec{e}_b)} \\
&= \left\langle \sum_i (e_a^i)^2 (e_b^i)^2 \right\rangle_{P(\vec{e}_a, \vec{e}_b)} \\
&= \sum_i \langle (e_a^i)^2 \rangle_{P(\vec{e}_a)} \langle (e_b^i)^2 \rangle_{P(\vec{e}_b)} \\
&\stackrel{3.}{=} \sum_i \frac{1}{d} \sum_p \langle (e_a^p)^2 \rangle_{P(\vec{e}_a)} \frac{1}{d} \sum_q \langle (e_b^q)^2 \rangle_{P(\vec{e}_b)} \\
&= \sum_i \left\langle \frac{1}{d} \sum_p (e_a^p)^2 \right\rangle_{P(\vec{e}_a)} \left\langle \frac{1}{d} \sum_q (e_b^q)^2 \right\rangle_{P(\vec{e}_b)} \\
&= d \cdot \frac{1}{d} \frac{1}{d} = \frac{1}{d} & (3.15)
\end{aligned}$$

Where \vec{e}_y^x denotes the component x of an arbitrary normalized aberration vector y and $\langle \dots \rangle_{P(\vec{e}_a, \vec{e}_b)}$ stands for the average over all \vec{e}_a, \vec{e}_b orientations. Here we used that the average of the product of different aberrations is always zero, and that the average square is the same for all components. Using these relations, we can further simplify the Equation (3.13):

$$\begin{aligned}\langle SR_T \rangle_{P(\vec{e}_T, \vec{e}_I)} &\approx \frac{SR_C}{SR_I} \exp\left(-2 \langle \cos(\theta) \rangle_{P(\vec{e}_T, \vec{e}_I)} \sqrt{\log SR_T \log SR_I}\right) \\ &= \frac{SR_C}{SR_I}\end{aligned}\quad (3.16)$$

this means, to first order we can correct for imaging imperfections by simply dividing the "complete" Strehl ratio, by the imaging Strehl ratio. To estimate the error bar, we insert the standard deviation of $\cos(\theta)$ into the equation using $d = 7$ according to assumption 1. This yields the error range:

$$\frac{SR_C}{SR_I} \exp\left(-\frac{2}{\sqrt{7}} \sqrt{\log SR_C \log SR_I}\right) \leq SR_T \leq \frac{SR_C}{SR_I} \exp\left(\frac{2}{\sqrt{7}} \sqrt{\log SR_C \log SR_I}\right) \quad (3.17)$$

As Equation (3.13) is transcendental, we approximated SR_T within the square root by SR_C . This leads to a reasonable estimate for the solution for the lower bound, while the numerical simulation shows, that the upper bound is overestimated by roughly 0.01.

Since this effect, as well as the discretization compensation, follow from the least rigorous derivations/simulations, they are computed and illustrated separately for every analysis, as annotated in the figures. Even though their impact makes physical sense and helps to explain observations like the SR exceeding one for the green light imaging measurements, or the rather bad SR for the Gaussian input beam tweezers that however reach the diffraction limit in the fits, these contributions still contain a rather large uncertainty.

3.5.9 Fluctuation effects

There are two main sources of random noise that might affect image quality, shot to shot changes in image quality and pixel noise. The former can be caused by mechanical vibrations affecting the system or air fluctuations in the beam path, whose impact is discussed in more detail in Appendix C. This causes individual images to have different quality than the recordings in neighbouring positions in the focus scan. Moreover, since this effect is random and can in general lead to reduced or improved image quality, it is accounted for by averaging over several images in the focus, when condensing scans into a single number.

The latter can be caused by all sorts of technical imperfections of the data acquisition and appears as a distortion of the ideally smooth intensity envelope. Since the Strehl ratio is very sensitive to the peak value of a given picture, these fluctuations are taken into account by adding a contribution to the overall error bar, which is proportional to the normalized standard deviation of the four brightest pixels of a particular image. If there is one pixel that is significantly brighter than its surrounding, this is probably due to a statistic pixel error and respected in the error estimate.

3.5.10 Summary

To conclude this chapter about technical uncertainties and error sources, the following table summarizes again all effects, the quantities that are impacted, the measures taken to account for these and the critical quantity/quantities that predominantly determine their strength.

Source of error	Quantities	Measure	Critical quantity
Pixel centering	SR	Compensation	Eff. pixel size / ξ_0
Pixel averaging	SR, ξ	Compensation	Eff. pixel size / ξ_0
Background	SR	Compensation + statistical error	System shielding, lab brightness
ROI truncation	SR	Statistical error	ROI size / ξ_0
Discretization	SR	Compensation + statistical error	Bit depth, eff. dynamic range
Tweezer overlap	SR, ξ	Compensation	ξ_0 / tweezer distance
Pinhole convolution	SR, ξ	Compensation + systematic error	Pinhole size / ξ_0
Tweezer imaging	SR, ξ	Compensation + systematic error	Imaging system SR
Image shaking, pixel noise	all SR	Compensation + statistical error	System stability, system shielding
Magnification	SR, ξ	Systematic error	Calibration quality
Picomotor step size	w_{ax}	Systematic error	Calibration quality

Table 3.12 – Overview on the technical sources of error

To build a feeling for the uncertainties that remain after compensating the main error source, the following table illustrates the typical magnitude for residual Strehl ratio uncertainty in %. It summarizes selected error bar contributions for the *best-SR single image* of a Gaussian input beam "real tweezer" measurement and a $\lambda = 399$ nm imaging test.

Source of error	Real tweezer	Blue imaging
Background	0.00 %	0.07 %
ROI truncation	0.58 %	0.73 %
Discretization	0.07 %	0.48 %
Pinhole convolution	—	1.23 %
Tweezer imaging	5.16 %	—
Pixel noise	0.96 %	3.19 %

Table 3.13 – Typical Strehl ratio error contributions after compensation

Finally, to illustrate the effect of the different compensation steps on the observables, Figure 3.61 depicts the fitted Rayleigh resolution (tweezer size) and the esti-

mated Strehl ratio for two typical measurements, along the different stages of compensation. The measurements are the same as for the previous table, a $2w_G/D_0 = 0.94$ Gaussian input beam tweezer and a $\lambda = 399$ nm imaging measurement. The corresponding relative pixel sizes are given in the subfigure titles. Note that the data points show the determined quantities for *an entire focus scan (single focus)* rather than for an individual image. For the Strehl ratio, the straight forward compensation steps are marked with navy-colored points, while as for the previous analyses, discretization and imaging corrections are shown with green empty circles.

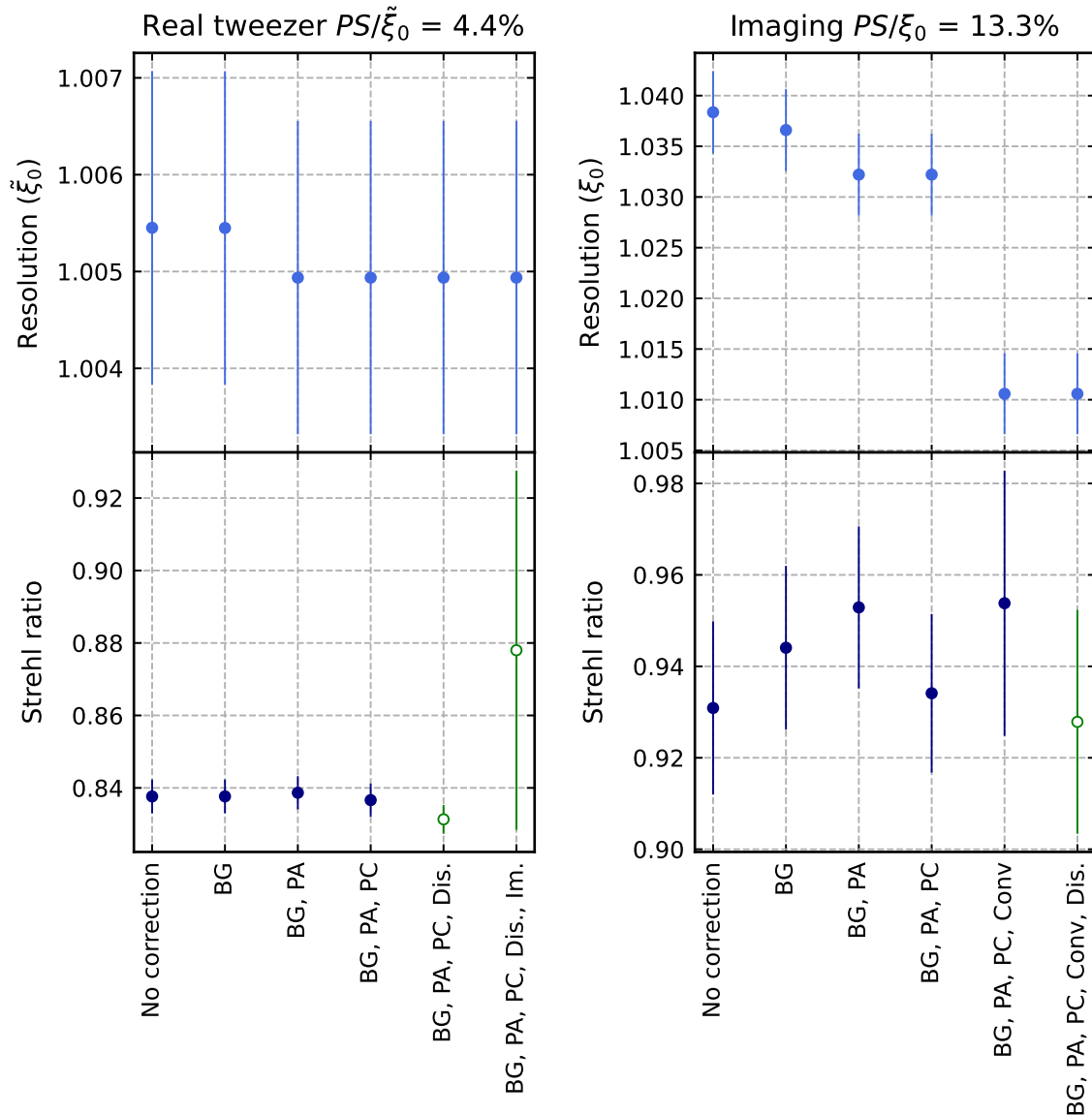


Figure 3.61 – Overview on the effect of error compensation for two representative measurements. Two focus scans are compared with respect to their analysis results ξ and SR for different correction steps. On the left, a typical Gaussian beam tweezer measurement is shown, while on the right a 399 nm light imaging measurement is depicted. The corresponding relative pixel sizes are given in the headings. The compensation steps are labeled like in the previous analysis figures.

Starting with the tweezer measurement, we find the only correction on the tweezer size that has non-negligible impact is pixel averaging, yet it only accounts for a barely noticeable change in ξ . In terms of Strehl ratio, all background subtraction, pixel averaging and centering have close to no effect, owed to the small effective pixel size and the low background level. Discretization compensation notably changes the Strehl ratio, however the largest effect is the expected impact of the imperfect imaging system, accounting for a change in SR of more than 0.04 SR. As this correction is only a stochastic estimate, it is accompanied by the largest error bar.

In the imaging case, we find that the resolution is affected by both, background subtraction as well as pixel averaging, that improve the resolution by 0.25 / 0.5 % respectively. As expected, pixel centering correction does not change the fitted PSF size, but deconvolution does. In fact, accounting for the finite size of the pinhole in case of a relative pinhole size $PH/\xi_0 = 70\%$ this systematic amounts to a significant contribution of 2.25% $\xi_0 = 7.8$ nanometers. Discretization does also not affect the resolution. When inspecting the Strehl ratio curve, we also find background subtraction and pixel averaging improving the result by more than 1%, that is however compensated again by the pixel centering correction. As for the resolution, deconvolution significantly increases the Strehl ratio by 0.02 which is in agreement with the simulation in Figure 3.60. At the end, discretization compensation reduces the SR estimate again which leads to the interesting result, that the SR without any and containing all corrections happen to be the same, as the contributions precisely cancel in this particular case.

Conclusion and Outlook

To conclude, in this thesis we characterized the imaging and tweezer-generating performance of our custom high-resolution objectives before integrating one of them in our main experiment.

This was realized by setting up and improving an optical test setup, equipped with self-built mounts with a large number of degrees of freedom and thoroughly calibrated precision devices such as the SEM-measured test chart, the interferometrically tested picomotors and the frequently tested Nikon imaging objective. Initial challenges concerning setup instabilities and image shaking that arose from mechanical fluctuations and air currents were identified and overcome by shielding the setup. To assess the imaging performance and tweezer quality, image series were recorded in automated focus scans for hundreds of measurements. As this amount of data required a reliable, easy-to-use and reproducible analysis program, a complete focus scan analysis script was written that can analyze both imaging and tweezer measurements, compute a variety of quantities such as the resolution, radial and axial Gauss fits, Strehl ratio and also yields the trap parameters for tweezer measurements. Furthermore, the code offers a range of complex error computation, propagation and compensation steps that are explained in detail in the thesis. To this end, we also conducted simulations on the expected measurement results and possible sources of error including pixel centering and averaging effects, background light, region of interest size, camera discretization, convolution with a pinhole and tweezer imaging infidelities.

The data was classified and condensed into meaningful analyses that confirmed diffraction-limited imaging operation of both SQM objectives for the wavelengths 399 and 532 nm. Furthermore, we found that these results were highly reproducible and the analyses generally agreed within a few percent for the same measurement as well as among different alignments. We noticed that after spherical aberration and coma corrections, objective 001 is limited by slight astigmatism, while objective 002 exhibits clear trefoil aberration. Even though the imaging performance for blue light was significantly worse than for the green, both objectives were also found to perform up to specifications within the FOV of 100 μm .

With respect to the second task, the generation of optical tweezer arrays, we confirmed the diffraction-limited performance also for the reversed light propagation direction. In particular, we tested the optical tweezer generation with a single tweezer generated by an incoming beam of different size. Even for the Gaussian envelope

beams, the tweezer size agreed well with the simulated predictions and was also close to the imaging results. To detect and eliminate any systematic effects on the observed tweezer quality, test series with different camera settings and AOD input amplitude were conducted, not finding any significant impact.

After confirming diffraction-limited single tweezers, the AODs were included in the setup and 2D tweezer arrays were successfully generated. Those were also used to again test the FOV with enhanced statistics from the large amount of tweezers contained in the arrays. Surprisingly, we found that the Nikon FOV deteriorated the apparent tweezer quality towards the edges of the FOV. Taking this effect into account, the objective exhibits great tweezer performance across the full specified FOV which is welcomed for future experiments.

The effect of various optics in the beam path was also tested in detail with the tweezer and imaging test setups as well as independent measurements with a Zygo interferometer. This allowed us to identify insufficient parts which enabled us to only use those optics with the best surface quality in the main setup, which will be of great value for the final tweezer quality. Apart from this, systematic measurements of the alignment sensitivity of various elements have been conducted which proved essential to set up a practical alignment strategy that still allows for sufficiently accurate alignment of the most crucial optics. In particular, we identified the critical value of about 0.5 mrad for the relative objective-glass cell angle beyond which the tweezer quality drops significantly, which is an essential result.

Taking everything into account, we set up all previously tested optics on the main table to integrate the option for high-resolution imaging and tweezer generation into the experiment. Unfortunately, we found that the better performing objective 002 had a manufacturing defect that prevented us from mounting it in our custom holder. We thus swapped to objective 001 for which we optimized several parameters directly in the main setup. After preparing an optimized alignment strategy that we tried with another test setup on the main table, we finally integrated all elements to the machine and aligned them carefully. After finding the first signal, we were trapping atoms in optical tweezers without having to re-iterate any process.

As of now, we managed to trap atoms in 5x5 optical tweezer arrays and image them using fluorescence. The light scattering statistics indicate that we indeed have single atoms in our tweezers, however in the future trap depth and trap frequency measurements need to be conducted to assess the tweezer quality properly. Furthermore, measurements of the life time of the atoms in the tweezers are required to estimate the trap fidelity and limitations for future experiment cycle times. In addition, since the homogeneity is not optimal yet, the active feedback algorithm still needs improvement. Finally, the next major challenge will be to put together the optical tweezers with the horizontal 2D lattice and to load atoms from the tweezers into particular lattice sites to demonstrate the hybrid tweezer lattice in our experiment.

Construction and alignment of a high-resolution imaging system

This Chapter provides a detailed guide on the required steps to build and align a high-resolution optical imaging setup for objective PSF characterization or optical tweezer imaging. The contents are summarized experiences accumulated during this thesis and might vary slightly in applicability to different setups.

The infinity-corrected setup is assumed to have the same composition as illustrated in Figure 3.3. The relevant optics are (focusing lens), test target, (glass window), microscope objective, tube lens, camera which are aligned last-to-first. The incoming laser beam might be focused onto the test target to increase the throughput and thus the signal to noise ratio while noise caused by objective internal back reflections of bright and large, off-focus structures from the target are avoided. The target then provides the point-like source that is used to characterize the PSF of the objective that is placed right after the test target. In case the objective is corrected for a glass plate of a certain thickness, it is absolutely essential to include an identical window in the test setup to prevent severe spherical aberrations from affecting the imaging performance. The light is then focused by the tube lens on the camera to form an image. A list of the required steps from preparation up to optimized data acquisition is prepared below:

1. Choose optics and devices.

- (a) The **camera** sensor should offer a low pixel size, to reduce pixelation effects, and a sufficiently large sensor to be able to simultaneously capture a large portion of the FOV. Check that the computer connection supports the data transfer rate to avoid incomplete data saving or distorted imaged in the case of row-by-row sensor readout. One needs to make sure to use the maximum possible dynamic range that the camera is capable of to not be limited by discretization effects. Generally, it is useful to work with low exposure times and a high frame rate to reduce the impact of image blur and slow drifts respectively. The gain setting should usually be set to zero as it mostly creates unnecessary noise. Even though in this work the camera had a thin protection glass in front of the sensor, generally is it probably better to have a bare sensor.

- (b) The focal length of the **tube lens** should be large enough to ensure a high magnification which leads to small effective pixel size and thus sufficient PSF sampling on the camera. A relative effective pixel size of less than $0.2 \xi_0$ is recommended. Furthermore, the large focal length also reduces the risk of aberrations due to smaller lens surface curvature.
 - (c) Use **mirrors** that are suitable for the wavelength used to prevent the loss of laser power. In the case that mirrors are required to fold the beam within the imaging path, make sure that the mirrors have sufficient surface flatness. To this end it is useful to glue the mirrors instead of clamping them into the mounts by applying only 3 small spots of epoxy glue at the edges to prevent deformation during the curing process.
 - (d) Choose a **test target** that offers both, structures to easily calibrate the magnification of the system, and pinholes which have a diameter of at most half the expected resolution ξ_0 . For larger pinhole the error will exceed 1% and deconvolution is required to obtain reliable results.
 - (e) **Reduce the number of optics** as much as possible, since no element is perfect and one aims to avoid measuring a PSF that is artificially deteriorated by bad auxiliary optics. Therefore, it is recommended to use a single large-focal length lens instead of a multiple telescopes, and ideally no additional folding mirrors between the objective and the camera, as there the beam has reached its maximum size and is thus most susceptible to the impact of imperfect surfaces.
2. **Prepare mounts and optics holders.** In general the mounts need to be stable in particular against slow drifts that can make later alignment very tedious. In case a larger exposure time is required, the setup should also be well damped against high-frequency mechanical noise that might blur the image or lead to stochastic image imperfections. Note that any oscillations on the order of a few 100 nm will be visible in the imaging process. All multi-axis translation stages need to be constructed as orthogonal as possible to reduce coupling between the axes.
- (a) The **focusing lens** is not that crucial, a simple 3-axis translation stage is sufficient, while it can be useful to have a large range in the axial direction.
 - (b) The **target** mount needs highly accurate and stable 3-axis translation stages that allow to smoothly navigate on the test chart without further drifts after positioning. While precise axial position can in principle also be achieved using the objective mount, it is recommended to use the target mount for precise focusing, as slight misalignment of the target during that process is much less problematic than tilting a window-corrected objective that needs 0.5 mrad angle precision. For easier focusing and to acquire automated focus scans, using a picomotor for the axial direction of the target is very advantageous. In addition, for easier focusing and navigation on the test

chart, direct and non-distorted view on the pinhole and laser safety (most of the incident light is reflected by the metallic surface), the target should also be aligned with respect to tip and tilt. We placed our target on a mirror holder that enabled precise angle adjustments. Lastly, for the target mount it is also of special importance to ensure that the translation stages, in particular the axial one, are well aligned with the laser coordinate system. Otherwise the pinhole might move out of the imaged region of interest during a focus scan.

- (c) The **glass window** requires only tip and tilt degrees of freedom that however need to be particularly robust. Similar to the objective, the glass window requires an angular alignment fidelity of about 0.5 mrad (see Figure 3.43), which is easy to achieve once the mount offers high quality adjustment screws.
 - (d) The **objective** is usually the heaviest and most critical element with respect to alignment and image quality. While the mount needs to be stable and well isolated, it also required 3 robust translation stages with comparably large travel range and fine position control. Furthermore, due to the angle sensitivity tip and tilt degrees of freedom are essential.
 - (e) The **tube lens** is in general not that sensitive to alignment imperfection as they will generally first affect the image position before altering the PSF shape (see Figure 3.42). Nevertheless for the test setup robust, low-travel range x-y translation stages are sufficient with two additional angular degrees of freedom.
 - (f) The **camera** mount does not require designated angular control, however one should make sure that the sensor is perpendicular to the optical axis. Translation control in 3D is required though, in particular for centering on the optical axis, FOV measurements where the sensor cannot capture the whole plane and spherical aberration compensation that requires the axial degree of freedom. In addition, it is useful for the signal-to-noise ratio to put a sufficiently long lens tube on the camera to shield it from stray light.
3. Another consideration is whether to **place the optics on a rail**. In general, as one needs to frequently adjust the position of the parts for re-alignments or optimizations, it is useful to place all elements on rail mounts. This allows for easy axial adjustments, greatly enhanced reproducibility of the setup and exploits the translational symmetry of the setup along the optical axis. In addition, fixed pinhole mounts can thereby be quickly exchanged and displaced axially which helps with the alignment. If one has decided in favor of the rail system, one can also prepare simple labeled rail-sleds to precisely mark and fix the position of every optic. This provides reference and great reproducibility for future alignments. However, mounting all parts on rail mounts takes significantly more time than using simple pedestals to clamp on the optical table. Note that pictures from the mounts used in this work are shown in Appendix D.

4. **Clean** the optics. As the microscopy setup is very sensitive to any irregularities on the wavefront, we need to make sure that the mirrors and the other optics are dust-free and clean. This holds in particular for all optics after the test target.
5. **Isolate the setup from vibrations.** A detailed discussion about the effects of stabilization can be found in Appendix C. To this end, one can
 - (a) Float the optical table
 - (b) Build stable mounts without strong cantilevers, using larger screws, massive parts preferably made out of steel, include proper vibration damping materials
 - (c) Shield the sensitive part of the setup (usually where the beam has the largest diameter) from airy currents by covers or curtains
 - (d) Identify and isolate the main sources of vibrations in the lab
6. Decide on the **laser source** that is to be used. Ideally, the wavelength at which the objective is tested can also be used as the alignment beam for the optical setup. In case the wavelength is not or only barely visible, one can use a well-visible auxiliary beam for alignment and switch to the testing beam for the actual measurements. In case the measurements are to be repeated with different wavelengths, it is useful to overlap both lasers collinear on a dichroic mirror. Then one can easily switch between both wavelengths by blocking the other. Note that this only holds as long as all components are sufficiently achromatic. In case of strong chromatic spherical aberrations, calibrations have to be repeated.
7. Check the **light source stability.** Fluctuating beam pointing can conflict with fixing an alignment for the optical system and intensity instability might lead to over- or underexposed images. Using a beam from the output of an optical fiber usually helps to fix the beam pointing.
8. Ensure the light source is **well-collimated** before starting the alignment process.
9. Prepare one or two **back reflection papers** of different size that help with the observation of lens back reflections. They should offer a large white area centered around a tiny hole in the center that transmits the laser beam. To ensure one only inspects the actual back reflection of certain optics, it is useful to add black aluminum foil/cardboard to the backside of the card. Thereby, artifacts from the laser source will be blocked. Examples can be found in Figure D.2 A-C.
10. Prepare two **labeled alignment pinholes** of about 1 mm diameter to help fixing the beam position. It is important that the pinholes are labeled and the mounts are rigid such that reproducible alignment is ensured. Fixed pinholes on rail mounts determine the height of the optical axis in our setup.

11. **Plan the setup layout** and the mirror positions. Measure at which position the optics need to be placed and decide where to position any required mirrors while keeping enough tolerance for lens position adjustments. It can be useful to have a very long path (3+ meters) before the target position to increase the accuracy of the back reflection alignment for all elements. The distance between objective and tube lens is not particularly important for single-plane imaging and larger distances make the setup more susceptible to mechanical vibrations. However, a $4f$ setup has the advantage that translation alignment is easier, as the beam after the tube lens is collimated for a collimated beam incident on the objective. Since the goal is to reduce the number of optics between the objective and the camera as much as possible, the imaging setup would ideally lie on a straight line of length $\leq 2f_{obj} + 2f_{tube}$. The height of the setup is usually determined by the least-flexible element / mount in the setup, while simultaneously trying to keep it as low as possible. Next one might place the mirrors that will now define the table grid lines along which the optical axis will be oriented. Along those grid lines place the rails where required.
12. **Align the reference beam** onto the pinholes that are placed on the rails by adjusting the mirrors. Now the pinholes and the beam define the optical axis, so one needs to avoid accidentally misaligning the mirrors. For maximum accuracy the pinholes should be placed with great distance to one another at positions that are ideally later still accessible after the other optics are placed.
13. **Place the camera** at its approximate location and adjust its lateral position such that the reference laser hits its center. As this step is essential to fix the camera position to the center of the FOV, the accuracy can be improved by placing a pinhole right in front of the camera. In the case of a field of view measurement, where the camera has to be moved, note down the micrometer positions that correspond to be on axis.
14. **Place the tube lens** about one focal length in front of the camera. Mind the lens orientation as indicated by the manufacturer. Usually, the surface with greater curvature faces the objective to minimize aberrations.
15. **Align the tube lens** starting with its translation by placing a pinhole right in front of the camera. The x-y translation stages can now be used to move the focus of the lens onto the pinhole. On the camera one finds the pinhole as a more or less bright spot whose intensity needs to be maximized in order to perfectly center the lens (see Figure A.6). Alternatively, one can also directly view the beam on the camera, as it was previously aligned to be centered on the optical axis. One needs to be careful though to not damage the sensor and reduce the laser power beforehand.

We continue with the angular alignment of the lens by observing its back reflection on the previously prepared detector card. In case of a strongly misaligned

lens and a comparably small laser beam/hole in the card, we will observe multiple well-separated reflections from the each interface (see Figure A.5 A). Some might be more pronounced than others, depending on the surface coatings. The points will only be clearly separated if the centering of the lens is bad, such that one first needs to optimize its position to overlap them, before continuing with the angular alignment to overlap the single spot with the incident beam. Therefore, in principle the whole lens alignment can be performed relying only on the reflection, however this is more challenging than using the two individual signals from the lens transmission and reflection. For ideal alignment, all reflections overlap and create a radially symmetric concentric ring pattern, also called *Newton rings* (see Figure A.5 B-J). As lenses and objectives are usually anti-reflection (AR) coated, finding the back reflections is easier for larger laser power. It can also be helpful to frequently unblock the beam which makes the reflections blink.

Note that the well-overlapped spot shows a superposition of concentric ring patterns with different frequency. Those originate from the different curvature of the individual surfaces such that the largest spacing corresponds to the interface with strongest curvature and vice versa. The lens is well aligned if *all* patterns overlap in the most symmetric way. This means that extremely long paths for back reflection observation are not feasible since one only views the central rings corresponding to the surface with least curvature to which one aligns the lens. As the single lens however does not contain information about the other surfaces, this approach is risky and misleading. At least a few different fringe frequencies should be visible on the detection card to be sure that one aligns to the correct signal. This also means that because more fringe frequencies and thus more information on the individual lens surfaces is included, for the angle alignment a *larger* input beam size is preferred. This stands in contrast to the naive assumption that a smaller beam should ease optimizing the angular offset from center.

For bad initial alignment, both steps might need to be repeated iteratively, however for good alignment both degrees of freedom decouple such that one can align the lens in only one go. Note that it might not be possible to perfectly align the concentric rings of a certain lens in case its individual surfaces are imperfect to begin with. In Figure A.5 F the reflection of our 1 meter tube lens is shown in a few meters distance and one clearly finds a secondary peak that can never be overlapped with the main rings, indicating a small error in manufacturing. Furthermore, it is important not to confuse the reflections of the lens with light coming from the camera sensor.

16. To **move the camera into the focus of the lens** is rather challenging due to its large focal length. It is recommended to simply place the camera at the theoretically expected position and fine-tune the distance later during imaging.

-
17. **Place the objective** as close as possible to the tube lens to minimize the image shaking in the measurements. Also **vignetting effects** where collimated beams that exit the objective in an angle are clipped by the tube lens aperture is avoided this way.
 18. **Align the objective** similarly as the tube lens. For the centering we use two pinholes (or a pinhole and the camera sensor) where one is placed close to the objective to truncate the beam and the other in front of the camera for reference. Note that for imperfect rails it can be that using the same pinhole at the center of a rail does not fix the same optical axis as placing them at the ends of the rail. Therefore, it can be useful to restrict the pinhole positions to those used to fix the optical axis. While it can be favorable to use smaller pinholes for enhanced precision, due to diffraction and the loss of intensity there exists an optimum for the pinhole size with respect to objective translation alignment. A different strategy for the translation alignment of high-NA objectives is to focus on a bright spot in the center of the transmission signal that is similar to the *Poissonian spot*. It is very pronounced for our 0.9 NA Nikon objective and can be used reliably to track the center of the transmitted beam (see Figure A.6 F-I).

The angular alignment of the objective is identical to lens, however it can be slightly more challenging due to the much larger beam divergence. Furthermore, high-NA objectives composed of plenty individual lenses exhibit much larger coupling between translation and rotation making iteration essential. It can be necessary to block the tube lens reflection before starting the angular alignment.

19. **Place and align the glass window.** In case the mount does not offer translation degrees of freedom, first fix the window height and place it in front of the objective. Precisely measure the distance to the objective such that there is enough space for the target. Align the window angle precisely as this element is the most sensitive along with the objective. To this end we tip and tilt the window until the back reflection lies on top of the incident beam in a distance of at least 2 meters. This is however rather easy to accomplish as the window creates a non-diverging reflection which is easily found and overlapped. It can be useful to block the objective reflection before starting the angular alignment, even though the window reflection should be dominant in any distance. Alternatively, the glass window can be aligned via overlapping concentric rings on the camera or removing coma aberration visible for an imaged point-source.
20. **Optimize camera settings** to use an appropriate exposure, zero gain and the optimal shutter mode.
21. **Wait** until the newly set up mounts have relaxed and double check the alignment afterwards.
22. **Place and prepare the target** in front of the glass plate. Align it on the reference beam and coarsely optimize its distance to the objective. Ensure that all relevant

structures on the chip can be reached with the degrees of freedom offered by the mount. Next it is useful to also align the target perpendicular to the reference beam. Note that for metallic targets their reflection nearly contain the full laser power and need thus to be aligned carefully. This also has the advantage that navigation on the chip is much easier without strong defocusing and all elements in the FOV will be focused simultaneously. To generate a first image, aim on larger structures like stripe-patterns for magnification calibration tests and focus their edges using the axial degree of freedom of the target mount. At this point one can already save a few images to later calibrate the magnification. One can continue by searching for a suitable point-source on the chip while constantly refocusing which is particularly important for high-NA systems.

23. **Improve the signal to noise ratio** to obtain high quality images that can be used for analysis. There are several measures one can take:

- (a) **Turning off the lights** in the laboratory to reduce background light.
- (b) **Covering the setup** to actively shield it from stray light (see Figure C.1).
- (c) **Increasing the laser power** to use the whole dynamic range of the camera sensor. In case the images are saturated, try reducing the exposure time, or inserting an attenuation wheel before the target.
- (d) Placing a **focusing lens** in front of the target (e.g. $f = 60$ mm) that increases the light throughput through the sub-wavelength hole and reduces background on the images that is attributed to **internal back reflections** inside the objective. Those arise when the imaging system is well-aligned and a significant portion of light enters the objective through well-illuminated, yet *non-imaged* areas of the test chart. Thereby, the relative intensity of internal back reflections inside the objectives becomes comparable to the brightness of the actual image of the pinhole, leading to pronounced, off-focus patterns in the image (see Figure A.1).

The lens can be aligned by maximizing the intensity of the pinhole image. Note that perfect focusing is not required, it is sufficient to use the lens only to restrict the illuminated area to the vicinity of the pinhole. An image of a stripe pattern that is inhomogeneously illuminated by the small focus of the lens is shown in Figure A.3. Note that the pinhole is still a few orders of magnitude smaller than the size of the focus.

24. If desired, after the optical alignment we now have the opportunity to systematically **compensate two kinds of aberrations**.

- (a) **Spherical aberrations** that arose from having the wrong camera-tube lens distance as well as those intrinsic to the objective can usually be compensated by adjusting the camera-tube lens distance. Thereby, the image and thus object distances of the imaging setup will change which makes the setup deviate from a pure infinity-corrected imaging system. This leads to

different angles of incidence of the outermost partial waves on the objective and tube lens surfaces which can create positive or negative spherical aberrations. Due to the linearity of the system, they will add up with the existing aberration vector and can thus compensate intrinsic spherical aberrations. However, it is hard to distinguish between wrong camera-lens distance and actual objective aberrations. Nevertheless one can compare the degree of spherical aberrations for different objectives/glass windows by noting down the changing camera/lens position. In practice, we always compensated for spherical aberrations in every setup by conducting a measurement series with changed camera-lens distance and picking the position at which the axial focus scan symmetry is maximized. This procedure is visualized in Figure A.2 and markings from the experiment are shown in Figure A.4.

(b) **Comatic aberration** can also be easily compensated in the case of objectives that are corrected for a glass window. To this end, after initial purely optical alignment, the PSF might suffer from comatic aberration that is for proper alignment of the imaging system completely based on intrinsic aberrations of the objective. This aberration can then be removed by simply turning the glass window until the coma tail vanishes.

25. **Take measurements** like individual well focused images of the pinhole or focus scans as described in Chapter 3.2.1. One can also move the target across the FOV and referencing the images by their relative position to the sensor center.
26. **Analyze the data** with paying special attention to the particularities explained in Chapter 3.5.

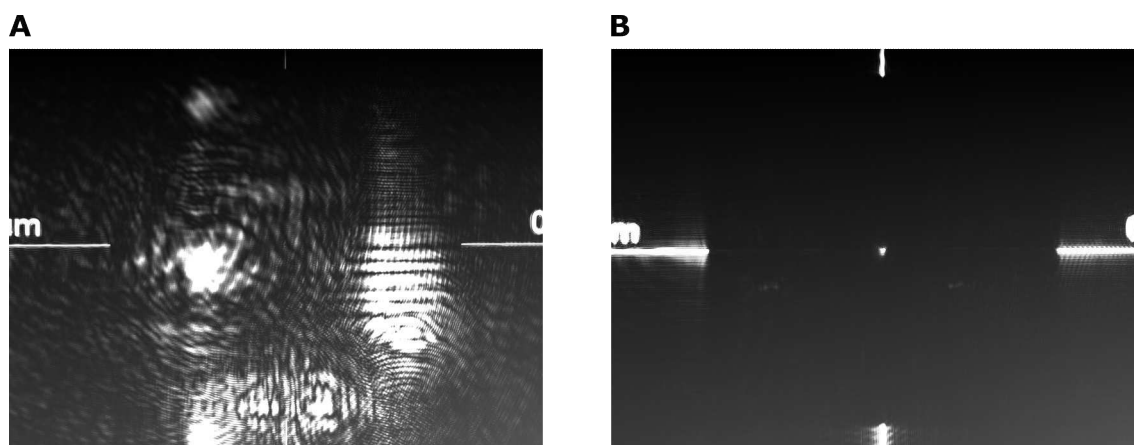


Figure A.1 – Raw camera images from the 250 nm pinhole without (A) and with (B) a $f = 60$ mm lens focusing the beam on the target. The laser power, exposure time, gain and wavelength are the same. A strong impact on the visibility of internal back reflections is observed.

Example pictures from alignment

In Figure A.5 the angle alignment of different lenses is displayed. The picture in A shows the non-overlapping back reflections of the SQM objective for a strongly misaligned horizontal angle. If adjusted, the spots overlap and interfere to create a pattern like shown in B. The asymmetry indicates an alignment that is not yet optimal and needs further optimization. Similarly, in C the reflections are shown on the detector card for a vertically misaligned objective angle. In D, E (F, G) the well-aligned reflections of the 1 m tube lens and the SQM objective are shown respectively for 399 (532) nm light. As the pictures were taken from the same position in the optical setup, one can compare the reduced reflection divergence of the tube lens compared to the objective. The blue and green images were taken about 5 and 3 meters from the reflecting surface respectively. In F the reflection is aligned slightly too far to the right and does not overlap with the incoming beam. Still, as it consists only of three interfaces, the Newton rings are not distorted by the slight misplacement which is in strong contrast to picture C where an immediate scrambling of the pattern is found. Furthermore Newton rings for all three unique pairs of interfaces can be found in F, distinguished by different brightness and fringe frequency. Note that this also allows to spot manufacturing errors as the faint spot in the top right corner that never overlaps with the others, irrespective of the angular or translation alignment. The pictures H and I show the back reflection of the Nikon objective at a distance of 60 cm. Due to the high NA of 0.9, the divergence angle of the reflection is much larger than for the SQM objective with NA 0.7, which makes alignment more challenging. In H a slightly horizontally misaligned and in I a well aligned pattern are depicted. In I we also note the arc to the right of the incoming beam that does not originate from the reflection but is caused by the transmission of the input beam through an AOD (see Figure B.3). In addition there is a tiny ring structure to the top right of the hole in the paper. Most likely, this structure indicates an imperfection of

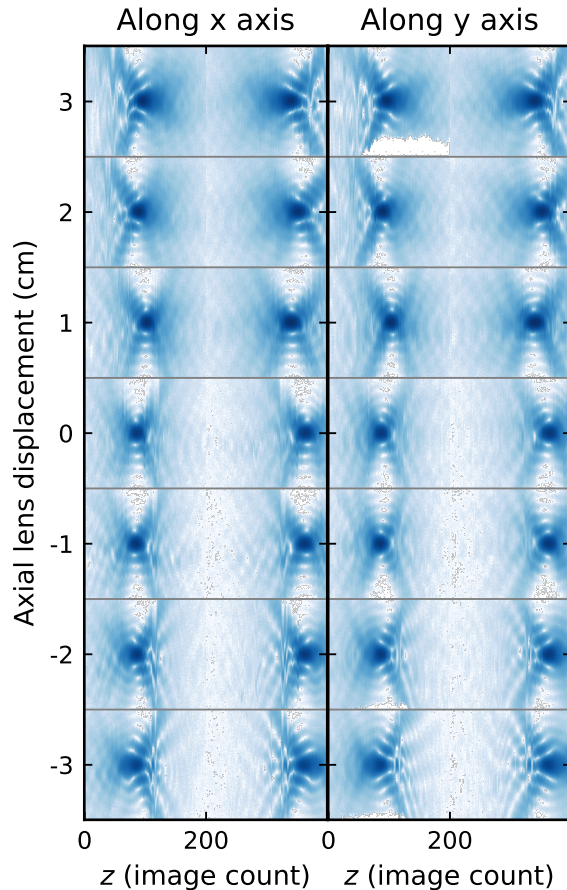


Figure A.2 – Image series demonstrating spherical aberration compensation. In an ideal tweezer measurement series the lens L4 position has been changed in steps of 1 cm. Cuts along the x (y) and z axes are shown on the left (right).

the objective which leads to not all Newton rings being aligned for a perfectly oriented mount. Finally in J a blue light back reflection of the SQM objective 002 is shown after of propagation distance of about 3 meters. The part of the reflection that is not caught by the mirror and is thus not contributing to the pattern in E, illuminates the paper in the back on which well-aligned concentric rings are visible.

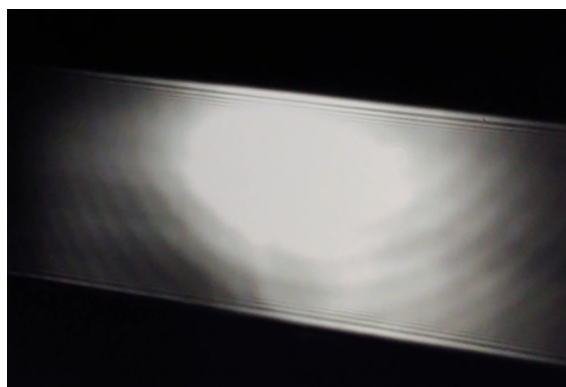


Figure A.3 – An image of a 70 μm wide stripe from the test chart that is illuminated by a tightly focused laser beam.

Examples for translation alignment of different optics are given in Figure A.6. In general, the goal is to translate an optical element until it is centered on the optical axis such that the transmitted beam travels parallel to it. The deviation from a parallel beam is tested in the following. Images A to C illustrate the basic translation alignment steps for an imaging setup as described in Chapter 3.2.1. In A, the reference beam is aligned onto two pinholes that are placed in roughly 2.5 meters distance on a rail, leading to an Airy pattern on the second which is visible in the picture. After the main camera has been positioned, the second pinhole is put in front of it to align the light focused by the tube lens, as shown in B. Picture C shows the transmission of the combined tube lens-objective system for good alignment. Since the transmitted beam after the objective expands rapidly, pinhole one is placed behind it to narrow the beam and make aligning on the pinhole easier. To increase the accuracy of the alignment, the signal on the camera may be used to complement the visual alignment on the pinhole center. The pictures D and E are taken from the auxiliary translation alignment path of the optical tweezer setup as described in Chapter 3.3.1. They show both irises used to align transmitted beams of various sizes starting by the truncating iris in D and followed by the target iris in E that is followed by the auxiliary camera. The inset in E shows an example camera image taken from the initial reference beam alignment. Picture F highlights the "Poissonian spot"-like intensity maximum in the center of the transmitted beam for the Nikon objective. This tiny peak can also be used for translation alignment as it lies on the optical axis due to symmetry considerations. In G this particular spot is used and viewed after the second iris on a piece of paper that is located about 4 meters from the objective. The picture in H illustrates that without closing both irises, the point is still clearly visible at the position of iris 2. In case the paper in G is replaced by the camera shown in E, we can observe the bright

spot in the camera image in I. Note that the Nikon objective imperfection discussed in the last paragraph also appears in transmission (see H and I).

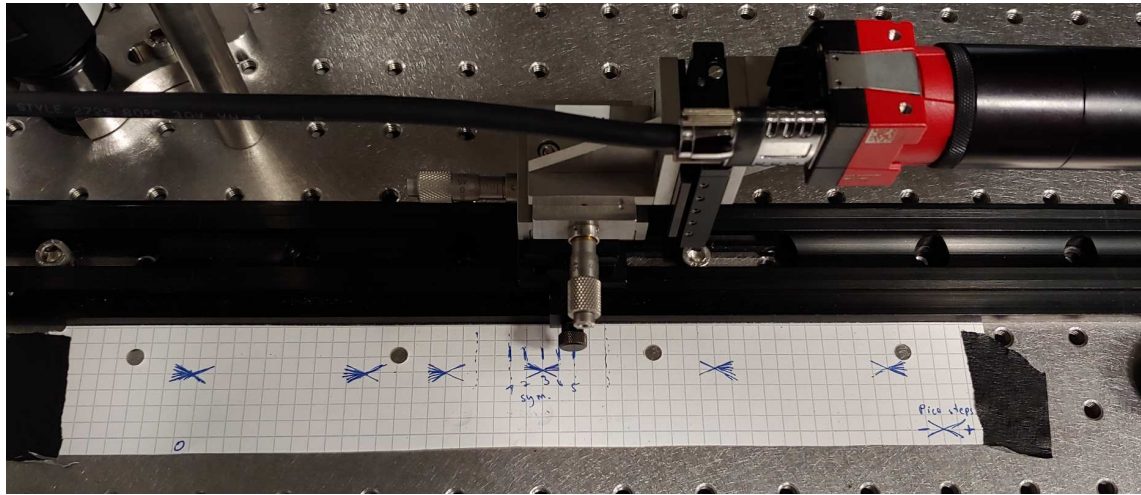


Figure A.4 – Markings on paper used to optimize the camera position to reduce spherical aberrations in an imaging measurement.

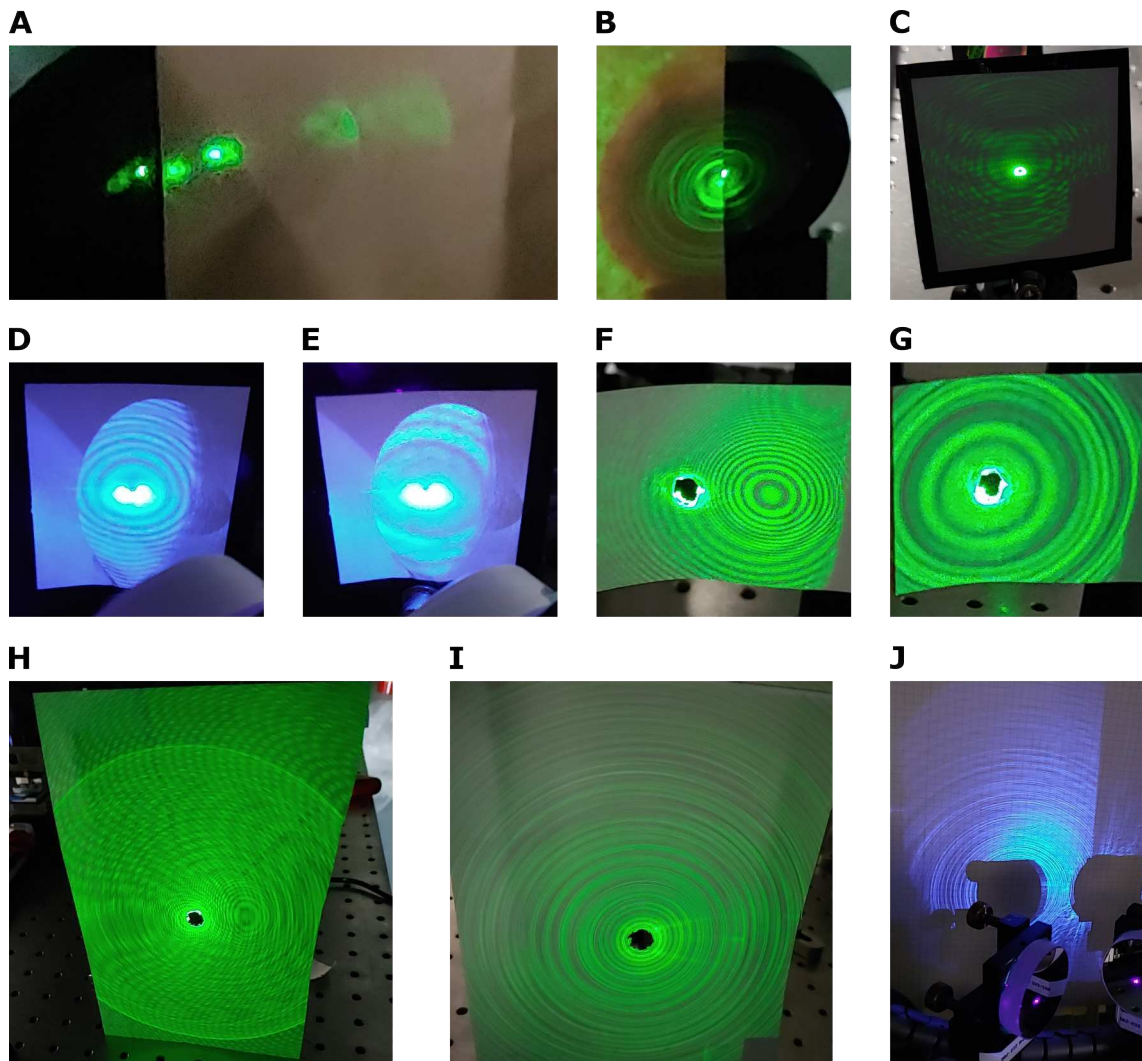


Figure A.5 – Example pictures of back reflections used for the angle alignment of optics. **A** and **B** show badly and well aligned reflections of the individual lenses of the SQM objective at a distance from the reflecting surface that is less than a meter. In **C**, a slightly misaligned reflection from the SQM objective is visible that is viewed in a distance of about 2 meters. **D** and **E** (**F** and **G**) show the reflection of the tube lens and the objective for 399 (532) nm light in a distance of 5 (3) meters from the surface. Nikon objective reflections in a distance of 60 cm are showed for a misaligned and well aligned case in pictures **H** and **I** respectively. In **J** the reflection of a SQM objective is shown for 399 nm light in a distance of roughly 3 meters behind a mirror.

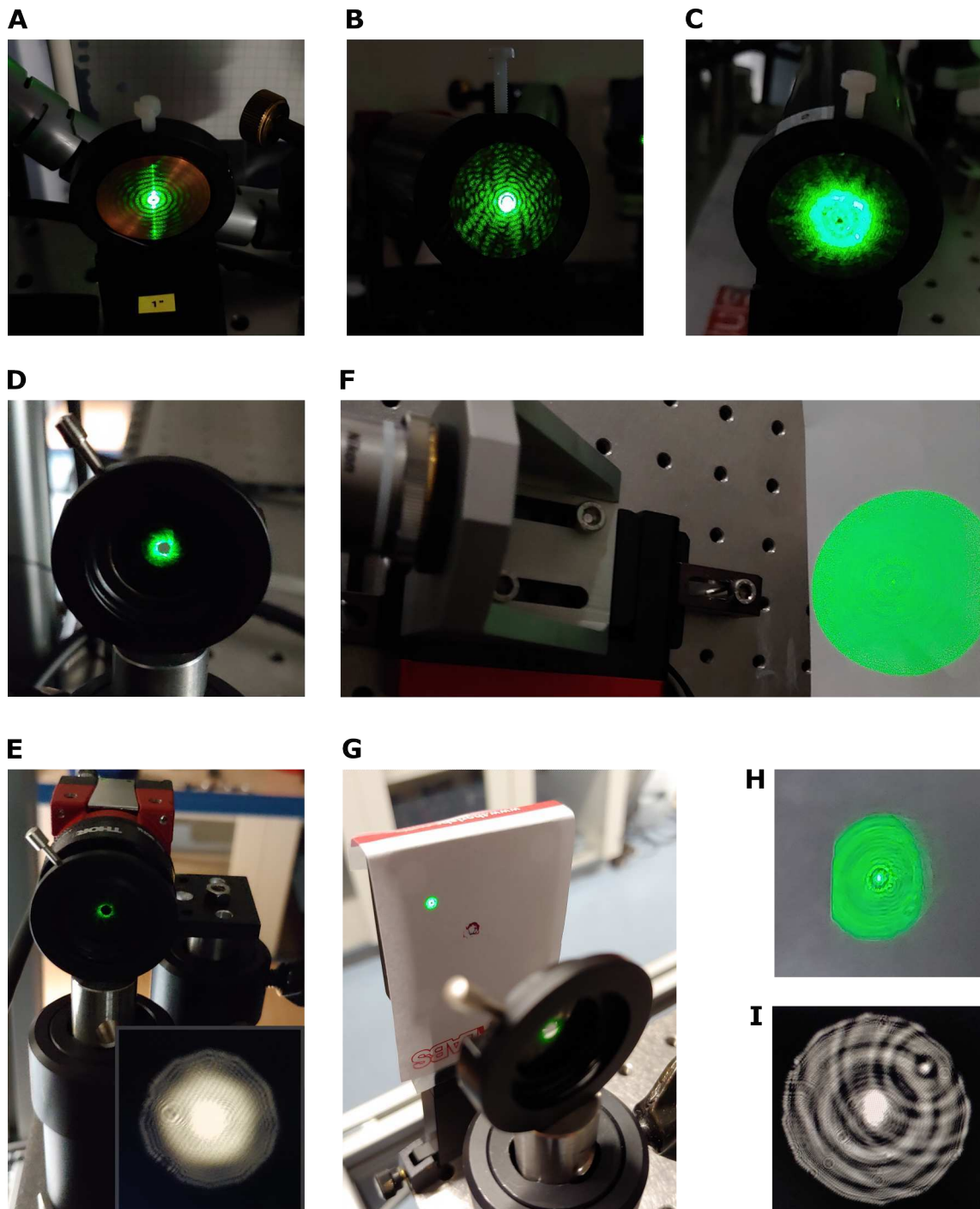


Figure A.6 – Example pictures from translation alignment using the transmitted beam. Pictures **A-C** show the translation alignment process of the imaging setup. In **A** the reference beam is aligned onto two pinholes, the second of which is displayed here. **B** and **C** show the transmission through the tube lens and the through the combined tube lens-objective system on pinhole 2 respectively. Note that in case of the objective, pinhole 1 is placed behind it to decrease the beam size. **D** and **E** display the reference beam alignment on the two irises in the tweezer test setup, with the inset showing the corresponding auxiliary camera image. Pictures **F-I** show how the bright spot in transmission of the Nikon objective can help with alignment. **G** and **H** depict the spot on paper at the position of iris 2 while **I** shows an image of the same on the auxiliary camera.

Construction and alignment of an AOD-based 2D tweezer array setup

In this Chapter, the setup construction and alignment procedure that leads to a 2D optical tweezer array is discussed in detail. We build on the considerations for aligning an imaging system from last Chapter. The setup that we are discussing is shown in Figure 3.17. We will refer to the different elements according to the labelling in the Figure, where each component is numbered according to its count, increasing along the light propagation direction. There exists a few significant differences between the optical tweezer generation and the high-resolution imaging system:

1. The **wavefront quality matters throughout the whole optical system** as is not limited to a certain section as for the imaging case. This means that one needs to plan carefully which, how many and where to place folding mirrors and transmissive optics. In general one aims to use as few and flat optics as possible and tries to place them at position where the beam size is at its minimum. It is advantageous to use a laser beam that is the output of an optical fiber, as this ensures a fairly clean and, for proper collimation, a flat wavefront.
2. The **axial distances of all elements matter** for the final tweezer array geometry. Errors need to be shifted to most irrelevant distance that is the objective-tube lens distance which only affects the optical tweezer relative angle along the axial direction while ideally the in-focus lateral distance is kept the same. It is useful to notice the pattern that collimated beams that have a non-zero relative angle and focused beams that run parallel are alternating in this setup between sections separated by lenses.
3. The **order of alignment changes** as the AOD will deflect the beam even at their center frequency and thus need to be placed and aligned first.
4. For a few lenses the **alignment is more difficult** as back reflections travel through AODs and are thus less accessible (see last paragraph of this chapter).
5. There is a significant **optical power difference** between alignment of the setup and the tweezer measurements, because the whole power of the laser beam is focused into the optical tweezer which stands in strong contrast to the imaging

measurements, where the optical power is restricted to the tiny portion transmitted through a 250 nm pinhole. Therefore, it is necessary to include suitable attenuation elements in the path that should in general be placed before the optical fiber to prevent deterioration of the wavefront.

In the following, an overview is given on the impact axial misplacement has on the generated 2D tweezer array under the assumption that the other position are correct:

1. **AOD1-L1 distance:**

Different axial "origin" of the tweezer array for its two dimensions, leading to rectangular instead of square arrays for square-like input frequency shape. The tweezers will no longer propagate in parallel along the deflection direction of AOD1. Off-axis tweezers will have reduced quality.

2. **L1-L2 distance:**

Collimation of the tweezer beams will not be optimal. This can lead to spherical aberrations and a different axial tweezer position.

3. **L2-AOD2 distance:**

Analog to AOD1-L1 distance.

4. **AOD2-L3 distance:**

The tweezers will no longer propagate in parallel along the deflection direction of AOD2. Off-axis tweezers will have reduced quality.

5. **L3-L4 distance:**

Analog to L1-L2 distance.

6. **L4-objective distance:**

Analog to AOD2-L3 distance.

In general the relative axial positions are sensitive on the order of the inverse distance to the next element. As there a few additional elements in this setup compared to the previously discussed imaging system, mount specifications for additional optics are listed below:

1. The **AOD mounts** require a precisely controllable angle degree of freedom for its orientation in the sound and light wave propagation plane, as this is essential for the diffraction efficiency. Vertical and horizontal displacement is also useful to prevent clipping on the usually rather small clear aperture. Rotation adjustments can also be advantageous to optimize the relative angle between both AODs which governs the lattice angle of the tweezer array. The vertical angle is not particularly important and can usually be left without optimization.
2. In the test setup the alignment of all **lenses** is important in particular for the lenses L1-3 that exhibit a rather short focal length. Thus we equipped them with 3-axis translation and tip/tilt degrees of freedom.

3. The high-resolution **tweezer imaging objective** is a compact, commercial microscope objective that requires a mount with exceptional stability, tip and tilt and lateral translation degrees of freedom and a motorized axial degree of freedom that allows for sub-wavelength scanning of the optical tweezers.
4. While the **auxiliary camera** does not need any degrees of freedom, a long travel range axial translation is required for the **monitoring camera** for distance calibrations. Two transverse translation stages can also be helpful.

As there are plenty of steps involved in setting up and aligning the 2D tweezer array setup, the following list enumerates and comments on the different steps. The process can be divided into three parts: preparation, calibrating and fixing the optimal axial distances and setting up the final system.

1. **Prepare the setup** by placing the folding mirrors, rails and aligning the tweezer beam on the optical axis. The tweezer beam will simultaneously serve as the reference beam for the alignment of all lenses in the setup. Make sure that all mirror positions work with the required lens and AOD distances, while ensuring enough play for axial optimizations and minimal phase error imprints by imperfect optics. It can be useful to place labeled rail sleds to mark the anticipated optics positions.
2. **Calibration of the axial distances**
 - (a) **Place and align AOD2** with paying particular attention to the angle enclosing the sound wave propagation vector and the optical axis. Pay attention to avoid clipping on the small aperture. Finally set the AOD to its center frequency and block the zeroth order behind it.
 - (b) **Align beam on the optical axis** with two additional mirrors.
 - (c) **Align the camera** on pinhole 2.
 - (d) Flip and align **flip mirror F1** and the following auxiliary mirror F2 to direct the beam through both irises. Make sure that the beam is visible centered on the alignment/auxiliary camera.
 - (e) **Build and align the tweezer imaging setup** using back reflection alignment and the previously aligned auxiliary translation alignment path with the irises. Note that it can be advantageous for alignment to prepare a $4f$ setup as the transmission of the objective through the tube lens will then be collimated. Remove the flip mirror from the beam path again.
 - (f) **Optimize the imaging system** by scanning the axial camera position until the test measurements are free of spherical aberrations. *Mark the optimal position.*
 - (g) **Calibrate the imaging system magnification** using suitable stripe patterns from the test target.

- (h) **Characterize the PSF of the imaging system** for this particular alignment.
- (i) **Place and align the glass window** using its back reflection.
- (j) **Place and align the tweezer-generating objective** by observing its back reflection and transmission with the tweezer-imaging system. After optimal focusing, as the beam incident on the objective is small a large tweezer will appear on the camera which can be used for translation alignment.
- (k) **Place and align the second pair of flip mirrors F3 and F4**, such that the transmitted beam passes through both irises.
- (l) **Place and align the lenses of the magnification telescope L3 and L4** starting with L4 and using the reflection and the transmission on the auxiliary camera as the alignment signals.
- (m) Remove the flip mirrors from the optical axis and **create a single high-NA optical tweezer** at the AOD center frequency and image it. Fine-tune the alignment of the tweezer-generating objective.
- (n) **Optimize the magnification telescope spacing** by scanning its distance and recording focus scans of the optical tweezer. *Mark the optimal distance.*
- (o) **Build the tweezer monitoring arm** by placing a beam splitter right after lens L3 and the monitoring camera right in focus of the reflected beam, such that it can be moved in and out of focus using its axial translation stage.
- (p) Generate two tweezer beams close to the edges of the AOD bandwidth. Then **calibrate the AOD2-L3 distance** by scanning it while taking pictures with the monitoring camera that is placed significantly *out of focus*. Take one additional image in focus. As the sketch in Figure B.1 A shows, the AOD-lens distance at which the tweezer beam distance d on the camera is equal to the distance of the beams when the camera is in focus, is the desired distance with a displacement x of zero. In B the measurement data is shown for the cases of AOD1 and AOD2 as a function of different displacements x . The distance as a function of displacement is then plotted in C with a linear fit (orange) and compared to the theoretical and measured spot spacing in focus. The upper plot shows the results for AOD1, the lower for AOD2. Finally, *mark the optimal distance.*
- (q) **Calibrate the L3-L4 telescope-objective distance.** To this end perform a measurement series with three tweezers distributed to cover a large RF frequency range. Move the *entire L3-L4 telescope* relative to the tweezer generating objective along the optical axis. Make sure that the telescope spacing is not changed from its optimal distance calibrated in step (n). This parameter is not very sensitive such that in our setup only a few position spaced by 4 cm were tested. Pick the optimal position where the Strehl ratio of *all three* tweezers is maximized. *Mark the optimal distance.*

Now the 1:1 telescope and the first AOD have to be integrated and optimized with respect to their axial distance. Therefore the alignment of the tweezer beam in the current 1D tweezer array setup will be lost.

- (r) Remove lenses L3, L4, place and align AOD1, L2 and L1. Make sure that AOD1 is set to its center frequency and block the zeroth order. Place a half-wave plate between AOD1 and AOD2 to match the light polarization to the sound wave propagation direction and maximize the transmission into the first diffraction order after AOD2. **Calibrate the 1:1 telescope distance** by collimation of the input beam over several meters. In Figure B.1 D pictures of this process are shown starting with the telescope on the left, the beam size one meter after the telescope in the middle and the beam size after 16 meters of propagation on the right. *Mark the optimal distance.*
- (s) Place and align lens L3 and remove L1 again. **Calibrate the L3-L2 spacing** by collimation of the telescope with AOD2 in place and operating. Note that the laser power needs to be kept low for this step, as lens L2 focuses the beam into AOD2 which could otherwise be damaged. To keep AOD2 between the lenses is however essential as it slightly shifts the focus of L2 and needs thus to be respected during the collimation process. Make sure to move L2 *and* L1 to maintain their distance determined in the previous step. The result for our test setup is shown in Figure B.1 E similar to D. The beam after L3 is a narrow vertical line that originates from the limited acceptance angle of the horizontal AOD. It only diffracts the part of the converging wavefront into the first order that lies in the horizontal center. After 16 meters of propagation the strongly confined direction will have expanded significantly while the vertical direction should be of equal size for ideal collimation. *Mark the optimal distance.*
- (t) Now place L1 back and input two frequencies into AOD1 that lie close to the edges of its bandwidth. Make sure that AOD2 still operates that the center frequency and **calibrate the AOD1-L1 distance** like previously in step p. Results from our results can be found in Figure B.1 B "AOD 1" and C, the upper plot. *Mark the optimal distance.*
- (u) Lastly one can use a 2D tweezer beam grid to **optimize the relative angle of the AODs** by adjusting their rotational degree of freedom. On the monitoring camera the current array geometry can be assessed.

3. Perform the final alignment using the calibrated axial distances from the previous section.

- (a) **Remove all optics again** as their alignment might have deteriorated during the series of axial calibration measurements. In the following, place all optics at the previously marked positions.
- (b) **Place and align both AODs** at their center frequency.

- (c) **Place waveplate 2** ideally right after AOD1 to ease lens alignment and maximize the transmission through AOD2.
- (d) **Place and align lenses L3, L2, L1** in this order. As L3 is going to be removed in the next step, its alignment is only preliminary. Note the paragraph about aligning lens back reflections through AODs that follows this list.
- (e) Remove lens L3 and **align the beam after AOD2 on the rails** using two mirrors.
- (f) **Set up the tweezer imaging system.**
- (g) **Calibrate the imaging system PSF.**
- (h) **Place and align window, objective, L4 and L3** in this order. Use the alignment strategies as discussed in A and the auxiliary camera (see 2.(l)).
- (i) Set the AOD input signals as desired and **create and image a 2D optical tweezer array.**

Following this alignment strategy, spherical aberrations are compensated and additional coma visible on the tweezers can be compensated by turning the window, as it is usually much more stable than turning the whole objective. Note that the order of some of the steps can also be exchanged.

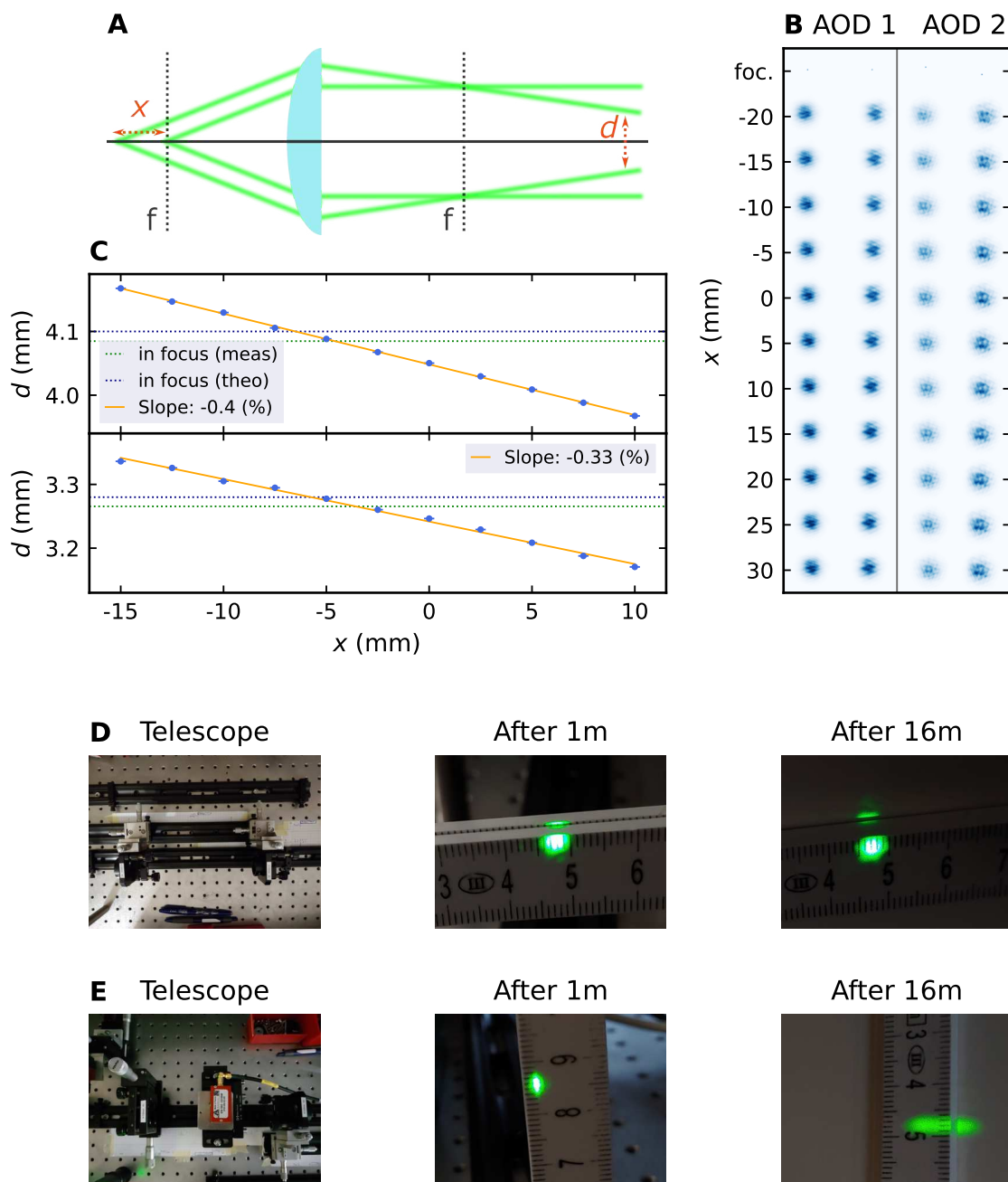


Figure B.1 – Overview of the different axial distance calibrations used for the 2D tweezer array setup. **A** illustrates the working principle of the AOD-lens spacing calibration measurements. The relative AOD-lens position x is changed and the distance d between two extreme beams is measured. If compared to the distance in focus, $x = 0$ can be found. In **B** the raw measurement data for AODs 1 and 2 is shown. The computed distances are plotted in **C** for AOD1 and AOD2 in the upper and lower plot respectively. A linear fit (orange) is applied and the measured and theoretical in-focus distances as indicated by dotted lines. **D** and **E** show pictures of collimation measurements for the telescopes depicted on the left. The beam sizes after 1 and 16 meters of propagation are depicted in the center and rightmost images.

Notes on the alignment of lenses through the AODs

The lenses L1, L2 and L3 are generally harder to align than typical free-standing lenses as their reflection propagates through different lenses and AODs, making it hard to spot. We consider the alignment order L3 (pre-alignment), L2, L1, L3 as required in the above alignment strategy. Translation alignment is not commented on further, as it is not significantly different from the usual procedure.

First it is crucial to understand how lens back reflections propagate through the AOD from which the laser beam came from. In contrast to the tweezer beams, the back reflections diverge more or less strongly along their propagation. This means that their wavefront is significantly curved which leads to a restricted transmission through the AODs to those partial waves that fulfill the diffraction criteria. Since the in-(diffraction-)plane acceptance angle for the first order is strongly limited, all partial waves whose in-plane wave vector projection on the sound wave propagation vector is not small enough, will not be diffracted back into the first order where the input beam came from, but instead will be deflected into the zeroth order. This connection leads to stripe-like back reflections after the AOD as shown in Figure B.2 A. The picture shows how the back reflection of the lens L3 looks like after back propagating through the AOD. The light impinging on the lens is the first diffraction order of the horizontally aligned AOD2. We observe a bright vertical line from the portion of the reflection that fulfills the first order diffraction condition of the AOD that naturally lies on top of the input beam. Furthermore, the characteristic Newton rings are found again, and besides the center maximum additional side-maxima can be seen that arise from almost perfectly phase-matched angles close to the Bragg angle. The complimentary pattern is only transmitted into the zeroth order to the right as the horizontal wave vector projection lies beyond the limits accepted by the AOD. In general, the contrast of the black stripe will be given by the RF signal amplitude that needs to be sufficiently high to ensure a significant diffraction efficiency.

When observing reflections through an AOD, the tip and tilt alignment of the lens can be accomplished by either aligning the center of the Newton rings on the black stripe in the zeroth order, while adjusting its height to the marked beam height on the alignment card, or alternatively by centering the lowest order interference rings directly on the input beam in the first order. Note that the latter strategy is only feasible if the propagation distance is sufficiently large such that the inner interference rings are visible to the eye. Therefore, in general it is recommended to search for the *non-diffracted* zeroth order Newton rings and align those to features that allow for the correct localization, like the above-mentioned black stripe, or the pinhole height of the detection card.

In case it is difficult to find such a reference feature, another approach allows us to find the optimal alignment by inspecting the interference fringe count across the parameter space. Following the triangle inequality, any non-ideal alignment will have an increased optical path and thus number of interference fringes compared to the ideal position. This can be tested by moving the Newton rings over the test paper, observing whether fringes "are generated" from the center and move radially outwards, or whether they are "absorbed" and move inwards. The latter case is desired

and, when followed, leads to the optimum with a stationary fringe count after which the trend flips again.

The picture in Figure B.2 B shows the whole reflection pattern as it was visible for the final setup from Chapter 3.3.1. Both AODs and lenses L1-3 are in place, with the waveplate located right in front of L2, to not clip any of the reflections from L3. We find various features among which the highlighted straight lines are of particular interest for the lens alignment. In *transmission* the same setup does not only create horizontal and vertical combinations of first and zeroth order beams, but also allows for higher diffraction orders with lower intensity as noted in the picture shown in the inset. Using the same numbering we can also identify what is the particular diffraction order combination for a certain pattern in the image. As the lines are caused by light impinging on the AOD at the angle optimized for first order diffraction, the line intersection points determine equivalent positions that correspond to beam alignment on the optical axis. Thus, analog to the previous two paragraphs, the goal is to align the lens back reflections on the crossings of the grid lines.

Furthermore, the pictures C, D and E show the same system, however the number of lenses contributing back reflections was restricted to L1 & L2 & L3, L1 & L2 and L1 respectively. In E, the lens was horizontally misaligned to show the Newton rings in the 1st order.

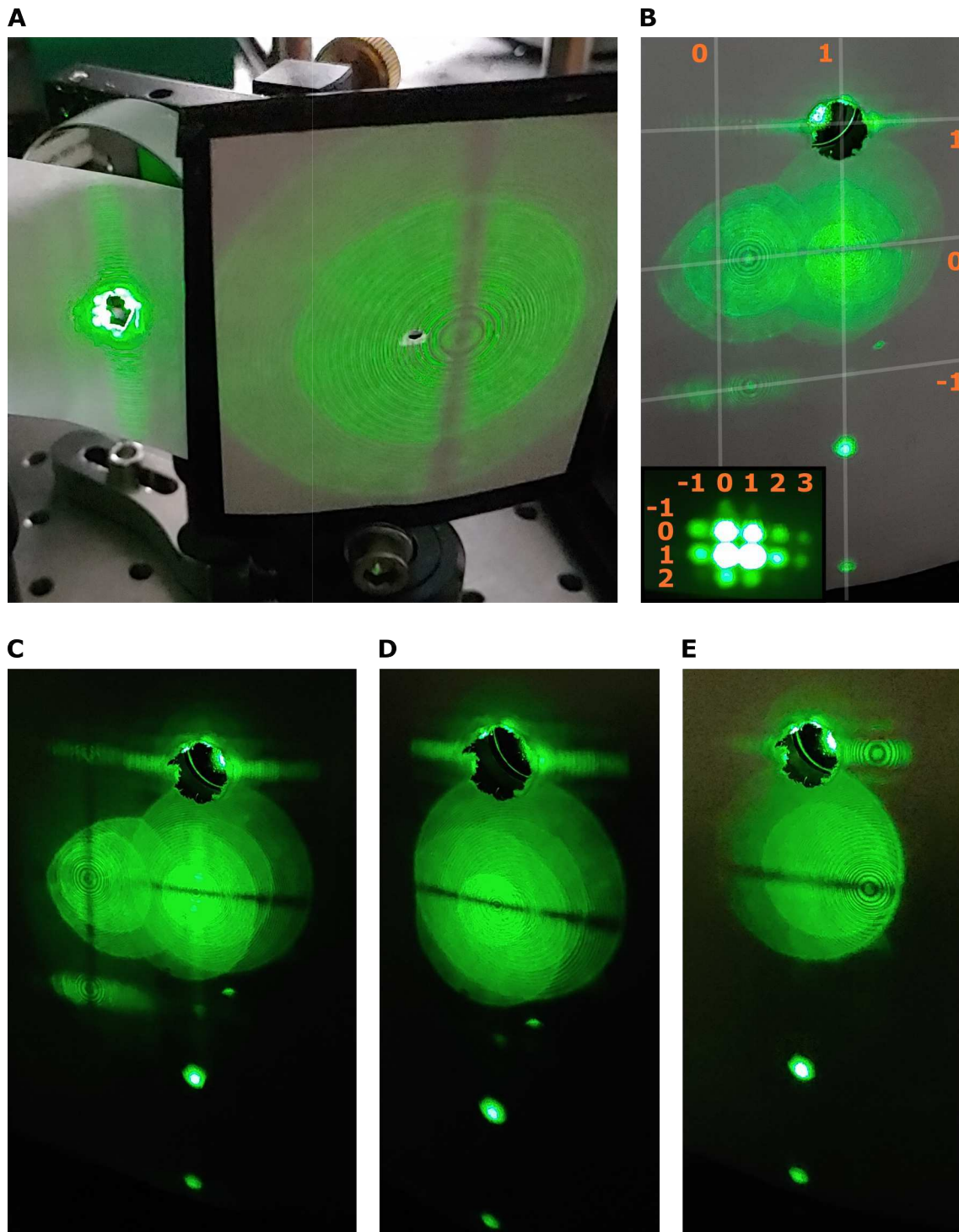


Figure B.2 – Lens back reflections viewed after the 2AOD setup. In **A** the reflection of a lens after a single, horizontally oriented AOD is shown. **B** illustrates the reflection of three lenses (L1-3) from the tweezer array setup, as visible before AOD1. In addition, lines indicate the vertical/horizontal diffraction order that the individual structures belong to. The inset illustrates the *transmission* through the 2AOD setup before lens L3 with the corresponding diffraction order. The pictures in **C-E** are from the same system, however with the back reflection blocked from no, lens L3, and lenses L3 and L2 respectively.

Notes on the beam shape after AODs

In Figure B.3 we inspect the beam shape after transmission through the AODs. In A the magnified tweezer beam ($2w_G/D_0 = 6.28$) without AODs in the path is shown that was used for the "flat-top" measurements in Chapter 3.3.3. The beam is homogeneous and without strong intensity envelope, while the shadow is caused by the 1 m tube lens. In contrast, B illustrates the beam shape as visible for measurements like in Chapter 3.3.4 using two AODs, both operating with a single RF tone at their center frequency. We observe a striking pattern that originates from the AODs and furthermore a significant intensity envelope that is due to the lower magnification that corresponds to $2w_G/D_0 = 0.94$. As comparing the measurements with and without AODs showed, mainly the low spatial frequency Gaussian beam shape affects the tweezer size, whereas the fine, grid-like pattern does not seem to have a significant effect. In case we create a 6x8 2D tweezer array, the different tweezer beams interfere a visible in C. The contour is caused by clipping on the dichroic mirror that was tested in this measurement. As already noted in context of the collimation process in Figure B.1 E, placing an AOD in focus between a 1:1 telescope alters the first order beam. This effect can be viewed clearly in D, where the zeroth order (left) and the first order (right) are recorded simultaneously. The curved wavefront of the focused beam causes the AOD to not homogeneously transmit the beam, but to selectively filter according to the angle of incidence of the partial waves. The first order shows the clear central line where the first-order Bragg condition is fulfilled and whose width is given by the acceptance angle. Further side-peaks can be found as expected to appear in an angle scan of the system. Picture E displays the output of a single AOD for a collimated input beam and relatively high RF signal amplitude. As discussed in Figure B.2 B, we find horizontal diffraction orders ranging from -1 to +3 while +1 is the most intense. Surprisingly, we also observe *vertical* orders different from 0, even though only the horizontal AOD is in operation. When focusing this output by lens L3, we generate the tweezer prototype that is to be imaged and demagnified by the tube lens-objective telescope. The result is shown in F. As expected, all previously observed diffraction orders have converged to sharp foci that are connected by rather faint arc-like structures. The origin of these structures is not clear and is probably connected to the details of the 2D acousto-optic interaction. For the optical tweezers those arcs were also found (see Figure 3.32), but were still significantly darker than the main peak. They scale with the intensity of the higher order peak that they connect such that changing the RF power does not change the *relative* tweezer-arc brightness. Therefore, for quite low RF signal amplitude, orders +2/+3 and their corresponding arcs are not visible.

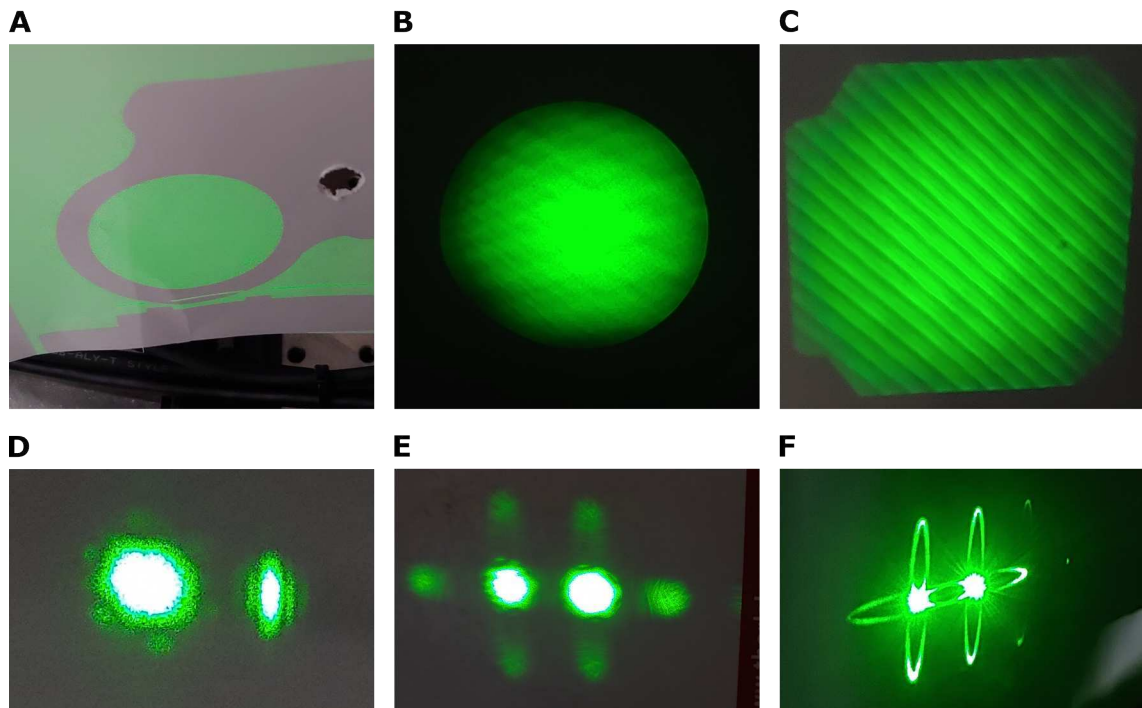


Figure B.3 – The beam shape after propagation through AODs is shown in different contexts. In **A** a magnified ($2w_G/D_0 = 6.28$) tweezer beam is shown with no AODs in the optical path while in **B** the same is depicted for $2w_G/D_0 = 0.94$ and two AODs. The interference pattern of a 6x8 tweezer beam array is illustrated in **C**. In **D** the zeroth (left) and first (right) order beams are shown for an AOD that is placed in focus of a 1:1 telescope. **E** shows the transmitted beams of a horizontally oriented AOD for high RF power which are focused by a lens in **F**.

Setup shaking and stabilization

As initially system stability was a severe problem, we conducted a series of measurements to find the origin of the shaking and to stabilize the setup to be less sensitive to exterior influences. Figure C.2 shows the results of a variety of shaking test measurements with different environmental conditions. To this end, different image series recorded of a $0.5\ \mu\text{m}$ and a $20\ \mu\text{m}$ pinhole have been taken over certain time intervals to compute the deviation of the peak position from its mean over the whole image set. The center position of the peak was determined using a Gaussian fit approach and a center of mass calculation. The results were averaged and are plotted as color coded histograms separately for the directions perpendicular and parallel to gravity.

The changes of experimental conditions included observation over different periods of time and slightly improved mount damping (see next Section) that were both omitted in the Figure labels as they had close to no impact on the observed shaking. Quantities that had a striking impact are listed and assessed as follows:

1. **Air conditioner.** The air conditioner in the lab could be turned off for a few measurements as labeled by *AC on/off*. We noticed that it was the main source of vibrations and strongly affected the pinhole shaking to deviations exceeding 100 nanometers in most cases.
2. **Objective-tube lens distance.** Since the separation of the objective and the tube lens does not matter in the pure imaging setup, we reduced it from the rather long "4f" setup distance denoted by *SD* - *small distance* in contrast to *LD* - *large distance*. Even for turned off AC, reducing this distance over which the collimated beam propagates with a diameter of 35 mm from 1 meter to only roughly 20 centimeters had a significant effect, as visible in the $20\ \mu\text{m}$ pinhole measurements.
3. **Setup shielding.** The most important active countermeasure that has been taken was to shield the setup using improvised cardboard *covers*. The inclusion of the covers lead to a factor of 3 to 4 decrease in the pinhole shaking standard deviation. It was double checked that air fluctuations and currents indeed contributed the most to the instabilities that we observed. As expected, shielding the 1 meter propagation distance near the camera "cam covered" was more effective than only covering up near the objective and the tube lens "obj covered",

which only corresponds to a protected path of about 20 cm. A picture of the shielding built from cardboard for this work is depicted in Figure C.1.

4. **Curtain closing.** The optical table where the setup was prepared offered curtains that could be closed for setup protection. We found that comparing closed with open curtain measurements, the shaking amplitude has again decreased on average by an additional factor of 1.5 to 2.

Even though the image position fluctuations were quite strong, they were assumed to have not strongly impacted the overall image quality, as they mostly created a global shift of the image rather than distorting it. However, this was not tested in greater detail. Note that the shielding was only applied to the imaging measurements, as the tweezer test setup did not provide enough space to place the cover.

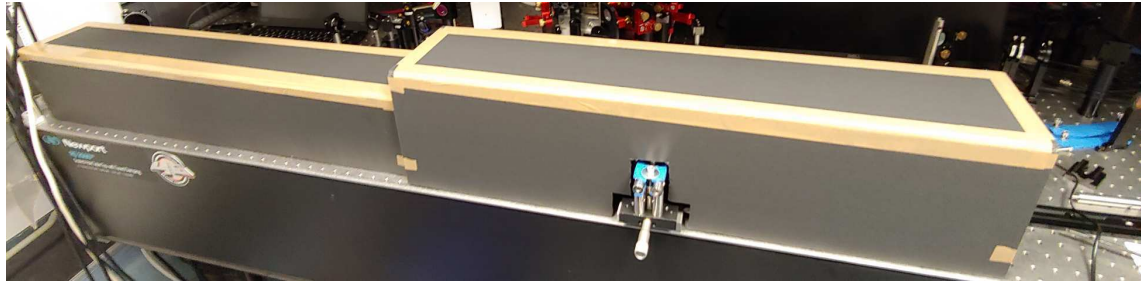


Figure C.1 - A picture of the two cardboard covers used for shielding and stabilizing the high resolution imaging measurements.

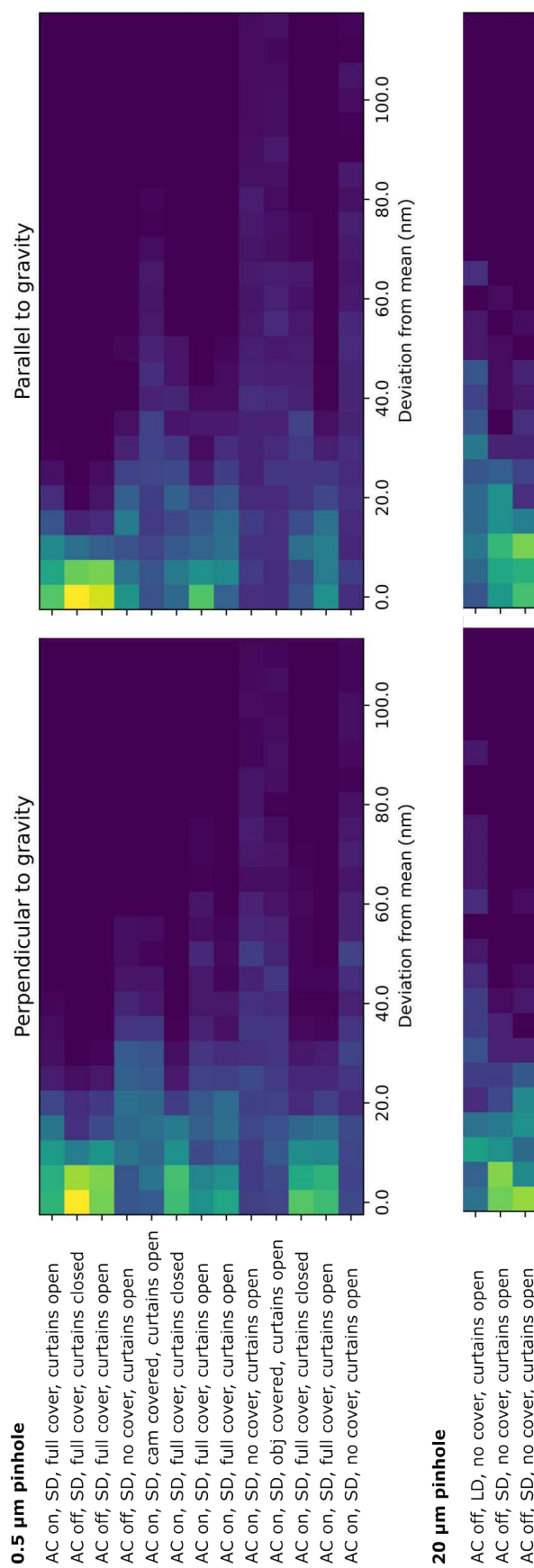


Figure C.2 – Imaging stability and shaking analysis. Histograms showing the pinhole position deviations from mean for a variety of measurement conditions.

Custom mounts

This chapter gives an overview of the self-build mounts used in this work. Only the final versions that were used most frequently are shown. Most mounts have been improvised using different parts from a lab that was being emptied at the time the mounts were built. In Figure D.1, picture A shows the focusing lens mount and B-D depict the target mount. Note the red picomotor for translations in the axial direction. To increase its stability and compactness, it contains a few parts that were custom designed and built by the university machine shop and are shown in more detail in D. In E the camera mount is shown while in F the objective mount is depicted. G shows the glass window holder and H and I display pictures of the tube lens mount. The picture in J displays a typical pinhole holder that is suitable for positioning on a rail. This part limited the beam height in our setup. The 20 μm pinhole that we used for the shaking analysis measurements, can be exchanged with any other pinhole, such as the 1 and 0.5 mm metal pinholes used in this work.

In Figure D.2 A to C illustrate white paper detector cards with a hole in the middle to ease back reflection viewing. Note that they are improved using black aluminum foil on their back to shield any speckle pattern from the light source. The D and E show the vertically oriented AOD1 and the horizontally oriented AOD2 mount respectively. Both are placed on a manual 5-axis translation stage¹. In F the monitoring camera mount from the tweezer setup is displayed and in G both holders for the L1-L2 telescope are shown. Finally, the image in H displays the Michelson interferometer setup used for picomotor step size calibration in Chapter 3.1.

¹Newport, 9081-M Five-Axis Aligner

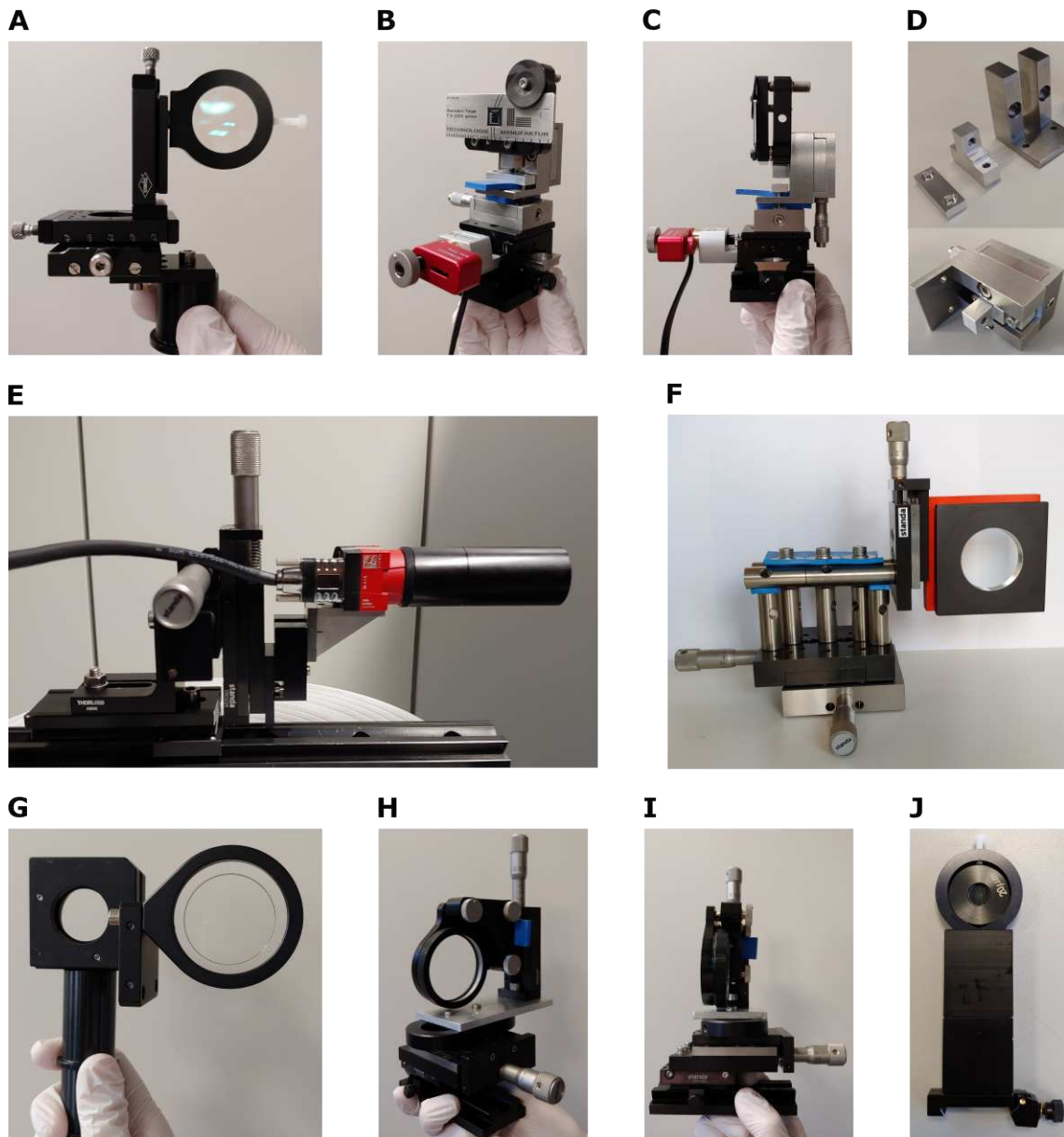


Figure D.1 – The first part of the relevant mounts and optics holders build and used in this thesis. A shows the focusing lens and the picture B-D illustrate the target mount. In D the custom made parts are highlighted. E displays the main camera mount while in F the objective mount is shown. The picture in G displays the window mount and H and I show the tube lens mount. The pinhole holder is shown in J.

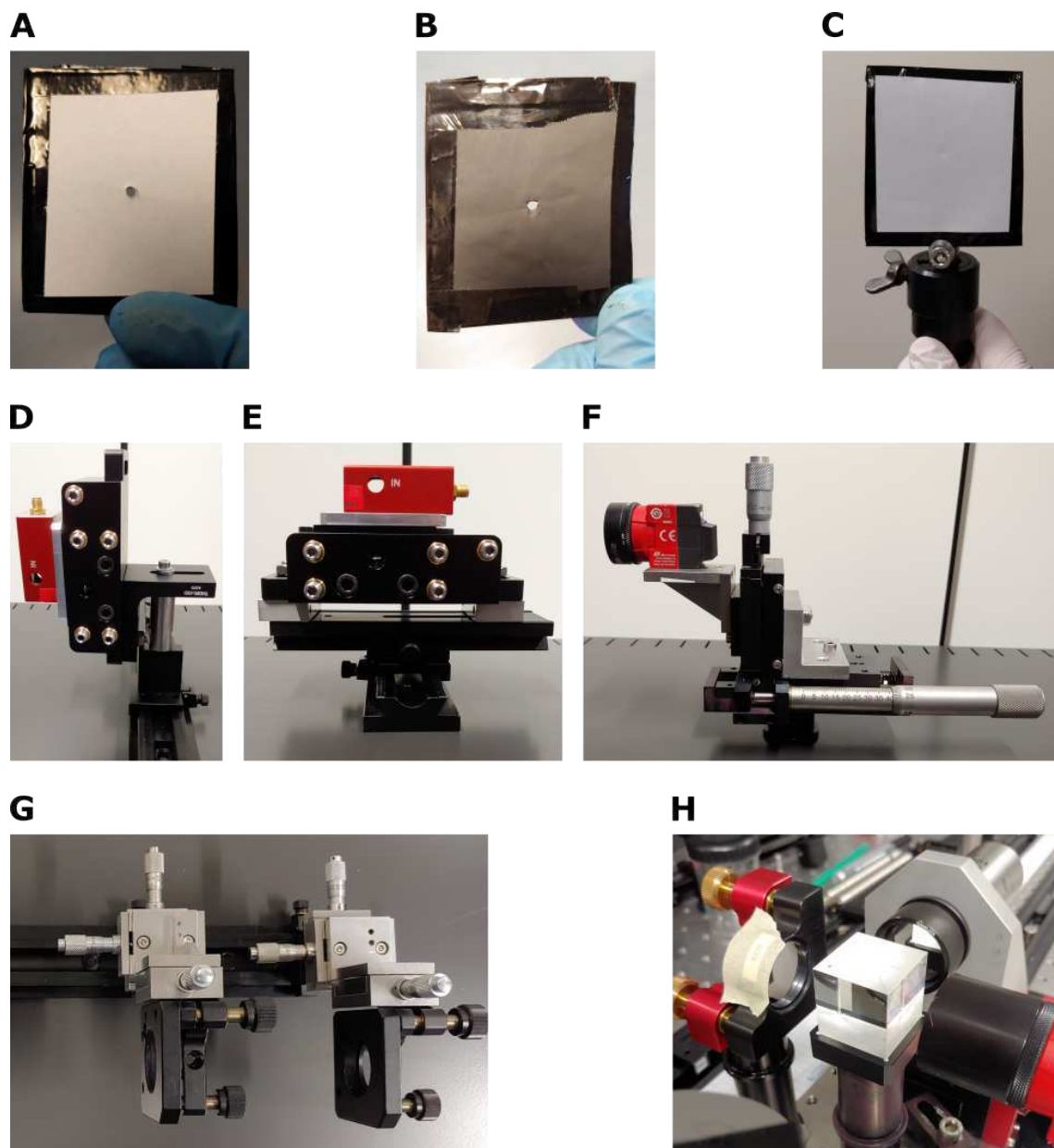


Figure D.2 – The second part of the relevant mounts and optics holders build and used in this thesis. The pictures **A-C** illustrate detector cards build for observation of back reflections. Note that **B** shows the backside of **A**. In **D** and **E** the vertical and horizontal AODs are depicted respectively. In **F** we find the monitoring camera from the tweezer setup and in **G** the 1:1 telescope lens holders. The picture in **H** shows the Michelson interferometer setup used for step size calibration in Chapter 3.1.

Cs objective tests

During this work, we also tested one of the main objectives from our neighboring lab the Cesium (Cs) experiment. As this objective did appear to not perform according to the specifications, it was test in our test setup before and after being sent back to repair. In this Section, the results are summarized. First, Table E.1 provides an overview of the ideal parameters for the objective that has an numerical aperture of 0.8. The results, separated into before and after repair, are then given in Table E.2. The corresponding scan analyses are shown on the following four pages. We find strong astigmatism before repair that wave removed mostly thereafter such that only trefoil aberration remained visible as for SQM objective 002. According to these tests, after repair the objective is diffraction-limited for $\lambda = 532$ nm.

Wavelength	532 nm
Numerical aperture	0.8
Rayleigh resolution ξ (nm)	405.6
Radial waist w_r (nm)	279.3
Axial waist w_{ax} (μm)	1.14
Strehl ratio	1

Table E.1 – Cs objective expected point spread function characteristics

532 nm light	original	repaired
Resolution min, max ξ (nm)	408.5(28), 437(3)	396.4(23), 427.0(24)
Radial waist min, max w_r (nm)	283.0(19), 302.2(21)	273.5(17), 293.2(18)
Axial waist w_{ax} (μm)	0.92(4)	0.96(3)
Strehl ratio (with all corrections)	0.826(16)	0.913(11)

Table E.2 – Cs objective imaging test results

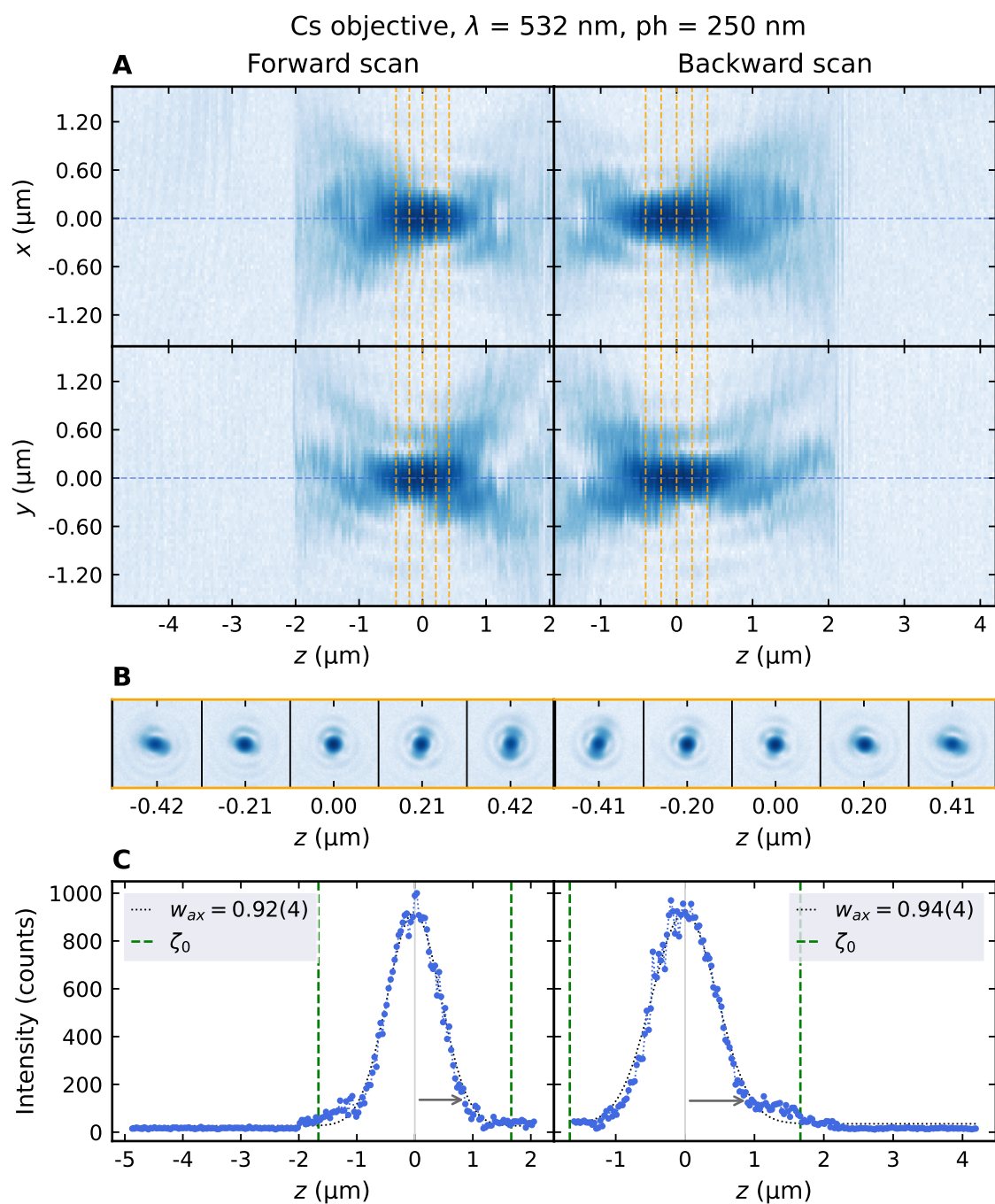


Figure E.1 – Imaging measurement with Cs-lab objective (old): Tweezer shape. The Figure has the same structure as Figure 3.5a.

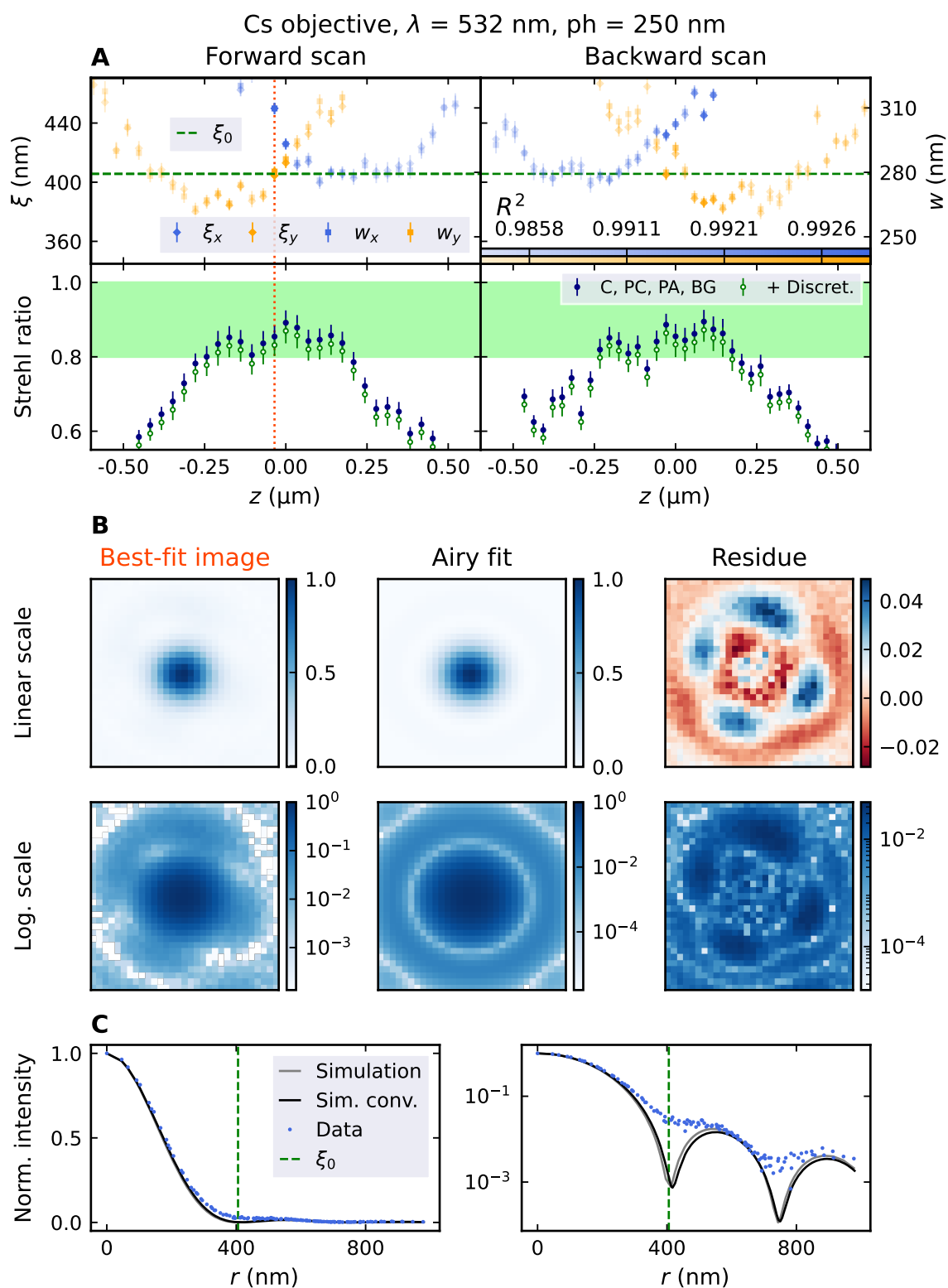


Figure E.2 – Imaging measurement with Cs-lab objective (old): Tweezer analysis. The Figure has the same structure as Figure 3.6.

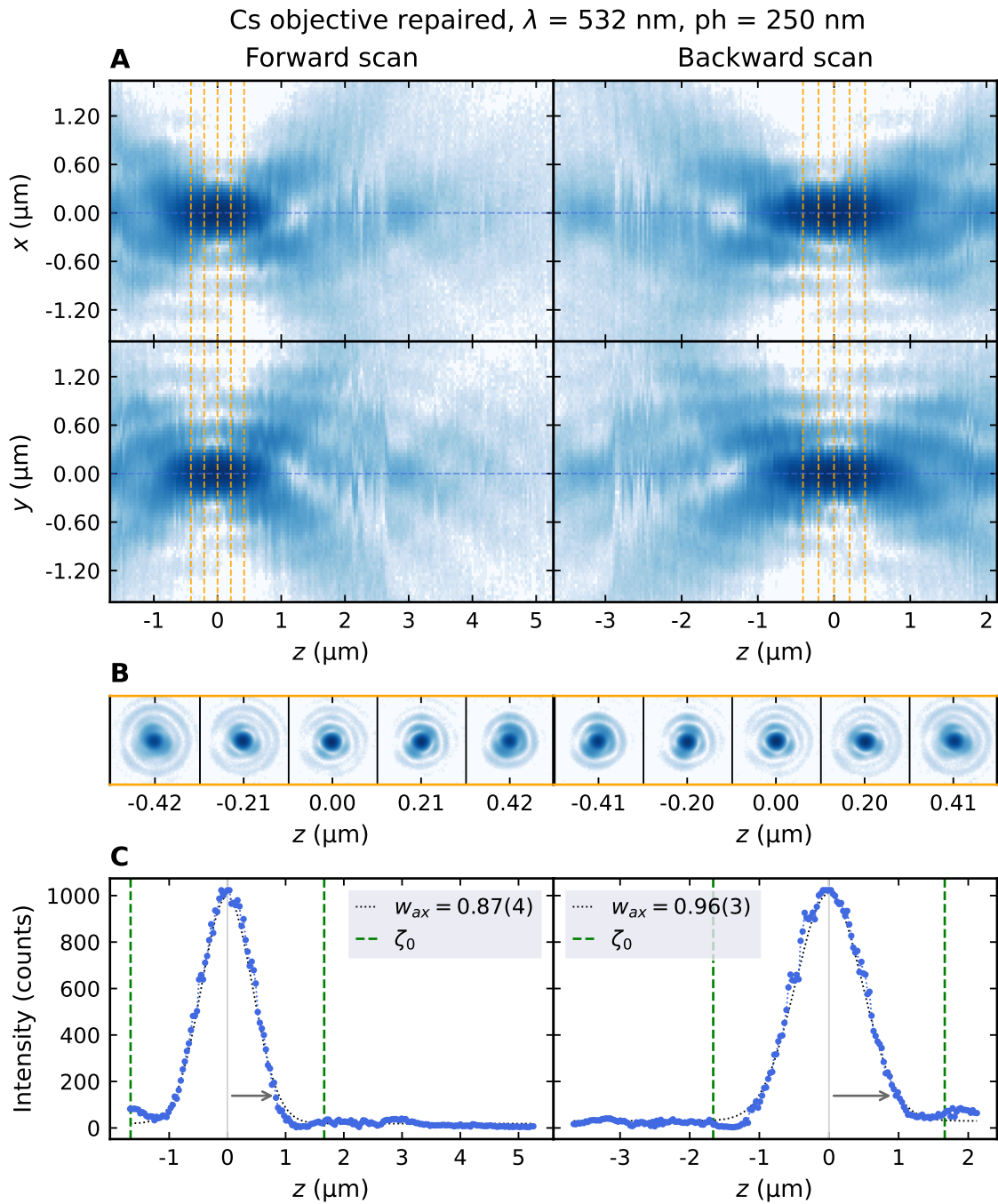


Figure E.3 – Imaging measurement with Cs-lab objective (repaired): Tweezer shape. The Figure has the same structure as Figure 3.5a.

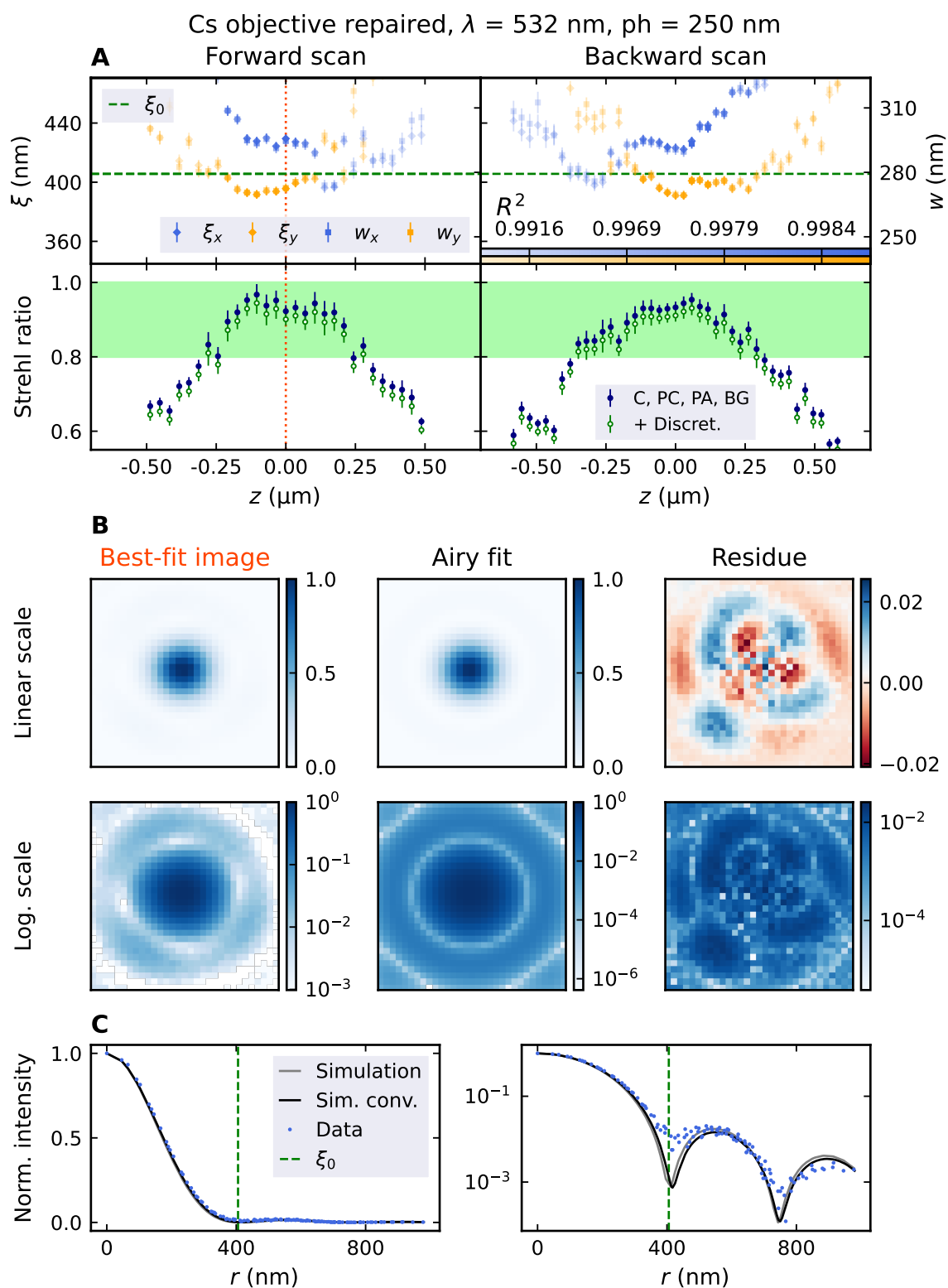


Figure E.4 – Imaging measurement with Cs-lab objective (repaired): Tweezer analysis. The Figure has the same structure as Figure 3.6.

APPENDIX F

Ideal and aberrated example scans

In this Section, we show selected examples that exhibit no, spherical, comatic and astigmatism aberrations. The purpose of these plots is to visualize measurement data of extreme cases of certain aberrations which can be directly connected to the analysis results. The different measurements are taken from the following source:

1. **Ideal PSF/tweezer.** This data corresponds to a diffraction-limited simulation of the ideal pattern. It was computed using Fresnel propagation of the light field expected in the focus of a homogeneously illuminated objective. The simulation parameters are: $NA = 0.7022$, $\lambda = 0.532$ nm, a pixel size of 3.45 μm and a magnification of 150.
2. **Spherical aberration example.** This data originates from an ideal tweezer measurement with objective 002 during a measurement series where the spherical aberrations were to be compensated.
3. **Comatic aberration example.** The measurement was conducted with objective 002 and an ideal tweezer, and is taken from the window-tilt measurement series.
4. **Astigmatism aberration example.** A 532 nm imaging measurement with objective 002 is displayed, where the beam was reflected off a severely curved dichroic mirror before imaging onto the camera.

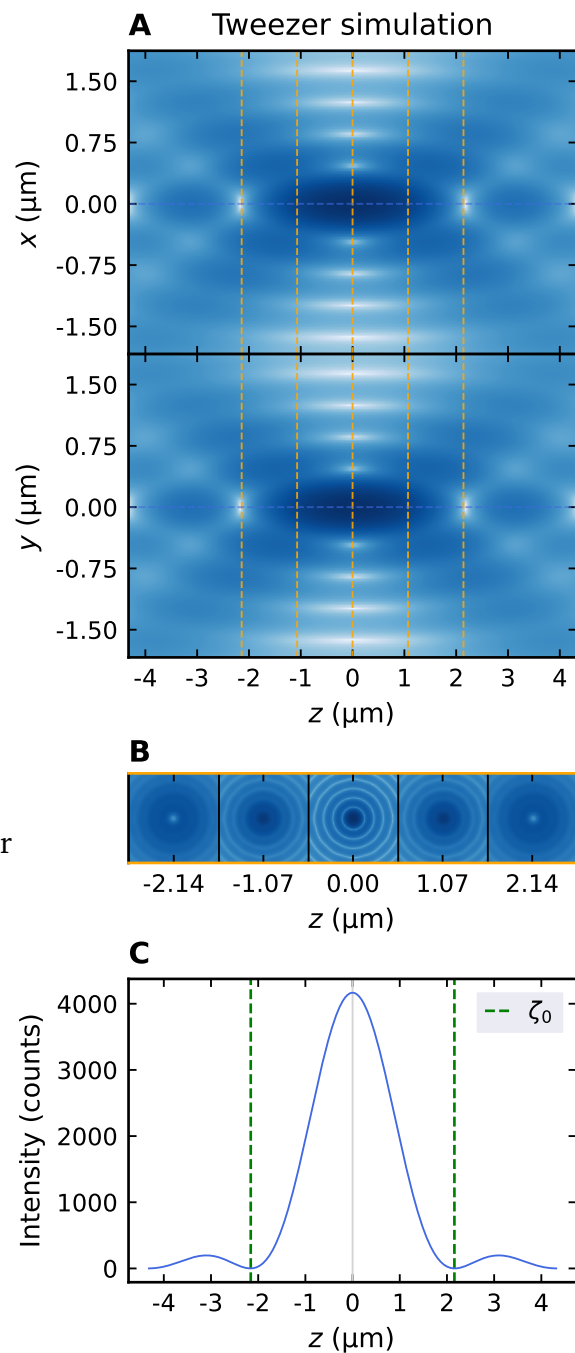


Figure F.1 – 3D simulation of a diffraction limited tweezer/PSF: shape. The Figure has the same structure as Figure 3.5.

The analysis of the ideal tweezer provides the interesting insight that the analysis code does recover the expected values in focus and predicts the distribution in the axial direction. It is unclear, why the residue image looks like secondary quadrafoil aberration, possibly some artifact from the simulation.

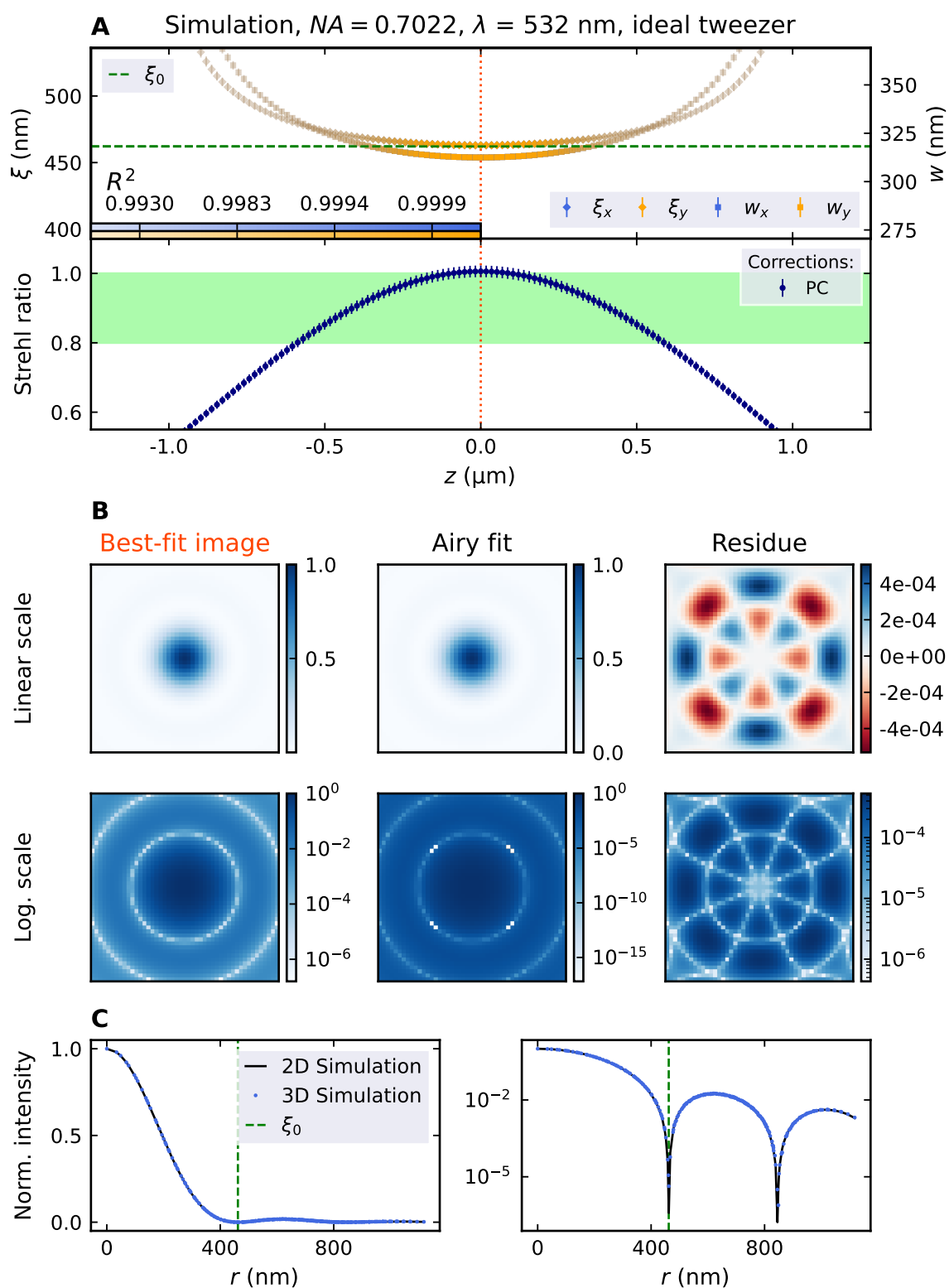


Figure F.2 – 3D simulation of a diffraction limited tweezer/PSF: analysis. The Figure has the same structure as Figure 3.6.

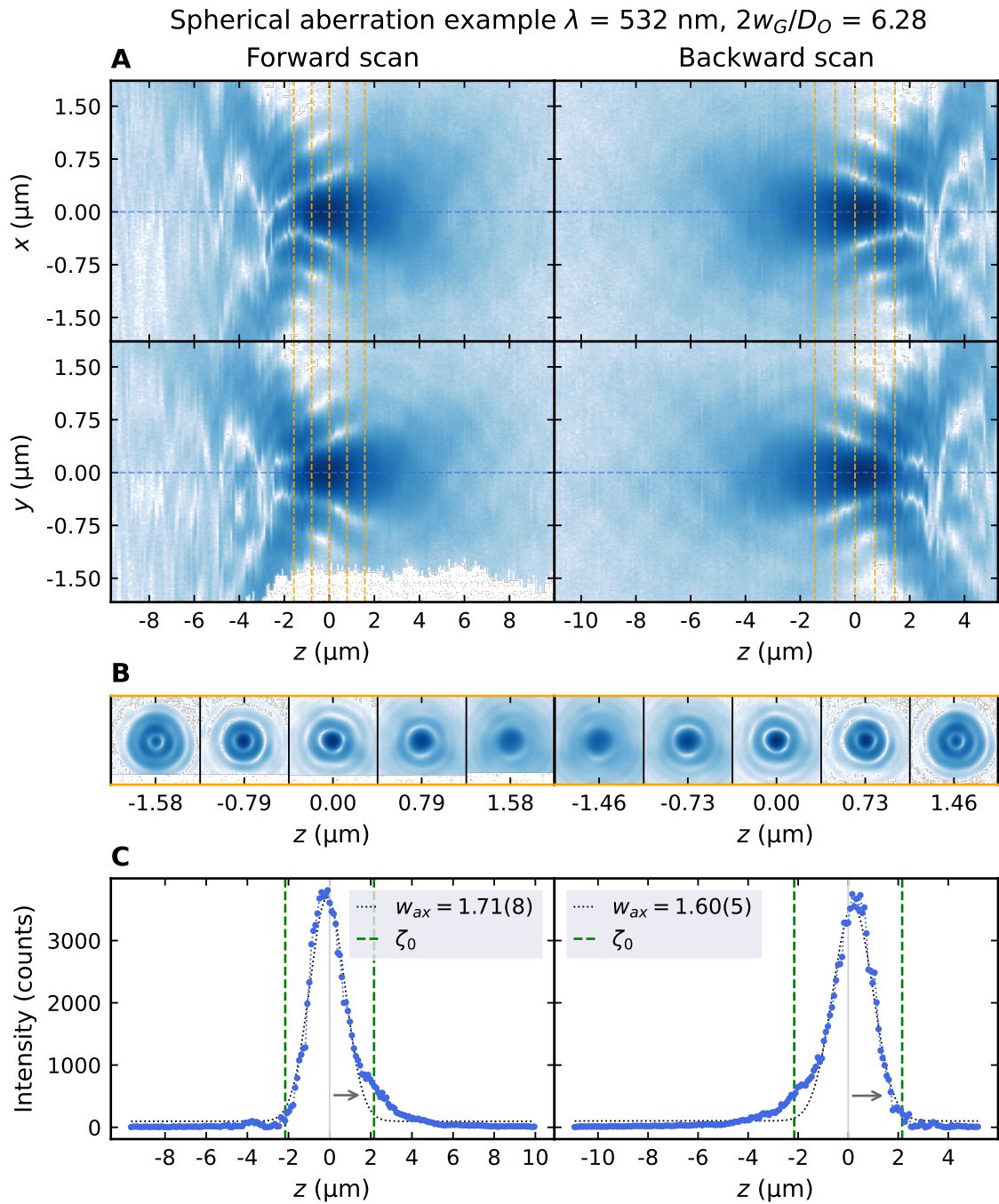


Figure F.3 – Single tweezer spherical aberration example, no AODs, $2w_G/D_0 = 6.28$, objective 002: Tweezer shape. The Figure has the same structure as Figure 3.24.

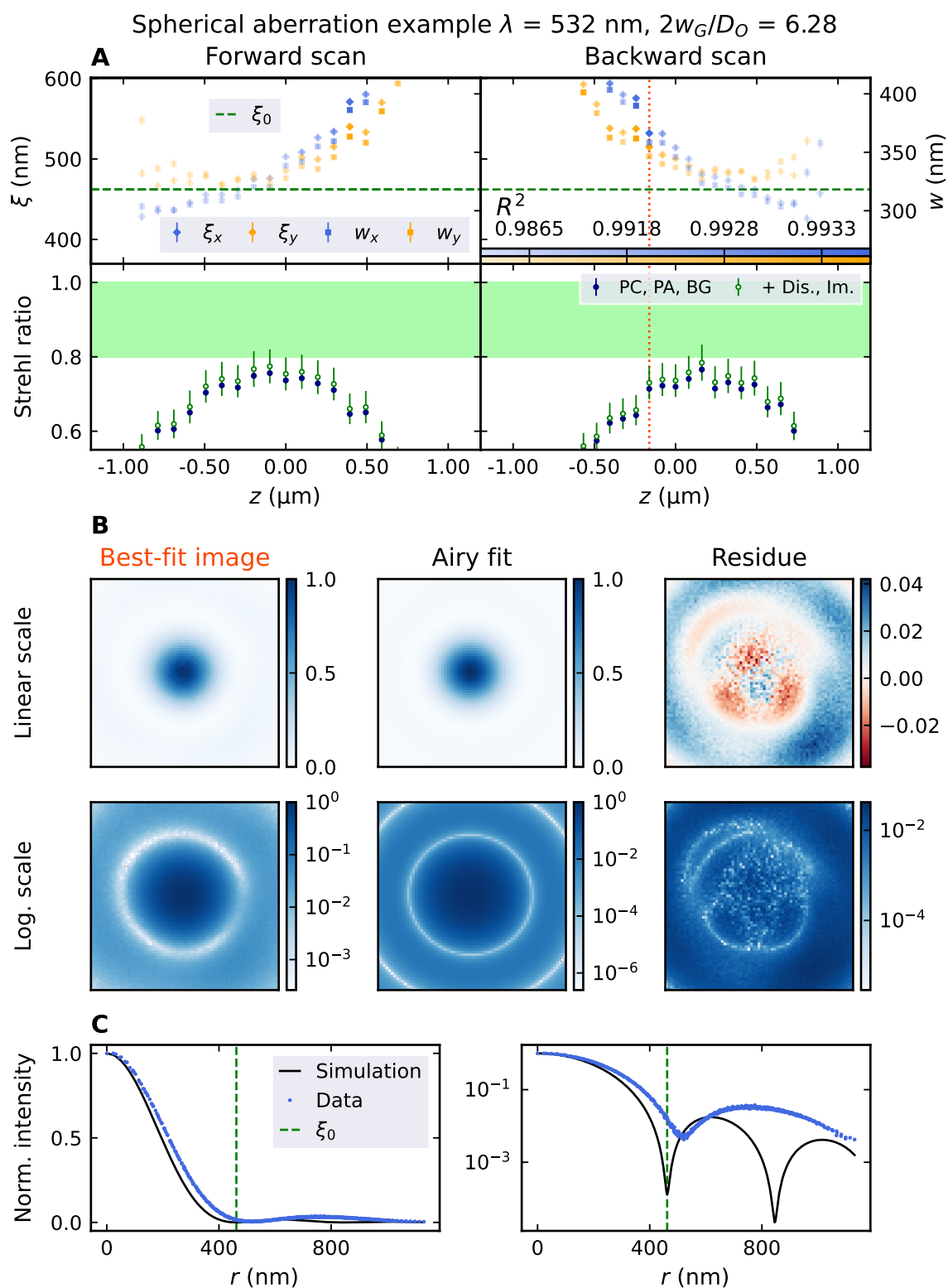


Figure F.4 - Single tweezer spherical aberration example, no AODs, $2w_G/D_0 = 6.28$, objective 002: Tweezer analysis. The Figure has the same structure as Figure 3.25.

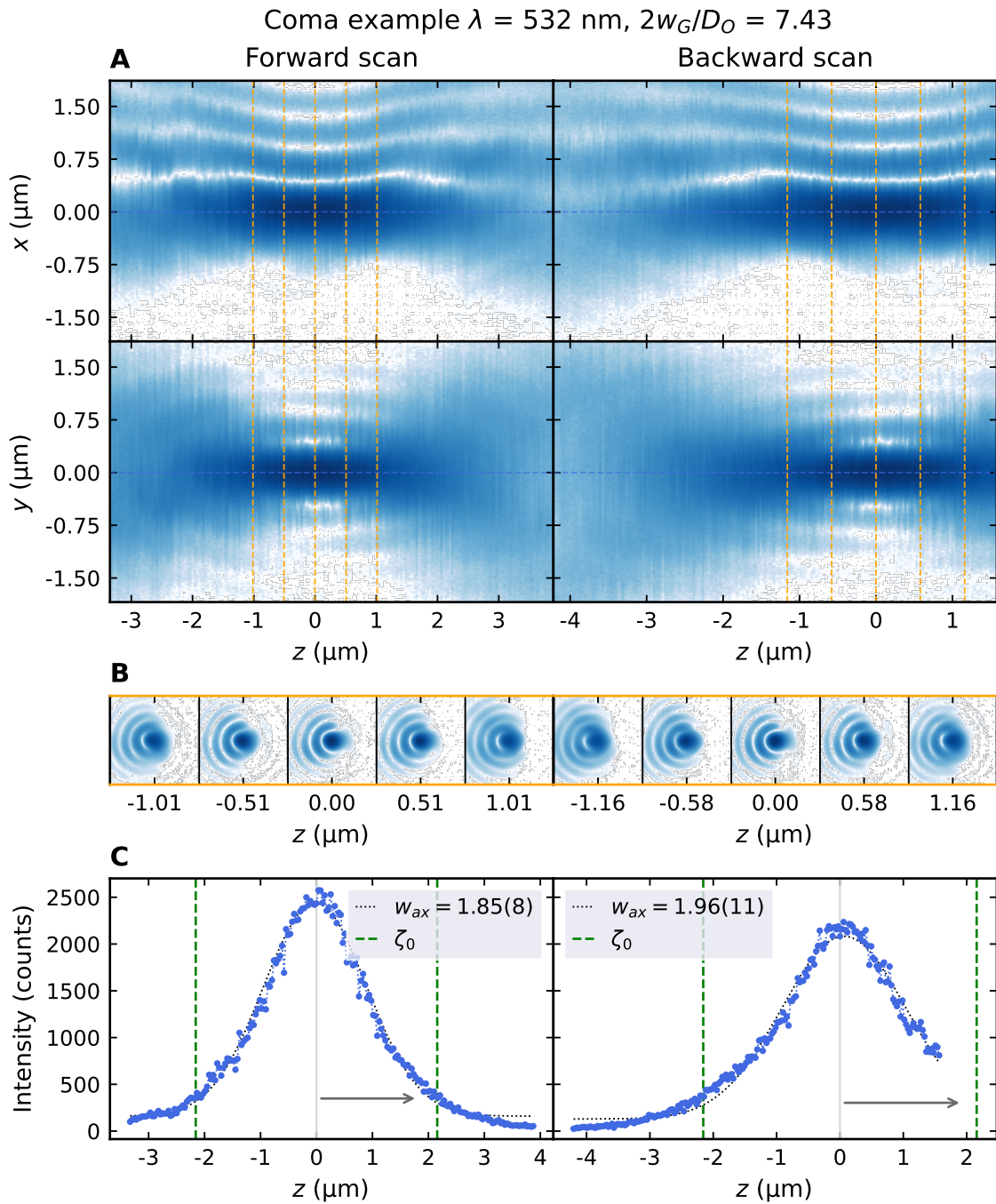


Figure F.5 – Single tweezer coma example, no AODs, $2w_G/D_0 = 7.43$, objective 002: Tweezer shape. The Figure has the same structure as Figure 3.24.

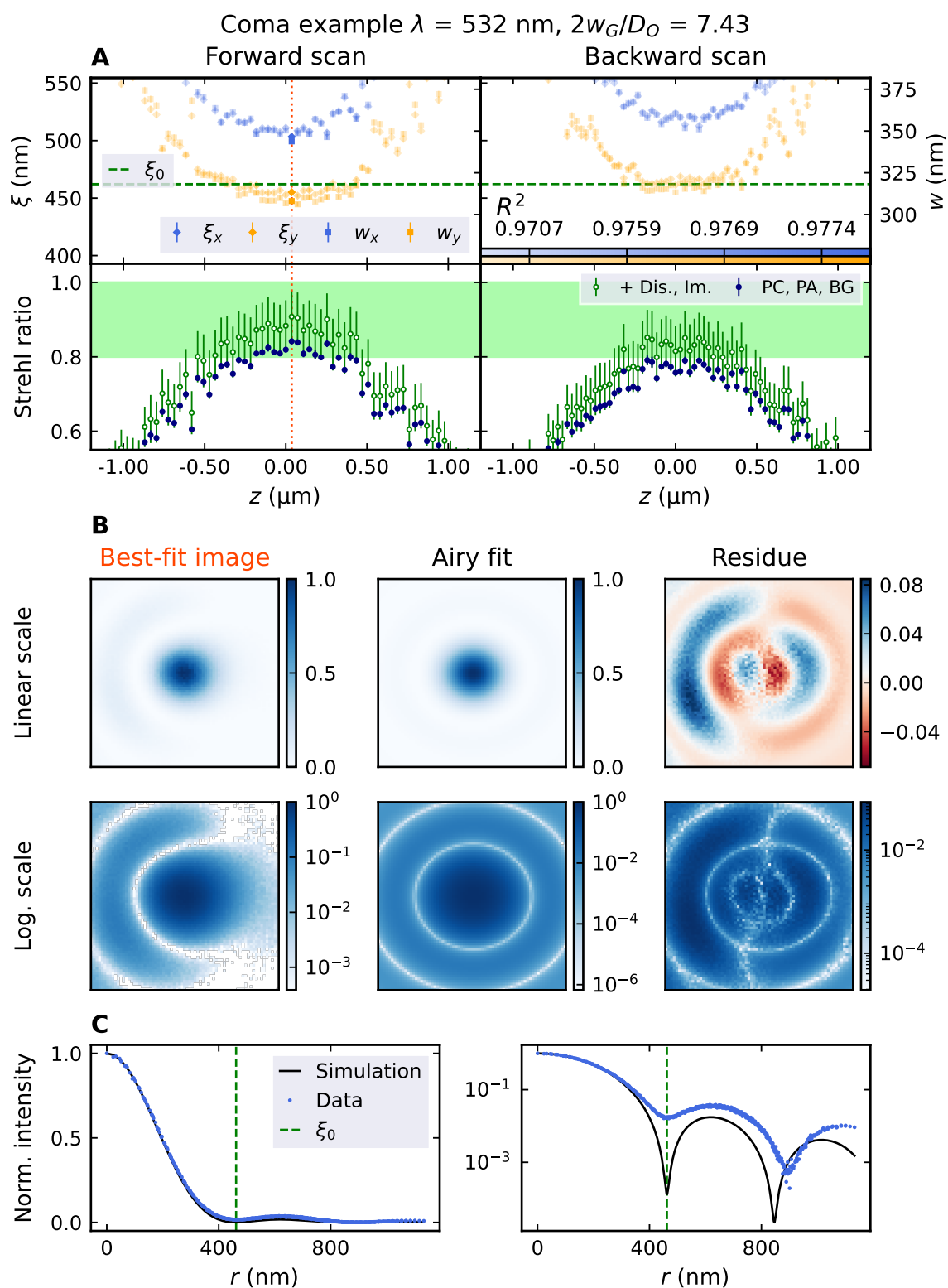


Figure F.6 – Single tweezer coma example, no AODs, $2w_G/D_0 = 7.43$, objective 002: Tweezer analysis. The Figure has the same structure as Figure 3.25.

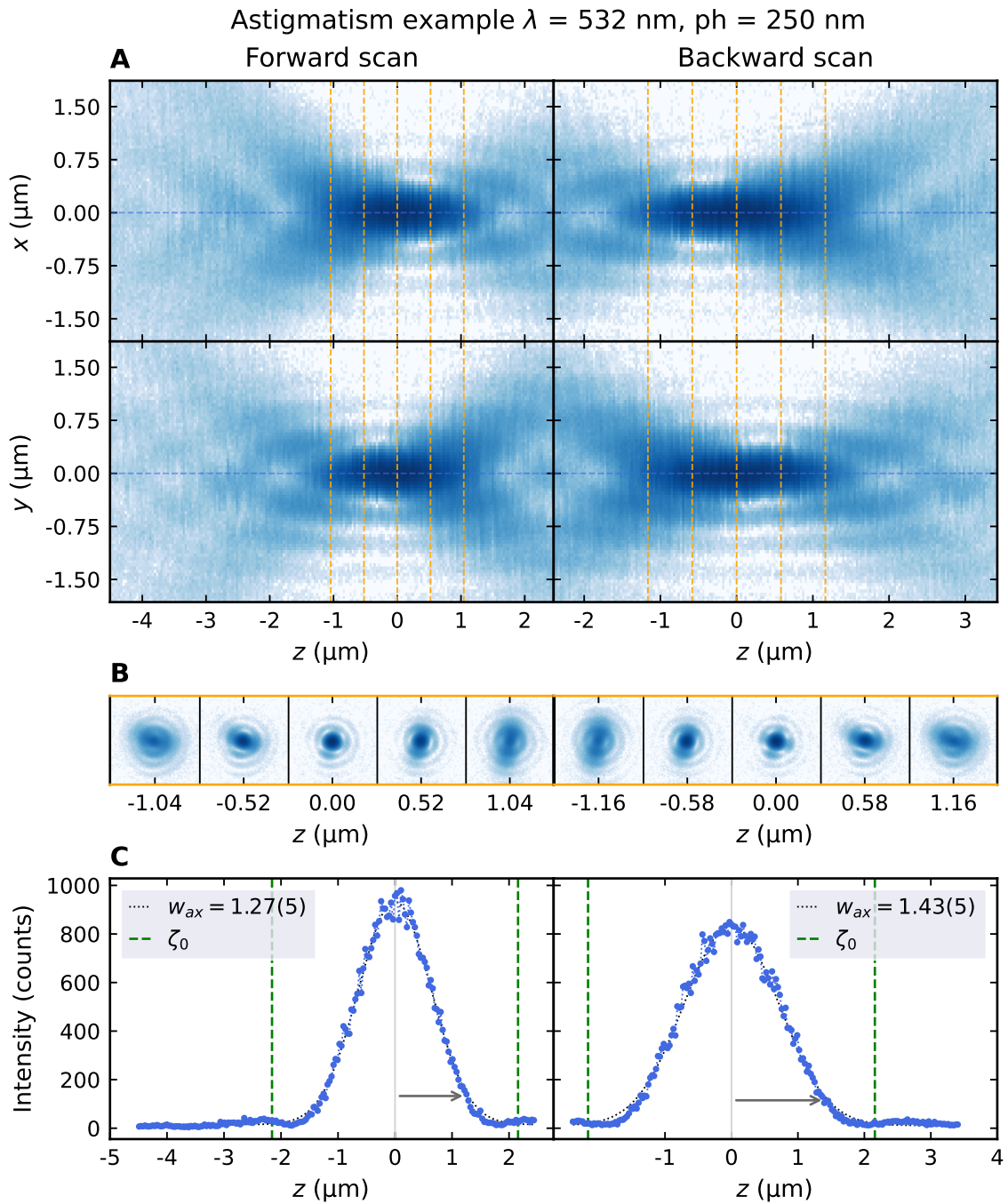


Figure F.7 – Imaging astigmatism example, curved dichroic mirror, objective 002: Tweezer shape. The Figure has the same structure as Figure 3.5a.

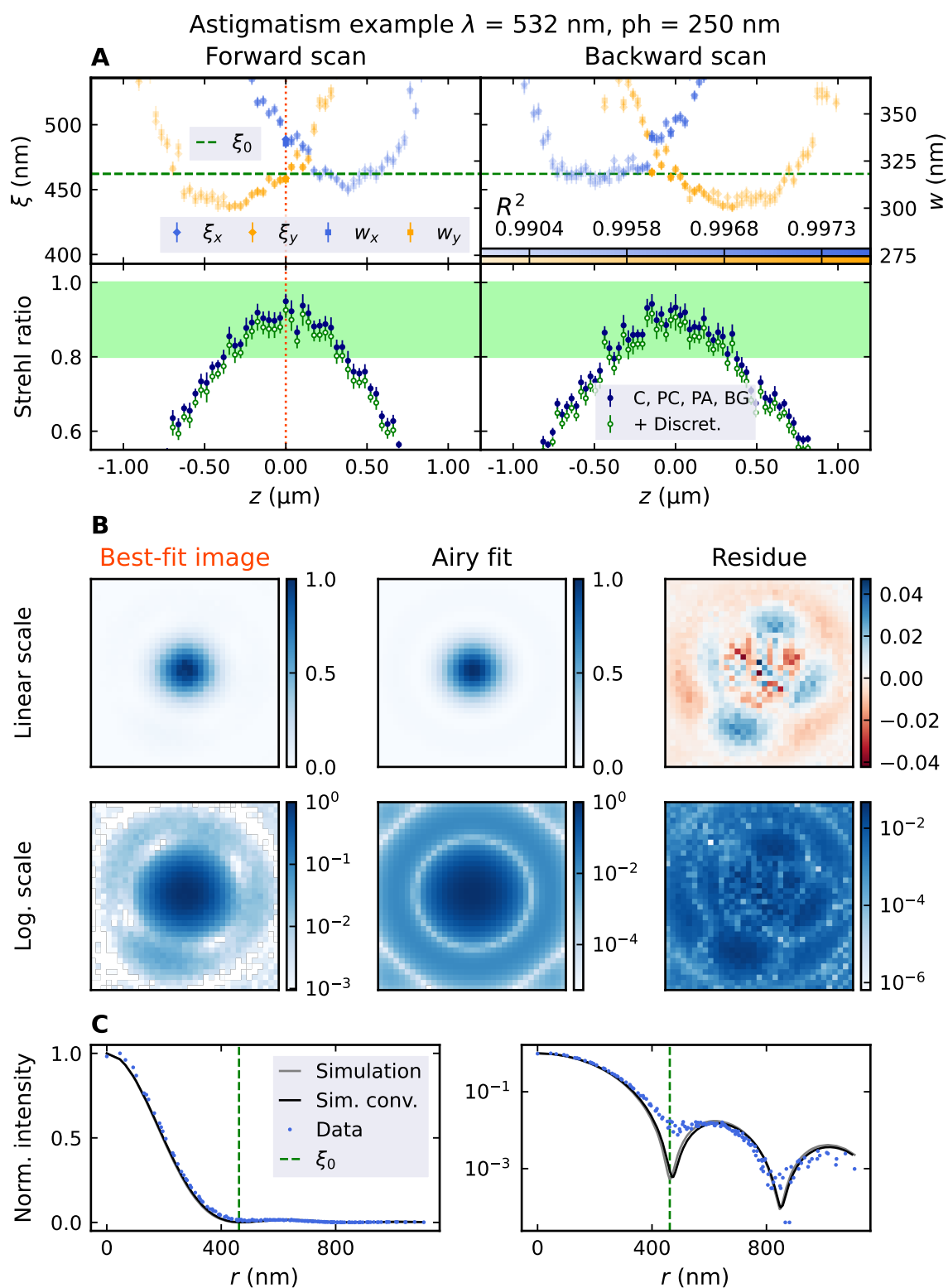


Figure F.8 – Imaging astigmatism example, curved dichroic mirror, objective 002: Tweezer analysis. The Figure has the same structure as Figure 3.6.

References

- [1] I. Bloch, J. Dalibard, and W. Zwerger, *Many-body physics with ultracold gases*, *Reviews of Modern Physics* **80**, 885–964 (2008) (cit. on p. 1).
- [2] H.-J. Briegel, T. Calarco, D. Jaksch, J. I. Cirac, and P. Zoller, *Quantum computing with neutral atoms*, *Journal of Modern Optics* **47**, 415–451 (2000) (cit. on p. 1).
- [3] J. Ye, H. J. Kimble, and H. Katori, *Quantum state engineering and precision metrology using state-insensitive light traps*, *Science* **320**, 1734–1738 (2008) (cit. on p. 1).
- [4] W. Li, I. Mourachko, M. W. Noel, and T. F. Gallagher, *Millimeter-wave spectroscopy of cold Rydberg atoms in a magneto-optical trap: quantum defects of the ns, np, and nd series*, *Physical Review A* **67**, 052502 (2003) (cit. on p. 1).
- [5] M. Greiner and S. Fölling, *Optical lattices*, *Nature* **453**, 736–738 (2008) (cit. on p. 1).
- [6] H. M. Price, O. Zilberberg, T. Ozawa, I. Carusotto, and N. Goldman, *Four-dimensional quantum hall effect with ultracold atoms*, *Physical Review Letters* **115**, 195303 (2015) (cit. on p. 1).
- [7] L.-M. Duan, E. Demler, and M. D. Lukin, *Controlling spin exchange interactions of ultracold atoms in optical lattices*, *Physical Review Letters* **91**, 090402 (2003) (cit. on p. 1).
- [8] W. H. Oskay, S. A. Diddams, E. A. Donley, T. M. Fortier, T. P. Heavner, L. Hollberg, W. M. Itano, S. R. Jefferts, M. J. Delaney, K. Kim, F. Levi, T. E. Parker, and J. C. Bergquist, *Single-atom optical clock with high accuracy*, *Physical Review Letters* **97**, 020801 (2006) (cit. on p. 1).
- [9] D. D. Yavuz, P. B. Kulatunga, E. Urban, T. A. Johnson, N. Proite, T. Henage, T. G. Walker, and M. Saffman, *Fast ground state manipulation of neutral atoms in microscopic optical traps*, *Physical Review Letters* **96**, 063001 (2006) (cit. on p. 1).
- [10] H. Katori, M. Takamoto, V. G. Pal'chikov, and V. D. Ovsiannikov, *Ultrastable optical clock with neutral atoms in an engineered light shift trap*, *Physical Review Letters* **91**, 173005 (2003) (cit. on p. 1).
- [11] A. J. Daley, M. M. Boyd, J. Ye, and P. Zoller, *Quantum computing with alkaline-earth-metal atoms*, *Physical Review Letters* **101**, 170504 (2008) (cit. on p. 1).
- [12] A. J. Daley, *Quantum computing and quantum simulation with group-II atoms*, *Quantum Information Processing* **10**, 865–884 (2011) (cit. on p. 1).

- [13] C. Chin, R. Grimm, P. Julienne, and E. Tiesinga, *Feshbach resonances in ultracold gases*, *Reviews of Modern Physics* **82**, 1225–1286 (2010) (cit. on p. 1).
- [14] D. Tong, S. M. Farooqi, J. Stanojevic, S. Krishnan, Y. P. Zhang, R. Côté, E. E. Eyler, and P. L. Gould, *Local blockade of rydberg excitation in an ultracold gas*, *Physical Review Letters* **93**, 063001 (2004) (cit. on p. 1).
- [15] J. N. A. Matthews, *Commercial optical traps emerge from biophysics labs*, *Physics Today* **62**, 26–28 (2009) (cit. on pp. 1, 24).
- [16] W. S. Bakr, J. I. Gillen, A. Peng, S. Fölling, and M. Greiner, *A quantum gas microscope for detecting single atoms in a hubbard-regime optical lattice*, *Nature* **462**, 74–77 (2009) (cit. on p. 1).
- [17] L. W. Cheuk, M. A. Nichols, M. Okan, T. Gersdorf, V. V. Ramasesh, W. S. Bakr, T. Lompe, and M. W. Zwierlein, *Quantum-gas microscope for fermionic atoms*, *Physical Review Letters* **114**, 193001 (2015) (cit. on p. 1).
- [18] C. Gross and W. S. Bakr, *Quantum gas microscopy for single atom and spin detection*, *Nature Physics* **17**, 1316–1323 (2021) (cit. on p. 1).
- [19] J. Koepsell, S. Hirthe, D. Bourgund, P. Sompet, J. Vijayan, G. Salomon, C. Gross, and I. Bloch, *Robust bilayer charge pumping for spin- and density-resolved quantum gas microscopy*, *Physical Review Letters* **125**, 010403 (2020) (cit. on p. 1).
- [20] J. Yang, L. Liu, J. Mongkolkiattichai, and P. Schauss, *Site-resolved imaging of ultracold fermions in a triangular-lattice quantum gas microscope*, *PRX Quantum* **2**, 020344 (2021) (cit. on p. 1).
- [21] C. Sträter, S. C. L. Srivastava, and A. Eckardt, *Floquet realization and signatures of one-dimensional anyons in an optical lattice*, *Physical Review Letters* **117**, 205303 (2016) (cit. on p. 1).
- [22] A. Ashkin and J. M. Dziedzic, *Optical trapping and manipulation of viruses and bacteria*, *Science* **235**, 1517–1520 (1987) (cit. on p. 2).
- [23] N. Schlosser, G. Reymond, I. Protsenko, and P. Grangier, *Sub-poissonian loading of single atoms in a microscopic dipole trap*, *Nature* **411**, 1024–1027 (2001) (cit. on p. 2).
- [24] C. Tuchendler, A. M. Lance, A. Browaeys, Y. R. P. Sortais, and P. Grangier, *Energy distribution and cooling of a single atom in an optical tweezer*, *Physical Review A* **78**, 033425 (2008) (cit. on p. 2).
- [25] A. M. Kaufman, B. J. Lester, and C. A. Regal, *Cooling a single atom in an optical tweezer to its quantum ground state*, *Physical Review X* **2**, 041014 (2012) (cit. on p. 2).
- [26] K.-N. Schymik, S. Pancaldi, F. Nogrette, D. Barredo, J. Paris, A. Browaeys, and T. Lahaye, *Single atoms with 6000-second trapping lifetimes in optical-tweezer arrays at cryogenic temperatures*, *Physical Review Applied* **16**, 034013 (2021) (cit. on p. 2).

- [27] M. A. Norcia, A. W. Young, W. J. Eckner, E. Oelker, J. Ye, and A. M. Kaufman, *Seconds-scale coherence on an optical clock transition in a tweezer array*, *Science* **366**, 93–97 (2019) (cit. on p. 2).
- [28] A. W. Young, W. J. Eckner, N. Schine, A. M. Childs, and A. M. Kaufman, *Tweezer-programmable 2d quantum walks in a hubbard-regime lattice*, Feb. 2, 2022, arXiv:2202.01204[cond-mat, physics:physics, physics:quant-ph] (cit. on p. 2).
- [29] J. P. Covey, I. S. Madjarov, A. Cooper, and M. Endres, *2000-times repeated imaging of strontium atoms in clock-magic tweezer arrays*, *Physical Review Letters* **122**, 173201 (2019) (cit. on p. 2).
- [30] C. Sheng, J. Hou, X. He, P. Xu, K. Wang, J. Zhuang, X. Li, M. Liu, J. Wang, and M. Zhan, *Efficient preparation of two-dimensional defect-free atom arrays with near-fewest sorting-atom moves*, *Physical Review Research* **3**, 023008 (2021) (cit. on p. 2).
- [31] P. Scholl, M. Schuler, H. J. Williams, A. A. Eberharter, D. Barredo, K.-N. Schymik, V. Lienhard, L.-P. Henry, T. C. Lang, T. Lahaye, A. M. Läuchli, and A. Browaeys, *Quantum simulation of 2d antiferromagnets with hundreds of rydberg atoms*, *Nature* **595**, 233–238 (2021) (cit. on p. 2).
- [32] Y. Wang, S. Shevate, T. M. Wintermantel, M. Morgado, G. Lothead, and S. Whitlock, *Preparation of hundreds of microscopic atomic ensembles in optical tweezer arrays*, *npj Quantum Information* **6**, 54 (2020) (cit. on p. 2).
- [33] H. Kim, W. Lee, H.-g. Lee, H. Jo, Y. Song, and J. Ahn, *In situ single-atom array synthesis using dynamic holographic optical tweezers*, *Nature Communications* **7**, 13317 (2016) (cit. on p. 2).
- [34] S. Saskin, J. T. Wilson, B. Grinkemeyer, and J. D. Thompson, *Narrow-line cooling and imaging of ytterbium atoms in an optical tweezer array*, *Physical Review Letters* **122**, 143002 (2019) (cit. on p. 2).
- [35] D. Barredo, S. de Léséleuc, V. Lienhard, T. Lahaye, and A. Browaeys, *An atom-by-atom assembler of defect-free arbitrary two-dimensional atomic arrays*, *Science* **354**, 1021–1023 (2016) (cit. on p. 2).
- [36] S. Ebadi, T. T. Wang, H. Levine, A. Keesling, G. Semeghini, A. Omran, D. Bluvstein, R. Samajdar, H. Pichler, W. W. Ho, S. Choi, S. Sachdev, M. Greiner, V. Vuletić, and M. D. Lukin, *Quantum phases of matter on a 256-atom programmable quantum simulator*, *Nature* **595**, 227–232 (2021) (cit. on p. 2).
- [37] K.-N. Schymik, B. Ximenez, E. Bloch, D. Dreon, A. Signoles, F. Nogrette, D. Barredo, A. Browaeys, and T. Lahaye, *In situ equalization of single-atom loading in large-scale optical tweezer arrays*, *Physical Review A* **106**, 022611 (2022) (cit. on p. 2).
- [38] G. Audi, O. Bersillon, J. Blachot, and A. Wapstra, *The nubase evaluation of nuclear and decay properties*, *Nuclear Physics A* **729**, 3–128 (2003) (cit. on p. 5).

- [39] W. Demtröder, *Experimentalphysik 2*, Springer-Lehrbuch (Springer Berlin Heidelberg, Berlin, Heidelberg, 2017) (cit. on pp. 6, 14, 17).
- [40] J. E. Greivenkamp, *Field guide to geometrical optics*, SPIE field guides v. FG01 (SPIE Press, Bellingham, Wash, 2004), 117 pp. (cit. on pp. 8, 9, 21).
- [41] R. Kingslake, *Lenses in photography: the practical guide to optics for photographers* (Case-Hoyt Corp. for Garden City Books, Garden City, N.Y, 1951) (cit. on pp. 9, 40).
- [42] J. W. Goodman, *Introduction to fourier optics* (Roberts and Company Publishers, 2005), 491 pp. (cit. on pp. 10, 11, 14).
- [43] M. V. Klein and T. E. Furtak, *Optics*, 2nd ed. (Wiley, 1986), 672 pp. (cit. on pp. 11, 13).
- [44] G. B. Airy, *On the diffraction of an object-glass with circular aperture*, Vol. 5 (Transactions of the Cambridge Philosophical Society, 1835), 476 pp. (cit. on p. 13).
- [45] B. R. Masters, *Superresolution optical microscopy: the quest for enhanced resolution and contrast*, Vol. 227, Springer Series in Optical Sciences (Springer International Publishing, Cham, 2020) (cit. on p. 14).
- [46] T. Latychevskaia, *Lateral and axial resolution criteria in incoherent and coherent optics and holography, near- and far-field regimes*, *Applied Optics* **58**, 3597 (2019) (cit. on pp. 14, 15).
- [47] F. Lord Rayleigh, *XXXI. investigations in optics, with special reference to the spectroscopy*, *The London, Edinburgh, and Dublin Philosophical Magazine and Journal of Science* **8**, Publisher: Taylor & Francis, 261–274 (1879), eprint: <https://doi.org/10.1080/14786447908639684> (cit. on p. 15).
- [48] M. Born and E. Wolf, *Principles of optics: 60th anniversary edition*, 7th ed. (Cambridge University Press, Dec. 19, 2019) (cit. on pp. 15, 17, 27).
- [49] B. Zhang, J. Zerubia, and J.-C. Olivo-Marin, *Gaussian approximations of fluorescence microscope point-spread function models*, *Applied Optics* **46**, 1819 (2007) (cit. on p. 17).
- [50] V. Lakshminarayanan and A. Fleck, *Zernike polynomials: a guide*, *Journal of Modern Optics* **58**, 545–561 (2011) (cit. on pp. 17, 18).
- [51] J. F. Bille, ed., *High resolution imaging in microscopy and ophthalmology: new frontiers in biomedical optics* (Springer International Publishing, Cham, 2019) (cit. on pp. 18, 21).
- [52] F. Wallner, *New Tools for Controlling Strontium Atoms with High Spectral and Spatial Resolution*, (2020) (cit. on pp. 19, 20).
- [53] V. N. Mahajan, *Strehl ratio for primary aberrations in terms of their aberration variance*, *Journal of the Optical Society of America* **73**, 860 (1983) (cit. on pp. 21, 22).

-
- [54] T. S. Ross, *Limitations and applicability of the maréchal approximation*, *Applied Optics* **48**, 1812 (2009) (cit. on p. 22).
- [55] R. Grimm, M. Weidemüller, and Y. B. Ovchinnikov, *Optical dipole traps for neutral atoms*, Feb. 24, 1999, arXiv:physics/9902072 (cit. on pp. 24, 25).
- [56] C. J. Foot, *Atomic physics*, Oxford master series in physics 7. Atomic, Optical, and laser physics, OCLC: ocm57478010 (Oxford University Press, Oxford ; New York, 2005), 331 pp. (cit. on p. 25).
- [57] J.-M. Liu, *Photonic devices* (Cambridge University Press, 2005) (cit. on pp. 27, 28).
- [58] A. Fuhrmanek, R. Bourgain, Y. R. P. Sortais, and A. Browaeys, *Light-assisted collisions between a few cold atoms in a microscopic dipole trap*, *Physical Review A* **85**, 062708 (2012) (cit. on p. 134).
- [59] L. C. Roberts Jr., M. D. Perrin, F. Marchis, A. Sivaramakrishnan, R. B. Makidon, J. C. Christou, B. A. Macintosh, L. A. Poyneer, M. A. van Dam, and M. Troy, *Is that really your strehl ratio?*, in (Oct. 25, 2004), p. 504 (cit. on p. 143).
- [60] A. P. Dhawan, R. M. Rangayyan, and R. Gordon, *Image restoration by wiener deconvolution in limited-view computed tomography*, *Applied Optics* **24**, 4013 (1985) (cit. on p. 154).
- [61] S. A. Hojjatoleslami, M. R. N. Avanaki, and A. G. Podoleanu, *Image quality improvement in optical coherence tomography using lucy-richardson deconvolution algorithm*, *Applied Optics* **52**, 5663 (2013) (cit. on p. 154).

Acknowledgements

First and foremost I want to thank **Prof. Monika Aidelsburger** for giving me the opportunity to be a part of this fascinating experiment, all the support also for my future plans and the new ideas suggested in the team meetings. In addition, she also provided highly appreciated words of motivation and acknowledgement and treated me at eye level with the PhD students.

Secondly, I thank my supervisor **Dr. Bharath Hebbe Madhusudhana** for our countless exciting discussions at the whiteboard, fast and profound simulations to solve open questions, and the freedom and individual responsibility he offered me in the lab. Learning from your hands-on way in building and adjusting parts in the lab was very helpful for creating the mounts, which would otherwise have consumed even more time. Finally, I thank you for your relaxed yet dedicated and open way, it was a pleasure working with you and I wish you all the best for your new lab.

Joining me as supervisor for the second half of my thesis, **Dr. Nelson Darkwah Oppong** helped me with his pragmatic way, never losing track of the main goal and thus saving me a lot of time when I concentrated too much on less relevant details. His suggestions were usually extremely accurate and proved to be immeasurably valuable. Your coding projects like the 3D tweezer simulation code and your broad IT knowledge were extremely helpful for me and the whole team and significantly contributed to my programming skills. I am also grateful for the LaTeX template you provided that enabled me to immediately start writing. Finally, I highly appreciated your funny and motivating words when you came by my setup and also wish you great results, now in your new team.

I also thank the entire SQM team for the great team work. In particular I want to express my gratitude to **Tim Höhn** and **Etienne Staub** who were always supportive even at the most uncommon times of the day, frequently showed interest in my project, even though we were on a different floor for more than half a year, and contributed funny conversations at lunch time. Towards the end of my thesis, it was particularly enjoyable to work with you in the main lab and I thank you for operating the experiment to trap the atoms in the tweezers.

Many thanks also go to **Clara Bachorz** and **Dalila Robledo** for the friendly and relaxed atmosphere in the office and the down-to-earth conversations. In particular, I thank Clara for our constructive arrangements that enabled us to work on the same optical table, in spite of my sensitive measurements.

Lastly I have to thank very much **Guillaume Brochier** as you convinced me close to the beginning of my thesis to use *scipy* for fitting the convolution, which I had previously programmed by hand and would have slowed down my data analysis by several orders of magnitude. Along those lines I also acknowledge the hint from **Lenny Romano** to use *numba* to speed up my code.

Furthermore, my thanks go to the whole quantum many-body systems group that always welcomed me and created a stimulating atmosphere. Especially I thank **Till Klostermann** and **Julian Wienand** for our objective discussions. In addition I thank **Paras Dwivedi** and **Justus Urbanetz** for the relaxing conversations in the prelab while my measurements were running.

My thanks also go to **Maximilian Ammenwerth**, who provided me with details of the objective characterization in the Strontium Rydberg lab and an enriching discussion about the Strehl ratio.

I also acknowledge the great support from **Ildiko Kecskesi** and **Bodo Hecker** for administrative and electronic questions during my time in SQM.

My particular thanks belong to the Kotthaus Chair at LMU and in particular **Philipp Altpeter** who made the SEM measurements possible.

In retrospective, I also thank **Dr. Alex Weigel** for teaching me good lab practice and a pragmatic way of thinking during my B.Sc., which proved essential during this thesis.

Very special thanks go to **Tim, Dalila, Etienne, Bharath** and **Sophie** for proof reading this thesis in a very limited period of time, which also fell into the holiday season. I greatly appreciated your help and learned a lot from your corrections.

Last but not least, I am particularly grateful to **Ulrike, Michael** and **Raphaela** and their exceptional support at home, their understanding when I worked late, and overwhelming respect for my dedication to this thesis.

Erklärung

Hiermit erkläre ich, die vorliegende Arbeit selbstständig verfasst zu haben und keine anderen als die in der Arbeit angegebenen Quellen und Hilfsmittel benutzt zu haben.

Ort, Datum

Unterschrift